frontiers | Research Topics

New insights into the mechanisms of resistance to anti-cancer drugs

Edited by
Simona Rapposelli and Francesco Bertoni

Published in
Frontiers in Oncology
Frontiers in Pharmacology

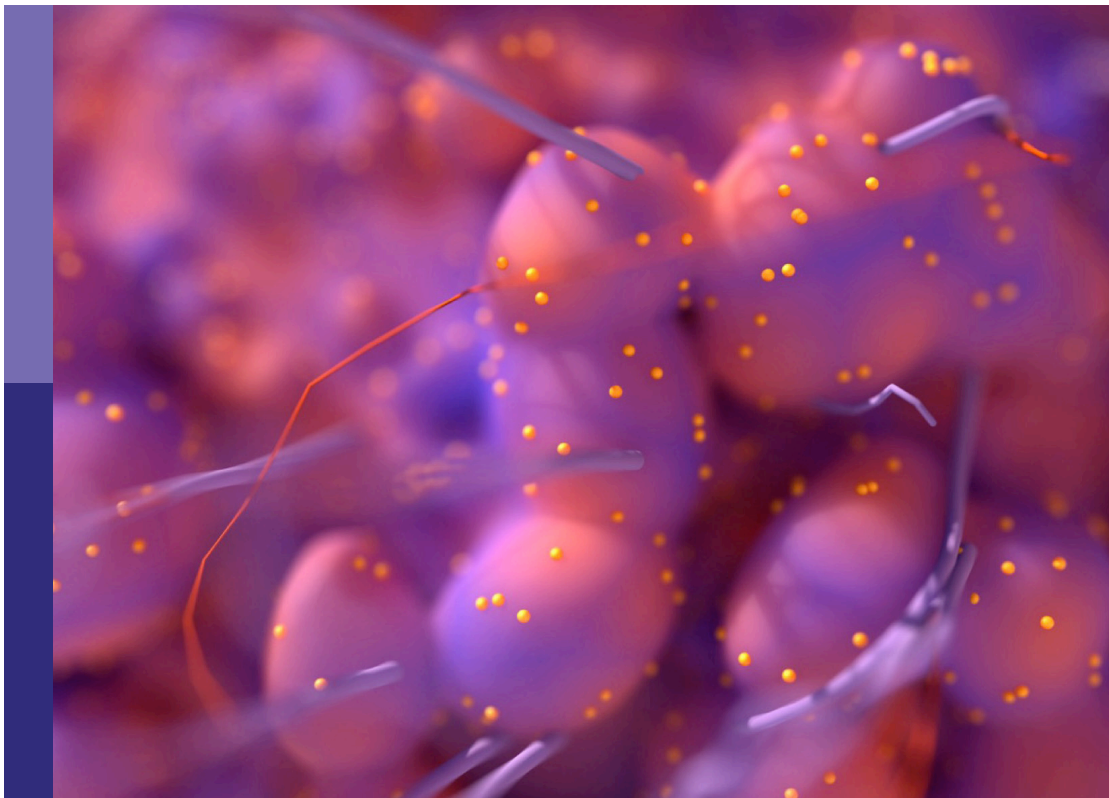

ISSN 1664-8714
ISBN 978-2-83251-896-0
DOI 10.3389/978-2-83251-896-0

About Frontiers

Frontiers is more than just an open access publisher of scholarly articles: it is a pioneering approach to the world of academia, radically improving the way scholarly research is managed. The grand vision of Frontiers is a world where all people have an equal opportunity to seek, share and generate knowledge. Frontiers provides immediate and permanent online open access to all its publications, but this alone is not enough to realize our grand goals.

Frontiers journal series

The Frontiers journal series is a multi-tier and interdisciplinary set of open-access, online journals, promising a paradigm shift from the current review, selection and dissemination processes in academic publishing. All Frontiers journals are driven by researchers for researchers; therefore, they constitute a service to the scholarly community. At the same time, the *Frontiers journal series* operates on a revolutionary invention, the tiered publishing system, initially addressing specific communities of scholars, and gradually climbing up to broader public understanding, thus serving the interests of the lay society, too.

Dedication to quality

Each Frontiers article is a landmark of the highest quality, thanks to genuinely collaborative interactions between authors and review editors, who include some of the world's best academicians. Research must be certified by peers before entering a stream of knowledge that may eventually reach the public - and shape society; therefore, Frontiers only applies the most rigorous and unbiased reviews. Frontiers revolutionizes research publishing by freely delivering the most outstanding research, evaluated with no bias from both the academic and social point of view. By applying the most advanced information technologies, Frontiers is catapulting scholarly publishing into a new generation.

What are Frontiers Research Topics?

Frontiers Research Topics are very popular trademarks of the *Frontiers journals series*: they are collections of at least ten articles, all centered on a particular subject. With their unique mix of varied contributions from Original Research to Review Articles, Frontiers Research Topics unify the most influential researchers, the latest key findings and historical advances in a hot research area.

Find out more on how to host your own Frontiers Research Topic or contribute to one as an author by contacting the Frontiers editorial office: frontiersin.org/about/contact

New insights into the mechanisms of resistance to anti-cancer drugs

Topic editors

Simona Rapposelli — University of Pisa, Italy

Francesco Bertoni — Institute of Oncology Research (IOR), Switzerland

Citation

Rapposelli, S., Bertoni, F., eds. (2023). *New insights into the mechanisms of resistance to anti-cancer drugs*. Lausanne: Frontiers Media SA.

doi: 10.3389/978-2-83251-896-0

Table of contents

frontiers | Frontiers in Oncology

TYPE Editorial
PUBLISHED 26 July 2022
DOI 10.3389/fonc.2022.990144

OPEN ACCESS

EDITED AND REVIEWED BY
Olivier Feron,
Universitécatholique de Louvain,
Belgium

*CORRESPONDENCE
Simona Rapposelli
simona.rapposelli@unipi.it
Francesco Bertoni
frbertoni@mac.com

SPECIALTY SECTION
This article was submitted to Pharmacology of Anti-Cancer Drugs, a section of the journal Frontiers in Oncology

RECEIVED 09 July 2022
ACCEPTED 11 July 2022
PUBLISHED 26 July 2022

CITATION
Bertoni F and Rapposelli S (2022) Editorial: New insights into the mechanisms of resistance to anti-cancer drugs.
Front. Oncol. 12:990144.
doi: 10.3389/fonc.2022.990144

Editorial: New insights into the mechanisms of resistance to anti-cancer drugs

Francesco Bertoni[1,2]* and Simona Rapposelli[3]*

[1]Institute of Oncology Research, Faculty of Biomedical Sciences, Università della Svizzera Italiana (USI), Bellinzona, Switzerland, [2]Oncology Institute of Southern Switzerland, Ente Ospedaliero Cantonale (EOC), Bellinzona, Switzerland, [3]Department of Pharmacy, University of Pisa, Pisa, Italy

KEYWORDS

chemoresistance, anti-cancer drugs, targeted-therapy, drug resistance, combination therapy

Editorial on the Research Topic
New insights into the mechanisms of resistance to anti-cancer drugs

The development of resistance after an initial response by tumor cells to anti-cancer therapies is perhaps one of the main causes that lead cancer patients to succumb to their disease. Resistance can develop against any type of therapies, including chemotherapy, targeted agents (small molecules or antibody-based) and cellular therapies. Several biological mechanisms are involved in drug resistance and include increased drug efflux, changes in drug metabolism, alterations in drug target interaction, evasion of apoptosis, and activation of alternative signaling pathways. Unfortunately, this high heterogeneity in response to treatments and the complexity of drug resistance, including the fact that multiple resistance mechanisms might be active at the same time in an individual patient, make it difficult to achieve complete responses and avoid tumor progressions and relapses. This Research Topic collects the latest data on mechanisms responsible for the onset of chemoresistance and presents new combination therapies to overcome the mechanisms of resistance in different types of cancer.

Two contributions are focused on triple-negative breast cancer, one of the tumors still much in need of effective therapies. Wu et al. explore modalities directly targeting the tumor cells, combining the mTOR inhibitor rapamycin with itraconazole, a broad-spectrum antifungal agent with also anti-tumor activity, achieving synergism although only in terms of increased cell cycle arrest but not in increased induction of cell death. Ghallab et al. instead explore a therapeutic modality targeting the interaction between the tumor cell and the tumor microenvironment. After studying CXCR2 and TFGbeta expression pattern and potential role in sustaining resistance to the chemotherapy agent doxorubicin, Ghallab et al. use AZD5069, a CXCR2 antagonist small molecule, to counteract this feedback and also to improve, at least in an *in vitro* system, the response to the anti-PDL-1 immune checkpoint modulator atezolizumab.

Three contributions are devoted to lung cancer. Zeng et al. describe two cases treated with the EGFR inhibitor osimertinib focusing on the genetic events preceding, and, especially, following the treatment with the tyrosine kinase inhibitor that might be involved in resistance to this targeted agent. The paper by Zeng et al. is on the role of glycosylation, and in particular of the resistance to cisplatin, and how, in cellular models of non-small cell lung cancer, the glycosylation inhibitor tunicamycin can reduce the chemoresistance. Xiang Li et al. look at the copper chelator ammonium tetrathiomolybdate (ATTM), used for the treatment of hereditary copper metabolism conditions and with possible anti-cancer properties.

In lung adenocarcinoma cells, the Authors observed that hydrogen sulfide, induced by the exposure to ATTM, might impede the anti-tumor activity of ATTM itself. Interestingly, hydrogen sulfide is also the topic of another work of this Research Topic. Indeed, Mao et al. provide evidence on the negative impact of hydrogen sulfide on the anti-tumor activity of the thioredoxin inhibitor PX-12.

Hu et al. have contributed to this issue with a comprehensive overview on the role of non-coding RNAs in sustaining the resistance to the multi-kinase inhibitor sorafenib in hepatocellular carcinoma, showing how non-genetic also contribute to the reduced activity of anti-cancer agents.

Finally, two contributions are on hematological cancers. Goel et al. use an *in vivo* model of T-cell lymphoma, namely the murine thymus-derived Dalton's Lymphoma to characterize the anti-tumor activity of the natural oxylipin methyl jasmonate, which appears to modulate the expression of various genes involved in drug resistance. Finally, Zhang et al. applied computer modeling to tackle the changes induced by the asciminib (ABL001), an allosteric BCR-ABL1 inhibitor, on BCR-ABL1 itself in its mutant and wild-type forms, to optimize co-administration of orthosteric tyrosine kinase inhibitors and allosteric drugs for chronic myeloid leukemia patients.

Author contributions

All authors listed have made a substantial, direct, and intellectual contribution to the work and approved it for publication

Conflict of interest

The authors declare that the research was conducted in the absence of any commercial or financial relationships that could be construed as a potential conflict of interest.

Publisher's note

frontiers in Oncology

ORIGINAL RESEARCH
published: 28 February 2020
doi: 10.3389/fonc.2020.00234

Is Hydrogen Sulfide a Concern During Treatment of Lung Adenocarcinoma With Ammonium Tetrathiomolybdate?

Xiang Li[1,2], Na Li[1,2], Li Huang[3], Shi Xu[4], Xue Zheng[1,2], Akil Hamsath[4], Mei Zhang[1,2], Lijun Dai[1,2], Hui Zhang[1,2], Justin Jong-Leong Wong[5], Ming Xian[4], Chun-tao Yang[1,2†] and Jinbao Liu[1,2*]*

[1] Affiliated Cancer Hospital & Institute of Guangzhou Medical University, Guangzhou, China, [2] Guangzhou Municipal and Guangdong Provincial Key Laboratory of Protein Modification and Degradation, School of Basic Medical Science, Guangzhou Medical University, Guangzhou, China, [3] Department of Pancreatobiliary Surgery, The First Affiliated Hospital of Sun Yat-sen University, Guangzhou, China, [4] Department of Chemistry, Washington State University, Pullman, WA, United States, [5] Epigenetics and RNA Biology Program Centenary Institute, The University of Sydney, Camperdown, NSW, Australia

OPEN ACCESS

Edited by:
Olivier Feron,
Université Catholique de Louvain, Belgium

Reviewed by:
Qi Zeng,
Xidian University, China
Wen Zhou,
Guangzhou University of Chinese Medicine, China

***Correspondence:**
Chun-tao Yang
cyang@gzhmu.edu.cn
Jinbao Liu
jliu@gzhmu.edu.cn

†ORCID:
Chun-tao Yang
orcid.org/0000-0002-5640-0930

Specialty section:
This article was submitted to Pharmacology of Anti-Cancer Drugs, a section of the journal Frontiers in Oncology

Received: 03 December 2019
Accepted: 11 February 2020
Published: 28 February 2020

Citation:
Li X, Li N, Huang L, Xu S, Zheng X, Hamsath A, Zhang M, Dai L, Zhang H, Wong JJ-L, Xian M, Yang C and Liu J (2020) Is Hydrogen Sulfide a Concern During Treatment of Lung Adenocarcinoma With Ammonium Tetrathiomolybdate? Front. Oncol. 10:234. doi: 10.3389/fonc.2020.00234

Ammonium tetrathiomolybdate (ATTM) has been used in breast cancer therapy for copper chelation, as elevated copper promotes tumor growth. ATTM is also an identified H_2S donor and endogenous H_2S facilitates $VitB_{12}$-induced S-adenosylmethionine (SAM) generation, which have been confirmed in m^6A methylation and lung cancer development. The m^6A modification was recently shown to participate in lung adenocarcinoma (LUAD) progression. These conflicting analyses of ATTM's anticancer vs. H_2S's carcinogenesis suggest that H_2S should not be ignored during LUAD's treatment with ATTM. This study was aimed to explore ATTM's effects on LUAD cells and mechanisms associated with H_2S and m^6A. It was found that treatment with ATTM inhibited cell growth at high concentrations, while enhanced cell growth at low concentrations in three LUAD cell lines (A549, HCC827, and PC9). However, another copper chelator triethylenetetramine, without H_2S releasing activity, was not found to induce cell growth. Low ATTM concentrations also elevated m^6A content in A549 cells. Analysis of differentially expressed genes in TCGA cohort indicated that m^6A writer METTL3 and reader YTHDF1 were upregulated while eraser FTO was downregulated in LUAD tissues, consistent with the findings of protein expression in patient tissues. ATTM treatment of A549 cells significantly increased METTL3/14 and YTHDF1 while decreased FTO expression. Furthermore, inhibition of m^6A with shMETTL3 RNA significantly attenuated eukaryotic translation initiation factor (eIF) expressions in A549 cells. Correlation analysis indicated that small nuclear ribonucleic protein PRPF6 was positively expressed with YTHDF1 in LUAD tissues. Knockdown of YTHDF1 partially blocked both basal and ATTM-induced PRPF6 expression, as well as A549 cell growth. Lastly, ATTM treatment not only raised intracellular H_2S content

but also upregulated H_2S-producing enzymes. Exogenous H_2S application mimicked ATTM's aforementioned effects, but the effects could be weakened by zinc-induced H_2S scavenging. Collectively, H_2S impedes ATTM-induced anticancer effects through YTHDF1-dependent PRPF6 m^6A methylation in lung adenocarcinoma cells.

Keywords: H_2S, m^6A methylation, Ammonium tetrathiomolybdate, lung cancer, PRPF6

INTRODUCTION

Ammonium tetrathiomolybdate (ATTM), with the formula $(NH_4)_2MoS_4$, is a strong copper chelator. It has been clinically used in the treatment of copper toxicosis for Wilson's disease. At high concentrations, copper is also known to promote angiogenesis, metabolism and oxidative phosphorylation, thereby leading to tumor growth (1–3). Consequently, copper-chelating agents, like ATTM and triethylenetetramine (TETA), have been investigated in the treatment of cancers, including breast cancer, thyroid cancer and liver cancer (4–8). Additionally, copper-dependent enzyme, superoxide dismutase (SOD) 1, has been reported to facilitate lung adenocarcinoma (LUAD) development (9). Therefore, ATTM therapy may theoretically be extended to LUAD.

Interestingly, our lab and others have recently discovered ATTM is a pH-dependent hydrogen sulfide (H_2S) donor (10, 11). There is no doubt that the development of ATTM as a therapeutic candidate must consider ATTM being both a copper chelator and a H_2S releaser. It should be noted that the links between H_2S and cancer development is still under debate (12). Some studies showed that elevated H_2S can induce angiogenesis and tumor cell proliferation, thereby contributing to cancer development (13–15). H_2S was also involved in $VitB_{12}$-induced S-adenosylmethionine (SAM) generation (16), and high $VitB_{12}$ has been found to raise the risk of lung cancer (17). Notably, in lung cancer tissues, endogenous H_2S and its producing enzymes, like cystathionine beta-synthase (CBS), cystathionine gamma lyase (CSE, also known as CTH) and 3-mercaptopyruvate sulfurtransferase (3-MST), are highly expressed thereby benefiting cancer development (18, 19).

N^6-Methyladenosine (m^6A) methylation is one major type of mRNA modification, dynamically modulated by the corresponding writers, erasers and readers (20). The m^6A methylation can differentially influence all fundamental aspects of mRNA metabolisms, including splicing, stability, and translation efficiency, when read by different m^6A readers (21–23). Recently, the m^6A methylation has been implicated in cancer pathogenesis, due to its induction of cell proliferation, invasion and immune disorders (24–28). Analysis of the cancer genome atlas (TCGA) cohort and recent studies (29, 30) indicated that m^6A writer, methyltransferase like (METTL) 3 is upregulated in LUAD. The eraser, fat mass and obesity-associated gene (FTO), is downregulated. Both increased METTL3 and decreased FTO strongly suggest that LUAD tissues exhibit high m^6A levels. However, no direct evidence has shown H_2S can regulate m^6A methylation, although H_2S enhances SAM generation (16), a cofactor of METTL3/14 complex. We therefore hypothesize that m^6A methylation is likely to be affected by H_2S derived from ATTM and participate in LUAD development.

In the present study, we observed the effects of ATTM on lung adenocarcinoma cells and explored the roles of m^6A in this process. Furthermore, we assessed the medication of H_2S in ATTM-induced tumor cell proliferation, invasion and growth. Lastly, a purposive strategy was developed to overcome ATTM's side-effects in LUAD therapy.

MATERIALS AND METHODS

Materials

ATTM and antibodies against METTL3 and METTL14 were purchased from Sigma-Aldrich Co. (St. Louis, MO, US). Antibodies against FTO and YTHDF1 were purchased from Abcam (Plc.Cambridge, MA, US). $CuSO_4$ and $Zn(OAc)_2$ were purchased from Meilun Biotechnology Co. (Dalian, China). TRIzol™ Regent (Invitrogen) was provide by Thermo Fisher Scientific Co. (Shanghai, China). Gemcell™ fetal bovine serum (FBS) was supplied by Gemini Company (Woodland, US).

Cell Culture, Growth, Proliferation, and Invasion Assays

Lung adenocarcinoma cell lines (A549 and HCC827) were purchased from Cell Bank of Type Culture Collection of Chinese Academy of Sciences (Shanghai, China), and PC9 was obtained from ATCC. The cells were maintained in RPMI-1640 medium supplemented with 10% FBS at 37°C under an atmosphere of 5% CO_2 and 95% air. They were passaged and harvested with 0.25% trypsin every other day.

Cell number was measured with Cell Counting Kit (CCK)-8 provided by Dojindo Lab (Kyushu, Japan). A549, HCC827, and PC9 cells were plated in 96-well plates at a density of 7, 000 cells/well. When grown to ∼60–70% confluence, the cells were treated correspondingly. After the treatments, the CCK-8 solution (100 μL) at a 1:10 dilution with FBS-free medium was added to each well-followed by a 2-h incubation at 37°C. Absorbance (*A*) was measured at 450 nm with a microplate reader (Molecular Devices, US).

Cell proliferation was tested with BeyoClick™ 5-Ethynyl-2′-deoxyuridine (EdU) kit (Haimen, China). After the treatment of A549 cells with ATTM for 48 h, EdU incorporation assay was performed according to the manufacturer's instructions. TMB-derived color was measured at 630 nm with the microplate reader.

Cell invasion was observed with Transwell Migration Assay, as described (31) with modifications. RPMI-1640 medium (1% FBS) containing ATTM or Na_2S in the absence or presence

of $Zn(OAc)_2$ was added to the lower chambers of the 12-well format transwells (8 μm-pore, BD Biosciences). A549 cells were seeded in the upper chambers at 10^5 cells per well, following a 48 h-culture. After that, the transwells were fixed in methanol, and stained with Giemsa solution. The unmigrated cells were removed from the top of the membranes using cotton swabs. To quantify the number of migrated cells in the bottom of the membrane, four random images of each group were taken at 10× under a light microscope. Migrated cell number was counted with Image J software.

Quantification of m^6A RNA Methylation

After treatments of A549 cells with increasing concentrations of ATTM for 24 h, total RNA was extracted using TaKaRa MiniBest kits (Kusatsu, Japan) and quantitated with NanoDrop 1000 spectrophotometer (Thermo Fisher, US). The m^6A RNA was detected with EpiQuik m^6A RNA Methylation Colorimetric kit (Farmingdale, US). Briefly, 200 ng of fresh extracted RNA sample was added into strip wells with RNA high binding solution, and incubated for 90 min at 37°C. After three washes, capture antibody, detection antibody, and enhancer solution were applied in turn, and incubated for 1 h at 37°C. After washes, color developing solution was added and incubated for 6 min in the dark. When the solution became blue in the m^6A positive wells, stop solution was added to turn the color into yellow. Lastly, the absorbance of stable yellow was measured at 450 nm with the microplate reader.

Western Blotting for Protein Expression

After exposed to 60 μM ATTM for 24 h, A549 cells were collected and split at 4°C. Total proteins in the lysate were quantitated with a BCA kit. Thirty micrograms of total protein sample were loaded in SDS-PAGE and electrophoresed. At the end of electrophoresis, the proteins were transferred to PVDF membranes. The membranes were blocked with 5% fat-free milk in Tris-base buffered saline containing 0.1% Tween-20 (TBS-T) for 1 h at room temperature, and then incubated with the primary antibodies against m^6A related proteins (METTL3, METTL14, FTO, and YTHDDF1), and H_2S-producing enzymes (CSE, CBS, and MPST), respectively, with gentle agitation overnight at 4°C. After three washes, corresponding HRP-conjugated secondary antibodies were applied and incubated for 1.5 h at room temperature. The signal was visualized using an enhanced chemiluminescence detection system. The intensity of bands was quantified with Image J software.

Analysis of TCGA Database and Measurement of Protein Expression of LUAD Patients

Transcriptional expressions of m^6A or H_2S related genes in primary tumor tissues and adjacent tissues of LUAD patients, as well as correlation analysis in tumor tissues, were performed through TCGA cohort research tool (*UALCAN*). Furthermore, the protein expressions of METTLE3, METTL14, and FTO in LUAD patients were verified with Western blotting assay as above.

Gene Knockdown

Gene expression microarray data were downloaded at https://www.ncbi.nlm.nih.gov/geo/query/acc.cgi?acc=GSE76367 (29). METTL3 was knocked down through short hairpin (sh) RNA in A549 cells, and gene expression was profiled by high throughput sequencing. Selected genes of eukaryotic translation initiation factors (eIFs) were shown as the maximum *vs.* minimum of the ratio shMETTL3 to shGFP.

Small interfering RNA (siRNA) against human YTHDF1 (Gene ID: 54915) was synthesized by GenePharma Co., Ltd (Shanghai, China). YTHDF1 siRNA and control random non-targeting siRNA were transfected into the A549 cells using Lipofectamine 2000 (Invitrogen, USA) (32). To raise the transfection efficiency, the cells were incubated with 20 nM YTHDF1 siRNA or Control siRNA for 6 h followed by a 24-h culture. The silencing ability was evaluated by Western blotting assay.

Quantitative Polymerase Chain Reaction for PRPF6 Gene Expression

Total RNAs were extracted from A549 cells and quantitated as above. First-strand cDNA was synthesized using TaqMan SYBR® Premix Ex TaqTM II (Tli RNase H Plus) virus reverse transcriptase and 2 μg RNA template in 20 μL reaction volume. The cDNA was used for real-time PCR with Prime Script RT reagent kit with gDNA Eraser (Life Technologies, US). Actin was used to normalize the expression of PRPF6. The results were analyzed using the comparative Ct method (2-ΔΔCt with logarithmic transformation). Primer sequences were displayed as below: PRPF6 forward 5-GTCATGCGTGCCGTGATTG-3 and reverse 5-TCCAGGGCATTGTGGGCTA-3, Actin forward 5-TGGCACCCAGCACAATGAA-3 and reverse 5-CTAAGTCATAGTCCGCCTAGAAGCA-3. PCRs were carried out as follows: initial denaturation at 95°C for 30 s, 40 cycles of 95°C for 5 s, 60°C for 34 s, and 95°C for 15 s, 60°C for 1 h, followed by a final extension at 95°C for 15 s.

Measurement of H_2S Levels

ATTM-mediated H_2S generation in cells was determined with a H_2S fluorescent probe WSP-5 (33). A549 cells were inoculated in 24-well plates and grown to 60∼70% confluence. After treated with ATTM, the cells were incubated with 10 μM WSP-5 in 1% FBS medium at 37°C for 30 min in the dark. Cell imaging was carried out after a slight wash with PBS. The intracellular H_2S-triggered fluorescence was visualized under AMG fluorescence microscopy (Advanced Microscopy Group, US).

For H_2S scavenging induced by $Zn(OAc)_2$, $CuSO_4$, $FeCl_3$ or $VitB_{12}$ was observed through a Unisense H_2S micro-sensor (Tueager 1, Denmark) (34). Into 5 mL PBS buffer, fresh Na_2S stock solution was added to produce a 100 μM Na_2S solution. When the curve reached the peak and kept stable, the same dose of above compounds was immediately added, respectively. The curves were recorded correspondingly with the H_2S sensor. For $Zn(OAc)_2$ or $CuSO_4$-induced continuous H_2S scavenging from ATTM solution was recorded for 6 h. Into 20 mL of 500 μM ATTM solution (pH 5), fresh $Zn(OAc)_2$ or $CuSO_4$ stock solutions was added, respectively, to produce a 250 μM solution. Real-time

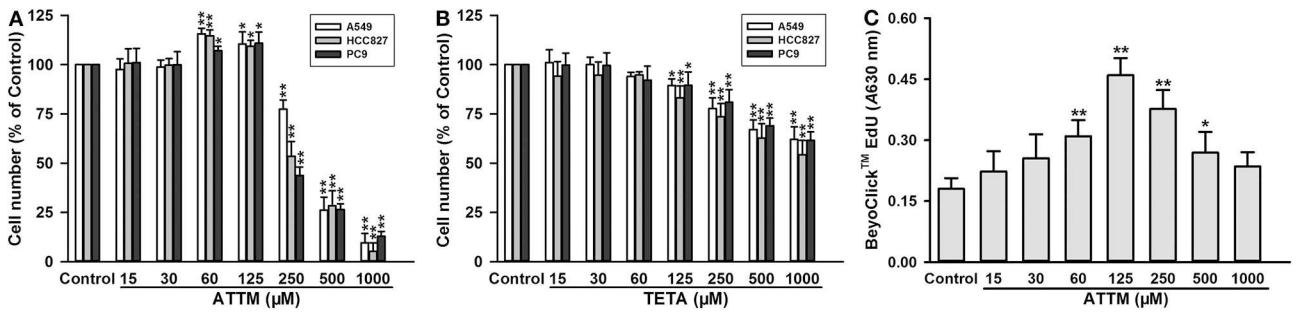

FIGURE 1 | Effects of copper chelators on LUAD cell growth and proliferation. After treatment with increasing concentrations of ATTM **(A)** or TETA **(B)** for 48 h, cell number of three cell lines (A549, HCC827, and PC9) was counted with CCK-8 assay. **(C)** After ATTM treatment for 48 h, the proliferation of A549 cells was tested with BeyoClick™ EdU kit. Data are expressed as mean ± SD of four independent experiments. $^*P < 0.05$, $^{**}P < 0.01$ vs. Control group.

H_2S content was monitored with the H_2S sensor and quantified against a standard curve.

Statistical Analysis

The experiment data are presented as means ± standard deviation (SD). Significance between groups was evaluated by one-way analysis of variance (ANOVA) followed by *Student-Newman-Keuls* test using GraphPad Prism 8 software (San Diego, US). A probability <0.05 was considered statistically significant.

RESULTS

Low ATTM Levels Enhanced Growth of Lung Adenocarcinoma Cells

As shown in **Figure 1A**, treatment with high concentrations (≥250 μM) of ATTM for 48 h remarkably reduced cell number, in three types of lung adenocarcinoma cells (A549, HCC827, and PC9). However, at low concentrations (from 60 to 125 μM), the treatment distinctively increased cell number. Notably, another copper chelator TETA, without H_2S releasing activity, was not found to elevate cell number at the same treatment profile (**Figure 1B**). Furthermore, 60–125 μM of ATTM treatment could also induce A549 cell proliferation as evaluated by EdU assay (**Figure 1C**). The result indicates that low ATTM concentrations are able to promote lung adenocarcinoma growth.

ATTM Induced mRNA m^6A Methylation in Lung Adenocarcinoma A549 Cells

To understand why ATTM enhanced lung adenocarcinoma growth, A549 cells were selected as a representative in the following experiments. Since mRNA m^6A methylation is involved in a variety of cancer growth including lung adenocarcinoma, intracellular m^6A mRNA level was then investigated. As shown in **Figure 2A**, the m^6A mRNA content was significantly elevated after the exposure of A549 cells to 60 μM ATTM for 24 h. However, the treatment duration (half of 48 h) did not alter cell number (**Figure 2B**) or growth status (**Figure 2C**). Notably, analysis of TCGA cohort shows that LUAD condition significantly upregulates the m^6A writer METTL3, while downregulates the m^6A eraser FTO (**Figure 2D**). The result indicates that ATTM can trigger mRNA m^6A methylation before cell growth in lung adenocarcinoma cells.

Upregulated m^6A Methylation Was Involved in LUAD Progression and ATTM-Induced mRNA Translation in Lung Adenocarcinoma A549 Cells

To uncover the mechanisms underlying the increased m^6A mRNA levels in ATTM-treated cells, m^6A related proteins were detected with Western blot. As shown in **Figures 3A,C**, comparing with the adjacent tissues, the writer (METTL3 and METLL14) expressions were upregulated in tumor tissues of LUAD patients, while the eraser FTO expression was downregulated. Importantly, the writer (METTL3 and METLL14) expressions in A549 cells could also be upregulated, while the eraser FTO could be downregulated under ATTM treatment (**Figures 3B,D**), supporting the finding of the increased intracellular m^6A content. To confirm the roles of m^6A methylation, we investigated gene expression profile in METTL3 knockdown A549 cells. As shown in **Figure 3E**, shRNA-mediated METTL3 knockdown significantly inhibited the expressions of translation initiation factors, including eIFs (2B3, 3B, 3C/CL, 3D, 3IP1, 4A1, and 5/5A). This suggests that m^6A methylation is necessary to translation process in A549 cells, and that the elevated m^6A levels may be important for LUAD progression and ATTM-induced tumor growth.

YTHDF1 Mediated ATTM-Induced Growth in Lung Adenocarcinoma A549 Cells

Although the increased m^6A writer METTL3/14 and the decreased eraser FTO can result in the enhancement of m^6A content, it is the m^6A readers that directly determine the outcome of m^6A methylated mRNA. With TCGA cohort, we examined the four common m^6A readers (YTHDF1, YTHDF2, YTHDF3, and YTHDC1) in LUAD tumor samples and normal samples, and found YTHDF1 highly expressed in tumor tissues (**Figure 4A**). The increased YTHDF1 continuously expressed within various stages of LUAD (**Figure 4B**). Importantly, it was found that treatment of A549 cells with 60 μM ATTM for 24 h remarkably upregulated YTHDF1 protein expression (**Figure 4C**). After

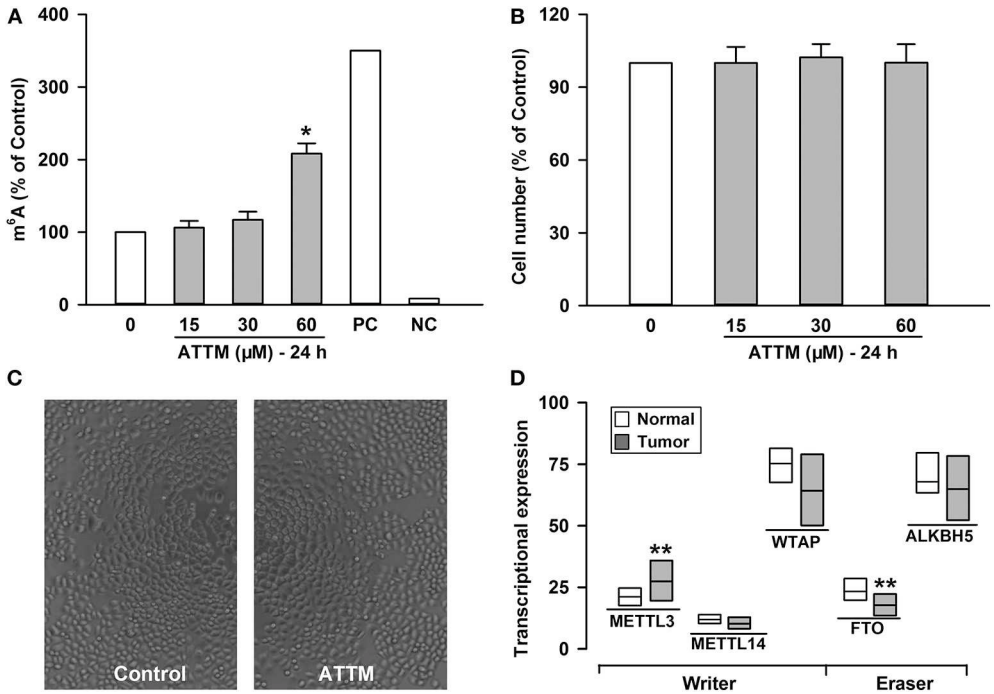

FIGURE 2 | Effects of ATTM on mRNA m^6A methylation in A549 cells. The cells were treated with ATTM at concentrations ranging from 0 to 60 μM for 24 h. **(A)** The content of m^6A mRNA was measured with a commercial kit (PC, positive control; NC, negative control). **(B)** The cell number was tested with CCK-8 assay. Data are presented as mean ± SD. $n = 4$. $^*P < 0.01$ vs. Control group. **(C)** Growth of quiescent A549 cells and cells exposed to 60 μM ATTM for 24 h were captured using digital microphotograph. **(D)** Expressions of the m^6A writers (METTL3, METTL14, and WTAP) and erasers (FTO and ALKBH5) were analyzed between LUAD primary tumor tissues ($n = 515$) and normal tissues ($n = 59$) in TCGA cohort. Data are showed as median ± quartile. $^{**}P < 10^{-4}$ vs. Normal tissues.

knockdown of YTHDF1 with siRNA in A549 cells (**Figure 4D**), both basal and ATTM-triggered cell growth were attenuated (**Figure 4E**).

YTHDF1-Mediated Cell Growth Was Associated With PRPF6 Induction in ATTM-Treated A549 Cells

To explore targets involved in YTHDF1-mediated A549 cell growth, we screened genes that are positively correlated with YTHDF1 in TCGA LUAD cohort. As shown in **Figure 5A**, PRPF6 was found to be positively expressed with YTHDF1 in LUAD tissues ($r = 0.72$). Similar to YTHDF1's expression profile, the increased PRPF6 expression lasted various stages of LUAD (**Figure 5B**). Furthermore, qPCR analysis showed that PRPF6 mRNA level was significantly reduced after YTHDF1 knockdown in A549 cells. Additionally, the knockdown attenuated ATTM-induced PRPF6 mRNA expression (**Figure 5C**). The result reveals that PRPF6 may be a potential target gene involved in YTHDF1-mediated A549 cell growth.

H_2S Was Significant to ATTM-Induced A549 Cell Growth and m^6A Methylation

ATTM was previously demonstrated to generate H_2S on acid conditions in our lab. As shown in **Figure 6A**, the exposure of A549 cells to ATTM markedly raised intracellular H_2S levels. With TCGA cohort, we studied endogenous H_2S synthetase expressions and, found that CSE/CTH, CBS and MPST expressions were enhanced in tumor tissues comparing with normal samples (**Figure 6B**). Additionally, the exposure of A549 cells to 60 μM ATTM for 24 h obviously upregulated CBS and MPST expressions (**Figures 6D,E**), however, remarkable change of CSE was not found (**Figure 6C**). Notably, direct H_2S donation (Na_2S) could also induce m^6A methylation (**Figure 6F**), as well as cell growth (**Figure 6G**), proliferation (**Figure 6H**) and invasion (**Figures 6I,J**), indicating H_2S being an effector in ATTM-induced m^6A methylation and cell growth.

H_2S Scavenging Attenuated ATTM-Induced A549 Cell Growth and m^6A Methylation

Since the enhanced H_2S generation was involved in ATTM-induced A549 cell growth and m^6A methylation, scavenging H_2S might overcome these side-effects of ATTM. Through testing several common H_2S scavengers, it was found that $Zn(OAc)_2$ and $CuSO_4$ had powerful ability to remove H_2S, while the ability of $VitB_{12}$ and $FeCl_3$ was weak or even undetectable (**Figure 7A**). Additional cell viability examination showed that both $Zn(OAc)_2$ and $CuSO_4$ were non-toxic at concentrations <25 μM (**Figures 7B,C**).

To make sure H_2S is necessary to ATTM-induced biological process in A549 cells, we observed the scavenging effect

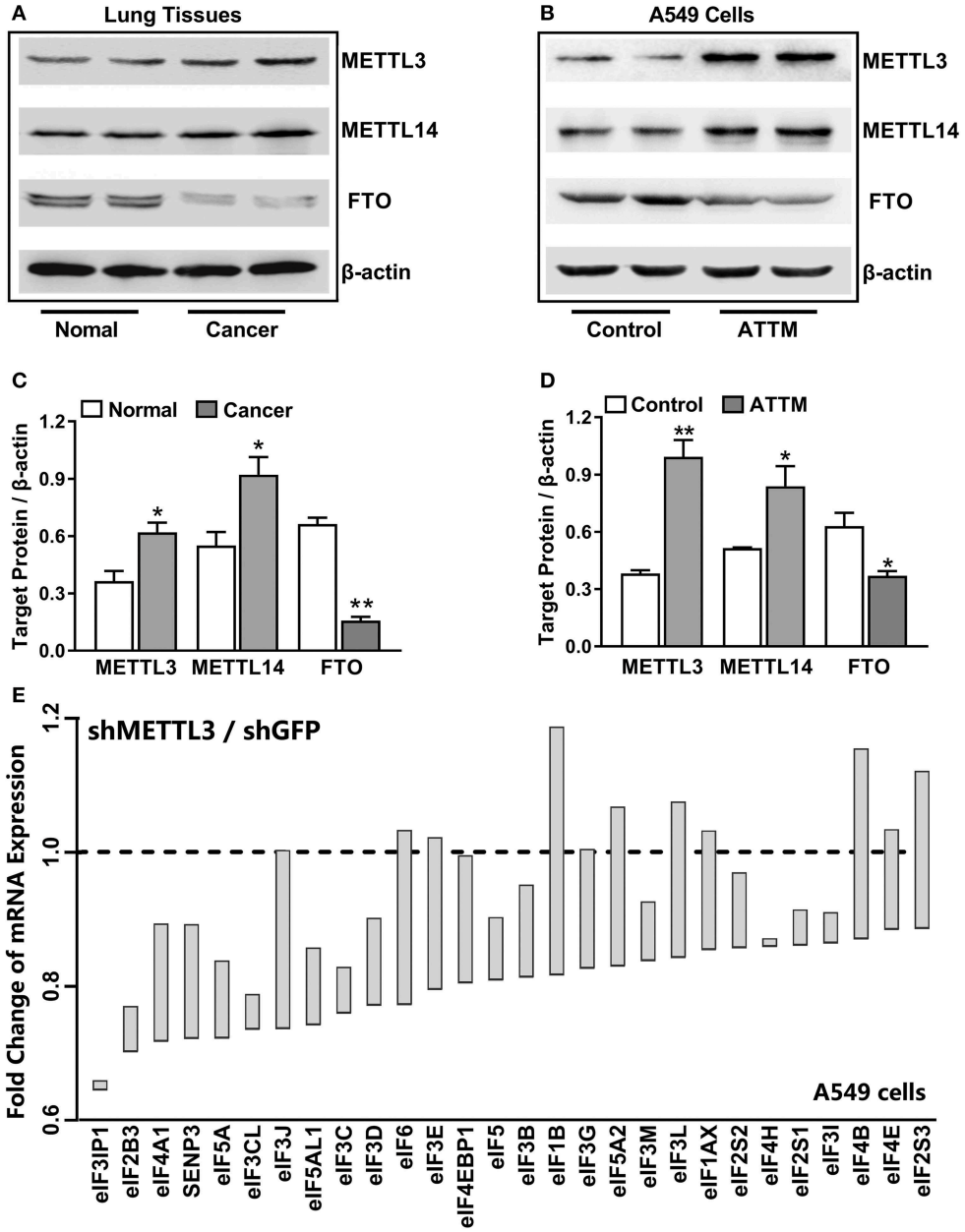

FIGURE 3 | Effects of lung cancer condition and ATTM treatment on m^6A related protein expression. **(A)** Confirmed LUAD patient tumor tissues and normal adjacent tissues, as well as **(B)** A549 cells treated with 60 μM ATTM for 24 h and normal cells, were collected and split. Total proteins were used for Western blot assay to measure the expressions of METTL3, METTL14, and FTO. Corresponding quantifications were shown as **(C,D)**, respectively. Data are presented as mean ± SD. $n = 2$. $^*P < 0.05$, $^{**}P < 0.01$ vs. Control group. **(E)** A549 cells transfected with shMETTL3 or shGFP were collected and gene expression was profiled by high throughput sequencing. Representative genes of eukaryotic translation initiation factors (eIFs) were analyzed and shown as the maximum *vs.* minimum of the ratio of shMETTL3 to shGFP (GSE76367).

of $Zn(OAc)_2$ or $CuSO_4$ on ATTM-induced H_2S release within a period of 6 h. As shown in **Figure 8A**, adding 25 μM $Zn(OAc)_2$ or $CuSO_4$ time-dependently attenuated ATTM-induced H_2S release. Notably, application of 25 μM $Zn(OAc)_2$ inhibited ATTM-induced cell growth (**Figure 8B**), proliferation (**Figure 6H**) and invasion (**Figures 6I,J**). More importantly, $Zn(OAc)_2$ was also able to attenuate ATTM-induced m^6A methylation (**Figure 8C**). Collectively, the result suggests that H_2S is necessary and sufficient to ATTM-induced biological changes, and scavenging H_2S can potentially overcome ATTM's side-effects in lung cancer treatment.

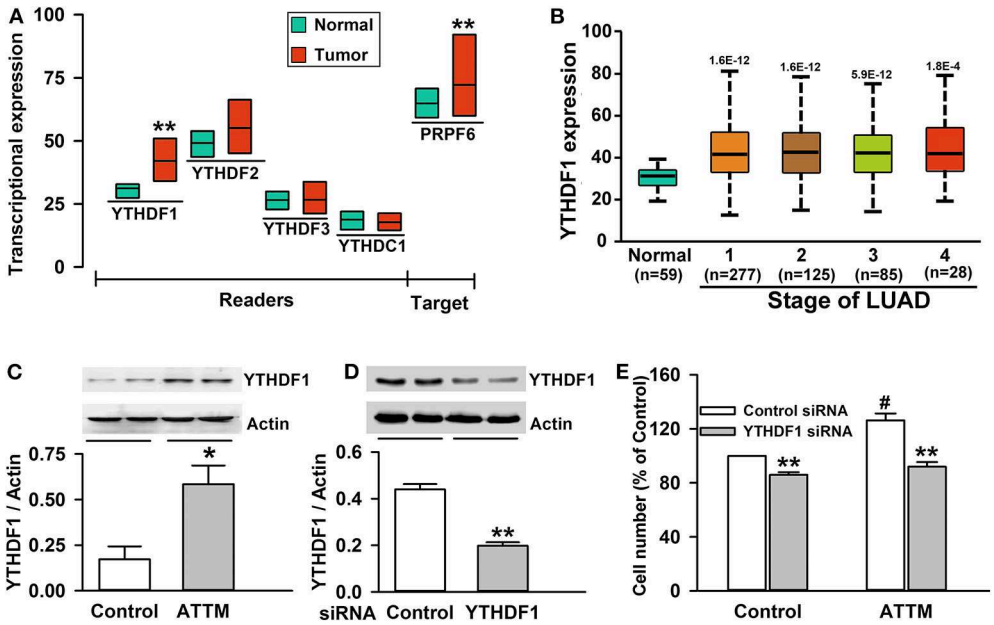

FIGURE 4 | Roles of YTHDF1 in ATTM-induced growth of A549 cells. **(A)** Expressions of m^6A readers (YTHDF1, YTHDF2, YTHDF3, and YTHDC1) and a potential target gene (PRPF6) were compared between LUAD patient primary tumor tissues ($n = 515$) and normal tissues ($n = 59$) in TCGA cohort. Data are shown as median ± quartile. $^{**}P < 10^{-7}$ vs. Normal tissues. **(B)** YTHDF1 gene expression in normal tissues and various LUAD stage tissues was analyzed in TCGA cohort. Data are shown in the box plot. **(C)** After treatment of A549 cells with 60 μM ATTM for 24 h, YTHDF1 protein expression was measured with Western blot assay, and the densitometric analysis was performed. Data are shown as mean ± SD. $n = 2$. $^{*}P < 0.05$ vs. Control group. **(D)** A549 cells were incubated with YTHDF1 siRNA or Control siRNA for 6 h followed by a 24-h culture, and the interference efficiency was determined with Western blot assay. **(E)** Normal A549 cells and YTHDF1-knocked down cells were treated with 60 μM ATTM for 48 h, and cell counting assay was performed. Data are presented as mean ± SD. $n = 4$. $^{**}P < 0.01$ vs. Control siRNA cells, $^{\#}P < 0.01$ vs. ATTM-free cells.

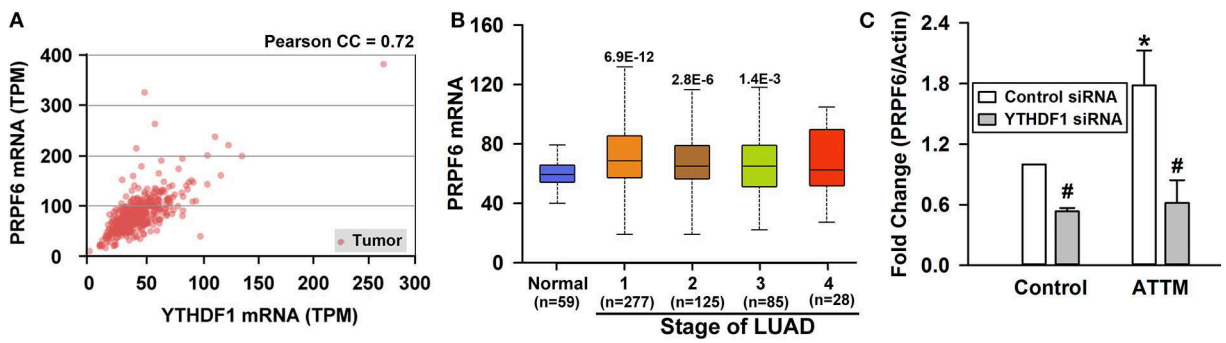

FIGURE 5 | Identification of PRPF6 as a target gene of YTHDF1. **(A)** TCGA-based correlation analysis between PRPF6 and YTHDF1. **(B)** PRPF6 gene expression in normal tissues and various LUAD stage tissues was analyzed through TCGA cohort. Data are shown in the box plot. **(C)** Normal A549 cells and YTHDF1-knocked down cells were treated with 60 μM ATTM and then mRNA was extracted for analysis of PRPF6 expression with qPCR. Data are shown as mean ± SD. $n = 4$. $^{*}P <$ 0.01 vs. ATTM-free cells. $^{\#}P < 0.01$ vs. Control siRNA cells.

DISCUSSION

In the present study, ATTM was found to promote cell growth, proliferation and invasion in lung adenocarcinoma cells, through YTHDF1-dependent PRPF6 m^6A methylation. H_2S was involved in the above effects of ATTM. Importantly, scavenging H_2S was proved to overcome the side-effects of ATTM in lung cancer therapy.

Copper ions are known to essentially maintain organism functions by regulating activity of key enzymes, like cytochrome C oxidase and SOD. However, its aberrant increase in plasma usually leads to pathological consequences, including Wilson's disease and cancers. During cancer development, high contents of copper are believed to enhance angiogenesis and blood supply, as well as activity of mitochondrial cytochrome C oxidase, thereby promoting solid tumor growth and metastasis (1–3, 35).

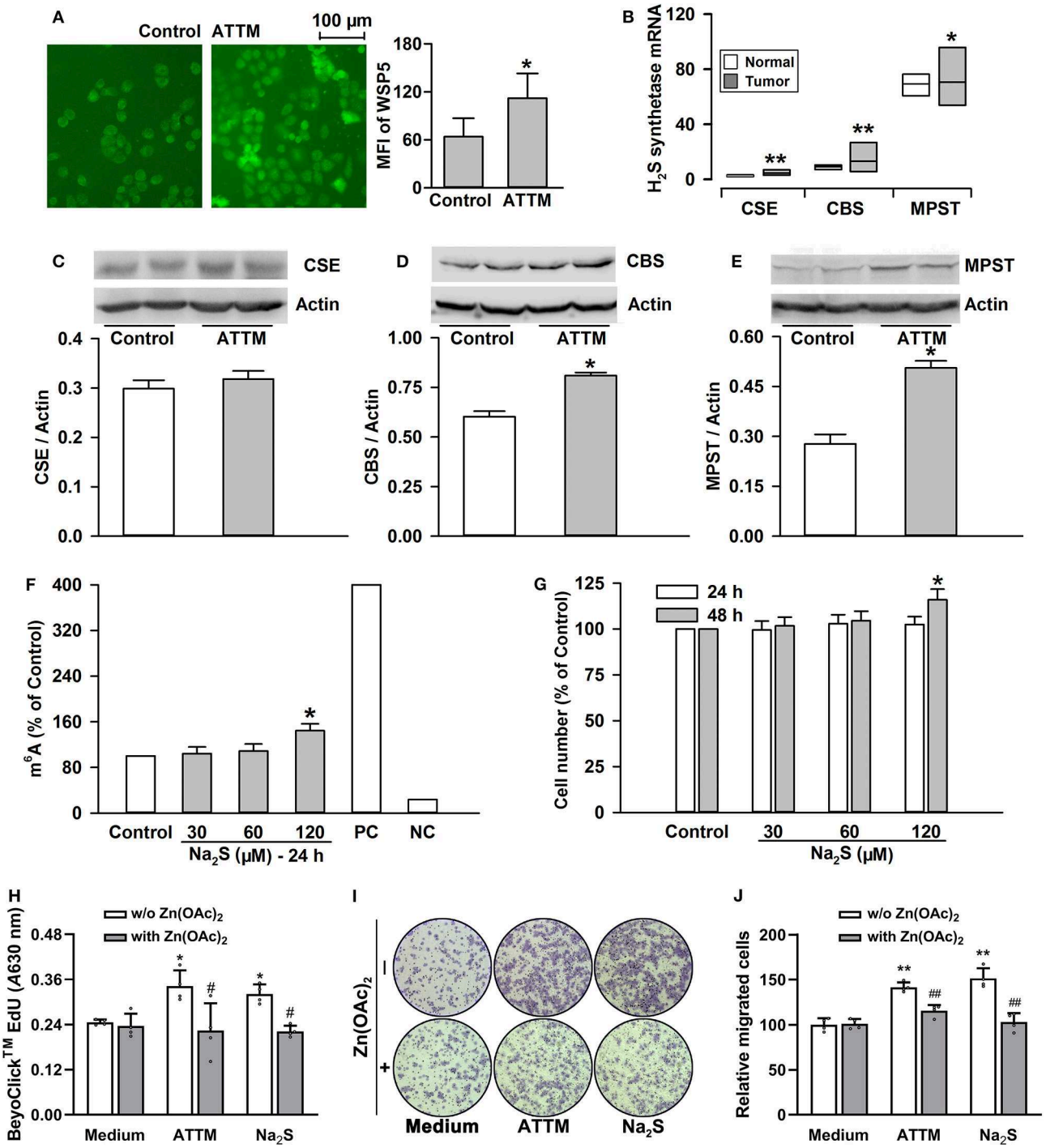

FIGURE 6 | Roles of H_2S in ATTM-induced m^6A methylation and growth in A549 cells. **(A)** A549 cells were treated with normal medium (Control) and 60 μM ATTM for 3 h. Intracellular H_2S content was observed with H_2S fluorescent probe WSP5 staining followed by fluorescence photography. **(B)** Expressions of H_2S synthetases (CSE, CBS and MPST) were compared between LUAD patient primary tumor tissues ($n = 515$) and normal tissues ($n = 59$) in TCGA cohort. Data are showed as median ± quartile. $^*P < 10^{-6}$, $^{**}P < 10^{-11}$ *vs.* Normal tissues. **(C–E)** After treatment of A549 cells with 60 μM ATTM for 24 h, the expressions of CSE **(C)**, CBS **(D)**, and MPST **(E)** were measured with Western blot, and then densitometric analysis were performed. Data are shown as mean ± SD. $n = 2$. $^*P < 0.05$ *vs.* Control. **(F)** A549 cells were treated with increasing concentrations of Na_2S for 24 h, intracellular m^6A mRNA was tested with a commercial kit. **(G)** A549 cells were treated with the indicated concentrations of Na_2S for 24 and 48 h, respectively. The cell number was measured with CCK-8 assay. **(H–J)** A549 cells were treated with 60 μM ATTM or 120 μM Na_2S in the absence or presence of 25 μM $Zn(OAc)_2$ for 48 h. Cell proliferation was tested with EdU incorporation assay **(H)**. Cell invasion was observed with Transwell Migration Assay **(I)** and migrated cells were counted using ImageJ software. Data are presented as the mean ± SD. $n = 4$. $^*P < 0.05$, $^{**}P < 0.01$ *vs.* Control/Medium. $^{\#}P < 0.05$, $^{\#\#}P < 0.01$ *vs.* $Zn(OAc)_2$ free group.

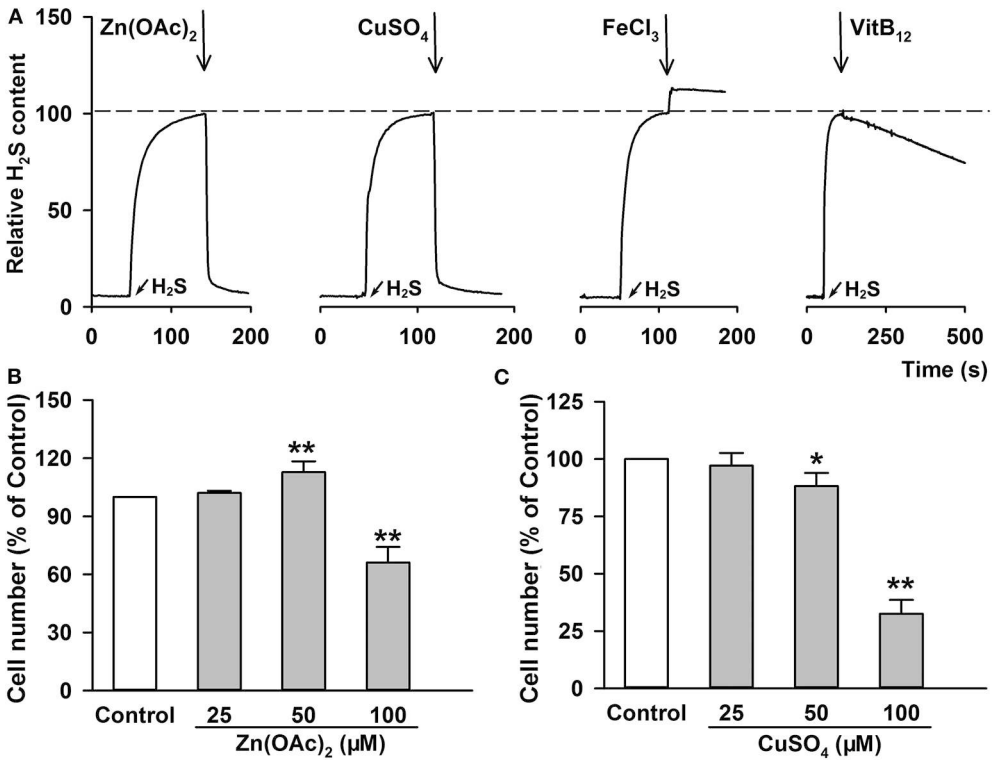

FIGURE 7 | H_2S removing efficiency and cell toxicity of the indicated H_2S scavengers. **(A)** After adding 100 μM Na_2S, the same amount of indicated H_2S scavengers, including $Zn(OAc)_2$, $CuSO_4$, $FeCl_3$ and $VitB_{12}$, were added, respectively. The content of H_2S molecule was monitored with a Unisense H_2S microsensor. **(B–C)** A549 cells were treated with increasing concentration of $Zn(OAc)_2$ **(B)** or $CuSO_4$ **(C)** for 24 h. The cell number was measured with CCK-8 assay. Data are shown as the mean ± SD. $n = 4$. $^*P < 0.05$, $^{**}P < 0.01$ *vs.* Control group.

Consequently, chelating agents of copper ions, like ATTM and TETA, have become promising anticancer drugs. The clinical trials of ATTM in breast cancer have recently made great progress (4–6). Notably, SOD1, a copper-dependent enzyme, was reported to participate in lung cancer growth and has become a significant therapeutic target (9). Therefore, ATTM may exert anticancer effects in lung adenocarcinoma through reduction of copper ions. In this study, at high concentrations, ATTM could indeed inhibit the growth of lung adenocarcinoma cells. However, at low concentrations, ATTM distinctively promoted tumor cell growth, as well as proliferation and invasion. The result was different from the reported effects of ATTM in breast cancer (6) and BRAF-driven papillary thyroid cancer (8), which suggests that the findings in other cancers should not be simply transplanted to lung cancer.

To uncover the mechanisms underlying ATTM-induced LUAD cell growth at low concentrations, we investigated mRNA m^6A methylation, which has been involved in different cancer growth, like liver cancer (25), endometrial cancer (26), and leukemia (36). The m^6A writer METTL3 has also been reported to promote lung cancer survival, growth, and invasion (29). We therefore speculated that the aberrant m^6A methylation was involved in ATTM-induced growth of LUAD cells. By measuring m^6A content in A549 cells, we found that the treatment with ATTM for 24 h significantly enhanced intracellular m^6A content, while it did not significantly alter cell growth, suggesting m^6A methylation occurs earlier than cell growth. Generally, m^6A methylated mRNA can be synthesized via methyltransferase complex m^6A writer, mainly consisting of METTL3, METTL14, and WTAP. Meanwhile, CH_3- can also be erased from the RNA using FTO and ALKBH5. Therefore, the process is dynamic and reversible (37). The increased METTL3 and decreased FTO in the present TCGA analysis indicate that the dysregulated writer and/or eraser may be responsible for the increased m^6A content in lung adenocarcinoma cells. This finding was supported by protein measurement in LUAD patients. Importantly, we found that the treatment with ATTM significantly augmented METTL3, but reduced FTO protein expression. ATTM could also upregulate METTL14 expression, which was not consistent with the TCGA analysis. We hypothesize that this difference may be due to the uncertainty of gene expression between mRNA level and protein level. Notably, for the increased METTL3 and decreased FTO, the present experiment matched the TCGA analysis. Such unique expressions, we believe, contribute to ATTM-induced m^6A increase in A549 cells.

However, the roles of m^6A in cancer biology are complicated and conflicting, i.e., tumor growth or anti-tumor (38). In addition, the binding of target mRNA with the writers or erasers is usually instantaneous. Therefore, it may be significant to examine the roles of m^6A readers. To date, YT521-B homology

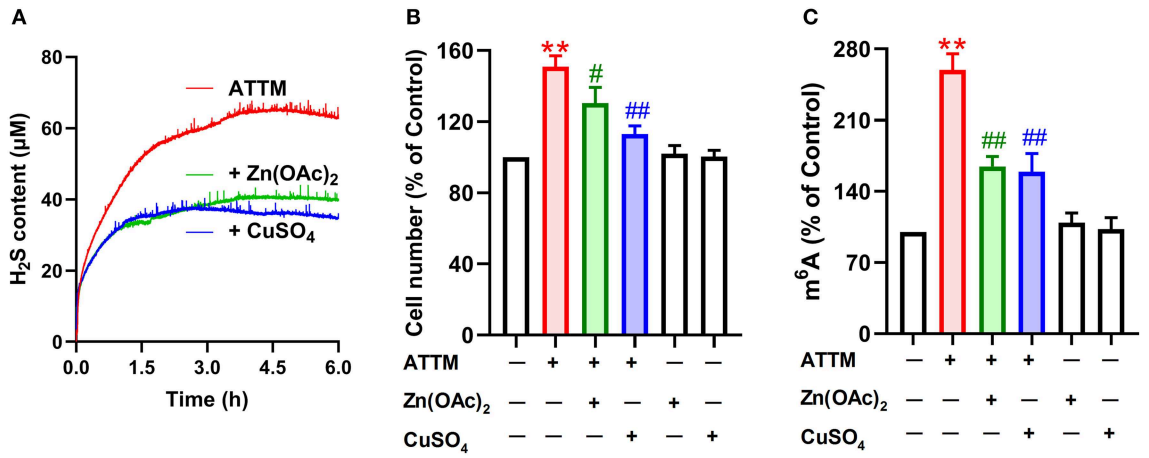

FIGURE 8 | Effects of H_2S scavengers on ATTM-induced A549 cell growth and m^6A methylation. **(A)** ATTM solutions were prepared in the presence or absence of 25 μM $Zn(OAc)_2$ or $CuSO_4$. Subsequently, released H_2S was recorded for 6 h with a H_2S micro-sensor. **(B)** A549 cells were treated with 60 μM ATTM for 48 h in the absence or presence of 25 μM $Zn(OAc)_2$ or $CuSO_4$. The cell number was measured with CCK-8 assay. **(C)** A549 cells were treated with 60 μM ATTM for 24 h in the absence or presence of 25 μM $Zn(OAc)_2$ or $CuSO_4$. Intracellular m^6A mRNA was tested with a commercial kit. Data are shown as the mean ± SD. $n = 4$. $^{**}P < 0.01$ *vs.* Control. $^{\#}P < 0.05$, $^{\#\#}P < 0.01$ *vs.* ATTM alone group.

(YTH) domain family of proteins, like YTHDF1, YTHDF2, YTHDF3, and YTHDC1, have been identified as m^6A readers. YTHDF1-mediated mRNA spicing can increase translation efficiency, whereas YTHDF2-mediated mRNA decay will inhibit gene expression (21). The TCGA analysis indicates that the expression of YTHDF1, instead of YTHDF2/3 or YTHDC1, was markedly increased in LUAD tissues. In A549 cells, the elevated m^6A mainly induced gene translation, evidenced by shMETTL3-mediated eIFs' downregulation (29). Western blot test showed that YTHDF1 expression could be upregulated by ATTM. Significantly, YTHDF1 siRNA inhibited basal and ATTM-induced cell growth, confirming the involvement of YTHDF1 in basal and environment-stimulated lung tumorigenesis.

As an m^6A reader, it is necessary to discover YTHDF1's target genes. The TCGA analysis shows that PRPF6 (a small nuclear ribonucleic protein) is positively expressed with YTHDF1. The GEO analysis shows that PRPF6 can be attenuated through METTL3 knockdown (shGFP 1023 vs. shMETTL3 848). Additional analysis of MeT V2.0 m^6A database indicates that m^6A PRPF6 mRNA can be discerned and read by YTHDF1 in Hela cells via GRAC motif (R is G or A) (21). Actually, PRPF6 has been reported to promote lung cancer growth (39, 40). With these bioinformatics analyses and reports, PRPF6 is probably a target gene of YTHDF1. Importantly, the present experiment showed that ATTM treatment not only induced YTHDF1 expression, but also enhanced PRPF6 mRNA abundance. Both basal and ATTM-induced PRPF6 upregulation was significantly reduced by YTHDF1 knockdown, which was supported by previous reports (39, 40). As documented, the increased PRPF6 can alter the constitutive and alternative splicing of ZAK kinase, thereby activating cancer-related pathways, like AP-1, ERK, and JNK (41). In sum, it is believed that ATTM treatment upregulated METTL3/14 and downregulated FTO, raising intracellular m^6A mRNA like PRPF6. Furthermore, these specific mRNAs were read by YTHDF1, and the spicing and translation of cancer growth-related genes were induced, thereby promoting LUAD tumor growth.

Significantly, we dissected the cause of ATTM-induced m^6A methylation and cell growth. Copper chelating can exert anticancer effects through inhibiting angiogenesis (4, 6, 8). However, apart from copper chelating, ATTM can release H_2S (10, 11). Studies have shown that the homeostasis of H_2S is essential in organisms (42–46). In this study, we found that intracellular H_2S level was markedly raised after ATTM treatment. Nevertheless, another copper chelator without H_2S releasing ability, TETA, did not alter tumor cell growth. Direct H_2S donation exerted similar effects to ATTM. The effects of ATTM or H_2S could be abolished by $CuSO_4$ or $Zn(OAc)_2$. Besides H_2S releasing, we found ATTM induced the expressions of H_2S-production enzymes, which have been reported to participate in survival and chemoresistance of LUAD cells (18). Therefore, H_2S is significant and necessary for ATTM-induced m^6A methylation and lung cancer growth.

In healthy individuals, plasma free copper ion content is <20 μM (47), but for cancer patients, the recommended daily ATTM dosage was 90 mg (48). Therefore, the initial plasma ATTM should be much higher than that of free copper ions, so the free ATTM will release H_2S during the clinical application (11). Of course, zinc application maybe overcomes ATTM's side-effects in LUAD therapy, while copper should not be recommended because of its tumorigenesis risk.

Interestingly, during the examination of $VitB_{12}$ roles, it was found that $VitB_{12}$ enhanced ATTM-induced LUAD cell growth (**Supplementary Figure 1**), unlike zinc or copper's inhibitory effects. However, both our study and previous reports suggest

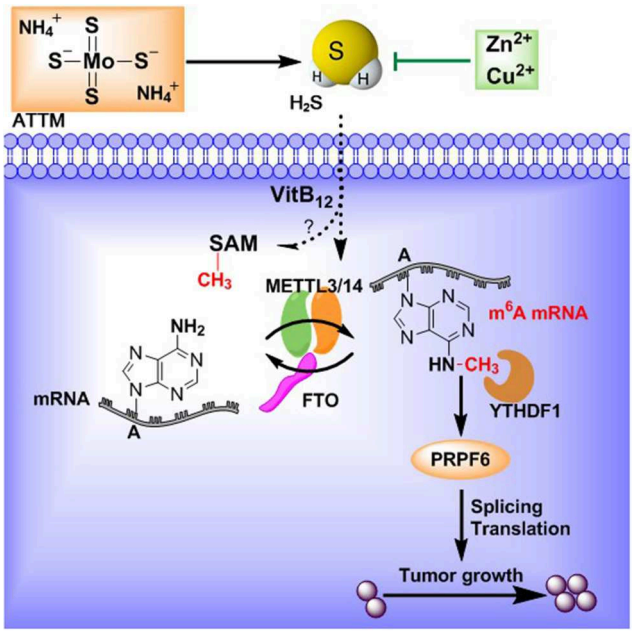

FIGURE 9 | ATTM-produced H_2S induces mRNA m^6A methylation and promotes lung adenocarcinoma growth.

$VitB_{12}$ is a H_2S scavenger (34, 49). In fact, it has been documented that high $VitB_{12}$ can raise the risk of lung cancer (17). H_2S can also facilitate $VitB_{12}$-induced SAM generation (16) that is the first substrate of METTTL3/14 complex. These findings further support H_2S-induced m^6A methylation promotes LUAD tumor growth.

In conclusion, the present study demonstrated that ATTM can induce m^6A methylation through upregulation of METTL3 and downregulation of FTO in LUAD cells. YTHDF1-mediated PRPF6 expression is probably a pivotal reason. The effects of ATTM are closely associated with H_2S generation (**Figure 9**). For the first time, this work reveals a potential risk and mechanism for ATTM application in LUAD treatment. Meanwhile, this is the first report on the roles of H_2S in m^6A methylation.

DATA AVAILABILITY STATEMENT

The datasets generated for this study can be found in TCGA LUAD (http://ualcan.path.uab.edu/analysis.html), GSE76367 (https://www.ncbi.nlm.nih.gov/geo/).

ETHICS STATEMENT

The studies involving human participants were reviewed and approved by Medical Ethics Committee of Guangzhou Medical University. The patients/participants provided their written informed consent to participate in this study.

AUTHOR CONTRIBUTIONS

CY, MX, JL, and JW designed the experiments and wrote the manuscript. XL, NL, SX, and XZ performed all the experiments and statistical analyses. LH and HZ analyzed the clinical data and provided the patient tissues. LD, MZ, and AH provided the critical suggestions. All the authors reviewed the final manuscript.

FUNDING

This work was supported by Natural Science Foundation of Guangdong Province Grant (2017A030313892), Guangzhou Key Medical Discipline Construction Project.

ACKNOWLEDGMENTS

We thank R. Gregory and S. Lin in Harvard Medical School for their mRNA expression array. We also thank the reviewers for the careful and valuable work.

SUPPLEMENTARY MATERIAL

The Supplementary Material for this article can be found online at: https://www.frontiersin.org/articles/10.3389/fonc.2020.00234/full#supplementary-material

Supplementary Figure 1 | Effects of $VitB_{12}$ on ATTM-induced A549 cell growth.

REFERENCES

1. Raju KS, Alessandri G, Ziche M, Gullino PM. Ceruloplasmin, copper ions, and angiogenesis. *J Natl Cancer Inst.* (1982) 69:1183–8.
2. Ishida S, Andreux P, Poitry-Yamate C, Auwerx J, Hanahan D. Bioavailable copper modulates oxidative phosphorylation and growth of tumors. *Proc Natl Acad Sci USA.* (2013) 110:19507–12. doi: 10.1073/pnas.1318431110
3. Hyvonen MT, Ucal S, Pasanen M, Peraniemi S, Weisell J, Khomutov M, et al. Triethylenetetramine modulates polyamine and energy metabolism and inhibits cancer cell proliferation. *Biochem J.* (2016) 473:1433–41. doi: 10.1042/BCJ20160134
4. Yoshii J, Yoshiji H, Kuriyama S, Ikenaka Y, Noguchi R, Okuda H, et al. The copper-chelating agent, trientine, suppresses tumor development and angiogenesis in the murine hepatocellular carcinoma cells. *Int J Cancer.* (2001) 94:768–73. doi: 10.1002/ijc.1537
5. Sproull M, Brechbiel M, Camphausen K. Antiangiogenic therapy through copper chelation. *Expert Opin Ther Targets.* (2003) 7:405–9. doi: 10.1517/14728222.7.3.405
6. Garber K. BIOMEDICINE. Targeting copper to treat breast cancer. *Science.* (2015) 349:128–9. doi: 10.1126/science.349.6244.128
7. Chan N, Willis A, Kornhauser N, Ward MM, Lee SB, Nackos E, et al. Influencing the tumor microenvironment: a phase II study of copper depletion using tetrathiomolybdate in patients with breast cancer at high risk for recurrence and in preclinical models of lung metastases. *Clin Cancer Res.* (2017) 23:666–76. doi: 10.1158/1078-0432.CCR-16-1326
8. Xu M, Casio M, Range DE, Sosa JA, Counter CM. Copper chelation as targeted therapy in a mouse model of oncogenic BRAF-driven papillary thyroid cancer. *Clin Cancer Res.* (2018) 24:4271–81. doi: 10.1158/1078-0432.CCR-17-3705

9. Somwar R, Erdjument-Bromage H, Larsson E, Shum D, Lockwood WW, Yang G, et al. Superoxide dismutase 1 (SOD1) is a target for a small molecule identified in a screen for inhibitors of the growth of lung adenocarcinoma cell lines. *Proc Natl Acad Sci USA.* (2011) 108:16375–80. doi: 10.1073/pnas.1113554108
10. Xu S, Yang CT, Meng FH, Pacheco A, Chen L, Xian M. Ammonium tetrathiomolybdate as a water-soluble and slow-release hydrogen sulfide donor. *Bioorg Med Chem Lett.* (2016) 26:1585–8. doi: 10.1016/j.bmcl.2016.02.005
11. Dyson A, Dal-Pizzol F, Sabbatini G, Lach AB, Galfo F, Dos Santos Cardoso J, et al. Ammonium tetrathiomolybdate following ischemia/reperfusion injury: chemistry, pharmacology, and impact of a new class of sulfide donor in preclinical injury models. *PLoS Med.* (2017) 14:e1002310. doi: 10.1371/journal.pmed.1002310
12. Hellmich MR, Szabo C. Hydrogen sulfide and cancer. *Handb Exp Pharmacol.* (2015) 230:233–41. doi: 10.1007/978-3-319-18144-8_12
13. Szabo C, Coletta C, Chao C, Modis K, Szczesny B, Papapetropoulos A, et al. Tumor-derived hydrogen sulfide, produced by cystathionine-beta-synthase, stimulates bioenergetics, cell proliferation, and angiogenesis in colon cancer. *Proc Natl Acad Sci USA.* (2013) 110:12474–9. doi: 10.1073/pnas.1306241110
14. Untereiner AA, Olah G, Modis K, Hellmich MR, Szabo C. H_2S-induced S-sulfhydration of lactate dehydrogenase a (LDHA) stimulates cellular bioenergetics in HCT116 colon cancer cells. *Biochem Pharmacol.* (2017) 136:86–98. doi: 10.1016/j.bcp.2017.03.025
15. Das A, Huang GX, Bonkowski MS, Longchamp A, Li C, Schultz MB, et al. Impairment of an endothelial NAD(+)-H_2S signaling network is a reversible cause of vascular aging. *Cell.* (2018) 173:74–89e20. doi: 10.1016/j.cell.2018.02.008
16. Toohey JI. Possible involvement of hydrosulfide in B_{12}-dependent methyl group transfer. *Molecules.* (2017) 22:E582. doi: 10.3390/molecules22040582
17. Fanidi A, Carreras-Torres R, Larose TL, Yuan JM, Stevens VL, Weinstein SJ, et al. Is high vitamin B_{12} status a cause of lung cancer? *Int J Cancer.* (2019) 145:1499–503. doi: 10.1002/ijc.32033
18. Szczesny B, Marcatti M, Zatarain JR, Druzhyna N, Wiktorowicz JE, Nagy P, et al. Inhibition of hydrogen sulfide biosynthesis sensitizes lung adenocarcinoma to chemotherapeutic drugs by inhibiting mitochondrial DNA repair and suppressing cellular bioenergetics. *Sci Rep.* (2016) 6:36125. doi: 10.1038/srep36125
19. Yang CT, Devarie-Baez NO, Hamsath A, Fu XD, Xian M. S-persulfidation: chemistry, chemical biology, and significance in health and disease. *Antioxid Redox Signal.* (2019). doi: 10.1089/ars.2019.7889. [Epub ahead of print].
20. Roundtree IA, Evans ME, Pan T, He C. Dynamic RNA modifications in gene expression regulation. *Cell.* (2017) 169:1187–200. doi: 10.1016/j.cell.2017.05.045
21. Wang X, Zhao BS, Roundtree IA, Lu Z, Han D, Ma H, et al. N^6-methyladenosine modulates messenger RNA translation efficiency. *Cell.* (2015) 161:1388–99. doi: 10.1016/j.cell.2015.05.014
22. Yue Y, Liu J, He C. RNA N^6-methyladenosine methylation in post-transcriptional gene expression regulation. *Genes Dev.* (2015) 29:1343–55. doi: 10.1101/gad.262766.115
23. Li HB, Tong J, Zhu S, Batista PJ, Duffy EE, Zhao J, et al. m^6A mRNA methylation controls T cell homeostasis by targeting the IL-7/STAT5/SOCS pathways. *Nature.* (2017) 548:338–42. doi: 10.1038/nature23450
24. Fu Y, Dominissini D, Rechavi G, He C. Gene expression regulation mediated through reversible m^6A RNA methylation. *Nat Rev Genet.* (2014) 15:293–306. doi: 10.1038/nrg3724
25. Chen M, Wei L, Law CT, Tsang FH, Shen J, Cheng CL, et al. RNA N^6-methyladenosine methyltransferase-like 3 promotes liver cancer progression through YTHDF2-dependent posttranscriptional silencing of SOCS2. *Hepatology.* (2018) 67:2254–70. doi: 10.1002/hep.29683
26. Liu J, Eckert MA, Harada BT, Liu SM, Lu Z, Yu K, et al. m^6A mRNA methylation regulates AKT activity to promote the proliferation and tumorigenicity of endometrial cancer. *Nat Cell Biol.* (2018) 20:1074–83. doi: 10.1038/s41556-018-0174-4
27. Liu ZX, Li LM, Sun HL, Liu SM. Link between m^6A modification and cancers. *Front Bioeng Biotechnol.* (2018) 6:89. doi: 10.3389/fbioe.2018.00089
28. Pan Y, Ma P, Liu Y, Li W, Shu Y. Multiple functions of m^6A RNA methylation in cancer. *J Hematol Oncol.* (2018) 11:48. doi: 10.1186/s13045-018-0590-8
29. Lin S, Choe J, Du P, Triboulet R, Gregory RI. The m^6A methyltransferase METTL3 promotes translation in human cancer cells. *Mol Cell.* (2016) 62:335–45. doi: 10.1016/j.molcel.2016.03.021
30. Zeng Y, Wang S, Gao S, Soares F, Ahmed M, Guo H, et al. Refined RIP-seq protocol for epitranscriptome analysis with low input materials. *PLoS Biol.* (2018) 16:e2006092. doi: 10.1371/journal.pbio.2006092
31. Jiang L, Sun Y, Wang J, He Q, Chen X, Lan X, et al. Proteasomal cysteine deubiquitinase inhibitor b-AP15 suppresses migration and induces apoptosis in diffuse large B cell lymphoma. *J Exp Clin Cancer Res.* (2019) 38:453. doi: 10.1186/s13046-019-1446-y
32. Yang C, Ling H, Zhang M, Yang Z, Wang X, Zeng F, et al. Oxidative stress mediates chemical hypoxia-induced injury and inflammation by activating NF-κb-COX-2 pathway in HaCaT cells. *Mol Cells.* (2011) 31:531–8. doi: 10.1007/s10059-011-1025-3
33. Peng B, Chen W, Liu C, Rosser EW, Pacheco A, Zhao Y, et al. Fluorescent probes based on nucleophilic substitution-cyclization for hydrogen sulfide detection and bioimaging. *Chemistry.* (2014) 20:1010–6. doi: 10.1002/chem.201303757
34. Yang CT, Wang Y, Marutani E, Ida T, Ni X, Xu S, et al. Data-driven identification of hydrogen sulfide scavengers. *Angew Chem Int Ed Engl.* (2019) 58:10898–902. doi: 10.1002/anie.201905580
35. Alvarez HM, Xue Y, Robinson CD, Canalizo-Hernandez MA, Marvin RG, Kelly RA, et al. Tetrathiomolybdate inhibits copper trafficking proteins through metal cluster formation. *Science.* (2010) 327:331–4. doi: 10.1126/science.1179907
36. Weng H, Huang H, Wu H, Qin X, Zhao BS, Dong L, et al. METTL14 inhibits hematopoietic stem/progenitor differentiation and promotes leukemogenesis via mRNA m^6A modification. *Cell Stem Cell.* (2018) 22:191–205e199. doi: 10.1016/j.stem.2017.11.016
37. Wu D, Li M, Tian W, Wang S, Cui L, Li H, et al. Hydrogen sulfide acts as a double-edged sword in human hepatocellular carcinoma cells through EGFR/ERK/MMP-2 and PTEN/AKT signaling pathways. *Sci Rep.* (2017) 7:5134. doi: 10.1038/s41598-017-05457-z
38. Wang S, Chai P, Jia R, Jia R. Novel insights on m^6A RNA methylation in tumorigenesis: a double-edged sword. *Mol Cancer.* (2018) 17:101. doi: 10.1186/s12943-018-0847-4
39. Adler AS, McCleland ML, Yee S, Yaylaoglu M, Hussain S, Cosino E, et al. An integrative analysis of colon cancer identifies an essential function for PRPF6 in tumor growth. *Genes Dev.* (2014) 28:1068–84. doi: 10.1101/gad.237206.113
40. Pan Y, Liu H, Wang Y, Kang X, Liu Z, Owzar K, et al. Associations between genetic variants in mRNA splicing-related genes and risk of lung cancer: a pathway-based analysis from published GWASs. *Sci Rep.* (2017) 7:44634. doi: 10.1038/srep44634
41. Yang JJ, Lee YJ, Hung HH, Tseng WP, Tu CC, Lee H, et al. ZAK inhibits human lung cancer cell growth via ERK and JNK activation in an AP-1-dependent manner. *Cancer Sci.* (2010) 101:1374–81. doi: 10.1111/j.1349-7006.2010.01537.x
42. Du J, Hui Y, Cheung Y, Bin G, Jiang H, Chen X, et al. The possible role of hydrogen sulfide as a smooth muscle cell proliferation inhibitor in rat cultured cells. *Heart Vessels.* (2004) 19:75–80. doi: 10.1007/s00380-003-0743-7
43. Akaike T, Ida T, Wei FY, Nishida M, Kumagai Y, Alam MM, et al. Cysteinyl-tRNA synthetase governs cysteine polysulfidation and mitochondrial bioenergetics. *Nat Commun.* (2017) 8:1177. doi: 10.1038/s41467-017-01311-y
44. Zheng Y, Yu B, De La Cruz LK, Roy Choudhury M, Anifowose A, Wang B. Toward hydrogen sulfide based therapeutics: Critical drug delivery and developability issues. *Med Res Rev.* (2018) 38:57–100. doi: 10.1002/med.21433

45. Cui Q, Yang Y, Ji N, Wang JQ, Ren L, Yang DH, et al. Gaseous signaling molecules and their application in resistant cancer treatment: from invisible to visible. *Future Med. Chem.* (2019) 11:323–36. doi: 10.4155/fmc-2018-0403
46. Shinkai Y, Kumagai Y. Sulfane sulfur in toxicology: a novel defense system against electrophilic stress. *Toxicol Sci.* (2019) 170:3–9. doi: 10.1093/toxsci/kfz091
47. Twomey PJ, Viljoen A, House IM, Reynolds TM, Wierzbicki AS. Relationship between serum copper, ceruloplasmin, and non-ceruloplasmin-bound copper in routine clinical practice. *Clin Chem.* (2005) 51:1558–9. doi: 10.1373/clinchem.2005.052688
48. Brewer GJ, Dick RD, Grover DK, LeClaire V, Tseng M, Wicha M, et al. Treatment of metastatic cancer with tetrathiomolybdate, an anticopper, antiangiogenic agent: phase I study. *Clin Cancer Res.* (2000) 6:1–10.
49. Van de Louw A, Haouzi P. Ferric iron and Cobalt (III) compounds to safely decrease hydrogen sulfide in the body? *Antioxid. Redox Signal.* (2013) 19:510–6. doi: 10.1089/ars.2012.4513

Conflict of Interest: The authors declare that the research was conducted in the absence of any commercial or financial relationships that could be construed as a potential conflict of interest.

frontiers in Oncology

ORIGINAL RESEARCH
published: 10 March 2020
doi: 10.3389/fonc.2020.00252

Hydrogen Sulfide Mediates Tumor Cell Resistance to Thioredoxin Inhibitor

Zhimin Mao[1,2], Xiawen Yang[1], Sayumi Mizutani[3], Yanru Huang[1], Zhen Zhang[1], Hideyuki Shinmori[3], Kun Gao[4] and Jian Yao[1]**

[1] Division of Molecular Signaling, Department of the Advanced Biomedical Research, Interdisciplinary Graduate School of Medicine, University of Yamanashi, Kofu, Japan, [2] Institute of Reproductive Medicine, School of Medicine, Nantong University, Nantong, China, [3] Department of Biotechnology, Faculty of Life and Environmental Sciences, Graduate Faculty of Interdisciplinary Research, University of Yamanashi, Kofu, Japan, [4] Division of Nephrology, Affiliated Hospital of Nanjing University of Chinese Medicine, Jiangsu Province Hospital of Chinese Medicine, Nanjing, China

Thioredoxin (Trx) is a pro-oncogenic molecule that underlies tumor initiation, progression and chemo-resistance. PX-12, a Trx inhibitor, has been used to treat certain tumors. Currently, factors predicting tumor sensitivity to PX-12 are unclear. Given that hydrogen sulfide (H_2S), a gaseous bio-mediator, promotes Trx activity, we speculated that it might affect tumor response to PX-12. Here, we tested this possibility. Exposure of several different types of tumor cells to PX-12 caused cell death, which was reversely correlated with the levels of H_2S-synthesizing enzyme CSE and endogenous H_2S. Inhibition of CSE sensitized tumor cells to PX-12, whereas addition of exogenous H_2S elevated PX-12 resistance. Further experiments showed that H_2S abolished PX-12-mediated inhibition on Trx. Mechanistic analyses revealed that H_2S stimulated Trx activity. It promoted Trx from the oxidized to the reduced state. In addition, H_2S directly cleaved the disulfide bond in PX-12, causing PX-12 deactivation. Additional studies found that, besides Trx, PX-12 also interacted with the thiol residues of other proteins. Intriguingly, H_2S-mediated cell resistance to PX-12 could also be achieved through promotion of the thiol activity of these proteins. Addition of H_2S-modified protein into culture significantly enhanced cell resistance to PX-12, whereas blockade of extracellular sulfhydryl residues sensitized cells to PX-12. Collectively, our study revealed that H_2S mediated tumor cell resistance to PX-12 through multiple mechanisms involving induction of thiol activity in multiple proteins and direct inactivation of PX-12. H_2S could be used to predict tumor response to PX-12 and could be targeted to enhance the therapeutic efficacy of PX-12.

Keywords: PX-12, H_2S, sulfhydration, chemotherapy, drug resistance, Trx, albumin

OPEN ACCESS

Edited by:
Simona Rapposelli, University of Pisa, Italy

Reviewed by:
Vincenzo Brancaleone, University of Basilicata, Italy
Eugenio Gaudio, Istituto Oncologico della Svizzera Italiana, Switzerland

***Correspondence:**
Kun Gao
dr.gaokun@outlook.com
Jian Yao
yao@yamanashi.ac.jp

Specialty section:
This article was submitted to Pharmacology of Anti-Cancer Drugs, a section of the journal Frontiers in Oncology

Received: *19 December 2019*
Accepted: *13 February 2020*
Published: *10 March 2020*

Citation:
Mao Z, Yang X, Mizutani S, Huang Y, Zhang Z, Shinmori H, Gao K and Yao J (2020) Hydrogen Sulfide Mediates Tumor Cell Resistance to Thioredoxin Inhibitor. Front. Oncol. 10:252. doi: 10.3389/fonc.2020.00252

INTRODUCTION

Cancer is the leading cause of death worldwide. It is, therefore, highly desirable to understand the molecular mechanisms behind the initiation and development of cancer and to find effective therapeutic interventions. Many strategies against cancer have been developed. However, the self-protective mechanisms of tumors greatly limit the efficacy of cancer therapy (1).

Redox state in tumor cells plays an important role in tumor initiation, development and therapy (2, 3). The cellular metabolic activity is associated with production of the reactive oxygen species

(ROS). In normal cells, ROS is depleted by the antioxidative mechanisms. The decreased cellular defense against ROS leads to ROS accumulation, causing a situation called oxidative stress (2, 4, 5). In oxidative stress, ROS causes cell damage through modification of important molecules and activation of redox signaling pathway. In cancer cells, the metabolism is accelerated to meet the energy demand for abnormally high proliferation. The high metabolic rate leads to an increased ROS generation, which makes tumor cells under persistent oxidative stress. To escape from the stress-initiated cell injury, cancer cells develop several ways to enhance cell resistance against oxidative stress including activating alternative metabolic pathway to meet the energy demand without the large accumulation of ROS and increasing cell defense against ROS.

One of the well-documented mechanisms involved in tumor cell resistance to oxidative stress is the thioredoxin (Trx) system (6–9). The Trx system, composed of Trx reductase (TrxR), Trx, and NADPH, is one of the main thiol-dependent electron donor systems in the cells, which plays critical roles in maintaining cellular redox homeostasis and cell survival. Trx exerts its antioxidative actions via disulfide exchange. It directly scavenges ROS and plays a vital role in the control of the apoptosis signal-regulating kinase 1 (ASK1)/MAPK signaling pathway (10, 11). Besides, Trx also controls the activity of enzymes that counteract oxidative stress within cells. Trx is one of major molecules involved in the initiation and development of cancer. In many different cancers, the levels of Trx and TrxR are increased. High levels of Trx assist cancer development due to its growth-promoting and antiapoptotic functions. Trx also facilitates cancer progression through promotion of angiogenesis and metastasis. In addition, Trx contributes to tumor cell resistance to chemotherapy (9, 12, 13). Given the central roles of Trx in cancer cells, Trx has been developed as a therapeutic target to inhibit cancer growth, progression, and metastasis (14–16).

PX-12 (1-methylpropyl 2-imidazolyl disulfide) is a promising antitumor chemical that inhibit Trx activity through binding to the cysteine 73 residue of Trx (17, 18). PX-12 has shown excellent antitumor activity in both *in vitro* and *in vivo* experiments. It inhibits the growth of many different types of tumors, including human MCF-7 breast cancer and human acute myeloid leukemia cells (19, 20). Currently, PX-12 is undergoing pre-clinical trials for tumor therapy. However, factors governing tumor cell response to PX-12 are still largely unknown. To increase the therapeutic efficacy of PX-12, it is urgently needed to identify the molecules that interfere with the effects of PX-12 and to understand the mechanisms.

Hydrogen sulfide (H_2S) is an endogenous gaseous biological mediator produced by cells expressing H_2S synthesizing-enzymes cystathionine γ-lyase (CSE), cystathionine β-synthase (CBS), and 3-mercaptopyruvate sulfurtransferase (3-MST). H_2S has multifaced biological actions, including antioxidative property (21–23). It scavenges ROS and enhances cell defense against oxidative stress. Many types of antioxidative machinery, such as glutathione, SOD, and catalase, is activated by H_2S (24, 25). In many types of tumors, H_2S-producing enzymes are upregulated, which has been recognized as a cancer-promoting factor. The endogenous H_2S produced by tumor cells increases mitochondrial bioenergetics, accelerates cell cycle progression, stimulates cell proliferation, promotes angiogenesis and facilitates tumor cell migration and invasion (26–30). Furthermore, it enhances cell resistance to apoptosis and increases cell tolerance to several antitumor drugs (30–33).

We recently reported that H_2S exerts its antioxidative effects through regulating the redox state of Trx (10). Also, H_2S cleaves the disulfide bond in many molecules (10, 34, 35). These findings prompted us to speculate that H_2S may interfere with the effects of Trx-inhibiting chemicals. The purpose of this study was to test this hypothesis.

Here, we present our data that H_2S increases tumor cell resistance to PX-12 through multiple mechanisms, including promoting Trx reductivity, deactivating PX-12, and elevating sulfhydryl residues in proteins that competitively bind PX-12. Our study thus characterizes H_2S as a presently unreported molecule contributing to tumor cell resistance to PX-12. Targeting H_2S could be developed to enhance the tumor-killing efficacy of PX-12.

MATERIALS AND METHODS

Materials

PX-12 and anti-mouse antibody against CTH were obtained from Santa Cruz Biotechnology (Santa Cruz, CA). Beta-cyano-L-Alanine (BCA) was from Cayman Chemical (Ann Arbor, MI, USA). siRNAs of CTH1 and CTH2 were purchased from QIAGEN (Tokyo, Japan). 4-acetamido-4'-maleimidylstilbene-2, 2'-disulfonic acid (AMS) was bought from Life Technologies (Eugene, OR, USA). Alexa 680 C2 maleimide was from Thermo Scientific (Rockford, IL). Anti-rabbit antibodies against Trx1 (C63C6), horseradish peroxidase (HRP)-conjugated anti-rabbit or mouse IgG were bought from Cell Signaling Technology (Danvers, MA, USA). Sodium hydrosulfide hydrate (NaHS), L-cysteine hydrochloride, DL-Propargylglycine (PAG), recombinant Trx (rTrx) and all other chemicals were from Sigma (Tokyo, Japan).

Cells

Hepatoma G2 (HepG2), NRK52E and Hela cells were purchased from ATCC (American Type Culture Collection, Manassas, VA), which were maintained in Dulbecco's modified Eagle's medium/Ham's F-12 medium (DMEM/F-12; GIBCO-BRL, Gaithersburg, MD, USA) supplemented with 5∼10% fetal bovine serum (FBS; Sigma-Aldrich, Carlsbad, CA, USA) and 1% penicillin/streptomycin/antibiotic antimycotic solution (ABAM; Sigma-Aldrich, Carlsbad, CA, USA). For experiments, cells were exposed to stimuli in the absence of FBS.

Assessment of Cell Viability With WST Reagent

Cells were seeded onto 96-well culture plates and stimulated with various stimuli for the indicated time. WST reagent was added and allowed to react with cells for 30 min. The optical density (OD) was measured with a spectrometer at the wavelength of 450 nm. Cell viability was expressed as the percentage of OD value relative to the untreated control.

Calcein-AM/Propidium Iodide (PI) Staining

After various treatments, cells were exposed to a mixture of Calcein-AM (green) and PI (red) solution (Dojindo, Kumamoto, Japan) for 10–20 min, and observed under a fluorescent microscope. Calcein-AM positive green cells were considered alive, while PI-positive red cells were considered dead.

Transient Transfection

The HepG2 cells were transfected with a control siRNA or siRNA against CSE at the concentration of 20 nM using the HiPerFect transfection reagent for 36 h. Afterward, the cells were seeded onto 96- or 12-well plate, exposed to stimuli and detected for cellular expression of targeted protein and cell viability.

Western Blot Analysis

Western blot was performed as described previously (11). Briefly, extracted proteins were separated on 10 or 12% SDS–polyacrylamide gels and electro-transferred onto polyvinylidene difluoride membranes. The membranes were blocked with 5% non-fat dry milk in phosphate-buffered saline (PBS), followed by overnight incubation with primary antibody at 4°C. Afterward, the membranes were washed and probed with HRP-conjugated anti-rabbit or anti-mouse IgG. The signals in the membrane were visualized by Chemi-Lumi One L (NacalaiTesque, Kyoto, Japan) and captured with a Fujifilm luminescent image LAS-1000 analyzer (Fujifilm, Tokyo, Japan). β-tubulin or β-actin was used as an internal loading control. Quantification of the bands was performed using ImageJ software.

Lead Sulfide Method for Determination of H_2S Production Capacity

H_2S production capacity was determined according to the method described by Hine et al. (36). Briefly, H_2S test paper was soaked in 20 mM lead acetate solution and dried. To measure H_2S production capacity, we seeded the equal number of NRK, HepG2, or Hela cells onto 96-well culture plate. The cells were cultured in DMEM/F12 containing 10 mM L-cysteine plus 10 μM pyridoxal-5'-phosphate (PLP). The H_2S test paper was placed directly over the 96-well plate for 24 h and allowed to react with the cell-released gaseous H_2S. The reaction of H_2S with lead acetate causes the formation of lead sulfide, which darkens the paper and forms a visible black-colored circle. The intensity of the circle was analyzed using the IntDen measurement in ImageJ software.

Redox Western Analysis

Protein redox status was determined using AMS-shift assay reported by Chen et al. (37). Cellular proteins precipitated with 10% Trichloroacetic acid (TCA) were washed twice with 100% acetone and dissolved in lysis buffer (62.5 mM Tris-Cl, PH 6.8, 1% SDS). The dissolved proteins were allowed to react with 20 mM AMS at room temperature for 1 h. Afterward, the samples were subjected to Western blot analysis for the redox state of Trx under non-reducing condition.

Red Maleimide for Detection of Sulfhydryl (-SH) Groups

This assay was modified from the previous reports (38, 39). Proteins treated with or without the indicated stimuli was precipitated with TCA, washed with acetone, redissolved in PBS and allowed to react with Alexa Fluor 680 C2 maleimide (red fluorescence at the final concentration of 2 or 5 μM) at 4°C for 2 h. The unlabeled maleimide was removed with TCA/acetone precipitation. The re-precipitated proteins were equally divided into two tubes with or without 1 mM DTT. After one hour at 4°C, the protein samples were directly applied to 0.45-μm pore size nitrocellulose membrane in a commercial dot-blot apparatus (BioRad). The signal of fluorescent maleimide in the membranes was captured with a Fujifilm image LAS-1000 analyzer (Fujifilm, Tokyo, Japan) and quantified with ImageJ software. EZ blue staining or immunoblotting of the membrane with an anti-rabbit Trx1 antibody was performed to confirm the equal loading of proteins.

Absorption Spectroscopic Method for Detection of 2-Mercaptoimidazole

UV absorption spectra was measured to detect 2-Mercaptoimidazole (2-MI) produced by the reaction of PX-12 with NaHS using a Shimadzu UV-1800 recording spectrophotometer. Hundred micromolar PX-12 that was dissolved in a mixture of DMSO and ethanol was added into 1 mM NaHS in the volume of 1 ml PBS at room temperature for 1 h. 2-MI production was confirmed by the absorption band at 252 nm. Each measurement was repeated three times for all samples.

Statistical Analysis

Values are expressed as mean ± SE. Comparison of two groups was made by Student's *t*-test. For multiple comparisons, one-way analysis of variance was employed. Both analyses were performed with Microsoft Excel (Microsoft, Redmond, WA, USA) or Sigma plot software (Systat Software Inc., San Jose, CA). $P < 0.05$ was considered statistically significant.

RESULTS

H_2S Regulates Cell Sensitivity to PX-12

To determine the role of H_2S on tumor cell response to PX-12, we compared the effect of PX-12 among three different cell lines, NRK, HepG2 and Hela. **Figures 1A,B** show that these cell lines expressed different levels of H_2S-synthesizing enzyme CSE. The amount of CSE was abundant in HepG2 cells, moderate in Hela cells and deficient in NRK cells. Consistently, H_2S-producing capacity of these cells, as detected by using lead sulfide method, was in a direct proportion to CSE levels (**Figures 1C,D**). Furthermore, the level of intracellular H_2S was indeed different between HepG2 and NRK cells as measured by using the fluorescent probe HSip-1 DA (**Supplementary Figure 1**).

We, therefore, compared the sensitivity of these cells to PX-12. **Figure 2** shows that PX-12 caused a cell death in a concentration-dependent manner, which was most sensitive in CSE-deficient NRK cells and insensitive in CSE-rich HepG2 cells, while Hela

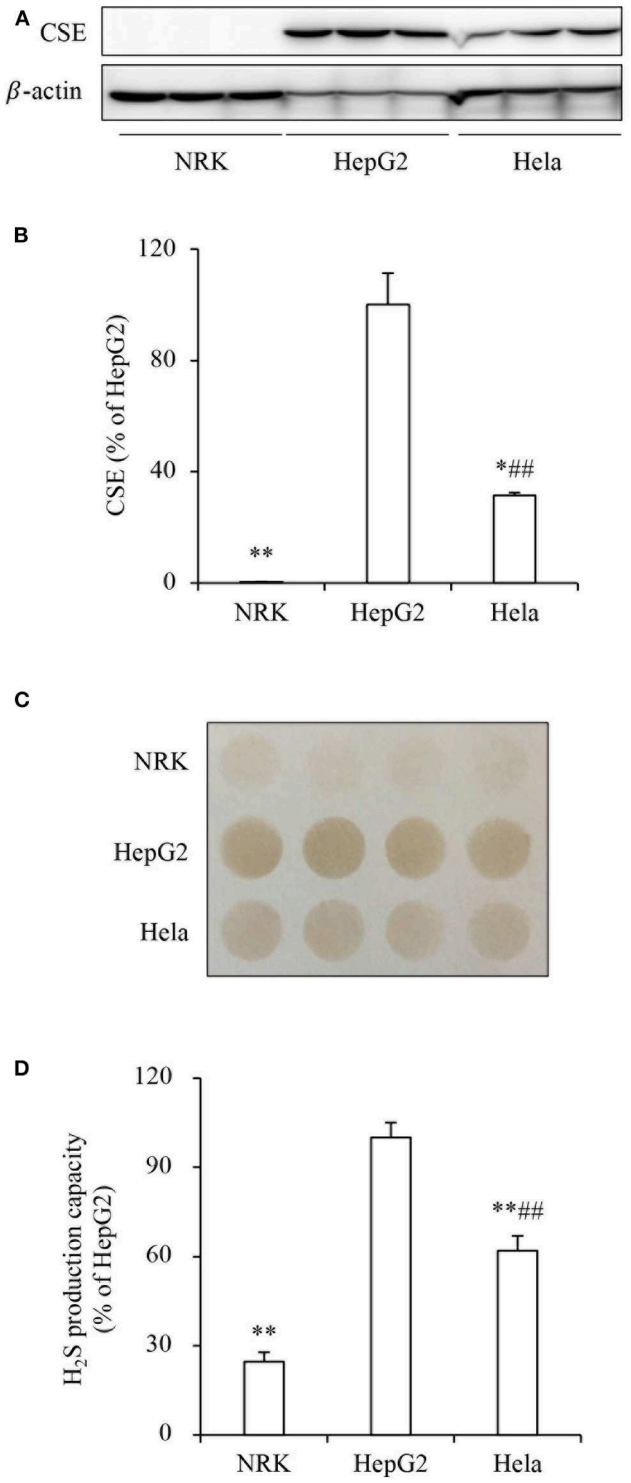

FIGURE 1 | Different levels of CSE and H_2S-producing capacity in three cell lines. **(A,B)** The protein level of CSE in NRK, HepG2, and Hela cells. The same amounts of cellular lysates from NRK, HepG2, or Hela cells were subjected to Western blot analysis for CSE **(A)**. The densitometric quantitation of the blot is shown in **(B)**. Data are expressed as percentage relative to HepG2 cells (mean ± SE, $n = 3$; $^{*}P < 0.05$, $^{**}P < 0.01$ vs. HepG2 cells; $^{\#\#}P < 0.01$ vs. NRK cells). **(C,D)** Comparison of H_2S production capacity among these cells.

(Continued)

FIGURE 1 | Cells were seeded into 96-well plate at the density of 4×10^5 and cultured in growth medium supplemented with 10 mM L-cysteine and 10 μM PLP for 24 h **(C)**. The capacity of H_2S production was determined based on the density of the black-colored circle in the test paper as described in the section of Materials and Methods. Densitometric analysis of the intensity of the black-colored circles is shown in **(D)**. Data are expressed as percentage relative to HepG2 cells (mean ± SE, $n = 4$; $^{**}P < 0.01$ vs. HepG2 cells; $^{\#\#}P < 0.01$ vs. NRK cells).

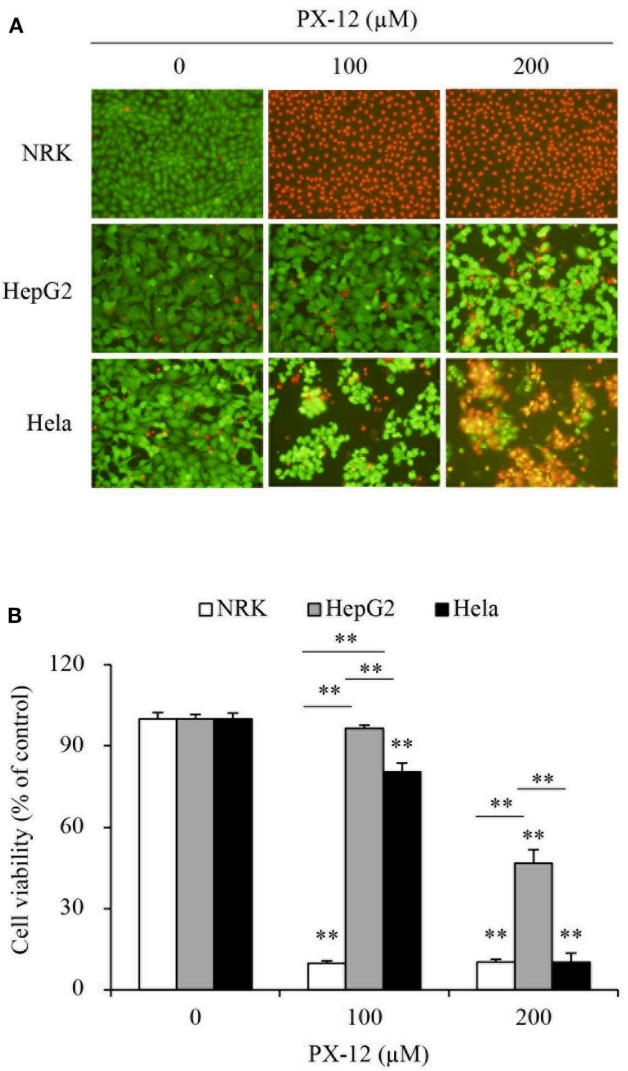

FIGURE 2 | Different cell response to PX-12. **(A,B)** Effect of PX-12 on cell shape and viability. NRK, HepG2 and Hela cells were incubated with the indicated concentrations of PX-12 for 7 h. Afterward, cells were stained with Calcein-AM/PI staining (**A**, magnification: × 400) and photographed. Cell viability was evaluated by WST assay **(B)**. Data in **(B)** are expressed as the percentage of living cells against the untreated control (mean ± SE, $n = 4$; $^{**}P < 0.01$ vs. respective control).

cells were in the middle. These observations suggest that the cell sensitivity to PX-12 was reversely correlated to the level of CSE.

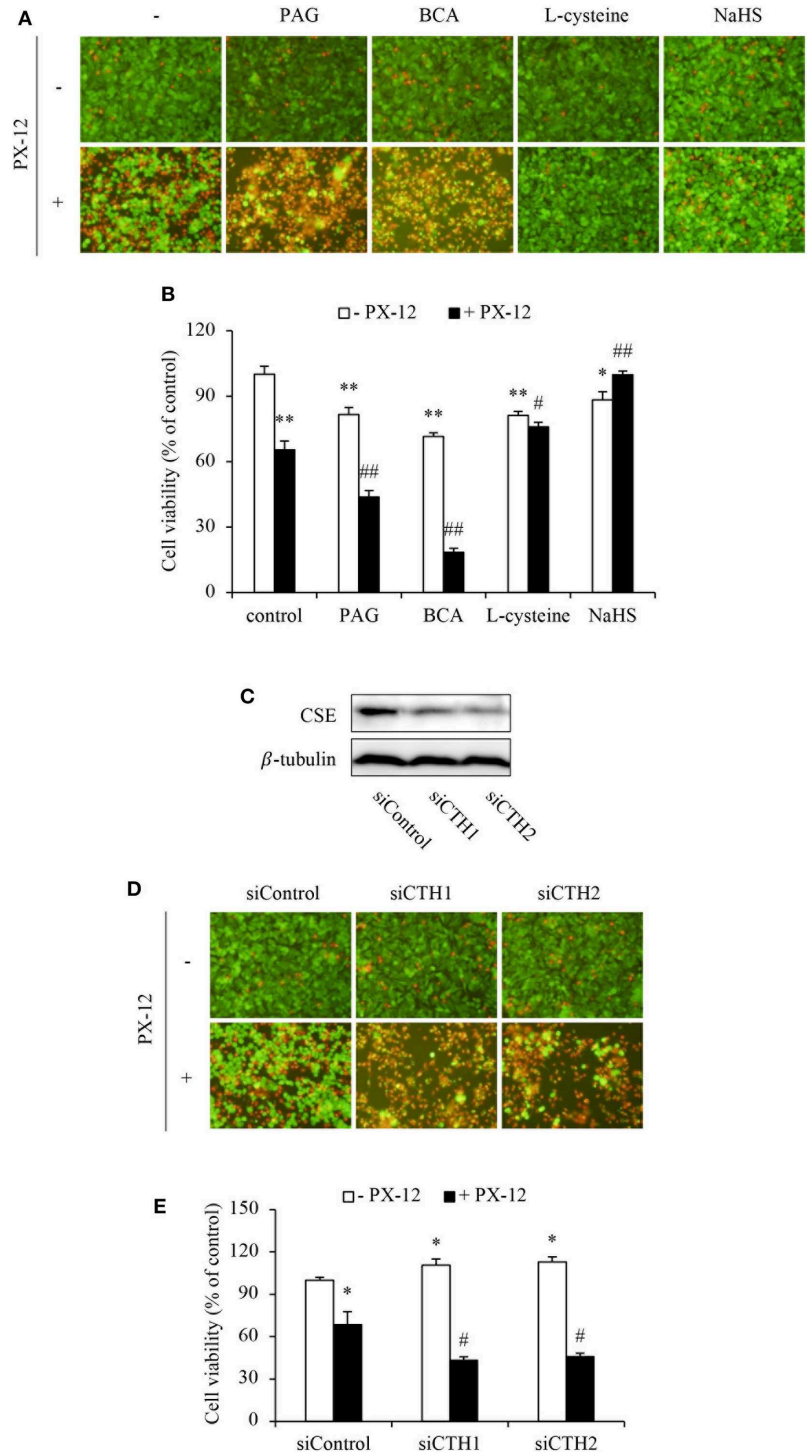

FIGURE 3 | Influence of H_2S on cell vulnerability to PX-12-induced cell death. **(A,B)** Effect of H_2S on PX-12-induced HepG2 cell death. HepG2 cells were incubated with 200 μM PX-12 in the presence or absence of 2 mM BCA, 3 mM PAG, 2 mM L-cysteine or 1 mM NaHS for 12 h. Then, the cells were either stained with Calcein-AM/PI (**A**, magnification: × 400) or assayed for formazan formation with WST reagent **(B)**. Data in **(B)** are expressed as the percentage of living cells against the untreated control (mean ± SE, $n = 4$; $^{*}P < 0.05$, $^{**}P < 0.01$ vs. control; $^{\#}P < 0.05$, $^{\#\#}P < 0.01$ vs. PX-12 alone). **(C–E)** Effect of CSE siRNA on PX-12-induced HepG2 cell injury. The HepG2 cells were transfected with control siRNA or siRNAs targeting different sequences of CSE (siCTH1 and siCTH2) as described in Method section. The cellular lysates were extracted and subjected to Western blot analysis for CSE **(C)**. The treated cells were also seeded into 96-well plate and exposed to 200 μM PX-12 for 12 h to evaluate cell viability through Calcein-AM/PI staining (**D**, magnification: × 400) and WST assay **(E)**. Data in **(E)** are expressed as the percentage of living cells against the untreated siControl (mean ± SE, $n = 4$; $^{*}P < 0.05$ vs. untreated siControl; $^{\#}P < 0.05$ vs. PX-12-treated siControl).

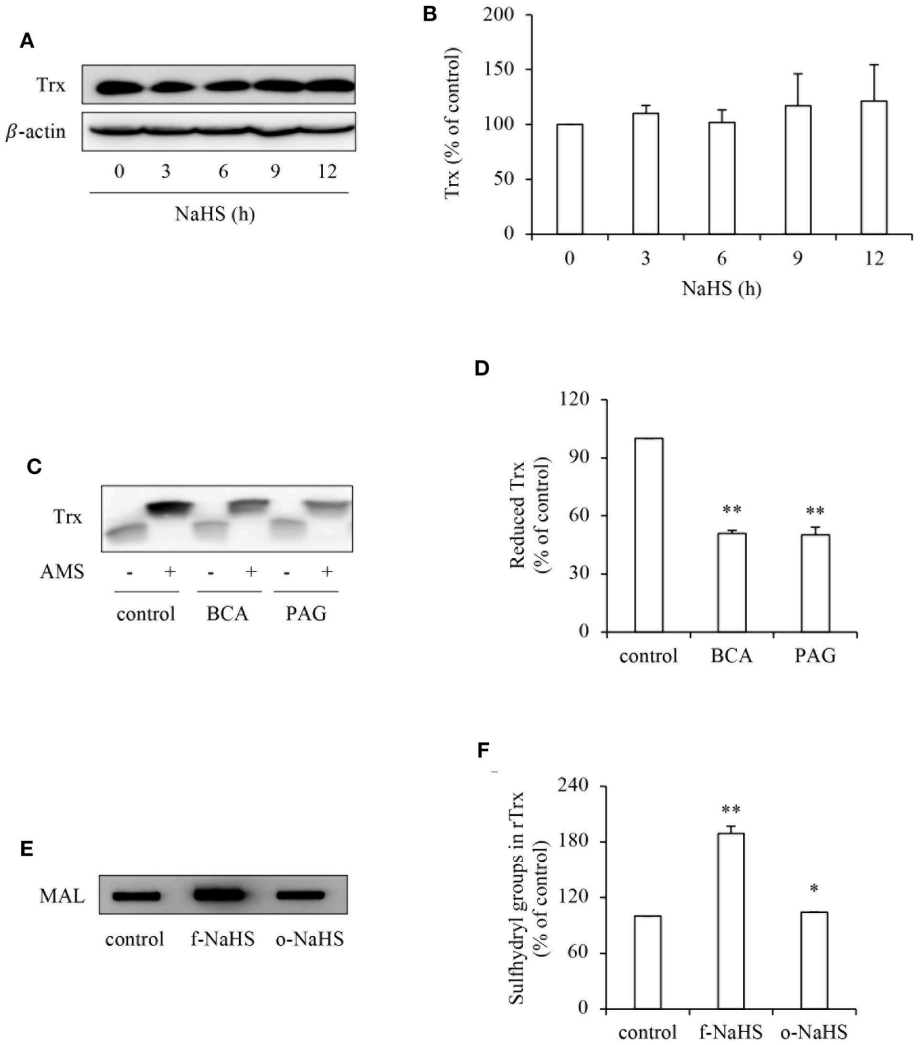

FIGURE 4 | Effect of H_2S on the redox state of Trx. **(A,B)** Effect of NaHS on Trx protein levels in HepG2 cells. HepG2 cells were exposed to 1 mM NaHS for the indicated time intervals. Cellular lysates were subjected to Western blot analysis of Trx **(A)**. Densitometric analysis of the blot in **(A)** was shown in **(B)**. Data shown are mean ± SE, ($n = 3$). **(C,D)** Effect of endogenous H_2S on the redox state of Trx. HepG2 cells were cultured with or without 2 mM BCA or 3 mM PAG for 12 h. Cellular proteins precipitated by TCA were dissolved in lysis buffer and allowed to react with thiol-binding AMS as described in Materials and Methods. The redox state of Trx was determined through the shift of Trx bands in western blot analysis. Note the obvious reduction of AMS-labeled reduced form of Trx (upper band; **C**). Densitometric analysis of the blot in **(C)** is shown in **(D)**. Data shown are mean ± SE, ($n = 3$, $^{**}P < 0.01$ vs. control). **(E,F)** Effect of H_2S on redox state of rTrx. rTrx (2 μg) was exposed to 1 mM freshly prepared NaHS solution (f-NaHS) for 2 h or solution that had been exposed to air for 2 days before the experiments (old NaHS: o-NaHS). The binding of fluorescence-labeled maleimide (MAL) was evaluated through the fluorescent intensity in dot blot **(E)**. Densitometric analysis of the blot was shown in **(F)**. Data shown are mean ± SE, ($n = 3$; $^{*}P < 0.05$, $^{**}P < 0.01$ vs. control).

To further establish the role of H_2S, we examined cell response to PX-12 in the presence of CSE inhibitors or H_2S donors. **Figures 3A–E** show that inhibition or downregulation of CSE in HepG2 cells with chemical inhibitors (BCA and PAG) or siRNA significantly sensitized cells to PX-12. On the contrary, the supplement of HepG2 cells with H_2S substrate L-cysteine or H_2S donor NaHS enhanced cell resistance to PX-12. The similar resistance was also achieved in CSE-deficient NRK cells (**Supplementary Figure 2**). Collectively, these results indicate that H_2S regulates cell sensitivity to PX-12.

H_2S Increases the Reductivity of Trx

To explore the mechanisms underlying the effect of H_2S, we first examined its effect on Trx, the therapeutic target of PX-12 (17, 18). **Figure 4** shows that H_2S donor NaHS did not affect the protein expression level of Trx (**Figures 4A,B**), whereas it greatly affected the Trx redox state. Inhibition of CSE in HepG2 cells with BCA or PAG decreased the reduced form of Trx as revealed by AMS-shift assay (**Figures 4C,D**). Further experiments using rTrx show that NaHS increased the free sulfhydryl residues, as evidenced by the increased binding of thiol-reactive maleimide. This effect of NaHS disappeared after exposure of the donor

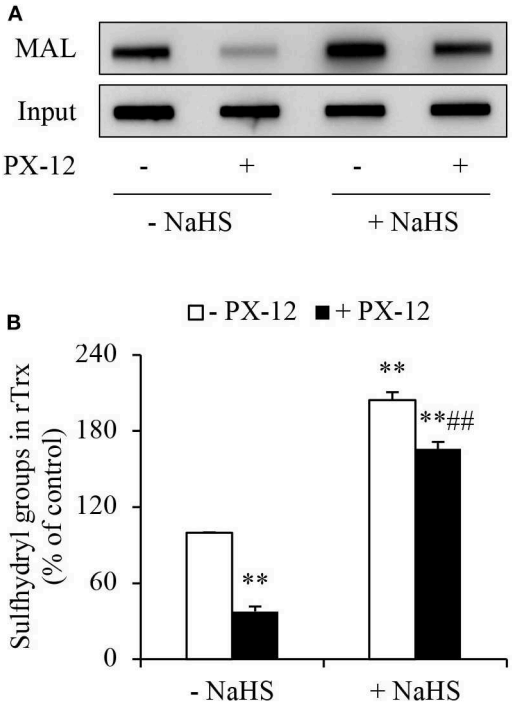

FIGURE 5 | Counteracting effect of H_2S on PX-12 binding to sulfhydryl residues in Trx. **(A,B)** Enhancement of Trx activity by H_2S. rTrx (2 μg) was treated with 250 μM PX-12 and 1 mM NaHS for 2 h and assayed for sulfhydryl groups as described in Materials and Methods. To confirm the equal loading of rTrx, the membrane was probed for Trx using anti-Trx antibody. Note the obvious increased MAL-labeled Trx after NaHS treatment in comparison with PX-12 alone **(A)**. Densitometric analysis of the blot was shown in **(B)**. Data shown are mean ± SE, ($n = 3$; $^{**}P < 0.01$ vs. untreated control; $^{\#\#}P < 0.01$ vs. PX-12 alone).

solution to air to release gaseous H_2S for 2 days, suggesting a mediating role of H_2S (**Figures 4E,F**). Collectively, these results indicate that H_2S stimulates the reductivity of Trx.

To determine whether H_2S interfered with the effect of PX-12 on Trx, we detected free sulfhydryl residues in Trx using thiol-reactive maleimide. As expected, PX-12 potently inhibited maleimide labeling, suggesting a loss of free thiol residues in Trx. In the presence of H_2S donor NaHS, however, the effect of PX-12 was largely abolished (**Figure 5**). These results indicate that H_2S counteracts the inhibitory effect of PX-12 on Trx activity.

H_2S Inactivates PX-12

Previous studies from our group showed that H_2S is a reducing chemical that cleaves disulfide bond (10, 34, 35). Given that there is a disulfide bond in the structure of PX-12, which is requisite for its function, we speculated that H_2S might directly inactivate PX-12 through reaction with disulfide bond. To test this possibility, we first examined whether pretreatment of PX-12 with H_2S donor NaHS could lead to a loss of PX-12 activity. **Figures 6A,B** show that freshly prepared NaHS abolished PX-12-mediated inhibition of Trx activity. Intriguingly, this effect of NaHS was also achieved by pretreatment of PX-12 with NaHS

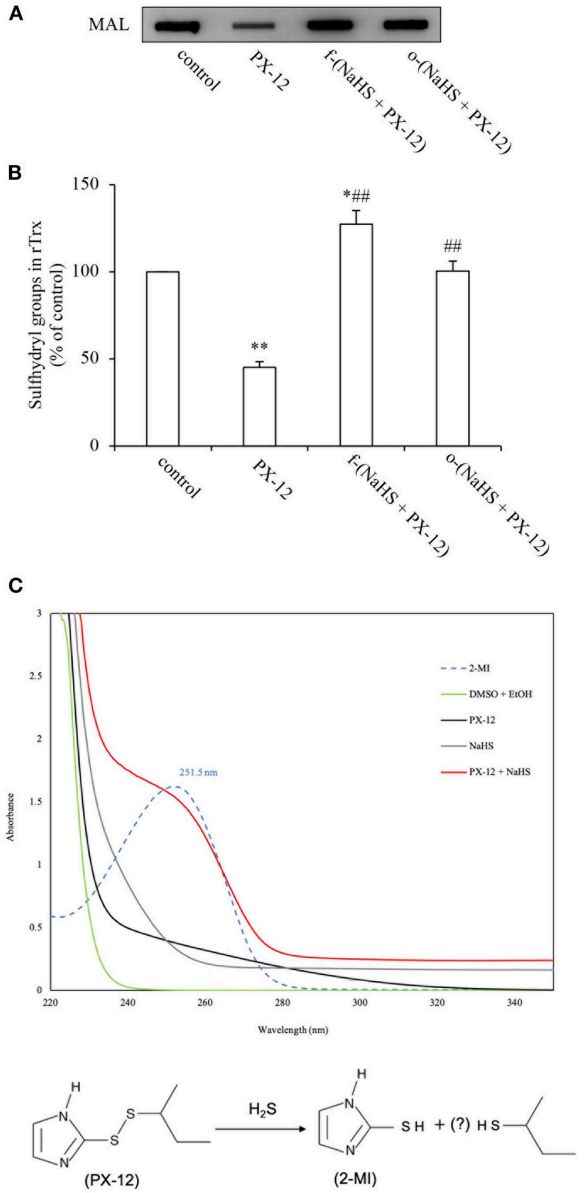

FIGURE 6 | Loss of PX-12 activity after reaction with H_2S. **(A,B)** Comparison of the effect of freshly prepared NaHS and H_2S pre-released solution on the thiol-binding activity of PX-12. rTrx (2 μg) was treated with 250 μM PX-12, or PX-12 plus freshly prepared 1 mM NaHS for 2 h [f-(NaHS + PX-12)], or a mixture of PX-12 and NaHS solution that had been prepared 2 days before the experiment to completely release gaseous H_2S [o-(NaHS + PX-12)]. Note that the pretreatment of PX-12 with NaHS led to a great loss of its binding ability to Trx, suggesting that H_2S may directly inactivate PX-12 **(A)**. Densitometric analysis of the blot in **(A)** was shown in **(B)**. Data shown are mean ± SE, ($n = 3$; $^{*}P < 0.05$, $^{**}P < 0.01$ vs. control; $^{\#\#}P < 0.01$ vs. PX-12 alone). **(C)** Production of 2-MI by the reaction of PX-12 with NaHS. 100 μM PX-12 were allowed to react with 1 mM NaHS for 1 h. The absorbance under UV-vis spectroscopic analysis was monitored. Upper panel shows the results of absorbance of different groups of chemicals. Note the appearance of a wave in NaHS plus PX-12 group (red line) at 252 nm, the peak position of the standard 2-MI (dotted line). Data shown is one of the representative of three separate experiments with similar results. Lower panel shows the scheme of potential reaction of H_2S with PX-12. H_2S reacted with PX-12, causing the release of 2-MI, a metabolite resulted from the cleavage of disulfide bond in PX-12.

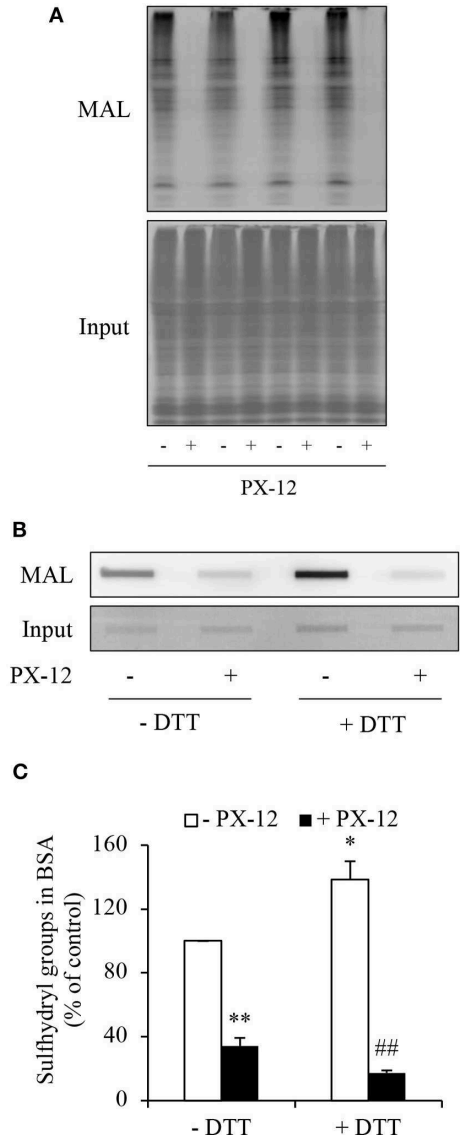

FIGURE 7 | Ability of PX-12 in binding to cellular proteins and albumin. **(A)** Effect of PX-12 on MAL binding to sulfhydryl residues of cellular proteins. Cellular lysates pretreated with or without 500 μM PX-12 were exposed to thiol-reactive MAL for 2 h. The cellular proteins were separated with SDS-PAGE and blotted onto PVDF membrane **(A)**. The signal of MAL-labeled proteins was detected. Note the blocking effect of PX-12 on MAL binding to protein thiol residues (**A**, upper part). The equal loading of cellular proteins was confirmed by staining the membrane with EZ blue (**A**, lower part). **(B)** Effect of PX-12 on MAL binding to native and reduced albumin. Albumin (12.5 μg) pretreated with or without the reducing chemical DTT was exposed to 250 μM PX-12 followed by reaction with MAL, and the signal of MAL-labeled albumin was detected using dot blot. Densitometric analysis of the blot in **(B)** was shown in **(C)**. Data shown are mean ± SE, ($n = 4$; $^{*}P < 0.05$, $^{**}P < 0.01$ vs. control; $^{\#\#}P < 0.01$ vs. PX-12 alone).

for 2 days, a condition that H_2S has been evaporated. This result suggests that H_2S might directly affect PX-12 activity.

To demonstrate that H_2S, indeed, disrupted PX-12 structure, we detected the formation of 2-MI, a metabolite resulted from the cleavage of the disulfide bond in PX-12. **Figure 6C** shows that standard 2-MI exhibited a peak absorbance at 252 nm under UV-vis detection (dotted line). Incubation of PX-12 with NaHS caused a formation of 2-MI, as evidenced by the appearance of a wave at the location of 2-MI (red line), which was not observed in PX-12, NaHS and dissolvent control. This result indicates that H_2S generated by the hydrolysis of NaHS can directly deactivate PX-12.

H_2S Stimulates Sulfhydryl Residues in Multiple Proteins That Contribute to PX-12 Drug Resistance

PX-12 is reported to react with thiols of Trx in a specific and irreversible way (17, 18). However, there is a report describing that PX-12 also bound tubulin and cysteine-dependent proteases (40). We, therefore, determined whether PX-12 also reacted with other cellular proteins. For this purpose, we pretreated cell lysates with PX-12 and detected its influence on thiol activity using maleimide labeling assay. **Figure 7A** shows that PX-12-pretreated proteins lost their binding abilities to thiol-reactive maleimide, suggesting that PX-12 was able to react with sulfhydryl groups of a wide range of cellular proteins.

Albumin is the most abundant serum protein that is produced by hepatocytes (41, 42). It is reported that albumin has active cysteine residues (43–45). We, therefore, tested whether PX-12 also reacts with albumin. **Figures 7B,C** show that albumin reacted with maleimide, which was potentiated by DTT, indicating the presence of sulfhydryl residues. Consistent with the notion that PX-12 also bound to proteins other than Trx, pretreatment of albumin with PX-12 caused a significant reduction in the subsequent maleimide binding. These results indicate that PX-12 reacts with sulfhydryl residues in albumin.

H_2S has reducing activity. We have reported that H_2S increases sulfhydryl residues of several proteins (10, 34). We, therefore, tested whether H_2S also influence the sulfhydryl residues in albumin. **Figures 8A,B** show that NaHS increased sulfhydryl residues of albumin in a way similar to DTT. This effect was associated with increased albumin sulfhydration (**Figures 8C–E**).

Given that the increased sulfhydryl residues in albumin may compete with Trx in binding PX-12, we speculated that this mechanism might also contribute to PX-12 resistance. To confirm this hypothesis, we examined the influence of sulfhydrated albumin on PX-12-initiated cell death. **Figures 8F,G** show that supplement of cells with H_2S-pretreated albumin significantly blunted the cell-killing action of PX-12.

Blockade of Extracellular Sulfhydryl Residues Enhances Cell Sensitivity to PX-12

To further confirm that the off-target binding of PX-12 to the sulfhydryl residues of proteins other than Trx may also contribute to drug resistance, we blocked extracellular thiol-active residues with membrane-impermeable AMS and maleimide and examined the changes in cell response. **Figure 9** shows that AMS and maleimide alone at the concentration used

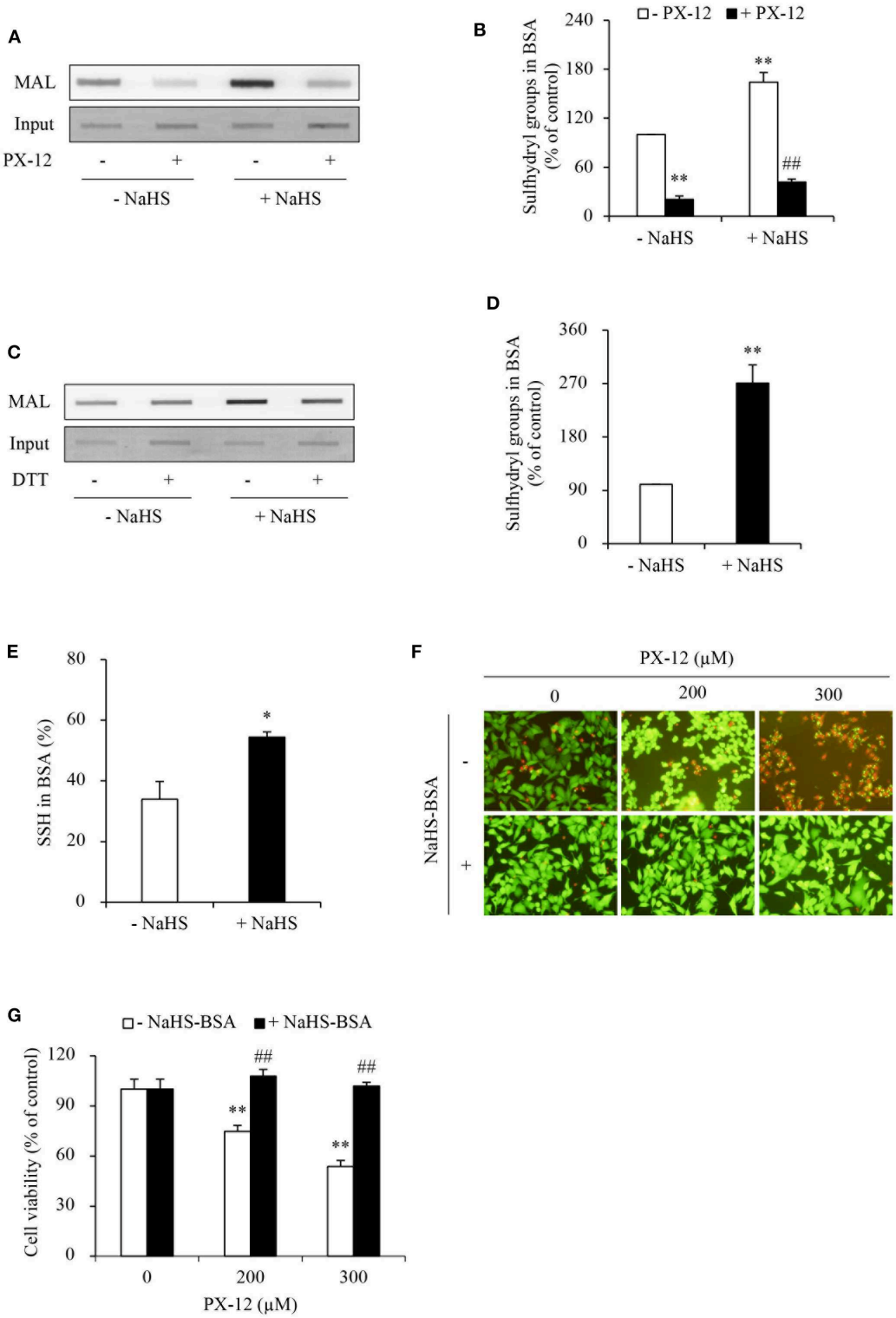

FIGURE 8 | Effect of H_2S-treated albumin on PX-12-induced cell death. **(A)** Induction of the reduced form of albumin by H_2S. Albumin (12.5 μg) pretreated with or without 1mM NaHS were exposed to 250 μM PX-12 followed by reaction with thiol-reactive MAL for 2 h. and the signal of MAL-labeled albumin was detected using dot blot. Densitometric analysis of the blot in **(A)** was shown in **(B)**. Data shown are mean ± SE, ($n = 4$; $^{**}P < 0.01$ vs. control; $^{\#\#}P < 0.01$ vs. PX-12 alone). **(C)** H_2S induced enhancement of sulfhydryl residues and sulfhydration in albumin. Albumin (12.5 μg) treated with or without 1 mM NaHS was assayed for sulfhydration as described in the section of Materials and Methods. The samples were added to dot-blot apparatus and detected for the fluorescent signal. To confirm the equal

(Continued)

FIGURE 8 | loading of albumin, the membrane was stained with EZ blue (**C**, input). Note the obvious increased MAL-labeled Trx after NaHS treatment in comparison with control and its reduction following DTT treatment. **(D)** Densitometric analysis of the intensity of bands between control and NaHS-treated samples without DTT treatment. **(E)** Quantitative calculation of sulfhydrated albumin by NaHS. The level of sulfhydration was calculated through the fluorescence loss after DTT treatment and expressed as a percentage against the intensity of fluorescence before DTT treatment. Data in **(D,E)** are representative of four independent experiments and values are expressed in mean ± SE, (*$P < 0.05$, **$P < 0.01$ vs. control). **(F,G)** Effect of NaHS-treated albumin on PX-12-induced cell death. HepG2 cells in 96-well plate were exposed to the indicated concentrations of PX-12 in the presence or absence of 20 mg/ml NaHS-treated albumin for 4 h. Then, the cells were stained with Calcein-AM/PI (**F**, magnification: × 400). Cell viability was determined by WST assay **(G)**. Data in **(G)** are expressed as the percentage of living cells against the respective control (mean ± SE, $n = 4$; **$P < 0.01$ vs. control; ##$P < 0.01$ vs. PX-12 alone).

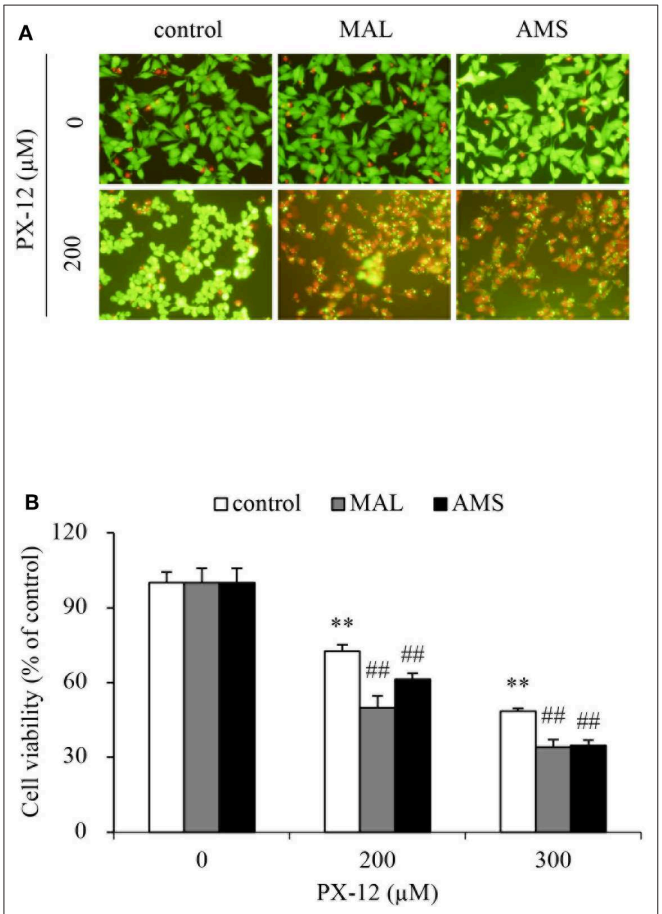

FIGURE 9 | Effect of blocking sulfhydryl residues with cell membrane-impermeable alkylating chemicals on PX-12-induced cell death. **(A,B)** HepG2 cells in 96-well were pretreated with 10 μM maleimide or 2 mM AMS for 1 h, followed by exposure to the indicated concentrations of PX-12 for an additional 4 h. Then, the cells were stained with Calcein-AM/PI (**A**, magnification: × 400). Cell viability was determined by WST assay **(B)**. Data in **(B)** are expressed as the percentage of living cells against the respective control (mean ± SE, $n = 4$; **$P < 0.01$ vs. control; ##$P < 0.01$ vs. PX-12 alone).

did not affect cell viability; however, they markedly sensitized cells to PX-12.

DISCUSSION

In this study, we characterized H_2S as a presently unrecognized molecule influencing cell response to PX-12. Furthermore, we revealed that this effect of H_2S was mediated through multiple mechanisms. The schematic depiction of the mechanisms has been shown in **Figure 10**. Given that H_2S is produced by many types of tumors and also exists in the tumor microenvironment, H_2S could be an important factor determining cell sensitivity to PX-12. Targeting H_2S could be a potential way to increase the efficacy of chemotherapy.

H_2S has been documented to increase tumor cell resistance to several drugs, such as 5-FU and oxaliplatin (30–33). In this study, we found that H_2S underlay cell resistance to PX-12. The evidence supporting this conclusion include that: (1) cell sensitivity to PX-12 was conversely correlated with the level of H_2S-producing enzyme CSE and H_2S production; (2) inhibition of endogenous H_2S sensitized cell to PX-12; and (3) supplement of cells with exogenous H_2S enhanced cell resistance to PX-12.

Redox state is a determinant factor of tumor initiation and development. It is also the target of tumor therapy (2–4). Many antitumor drugs, such as doxorubicin, cisplatin, and bleomycin, cause tumor senescence and death through the induction of oxidative stress (3, 46–48). Previous studies have shown that ROS also mediated the tumor-killing action of PX-12; inhibition of ROS abolished its antitumor actions (49–51). Given that H_2S regulates oxidative stress via multiple mechanisms, it is conceivable that these mechanisms could contribute to the observed effects in the current investigation.

PX-12 is an inhibitor of Trx, which inactivates Trx through interaction with the reduced thiols of Trx (17). In this study, we confirmed that the thiol activity of Trx was blocked by PX-12. Intriguingly, in the presence of H_2S, this effect of PX-12 was abolished. The question naturally occurs as to how H_2S prevented the effect of PX-12. Theoretically, it could be a result of its effects on Trx, PX-12, or both.

Regarding the effect of H_2S on Trx, we have reported that H_2S promoted the reductivity of Trx through sulfhydration (10). Here, we reconfirmed our previous finding that H_2S increased sulfhydryl residues in Trx. This increase counteracted the action of PX-12. Besides its action on Trx, our study also revealed that H_2S directly deactivated PX-12. This conclusion is supported by the fact that pretreatment of PX-12 with H_2S caused a loss of PX-12 activity and a formation of 2-MI, a metabolite resulted from the cleavage of the disulfide bond in PX-12. This action of H_2S was unexpected, but not surprising because H_2S, as a reducing chemical, has been shown to cleave disulfide bond in many proteins (10, 34, 35).

The antitumor action of PX-12 is generally accepted to be through its specific and irreversible binding to Trx. However, there are also reports that PX-12 has off-target effects. It bound to tubulin and cysteine-dependent proteases

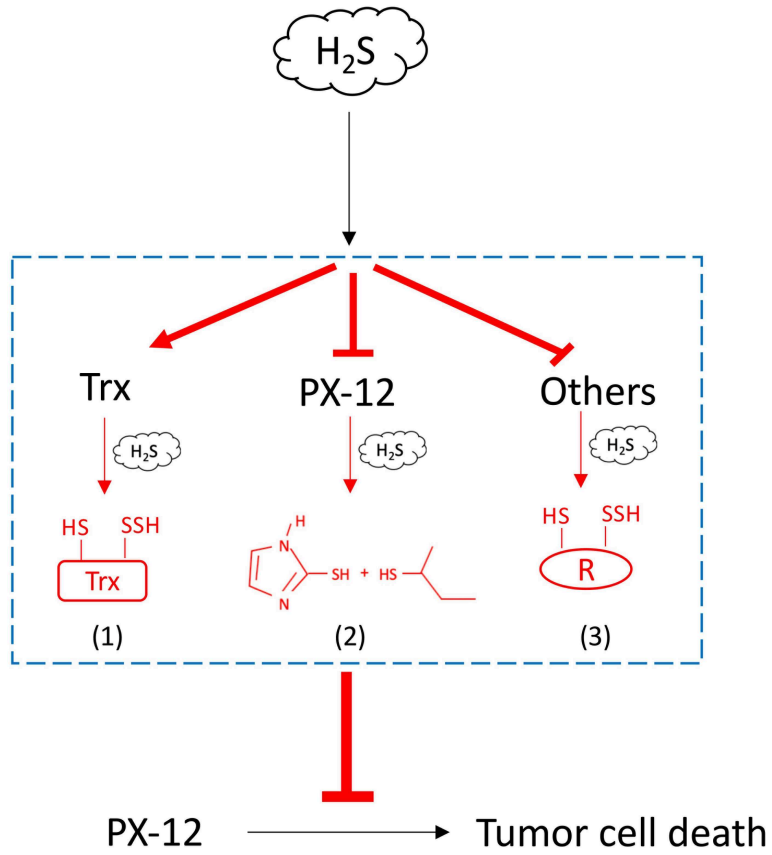

FIGURE 10 | Schematic depiction of the mechanisms involved in H_2S-mediated tumor resistance to PX-12. H_2S increased tumor cell resistance to H_2S through multiple mechanisms: (1) H_2S promotes Trx in the reduced state, counteracting the thiol-inhibiting effect of PX-12; (2) H_2S directly reacts with PX-12, leading to the cleavage of disulfide bond in PX-12 and PX-12 deactivation; and (3) H_2S induces sulfhydryl residues in proteins that competes with Trx in binding PX-12, causing a reduced binding of PX-12 to Trx.

(40). In this investigation, we found that PX-12 interacted with sulfhydryl residues of many cellular proteins, including albumin. Interestingly, our group showed that H_2S increased the sulfhydryl residues in many proteins, including IgG and albumin (10, 34). The observations promoted us to speculate that H_2S could enhance cell resistance through induction of sulfhydryl residues in these proteins. Our results support this idea. This is shown by the facts that supplement of cells with H_2S-treated albumin blunted the tumor-killing action of PX-12, and that blockade of extracellular sulfhydryl residues enhanced efficacy of PX-12. Thus, induction of sulfhydryl residues in proteins other than Trx by H_2S could be an unexpected, but important mechanism by which H_2S increased cell resistance to PX-12.

Of note, apart from CSE, CBS and 3-MST are also involved in the production of H_2S. In this study, their expression and roles in the tested cells have not been characterized. Given that the level of endogenous and exogenous H_2S was closely correlated with the cell sensitivity to PX-12, it is reasonable to conclude that H_2S is a determiant factor governing cell response to PX-12. Consistent with previous reports (52, 53), our study also indicates that CSE was the predominant enzyme for H_2S production in HepG2 cells. The inhibition or downregulation of CSE in HepG2 cells significantly sensitized cells to PX-12. In this context, the lack of the information about CBS and 3-MST should not greatly affect our conclusion.

It is also worth mentioning that our finding could also be applicable to tumor chemotherapy targeting Trx reductase such as auranofin and pleurotin. In our previous study, we have demonstrated that Trx reductase inhibitor auranofin-induced cell death was also prevented by H_2S (10). This effect of H_2S could be ascribed to its promoting action on Trx reductivity. In addition, it could also be due to its induction of sulfhydryl residues in other cellular proteins as revealed in this paper.

Our study could have important basic and clinical implications. First, we identified H_2S as a novel molecule rendering cell resistance to PX-12. In many types of tumors, increased expression of H_2S-synthesizing enzymes has been reported (26–30, 54). Besides, tumors could also occur at an environment exposed to H_2S, such as colon where up to millimolar H_2S has been reported (55, 56). Moreover, H_2S is also available from food and bacteria. This endogenous and exogenous H_2S could hinder the therapeutic efficacy of PX-12.

Strategies against H_2S can be developed to increase efficacy of tumor therapy. Moreover, H_2S could also be used as a potential marker predicting tumor response to PX-12.

Second, our study found that, other than Trx, PX-12 also reacted with a wide range of proteins through a thiol-disulfide exchange, including albumin, a protein that is abundant in hepatocytes and serum (41–43). Given the importance of thiol residues in protein functions, this finding should be important. It suggests that PX-12 may have a broader range of activity and applicability. It also hints that drug resistance to PX-12 should not be limited to Trx system, but also include other PX-12-reactive proteins. In this study, we showed that H_2S significantly increased the thiol activity in a wide range of proteins, including IgG (34) and albumin. Because these proteins are far more abundant than Trx, it may play an important role in drug resistance. Thus, prevention of the off-target binding of PX-12 could be an effective way to increase therapeutic efficacy.

Third, our study provides additional evidence supporting a regulatory role of H_2S on cysteine or disulfide bonds in multiple molecules, possibly through sulfhydration. Given thiol has been characterized as an important molecule involved in the regulation of oxidative and redox signaling, this effect of H_2S could be an important mechanism by which H_2S increases drug resistance. In this study, we also found that H_2S directly deactivated PX-12. This result suggests that, in analyzing the effect and mechanisms of H_2S on drug resistance, other than the important signaling molecules and cellular proteins, attention should also be paid to the possible direct chemical reaction between H_2S and drugs.

Of note, our study also has limitations. We have used a relatively high, non-physiological concentration of NaHS as an exogenous H_2S donor in some of the experiments regarding the effects of H_2S on recombinant Trx, albumin and PX-12. However, this shortcoming should not greatly affect our conclusion about the involvement of H_2S in cell resistance to Trx inhibitors because the similar results were also achieved through modulation of endogenous H_2S levels. Another limitation of this study is that our finding was obtained from cultured cells. It is necessary to verify the results in animal models. This will be the direction of our future research.

Collectively, we characterized H_2S as an important molecule governing cell response to PX-12. This effect of H_2S involved multiple mechanisms including increasing thiol activity in Trx and in the proteins that competitively bind PX-12, as well as direct inactivation of PX-12. Our study suggests that targeting H_2S and thiol residues could be an effective way to increase the tumor-killing efficacy of PX-12. H_2S can be used as a marker predicting tumor cell response to PX-12.

DATA AVAILABILITY STATEMENT

All datasets generated for this study are included in the article/**Supplementary Material**.

AUTHOR CONTRIBUTIONS

ZM performed research and wrote the manuscript. XY, YH, and ZZ provided experimental assistance. SM and HS performed 2-MI detection. KG provided crucial reagents, technical assistance, and intellectual input. JY designed the study and wrote the manuscript.

FUNDING

This work was supported by a grant from the Ministry of Education, Culture, Sports, Science and Technology, Japan (17K11176 to JY), as well as National Natural Science Foundation of China (81673912 to KG).

SUPPLEMENTARY MATERIAL

The Supplementary Material for this article can be found online at: https://www.frontiersin.org/articles/10.3389/fonc.2020.00252/full#supplementary-material

REFERENCES

1. Moscow JA, Cowan KH, Sikic BI, Morrow CS, Cowan KH. Drug resistance and its clinical circumvention. In: Holland JF, Frei E, editors. *Cancer Med*. BC Decker, Inc. (2006). p. 630–47.
2. Gill JG, Piskounova E, Morrison SJ, editors. Cancer, oxidative stress, and metastasis. *Cold Spring Harb Symp Quant Biol*. (2016) 81:163–75. doi: 10.1101/sqb.2016.81.030791
3. Cook JA, Gius D, Wink DA, Krishna MC, Russo A, Mitchell JB, editors. Oxidative stress, redox, and the tumor microenvironment. *Semin Radiat Oncol*. (2004) 14:259–66. doi: 10.1016/j.semradonc.2004.04.001
4. Cunningham GM, Roman MG, Flores LC, Hubbard GB, Salmon AB, Zhang Y, et al. The paradoxical role of thioredoxin on oxidative stress and aging. *Arch Biochem Biophys*. (2015) 576:32–8. doi: 10.1016/j.abb.2015.02.025
5. Sies H, Berndt C, Jones DP. Oxidative stress. *Annu Rev Biochem*. (2017) 86:715–48. doi: 10.1146/annurev-biochem-061516–045037
6. Lillig CH, Holmgren A. Thioredoxin and related molecules-from biology to health and disease. *Antioxid Redox Signal*. (2007) 9:25–47. doi: 10.1089/ars.2007.9.25
7. Karlenius TC, Tonissen KF. Thioredoxin and cancer: a role for thioredoxin in all states of tumor oxygenation. *Cancers*. (2010) 2:209–32. doi: 10.3390/cancers2020209
8. Arnér ESJ, Holmgren A. The thioredoxin system in cancer. *Semin Cancer Biol*. (2006) 16:420–6. doi: 10.1016/j.semcancer.2006.10.009
9. Kim SJ, Miyoshi Y, Taguchi T, Tamaki Y, Nakamura H, Yodoi J, et al. High thioredoxin expression is associated with resistance to docetaxel in primary breast cancer. *Clin Cancer Res*. (2005) 11:8425–30. doi: 10.1158/1078–0432.CCR-05–0449
10. Mao Z, Huang Y, Zhang Z, Yang X, Zhang X, Huang Y, et al. Pharmacological levels of hydrogen sulfide inhibit oxidative cell injury through regulating the redox state of thioredoxin. *Free Radic Biol Med*. (2019) 134:190–9. doi: 10.1016/j.freeradbiomed.2019.01.009
11. Gao K, Chi Y, Sun W, Takeda M, Yao J. 5′-AMP-activated protein kinase attenuates adriamycin-induced oxidative podocyte injury through thioredoxin-mediated suppression of the apoptosis signal-regulating kinase 1-P38 signaling pathway. *Mol Pharmacol*. (2014) 85:460–71. doi: 10.1124/mol.113.089458
12. Li C, Thompson MA, Tamayo AT, Zuo Z, Lee J, Vega F, et al. Over-expression of Thioredoxin-1 mediates growth, survival, and chemoresistance and is a

druggable target in diffuse large B-cell lymphoma. *Oncotarget*. (2012) 3:314. doi: 10.18632/oncotarget.463
13. Molina M, Camps C, De Las Penas R, Alonso G, Lopez-Vivanco G, Provencio M, et al. Elevated levels of thioredoxin (Trx) in serum correlate with poor outcome in docetaxel (doc)/cisplatin (cis)-treated stage IV non-small cell lung cancer (NSCLC) patients (p). *J Clin Oncol*. (2007) 25:7628. doi: 10.1016/S1359–6349(07)71362–9
14. Tonissen KF, Di Trapani G. Thioredoxin system inhibitors as mediators of apoptosis for cancer therapy. *Mol Nutr Food Res*. (2009) 53:87–103. doi: 10.1002/mnfr.200700492
15. Biaglow JE, Miller RA. The thioredoxin reductase/thioredoxin system: novel redox targets for cancer therapy. *Cancer Biol Ther*. (2005) 4:13–20. doi: 10.4161/cbt.4.1.1434
16. Raninga PV, Di Trapani G, Vuckovic S, Bhatia M, Tonissen KF. Inhibition of thioredoxin 1 leads to apoptosis in drug-resistant multiple myeloma. *Oncotarget*. (2015) 6:15410. doi: 10.18632/oncotarget.3795
17. Ramanathan RK, Kirkpatrick DL, Belani CP, Friedland D, Green SB, Chow HH, et al. A Phase I pharmacokinetic and pharmacodynamic study of PX-12, a novel inhibitor of thioredoxin-1, in patients with advanced solid tumors. *Clin Cancer Res*. (2007) 13:2109–14. doi: 10.1158/1078–0432.CCR-06–2250
18. Ramanathan RK, Abbruzzese J, Dragovich T, Kirkpatrick L, Guillen JM, Baker AF, et al. A randomized phase II study of PX-12, an inhibitor of thioredoxin in patients with advanced cancer of the pancreas following progression after a gemcitabine-containing combination. *Cancer Chemother Pharmacol*. (2011) 67:503–9. doi: 10.1007/s00280–010-1343–8
19. Tan Y, Bi L, Zhang P, Wang F, Lin F, Ni W, et al. Thioredoxin-1 inhibitor PX-12 induces human acute myeloid leukemia cell apoptosis and enhances the sensitivity of cells to arsenic trioxide. *Int J Clin Exp Pathol*. (2014) 7:4765–73.
20. Kirkpatrick DL, Ehrmantraut G, Stettner S, Kunkel M, Powis G. Redox active disulfides: the thioredoxin system as a drug target. *Oncol Res*. (1997) 9:351–6.
21. Kimura H. Hydrogen sulfide: its production, release and functions. *Amino acids*. (2011) 41:113–21. doi: 10.1007/s00726–010-0510-x
22. Kimura Y, Kimura H. Hydrogen sulfide protects neurons from oxidative stress. *FASEB J*. (2004) 18:1165–7. doi: 10.1096/fj.04–1815fje
23. Xie Z-Z, Liu Y, Bian J-S. Hydrogen sulfide and cellular redox homeostasis. *Oxid Med Cell Longev*. (2016) 2016:6043038. doi: 10.1155/2016/6043038
24. Lu M, Hu L-F, Hu G, Bian J-S. Hydrogen sulfide protects astrocytes against H2O2-induced neural injury via enhancing glutamate uptake. *Free Radic Biol Med*. (2008) 45:1705–13. doi: 10.1016/j.freeradbiomed.2008.09.014
25. Wang Q, Wang X-L, Liu H-R, Rose P, Zhu Y-Z. Protective effects of cysteine analogues on acute myocardial ischemia: novel modulators of endogenous H2S production. *Antioxid Redox Signal*. (2010) 12:1155–65. doi: 10.1089/ars.2009.2947
26. Hellmich MR, Szabo C. Hydrogen sulfide and cancer. *Handb Exp Pharmacol*. (2015) 230:233–41. doi: 10.1007/978–3-319–18144-8_12
27. Hellmich MR, Coletta C, Chao C, Szabo C. The therapeutic potential of cystathionine β-synthetase/hydrogen sulfide inhibition in cancer. *Antioxid Redox Signal*. (2015) 22:424–48. doi: 10.1089/ars.2014.5933
28. Szabo C, Coletta C, Chao C, Módis K, Szczesny B, Papapetropoulos A, et al. Tumor-derived hydrogen sulfide, produced by cystathionine-β-synthase, stimulates bioenergetics, cell proliferation, and angiogenesis in colon cancer. *Proc Natl Acad Sci USA*. (2013) 110:12474–9. doi: 10.1073/pnas.1306241110
29. Wu D, Si W, Wang M, Lv S, Ji A, Li Y. Hydrogen sulfide in cancer: friend or foe? *Nitric Oxide*. (2015) 50:38–45. doi: 10.1016/j.niox.2015.08.004
30. Wahafu W, Gai J, Song L, Ping H, Wang M, Yang F, et al. Increased H(2)S and its synthases in urothelial cell carcinoma of the bladder, and enhanced cisplatin-induced apoptosis following H(2)S inhibition in EJ cells. *Oncol Lett*. (2018) 15:8484–90. doi: 10.3892/ol.2018.8373
31. Untereiner AA, Pavlidou A, Druzhyna N, Papapetropoulos A, Hellmich MR, Szabo C. Drug resistance induces the upregulation of H2S-producing enzymes in HCT116 colon cancer cells. *Biochem Pharmacol*. (2018) 149:174–85. doi: 10.1016/j.bcp.2017.10.007
32. Bhattacharyya S, Saha S, Giri K, Lanza IR, Nair KS, Jennings NB, et al. Cystathionine beta-synthase (CBS) contributes to advanced ovarian cancer progression and drug resistance. *PloS ONE*. (2013) 8:e79167. doi: 10.1371/journal.pone.0079167
33. Szczesny B, Marcatti M, Zatarain JR, Druzhyna N, Wiktorowicz JE, Nagy P, et al. Inhibition of hydrogen sulfide biosynthesis sensitizes lung adenocarcinoma to chemotherapeutic drugs by inhibiting mitochondrial DNA repair and suppressing cellular bioenergetics. *Sci Rep*. (2016) 6:36125. doi: 10.1038/srep36125
34. Zhang Z, Fang X, Yang X, Mitsui T, Huang Y, Mao Z, et al. Hydrogen sulfide donor NaHS alters antibody structure and function via sulfhydration. *Int Immunopharmacol*. (2019) 73:491–501. doi: 10.1016/j.intimp.2019.05.052
35. Huang Y, Zhang Z, Huang Y, Mao Z, Yang X, Nakamura Y, et al. Induction of inactive TGF-β1 monomer formation by hydrogen sulfide contributes to its suppressive effects on Ang II-and TGF-β1-induced EMT in renal tubular epithelial cells. *Biochem Biophys Res Commun*. (2018) 501:534–40. doi: 10.1016/j.bbrc.2018.05.032
36. Hine C, Kim H-J, Zhu Y, Harputlugil E, Longchamp A, Matos MS, et al. Hypothalamic-pituitary axis regulates hydrogen sulfide production. *Cell Metab*. (2017) 25:1320–33.e5. doi: 10.1016/j.cmet.2017.05.003
37. Chen Y, Cai J, Jones DP. Mitochondrial thioredoxin in regulation of oxidant-induced cell death. *FEBS Lett*. (2006) 580:6596–602. doi: 10.1016/j.febslet.2006.11.007
38. Sen N, Paul BD, Gadalla MM, Mustafa AK, Sen T, Xu R, et al. Hydrogen sulfide-linked sulfhydration of NF-κB mediates its antiapoptotic actions. *Mol Cell*. (2012) 45:13–24. doi: 10.1016/j.molcel.2011.10.021
39. Liu Y, Yang R, Liu X, Zhou Y, Qu C, Kikuiri T, et al. Hydrogen sulfide maintains mesenchymal stem cell function and bone homeostasis via regulation of Ca2+ channel sulfhydration. *Cell Stem Cell*. (2014) 15:66–78. doi: 10.1016/j.stem.2014.03.005
40. Huber K, Patel P, Zhang L, Evans H, Westwell AD, Fischer PM, et al. 2-[(1-methylpropyl) dithio]-1H-imidazole inhibits tubulin polymerization through cysteine oxidation. *Mol Cancer Ther*. (2008) 7:143–51. doi: 10.1158/1535–7163.MCT-07–0486
41. Moshage H, Janssen J, Franssen J, Hafkenscheid J, Yap S. Study of the molecular mechanism of decreased liver synthesis of albumin in inflammation. *J Clin Invest*. (1987) 79:1635–41. doi: 10.1172/JCI113000
42. Woodworth CD, Isom HC. Regulation of albumin gene expression in a series of rat hepatocyte cell lines immortalized by simian virus 40 and maintained in chemically defined medium. *Mol Cell Biol*. (1987) 7:3740–8. doi: 10.1128/MCB.7.10.3740
43. Bourdon E, Loreau N, Lagrost L, Blache D. Differential effects of cysteine and methionine residues in the antioxidant activity of human serum albumin. *Free Radic Res*. (2005) 39:15–20. doi: 10.1080/10715760400024935
44. Oettl K, Marsche G. Redox state of human serum albumin in terms of cysteine-34 in health and disease. *Methods Enzymol*. (2010) 474:181–95. doi: 10.1016/S0076–6879(10)74011–8
45. Davies MJ, Gilbert BC, Haywood RM. Radical-induced damage to bovine serum albumin: role of the cysteine residue. *Free Radic Res Commun*. (1993) 18:353–67. doi: 10.3109/10715769309147502
46. Deavall DG, Martin EA, Horner JM, Roberts R. Drug-induced oxidative stress and toxicity. *J Toxicol*. (2012) 2012:645460. doi: 10.1155/2012/645460
47. Dasari S, Tchounwou PB. Cisplatin in cancer therapy: molecular mechanisms of action. *Eur J Pharmacol*. (2014) 740:364–78. doi: 10.1016/j.ejphar.2014.07.025
48. Cort A, Timur M, Dursun E, Kucuksayan E, Aslan M, Ozben T. Effects of N-acetylcystein on bleomycin-induced apoptosis in malignant testicular germ cell tumors. *J Physiol Biochem*. (2012) 68:555–62. doi: 10.1007/s13105–012-0173-z
49. You BR, Shin HR, Park WH. PX-12 inhibits the growth of A549 lung cancer cells via G2/M phase arrest and ROS-dependent apoptosis. *Int J Oncol*. (2014) 44:301–8. doi: 10.3892/ijo.2013.2152
50. You BR, Shin HR, Han BR, Park WH. PX-12 induces apoptosis in Calu-6 cells in an oxidative stress-dependent manner. *Tumor Biology*. (2015) 36:2087–95. doi: 10.1007/s13277–014-2816-x
51. Li G-Z, Liang H-F, Liao B, Zhang L, Ni Y-A, Zhou H-H, et al. PX-12 inhibits the growth of hepatocelluar carcinoma by inducing S-phase arrest, ROS-dependent apoptosis and enhances 5-FU cytotoxicity. *Am J Transl Res*. (2015) 7:1528–40.
52. Mani S, Yang G, Wang R. A critical life-supporting role for cystathionine γ-lyase in the absence of dietary cysteine supply. *Free Radic Biol Med*. (2011) 50:1280–7. doi: 10.1016/j.freeradbiomed.2011.01.038
53. Kabil O, Vitvitsky V, Xie P, Banerjee R. The quantitative significance of the transsulfuration enzymes for H2S production in murine

tissues. *Antioxid Redox Signal*. (2011) 15:363–72. doi: 10.1089/ars.2010.3781

54. Panza E, De Cicco P, Armogida C, Scognamiglio G, Gigantino V, Botti G, et al. Role of the cystathionine γ lyase/hydrogen sulfide pathway in human melanoma progression. *Pigment Cell Melanoma Res*. (2015) 28:61–72. doi: 10.1111/pcmr.12312
55. Wallace JL. Hydrogen sulfide-releasing anti-inflammatory drugs. *Trends Pharmacol Sci*. (2007) 28:501–5. doi: 10.1016/j.tips.2007.09.003
56. Magee EA, Richardson CJ, Hughes R, Cummings JH. Contribution of dietary protein to sulfide production in the large intestine: an *in vitro* and a controlled feeding study in humans. *Am J Clin Nutr*. (2000) 72:1488–94. doi: 10.1093/ajcn/72.6.1488

Conflict of Interest: The authors declare that the research was conducted in the absence of any commercial or financial relationships that could be construed as a potential conflict of interest.

frontiers in Oncology

ORIGINAL RESEARCH
published: 25 February 2021
doi: 10.3389/fonc.2021.619351

Tumor Decelerating and Chemo-Potentiating Action of Methyl Jasmonate on a T Cell Lymphoma *In Vivo*: Role of Altered Regulation of Metabolism, Cell Survival, Drug Resistance, and Intratumoral Blood Flow

*Yugal Goel[1], Saveg Yadav[1], Shrish Kumar Pandey[1], Mithlesh Kumar Temre[1], Babu Nandan Maurya[2], Ashish Verma[2], Ajay Kumar[3] and Sukh Mahendra Singh[1]**

[1] School of Biotechnology, Institute of Science, Banaras Hindu University, Varanasi, India, [2] Department of Radiodiagnosis and Imaging, Institute of Medical Sciences, Banaras Hindu University, Varanasi, India, [3] Department of Zoology, Institute of Science, Banaras Hindu University, Varanasi, India

OPEN ACCESS

Edited by:
Jiang-Jiang Qin, Chinese Academy of Sciences (CAS), China

Reviewed by:
Samik Chakraborty, Boston Children's Hospital and Harvard Medical School, United States
Naveen Vishvakarma, Guru Ghasidas Vishwavidyalaya, India
Swapna Chaudhuri, Chittaranjan National Cancer Institute, India

***Correspondence:**
Sukh Mahendra Singh
smsinghbiotech@bhu.ac.in

Specialty section:
This article was submitted to Pharmacology of Anti-Cancer Drugs, a section of the journal Frontiers in Oncology

Received: *20 October 2020*
Accepted: *18 January 2021*
Published: *25 February 2021*

Citation:
Goel Y, Yadav S, Pandey SK, Temre MK, Maurya BN, Verma A, Kumar A and Singh SM (2021) Tumor Decelerating and Chemo-Potentiating Action of Methyl Jasmonate on a T Cell Lymphoma In Vivo: Role of Altered Regulation of Metabolism, Cell Survival, Drug Resistance, and Intratumoral Blood Flow. Front. Oncol. 11:619351. doi: 10.3389/fonc.2021.619351

Methyl jasmonate (MJ), a natural oxylipin, possesses a broad spectrum of antineoplastic potential *in vitro*. However, its tumor growth impeding and chemo-potentiating action has not been adequately investigated *in vivo*. Using a murine thymus-derived tumor named Dalton's Lymphoma (DL), in the present study, we examined if intra-tumoral administration of MJ can cause tumor growth impedance. We also explored the associated molecular mechanisms governing cell survival, carbohydrate & lipid metabolism, chemo-potentiation, and angiogenesis. MJ administration to tumor-transplanted mice caused deceleration of tumor growth accompanying prolonged survival of the tumor-bearing mice. MJ-dependent tumor growth retardation was associated with the declined blood supply in tumor milieu, cell cycle arrest, augmented induction of apoptosis and necrosis, deregulated glucose and lipid metabolism, enhanced membrane fragility of tumor cells, and altered cytokine repertoire in the tumor microenvironment. MJ administration modulated molecular network implicating Hsp70, Bcl-2, TERT, p53, Cyt *c*, BAX, GLUT-1, HK 2, LDH A, PDK-1, HIF-1α, ROS, MCT-1, FASN, ACSS2, SREBP1c, VEGF, cytokine repertoire, and MDR1, involved in the regulation of cell survival, carbohydrate and fatty acid metabolism, pH homeostasis, and drug resistance. Thus, the present study unveils novel molecular mechanisms of the tumor growth decelerating action of MJ. Besides, this preclinical study also establishes the adjunct therapeutic potential of MJ. Hence, the present investigation will help to design novel anti-cancer therapeutic regimens for the treatment of hematological malignancies.

Keywords: methyl jasmonate, tumor growth impedance, cell survival and metabolic regulation, chemo-potentiation, intra-tumoral blood flow

INTRODUCTION

Global research efforts are focused on devising novel anti-cancer therapeutic strategies capable of specifically targeting the neoplastic cells. Thus, several agents capable of targeting one or more cancer hallmarks are being examined for their therapeutic efficacy. Methyl jasmonate (MJ), a natural oxylipin (Methyl(1R,2R)-3-Oxo-2-(2Z)-2-pentenyl-cyclopentaneacetate; http://www.chemspider.com/Chemical-Structure.4445210.html), possesses a promising antineoplastic potential, devoid of any harmful effects on healthy cells. The broad-spectrum anti-cancer action of MJ has been vividly demonstrated against neoplastic cells of diverse origins (1, 2). The cytotoxic activity of MJ against neoplastic cells has been shown to implicate a wide variety of molecular mechanisms but majorly through the induction of mitochondrial-mediated apoptotic cell death by involving altered functions of mitochondria (3, 4) and causing detachment of hexokinase from VADC (5). However, the bulk of data associated with MJ's antineoplastic action is mainly from *in vitro* studies performed against a wide variety of neoplastic cell lines (1, 2, 6, 7). However, to optimally realize its chemotherapeutic potential to establish MJ as a standard anti-cancer drug, it is essential to assess the *in vivo* anti-cancer therapeutic efficacy, which is mainly lacking in the case of MJ.

In vivo based investigations are crucial for understanding various critical issues related to a drug's ability to decelerate tumor progression. Moreover, other decisive aspects regulating tumor growth like dose, administration route, the bioavailability, mechanism(s) of action, side effects, toxicity, and different *in vivo* interactions also need to be worked out. However, only sporadic studies are available in this respect for MJ. The *in vivo* antitumor action of MJ has been investigated against only a limited type of malignancies, which includes breast cancer (8, 9), multiple myeloma (10), and murine lymphoma (11). However, these studies do not provide detailed mechanisms of *in vivo* antitumor efficacy/tumor growth retarding and chemo-potentiating MJ action. Thus, it is essential to investigate MJ's effect on the crucial cancer cell-specific metabolism & cell survival regulation, membrane stability, angiogenesis, and drug resistance in an appropriate *in vivo* model. This will help to achieve therapeutic optimization laying the foundation for further clinical trials. However, except for only one study mentioned above (1), to the best of our knowledge, so far, there has been no comprehensive investigation revealing mechanisms of the therapeutic potential of MJ against any progressive hematological neoplasms.

Additionally, it will also be essential to understand the efficacy of MJ's combinatorial use with other conventional anti-cancer drugs, which is only feebly investigated (1, 9). However, all of these studies were only *in vitro* based, with little clue about such combinations' therapeutic efficacy under *in vivo* tumor-bearing situation. Hence, it is also essential to work out the *in vivo* therapeutic potential of MJ in a combinatorial study and the associated mechanism(s), which will lower the doses and, subsequently, the massive side effects of standard anti-cancer drugs.

Considering the lack of knowledge regarding the *in vivo* antineoplastic and chemo-potentiation mechanisms of MJ, the present study was conducted on a thymus-derived murine tumor, Dalton's lymphoma (DL), to unravel the unknown mechanistic pathways. DL has been successfully used in our and other laboratories for exploring the therapeutic efficacy of several anti-cancer agents (12, 13). This is the first report on understanding MJ's therapeutic efficacy on a progressively growing thymoma, with a comprehensive investigation of the underlying unexplored molecular mechanisms and issues related to MJ's chemo-potentiating action *in vivo*.

MATERIALS AND METHODS

Tumor, Mice, and Reagents

Dalton's lymphoma initially discovered in the laboratory of A.J Dalton (NCI, Bethesda, USA) as a spontaneously originated thymoma in mice (14) and subsequently adapted for serial transplantation and ascitic growth (15), was used in the present investigation to understand antitumor action of MJ. We maintained this tumor in our laboratory by serial intraperitoneal transplantation in BALB/c mice for achieving ascitic tumor growth. Healthy male mice (6–8 weeks of age) were intraperitoneally transplanted with 5 x 10^5 cells. Mice fully grown ascitic tumor is apparent by 12–16 days following tumor transplantation. The average survival time of tumor-bearing mice is usually 22 ± 2 days under normal conditions. Mice handling and experimentations were carried out as per approval of the institutional animal ethical committee (Approval reference: BHU/DOZ/IAEC/2018-2019/019; dated: January 01, 2019). HuT-78 and J6 (human T cell lymphoma) cell lines were obtained from NCCS, Pune, India. Methyl Jasmonate was commercially procured from Sigma-Aldrich (USA) with 95% purity (catalog no. 392707). Most of the reagents were procured from Sigma-Aldrich (USA). Other reagents and biologicals were obtained from the following sources: Fetal calf serum (Hyclone, USA), and Annexin V/PI apoptosis detection kit (Imagenex, USA), Antibodies (Imagenex, USA, Sigma Aldrich, USA, Chemicon, USA, BD Pharmingen Inc, USA and e-Biosciences, USA), and Primers for RT-PCR (Eurofins, USA).

Administration of MJ to Tumor Transplanted Mice

To study the effect of MJ administration on tumor progression, we followed a protocol summarised in **Figure 1**. Tumor cells were harvested from the tumor-bearing mice administered with PBS alone or containing MJ (100 g/kg) on the indicated days. The remaining mice were left to study the rate of tumor progression and survival time. As body weight is reported to be a parameter for tumor progression in ascitic tumor growth (16), the same was used in the study to monitor tumor progression along with an estimation of the total volume of ascitic fluid and enumeration of viable tumor count (13). In each group, 10 mice were used.

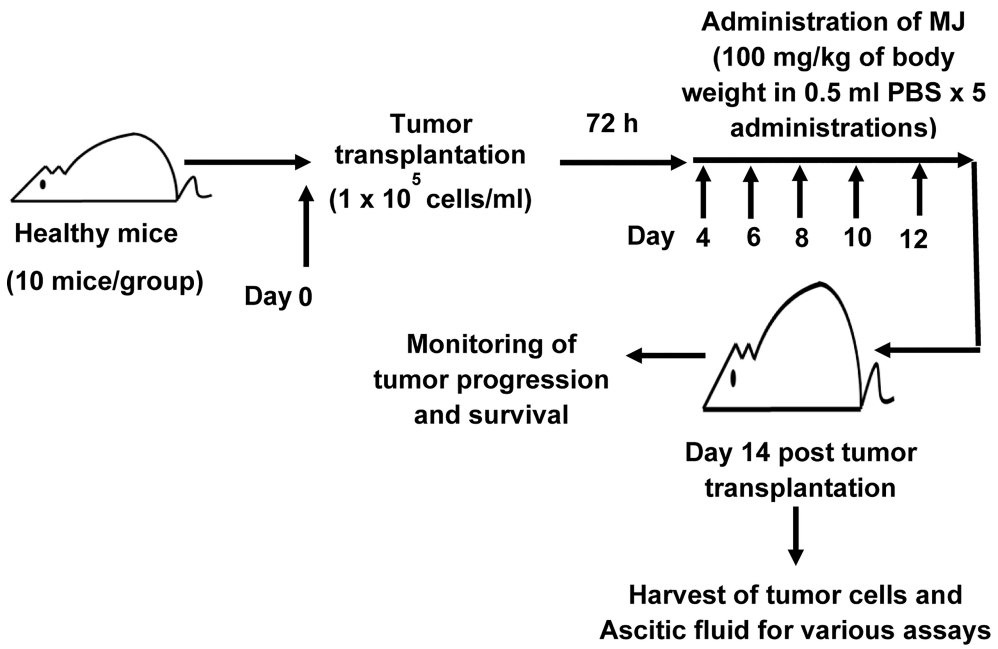

FIGURE 1 | Protocol for the administration of MJ to tumor-bearing mice. Mice in groups of 10 each were transplanted with 1 x 10^5 DL cells in 0.5 ml PBS per mouse (day 0), followed by intraperitoneal administration of MJ (100 mg/kg) or PBS on days 4, 6, 8, 10, and 12 post tumor transplantation. Tumor cells and ascitic fluid were collected and investigated for various assays on day 14. Remaining tumor-bearing mice were monitored for change of body weight and survival as parameters of tumor progression.

Dye Exclusion Test for Cell Survival

The number of viable tumor cells was enumerated using the standard trypan blue dye exclusion test (17).

MTT Assay

The MTT assay was used for estimating metabolic activity and calculated cytotoxicity following the method described by Mosmann (18), with slight modifications. The MTT solution (final concentration 0.5 mg/ml) was added to the wells containing the tumor cells in the medium, and further incubation was carried out for 4 h (37 °C in CO_2 incubator). The formazan crystals formed during the incubation period were solubilized using DMSO for overnight. Absorbance at 540 nm was measured by the ELISA plate reader (Labsystems Finland). ID_{50} values were calculated by following a method described by Vertosick et al. (19).

Estimation of Cytotoxicity

Cytotoxicity was assayed using a method described earlier (20), using MTT assay. The percentage of cytotoxicity was calculated using the following formula:

$$\% \text{ Cytotoxicity} = \frac{A-B}{A} \times 100$$

A: *Absorbance Control*

B: *Absorbance MJ*

Estimation of Cell Death

The apoptotic and necrotic modes of cell death were evaluated by microscopic observation of the control, and MJ exposed tumor cells using the standard Wright-Giemsa and Annexin V/PI staining (17, 21) following the manufacturer's instructions.

Cell Cycle Analysis

The cell cycle analysis was performed following a method described earlier (17) based on the method of Shen et al. (22). The tumor cells harvested from the tumor-bearing mice of control and treated groups were washed twice with chilled PBS, fixed in 70% ice-cold ethanol followed by incubation for 30 min at −20°C. The cells (1×10^5 cells/ml) were then washed with PBS, stained with PI (10 µg/ml) following incubation with 20 µg/ml of RNAase A solution for 30 min at 37°C in dark. Thereafter, cells were analyzed by the flow cytometer for cell cycle arrest. A total of 10,000 cells per sample was acquired on a flow cytometer (BD FACSCalibur) using a PI suitable band filter and the events below 400/Sec. The primary gate was on a dot plot with FSC vs. SSC. A secondary gate was applied around the FL2-A (pulse area) vs. FL2-W (pulse width). Finally, the data was recorded on a histogram plot with FL2-A at X-axis & cell counts at Y-axis, and analysis was quantified by the Cell Quest software (Becton Dickinson).

Detection of Cell Surface Expression of MCT-1, GLUT-1, and MDR1

The expression of MCT1, GLUT-1, and MDR1 was analyzed by flow cytometry (23, 24) along with Western blotting (25). Cells were incubated with primary antibody for 40 min, washed, and subsequently incubated with fluorochrome-conjugated secondary antibody for 30 min at 37 °C in a humidified atmosphere. The expression pattern of the indicated molecules was analyzed by flow cytometry.

Immunodetection of Cytokine Production in Ascitic Fluid

The levels of IL-6, IFN-ϒ, and TGF-β were detected by a standard ELISA in the ascitic fluid of control and MJ-exposed group (26). The ELISA plate wells were coated with 50 µl of ascitic fluid and kept at 4 °C overnight. The ELISA plates were extensively washed with PBS-Tween-20 (0.1% v/v), followed by blocking of unsaturated sited by BSA (1% w/v) solution in PBS. Washing was followed by incubation with the primary antibody and then with alkaline phosphatase-conjugated secondary antibody at room temperature. After washing, p-nitrophenyl phosphate (1 mg/ml) was added, followed by incubation for 30 min at room temperature. Absorbance was measured at 405 nm.

Immunodetection of Cytosolic Cyt *c*

Cytosolic Cyt *c* was immunodetected by Western blotting using cytosolic extract (27) as described earlier. Cell lysis was carried out by incubating cells in lysis buffer pH 7.5 [(HEPES 200 mM, $MgCl_2$ 1.0 mM, sucrose 250 mM, EGTA 1.0 mM, PMSF 0.1 mM, DTT 1.0 mM, KCl 2 µg/ml, aprotinin and leupeptin (2 µg/ml)] followed by homogenisation. Lysate thus obtained was centrifuged (16,000 x g, 4° C, 20 min). The harvested supernatant was used for immunoblotting for the detection of Cyt *c*.

Immunoblotting

Immunoblotting was carried out to detect the indicated proteins as described earlier (20, 25) using cytosolic extract, or cell lysates obtained by lysing cells for 30 min on ice with lysis buffer [(Tris-Cl 20 mM (pH 8.0), NaCl (137 mM), glycerol 10 (v/v), Triton X-100 1% (v/v), EDTA 2.0 mM, PMSF 1.0 mM, Leupeptin 20 mM, and aprotinin 0.15 U/ml)]. The standard Bradford method was used to estimate the protein content in cytosolic extract or cell lysates (28). Samples for loading of gel were prepared in a gel-loading buffer [(Tris-Cl 0.5 M (pH 6.8), β-mercaptoethanol 100 mM, SDS 20% (w/v), Bromophenol blue 0.1% (v/v), and glycerol 10% (v/v)] by heating on a boiling water bath for 3 min. Thirty µg protein per sample was loaded on the polyacrylamide-SDS gel for electrophoresis. After electrophoresis, transfer of proteins to the nitrocellulose membrane (Sartorius, Germany) was carried out, followed by incubation with primary antibodies against the respective proteins. After that, the membrane was incubated with an alkaline phosphatase-conjugated secondary antibody followed by BCIP/NBT solution to visualize bands. The intensity of each protein band was analyzed by 'ImageJ' software. β-actin was used as a loading control.

TABLE 1 | Primer sequence for RT-PCR.

Gene	Primer Sequence
ACSS2	F-5′GTGGATGAAAGGAGCAACTACA-3'; R-5′ GCCCTCCCAGTAAAAAGCAACT-3'
FASN	F-5′-AGGGGTCGACCTGGTCCTCA-3'; R-5′-GCCATGCCCAGAGGGTGGTT-3'
GLUT-1	F-5'-CTTTGTGGCCTTCTTTGAAG-3'; R-5'-CCACACAGTTGCTCCACAT-3'
LDH A	F-5'-TGTCTCCAGCAAAGACTACTGT-3'; R-5'-GACTGTACTTGACAATGTTGGGA-3'
PDK-1	F-5′-CCGGGCCAGGTGGACTTC-3′; R-5′-GCAACTCTTGTCGCAGAAACATAA-3′
HIF-1α	F-5'-CTCAAAGTCGGACAGCCTCA-3'; R-5'-CCCTGCAGTAGGTTTCTGCT-3'
β-Actin	F-5'GGCACAGTGTGGGTGAC-3'; R-5'-CTGGCACCACACCTTCTAC-3'

Reverse Transcriptase-Polymerase Chain Reaction (RT-PCR)

The expression of indicated RNA was estimated using standard protocol for RT-PCR following a method described earlier (17). cDNA was prepared using a cell to cDNA kit as per the manufacturer's instructions (Ambion, USA). Primers for the indicated genes were obtained from Eurofins; the detailed description is provided in **Table 1**. Thirty-five cycles of amplification were done with each comprising denaturation for 2 min at 94 °C, annealing at 55–60 °C as per the genes' primers, and elongation for 30 s at 72 °C. The DNA bands were separated on 2% agarose gel containing ethidium bromide (0.25% w/v) by electrophoresis and then visualized using a UV-transilluminator. The band intensity of each gene was analyzed by "ImageJ" software. β-actin was used as a loading control.

DCFDA Staining for Intracellular ROS Expression

Intracellular ROS expression was detected using DCDFDA staining as described by Furuta et al. with minor modifications (29). Tumor cells were incubated in HBSS containing DCFDA (0.1 mM) for 45 min at 37°C. After washing, DCFDA stained cells were observed under the fluorescence microscope (Nikon, Japan) at 400 X magnification. The fluorescence intensity was analyzed by "ImageJ".

Ultrasonographic Imaging

A transabdominal color Doppler was performed on control and MJ-administered mice for observing blood flow in the ascitic cavity with iU22 Ultrasound (Phillips, NL), as per the method described earlier (30). We used a linear multifrequency assay transducer (7–11 MHZ) for detecting alterations in blood flow in the peritoneal cavity (30).

Statistical Analysis

Experiments were conducted thrice. The statistical significance of differences between test groups was analyzed by Student's t-test. A p-value of less than 0.05 was considered as significant.

RESULTS

MJ Administration Retards Tumor Progression

Initial experiments were conducted to explore if MJ's administration impedes tumor progression following the protocols as shown in **Figure 1**. Tumor growth was examined by estimating body weight and time duration of the host survival. Administration of MJ impeded tumor growth compared to the control (**Figure 2A**). The survival time of MJ-administered mice was also increased significantly compared to the untreated group (**Figure 2B**). To corroborate the observations mentioned above, the volume of ascitic fluid was measured as an indicator of tumor size. The number of tumor cells in the ascitic fluid was also counted. Administration of MJ caused a significant waning of tumor size (**Figure 2C**) compared to the control. Similarly, a substantial reduction in tumor cell numbers (number of tumor cells/ml of ascitic fluid) was also observed following MJ administration compared to control (**Figure 2D**). These two parameters were further confirmed the tumor growth decelerating action of MJ.

MJ Displays Tumor Cell-Specific Cytotoxic Activity

To ascertain MJ's tumoricidal action spectrum, we also examined its *in vitro* cytotoxicity against DL, HuT-78, and J6 cells, along with splenocytes and hepatocytes obtained from healthy mice. As shown in **Figure 3**, treatment of tumor cells with MJ resulted in a significant dose-dependent cytotoxic action against DL (ID_{50}: 558 μg/ml), HuT-78 (ID_{50}: 280 μg/ml), and J6 (ID_{50}: 167 μg/ml) cells compared to their respective untreated controls. Further, *in vitro* exposure of normal cells, splenocytes, and hepatocytes to MJ, did not affect their survival (**Figure 3**).

Molecular Mechanisms Associated With MJ-Dependent Tumor Growth Deceleration

One of the principal focus of this investigation was to decipher the molecular mechanisms underlying the observed tumor growth retarding action of MJ. We analyzed the mode of cell death induction, cell cycle, and expression repertoire of proteins that regulate these events. The number of apoptotic and necrotic cells showed a significant rise in the MJ group compared to the control

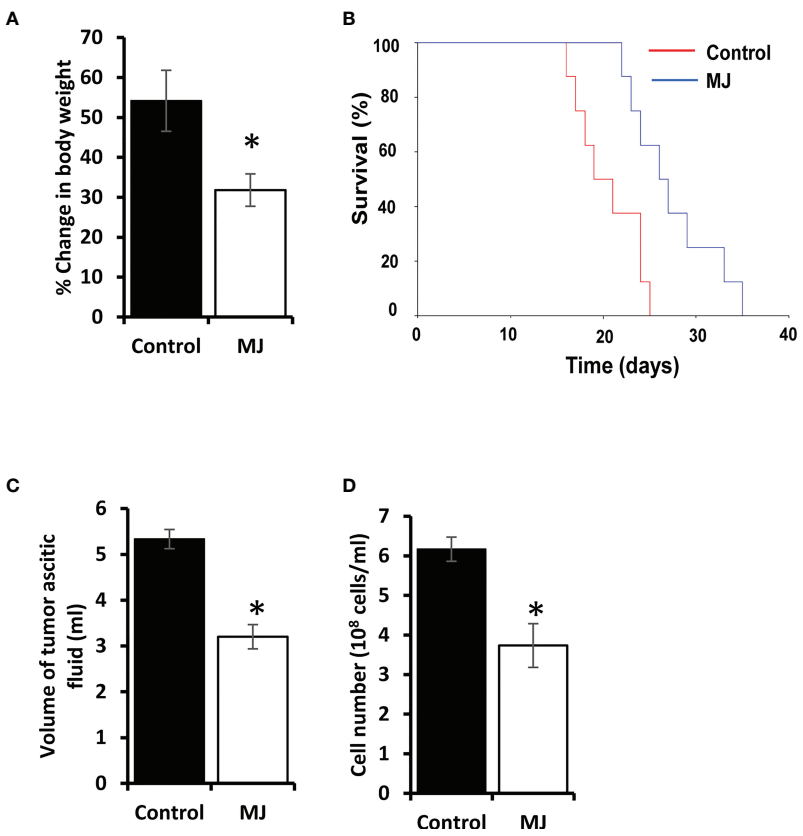

FIGURE 2 | MJ administration retards tumor progression. Tumor-transplanted mice were administered with PBS alone (control) or containing MJ (100 g/kg), as shown in **Figure 1**, followed by monitoring of tumor progression by the change of body weight **(A)** and survival of the tumor-bearing mice **(B)**, estimation of the volume of ascitic fluid **(C)**, and the number of viable tumor cells **(D)**. Values are shown in **(A**, **C**, **D)** are mean ± SD of three independent experiments. *$p < 0.05$ vs. respective control.

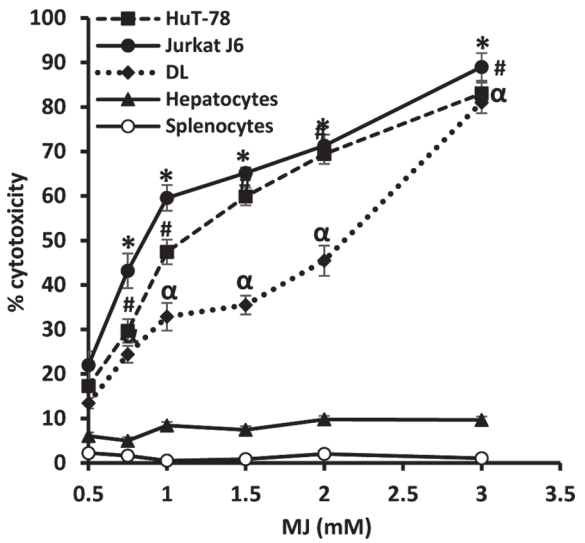

FIGURE 3 | *In vitro* tumor cell-specific cytotoxic action of MJ against neoplastic cells of human origin. Indicated tumor cell lines, hepatocytes, and splenocytes (1 x 106 cells/ml) were incubated in vitro for 12 h in medium alone or containing MJ followed by estimation of cytotoxicity by MTT assay. Values shown are mean ± SD of three independent experiments. *,α, #p < 0.05 vs. respective control.

(**Figure 4A**). These results indicate that MJ-administration triggers cell death *via* the induction of apoptosis and necrosis. As cell death is a direct consequence of cell cycle arrest (31), we also analyzed the cell cycle in tumor cells obtained from the control and MJ group of mice. Results presented in **Figure 4B** suggest that MJ arrests cell cycle in the G_0/G_1 phase. Because of these observations, next, we examined if the repertoire of proteins responsible for regulating cell cycle and apoptosis showed modulated expression in MJ-exposed tumor cells. Further, tumor cells harvested from the MJ group displayed a significantly declined Hsp70, Bcl-2, and TERT expression. In contrast, p53 and BAX expression levels were increased compared to tumor cells of control group (**Figure 5A**). Therefore, their modulated expression could underlie the observed altered survival of tumor cells exposed to MJ *in vivo*.

As altered mitochondrial membrane permeability is associated with the increased cytosolic release of Cyt *c*, reflecting the mitochondrial-dependent cell death induction, we also estimated the level of cytosolic Cyt *c* in MJ-exposed tumor cells. Results (**Figure 5B**) showed a significant increase in the level of cytosolic Cyt *c* in the MJ-exposed tumor cells compared to PBS-administered control (**Figure 5B**). As an increase of intracellular ROS is also implicated in the mitochondrial associated induction of apoptosis, next, we examined intracellular ROS level. We found dramatically increased intracellular ROS level in the tumor cells isolated from the MJ-administered group compared to the control group (**Figure 5C**).

MJ Administration Manifests Inhibition of Glycolysis in Tumor Cells

To understand if MJ administration modulated tumor cells' glucose metabolism as glycolysis has been noticed as one of the crucial regulators of apoptosis and necrotic cell death (3). Therefore, MJ administration's effect on the metabolic activity (**Figure 6A**) and repertoire of glucose metabolism regulatory molecules (**Figures 6B–E**) were examined. The results showed significant inhibition of metabolic activity in tumor cells exposed to MJ compared to PBS administered control. The inhibition of metabolic activity was accompanied by a suppressed expression of glucose metabolism regulatory molecules, namely HIF-1α, HK 2, LDH A, PDK-1, and GLUT-1.

As carbohydrate metabolism is intimately associated with altered pH homeostasis in neoplastic cells, MJ administration's effect on the pH of ascitic tumor fluid was also investigated. The MJ group's ascitic fluid displayed relative alkalinization compared to the control group (**Figure 6F**). This suggests a reversal of the acidic tumor microenvironment. Considering the critical role of pH regulator MCT-1 in the maintenance of pH homeostasis in tumor cells through regulating the transport of lactate across the plasma membrane, next, we checked the expression of MCT-1. The MJ-exposed group's tumor cells showed inhibited MCT-1 expression compared to control group tumor cells (**Figure 6G**).

MJ Exposure Alters Lipid Metabolism in Tumor Cells

Because lipid homeostasis is also impacted by altered carbohydrate metabolism and lipid biogenesis is a lifeline of tumor cell proliferation (20). Therefore, the effect of MJ on lipid metabolism was evaluated. Thus, the expression of lipid metabolism-regulating molecules was analyzed (**Figure 7A**). Significant down-regulated expression of fatty acid synthase (FASN) was observed in the MJ group compared to control, a key regulatory enzyme of *de novo* fatty acid synthesis (**Figure 7A**). Similarly, MJ-exposed tumor cells displayed inhibited expression of ACSS2, and SREBP1c (**Figure 7A**). The impact of inhibited expression of FASN, ACSS2, and SREBP1c in MJ-exposed tumor cells was also investigated by assessing tumor cell membrane's stability through examining the osmotic fragility (**Figure 7B**). MJ-exposed tumor cells showed a significant increase in osmotic fragility compared to control.

Altered Cytokines Repertoire in Ascitic Fluid

ELISA was performed on the ascitic fluid obtained from control and MJ groups to immunodetect the indicated cytokines (**Figure 8**). The MJ group's ascitic fluid showed elevated IL-6 and IFN-ϒ, accompanied by declined TGF-β levels compared to the PBS-administered control.

MJ Administration Modulates VEGF Expression and Intra-Tumoral Blood Flow

A color doppler ultrasonographic imaging was performed to understand if MJ-dependant tumor growth retardation also changed the pattern of blood flow in the vicinity of progressively growing ascitic tumors in the peritoneal cavity. The mesenteric blood flow was quantified for the peak-systolic velocity (PSV) and end-diastolic velocity (EDV), which

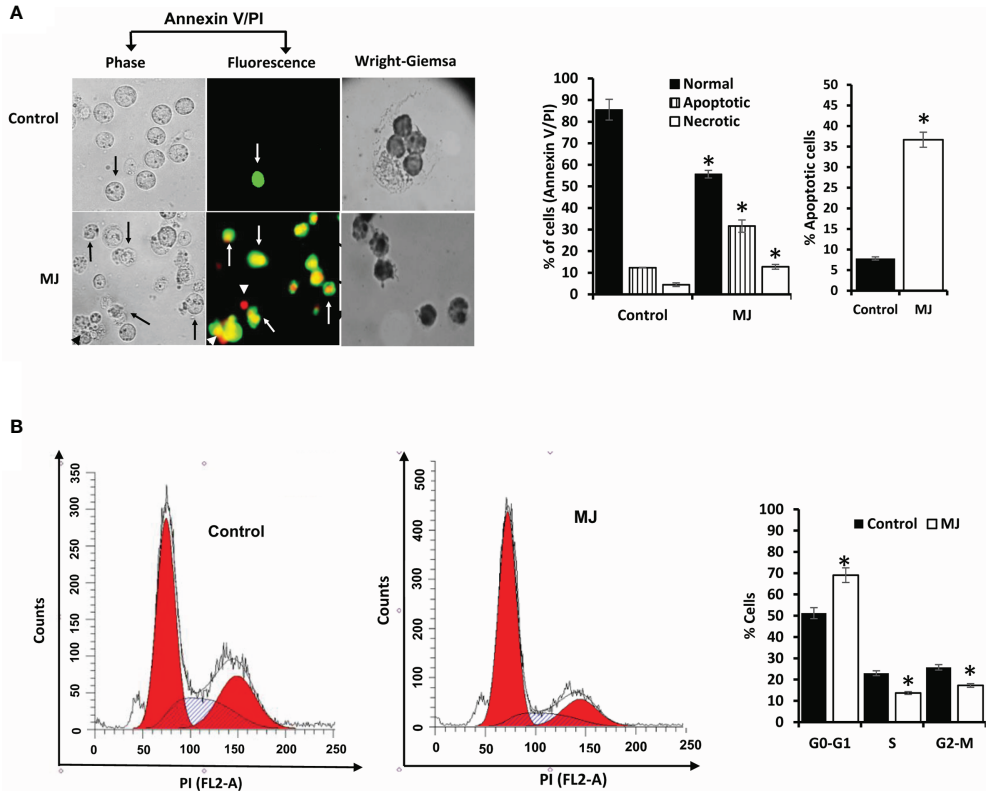

FIGURE 4 | MJ administration to tumor-bearing mice induces tumor cell death and cell cycle arrest. Tumor cells harvested from control and tumor-transplanted mice were examined for induction of cell death by Annexin V/PI staining using fluorescence microscopy and Wright-Giemsa staining **(A)**. Arrows indicate apoptotic cells, and arrowheads indicate necrotic cells. Tumor cells were also analyzed for cell cycle as described in materials and methods using flow cytometry **(B)**. Microscopic and flow cytometric images are from a representative experiment of three independent experiments with similar results. The accompanying bar diagrams are mean ± SD three independent experiments. *$p < 0.05$ vs. respective control.

significantly declined after MJ-administration compared to control (**Figures 9A, B**). These observations indicate that MJ inhibits blood flow in the ascitic cavity. Considering VEGF's implication in the regulation of tumor angiogenesis, we also examined if MJ could modulate VEGF level. Notably, the level of VEGF was found to decrease in MJ-exposed tumor cells (**Figure 9C**) and the ascitic fluid (**Figure 9D**) of the MJ group.

Chemo-Potentiating Action of MJ

As MJ on its own is not yet established as the drug of choice in the mainstream anti-cancer regimens, we checked if it can influence the tumor cell killing ability of standard anti-cancer drug cisplatin (CP) upon *in vivo* administration. Cell lysates were examined for MDR1 level by Western blotting (**Figure 10A**) and flow cytometry (**Figure 10B**). MJ-exposed tumor cells showed down-regulated expression of MDR1 compared to control. These observations indicate that *in vivo* exposure to MJ could enhance the cytotoxic ability of other anti-cancer drugs. This hypothesis was further confirmed by examining cytotoxicity (**Figure 10C**) and tumor cell viability (**Figure 10D**) in tumor cells isolated from tumor-bearing mice administered with PBS alone or containing MJ, CP, or a combination of both. Administration of MJ and CP markedly augmented cytotoxicity with a decreased number of viable cells compared to groups of cisplatin or MJ alone, indicating the chemo-potentiating effect of MJ for cisplatin.

DISCUSSION

Observations of the present study strongly suggest the tumor growth retarding action of MJ against a progressively growing lymphoma of thymic origin. Further, this investigation also explores the possible molecular mechanisms underlying the tumor growth impeding effect of MJ. Tumor cells harvested from MJ-administered tumor-transplanted mice displayed augmented induction of apoptosis and cell cycle arrest, which possibly led to a decline in tumor load. Further, *in vitro* exposure of MJ exhibited cytotoxic action against DL, HuT-78, and J6 cells without imparting any adverse effect on normal cells. This indicates the broad spectrum of tumor cell-specific cytotoxic action of MJ. Similar to our findings, other studies have shown that MJ does not harm normal cells (1, 32). Although the precise mechanism of the cell cycle interrupting and cell death-inducing action of MJ upon *in vivo* administration is not clear, one of the

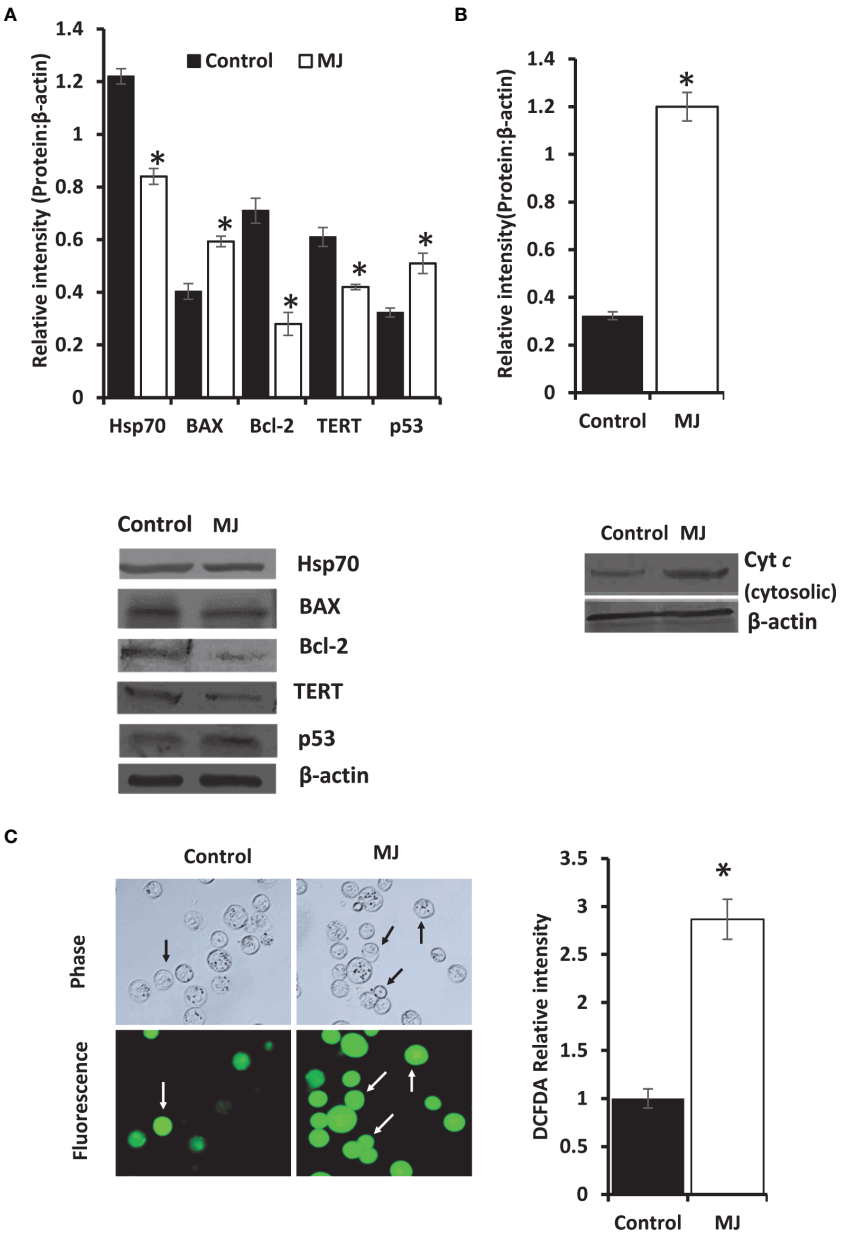

FIGURE 5 | Altered expression of cell survival regulatory molecules in tumor cells following *in vivo* exposure to MJ administration. Tumor cells (1 x 10^6 cells/ml) harvested from control and MJ-administered tumor-transplanted mice were analyzed for the expression of indicated cell survival regulatory molecules **(A)**. The cytosolic level of Cyt *c* was detected **(B)** as described in the materials and methods. Bands shown in **(A, B)** are from a representative experiment out of three independent experiments with similar results. Expression of intracellular ROS in tumor cells of control and MJ groups was estimated by DCFDA staining **(C)** as described in the materials and methods. Accompanying bar diagrams depicts densitometric analysis showing mean ± SD. *$p < 0.05$ vs. respective control.

likely causes could be the altered expression of tumor metabolism regulatory molecules. MJ-exposed tumor cells showed inhibition of HK 2, LDH A, PDK-1, and HIF-1α expression, which have a pivotal role in maintaining the predominant glycolytic phenotype of tumor cells, crucially required for augmented survival of neoplastic cells (33–36). Studies have overwhelmingly demonstrated that MJ could bind to and detach mitochondria linked HK 2 in malignant cells (5), leading to the decoupling of glycolysis and mitochondrial metabolism (37), with detrimental consequences on cell survival.

MJ dependent dissociation of HK 2 from voltage-dependent anion channel (VDAC) is also reported to trigger a dip in mitochondrial transmembrane potential, leading to increase release of Cyt *c* and induction of apoptosis (37). Indeed, we also observed an augmented level of cytosolic Cyt *c* in tumor cells exposed to MJ *in vivo*, reconfirming the mitochondrial mode of

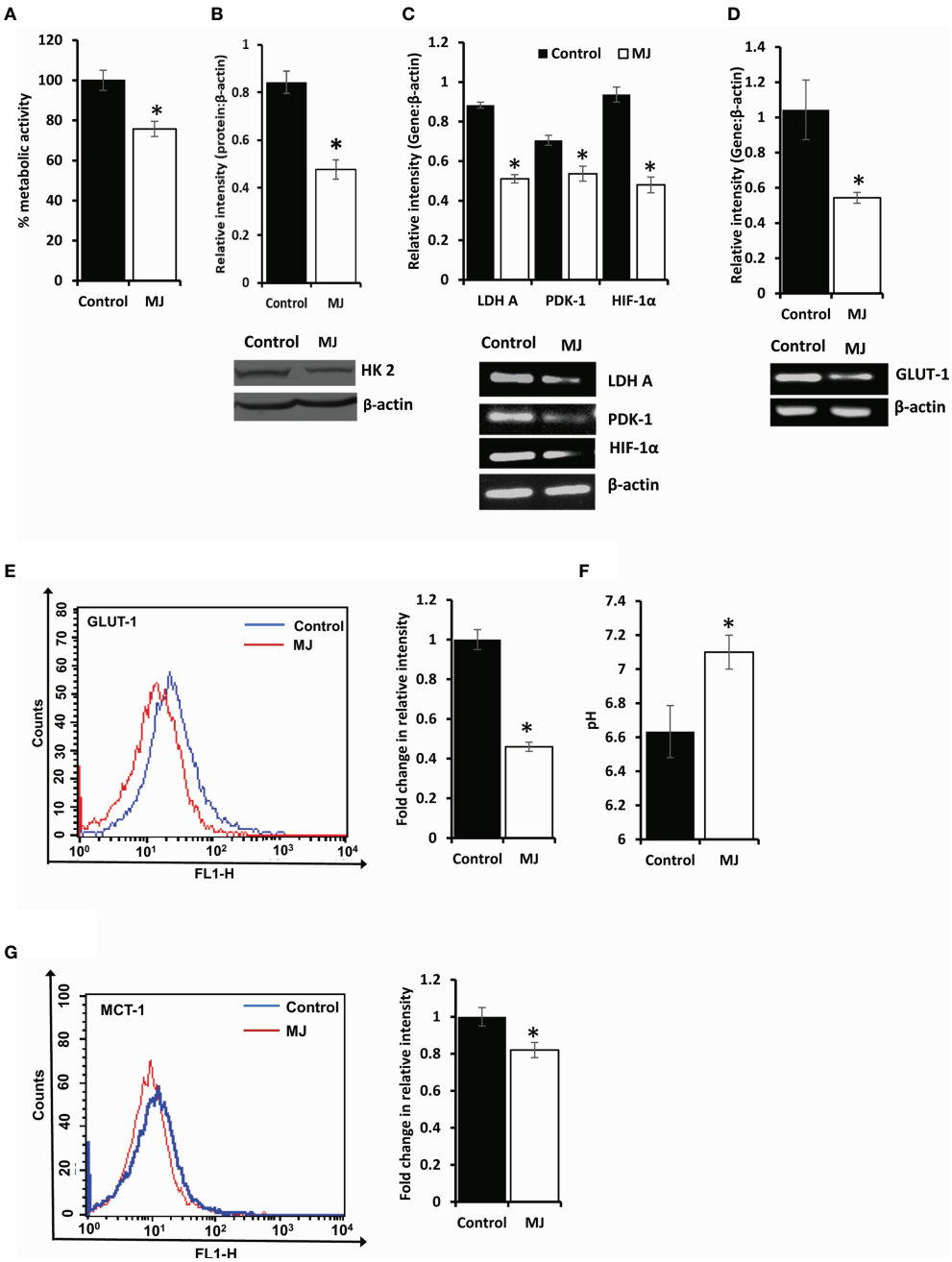

FIGURE 6 | MJ alters the metabolic activity of DL cells *in vivo*. Tumor cells (1 x 10^6 cells/ml) of control and MJ-administered tumor-bearing mice were analysed for metabolic activity by MTT assay **(A)**, expression of HK2 by Western blotting **(B)**, and other indicated metabolism regulatory molecules by RT-PCR **(C)**. The expression of GLUT-1 was analyzed by RT-PCR **(D)** and flow cytometry for membrane expression of GLUT-1 **(E)**. The pH of the control and MJ-administered groups' ascitic tumor fluid was measured **(F)** by pH meter. The expression of pH regulator MCT-1 was analysed by flow cytometry **(G)** in tumor cells harvested from control and MJ-administered tumor-bearing mice. Bands shown **(B, C, D)** and flow cytometric image **(E, G)** are from representative experiments out of three independent experiments with similar results. Values shown in bar diagrams are mean ± SD of three independent experiments. *$p < 0.05$ vs. respective control.

cell death. The necrotic cell population's surge also indicates the possibility of declined bioenergetics in MJ-exposed tumor cells, as induction of apoptosis is an ATP-dependent phenomenon (32). Thus, once ATP production is depleted in cells undergoing apoptosis, the necrotic mode of cell death can be ushered during the late stages of exposure to a metabolic inhibitor (17). The same could also underlie the inhibited expression of various metabolic molecules in MJ exposed tumor cells owing to increased cell death. Other studies have also indicated that hexokinase inhibited expression augments apoptosis induction,

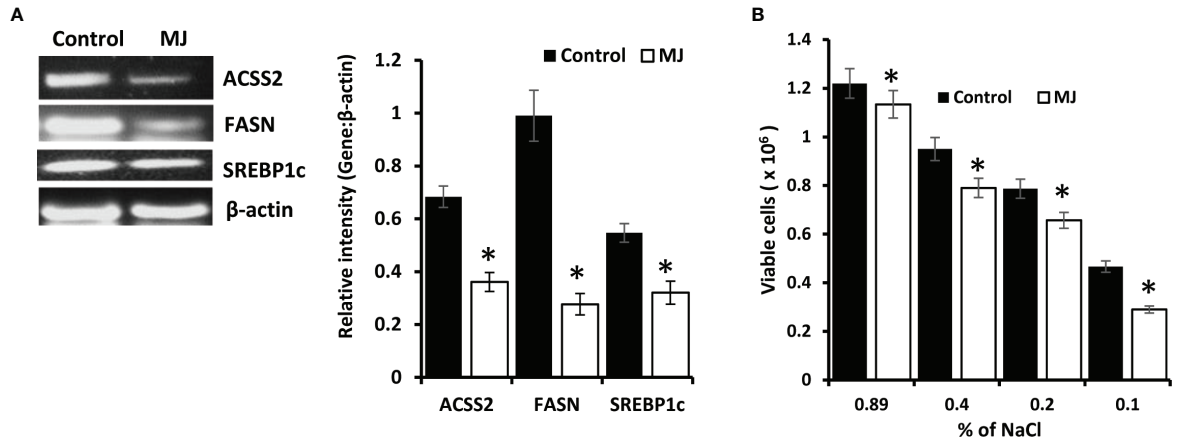

FIGURE 7 | MJ alters lipid homeostasis. Tumor cells (1 x 10^6 cells/ml) harvested from control and MJ administered tumor-bearing mice were analysed for the expression of ACSS2, FASN, and SREBP1c by RT-PCR **(A)**. Osmotic fragility **(B)** of control and MJ exposed tumor cells *in vivo* was analyzed, as described in the materials and methods. Bands shown in **(A)** are from a representative experiment out of three independent experiments with similar results. Values shown in bar diagrams **(A, B)** are mean ± SD of three independent experiments. *$p < 0.05$ vs. respective control.

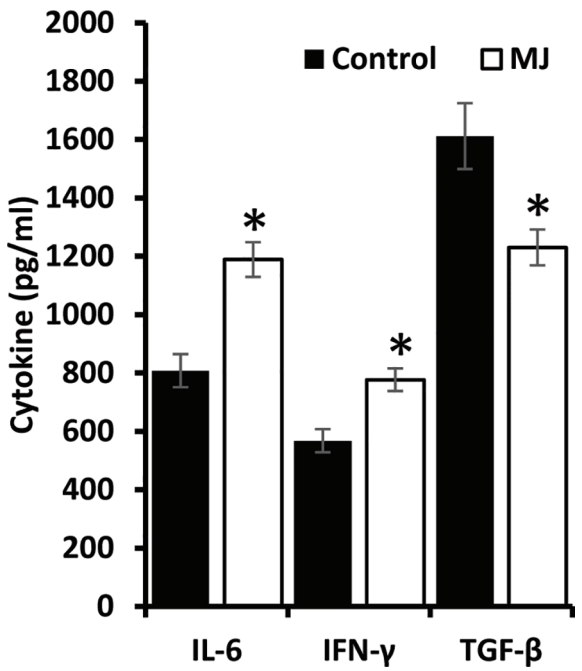

FIGURE 8 | MJ administration to tumor-bearing mice alters cytokine repertoire in ascitic fluid. The ascitic fluid of control and MJ administered tumor-bearing mice were analyzed for the levels of indicated cytokines by ELISA as described in the materials and methods. Values are mean ± S.D. *$p < 0.05$ vs. control.

and declines cell proliferation (13, 37). Blocked ATP synthesis in MJ-treated hepatocellular carcinoma cells owing to inhibited metabolism has been demonstrated to cause necrosis in the neoplastic cells (3). Further, G_0/G_1 arrest of the cell cycle is associated with mitochondrial mode of apoptosis (38). MJ-dependent cell cycle arrest has also been demonstrated in other neoplastic cell lines exposed to MJ *in vitro* in the G_0/G_1 and S phase of the cell cycle. The difference in the phases of cell cycle arrest by MJ may depend on the type of tumor cells' etiology (1).

We also observed an increase in intracellular ROS expression in tumor cells exposed to MJ *in vivo*. The augmented ROS level has been shown to induce apoptosis by causing the destruction of various macromolecules like proteins, lipids, and nucleic acids (39). Mitochondrial ROS triggers apoptosis induction *via* the intrinsic pathway, leading to activation of caspases (39). The increase of cytosolic Cyt *c* is reported to cause caspase activation (40). Caspase can also cause loss of mitochondrial functions and trigger an increased ROS generation (41).

There was no report regarding the effect of MJ *in vivo* on the expression of HIF-1α. HIF-1α plays a vital role in the reprogrammed cancer cell metabolism by enhancing the expression of GLUT-1, HK 2, LDH A, and PDK-1 (35). Hence, HIF-1α is considered both upstream and downstream master regulator of tumor metabolism (42). The inhibition of HIF-1α by exposure of tumor cells to MJ could induce mitochondrial passage of pyruvate, leading to activation of oxidative phosphorylation and ROS production with concomitant inhibition of GLUT-1, HK 2, LDH A, and PDK-1 axis (35), a lifeline of tumor metabolism. Nevertheless, LDH A inhibition causes a declined lactate production, leading to abrogation of tumor cell survival by disturbing the glycolytic bioenergetic homeostasis (33). HIF-1α also up-regulates the expression of pH regulator MCT-1 in tumor cells, regulating pH homeostasis (43, 44). Interestingly, we observed a reversal of tumor acidosis accompanied by a declined glucose uptake, glycolytic activity, and MCT-1 expression. As tumor acidosis is necessary to maintain cytosolic alkalinization of tumor cells, interference with the same is also reported to cause the induction of tumor cell death (45).

This is the first report to indicate the novel mechanism of *in vivo* antineoplastic action of MJ. We observed that MJ administration ushered modulation in the expression of crucial

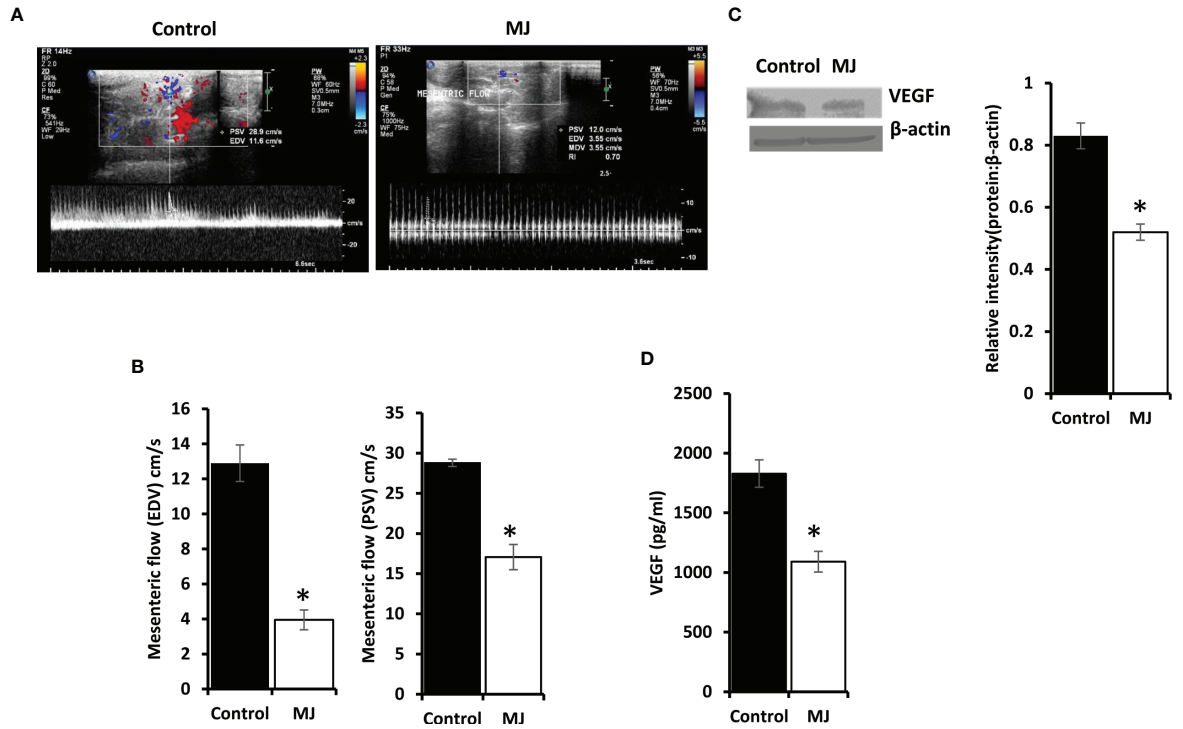

FIGURE 9 | Effect of MJ administration on intratumoral blood flow and VEGF expression. A color doppler sonographic imaging was performed on control and MJ-administered tumor-bearing mice, as described in materials and methods. Images of Peak Systolic Velocity (PSV) and End Diastolic velocity (EDV) shown in **(A)** are from a representative experiment out of three independent experiments with similar results. The accompanying bar diagrams **(B)** show the mean ± SD of PSV and EDV, respectively. Tumor cells (1 x 106 cells/ml) harvested from control and MJ-administered tumor-bearing mice were analysed for the expression of VEGF by Western blotting in cell lysate **(C)** and by ELISA in ascitic fluid **(D)**. Bands shown in **(B)** are from representative experiments out of three independent experiments with similar results. Values shown in bar diagrams **(B–D)** are mean ± SD of three independent experiments. *$p < 0.05$ vs. respective control.

cell survival regulatory molecules, notably the declined Hsp70 and Bcl-2, and increased p53 and BAX levels. Indeed, increased level of Bcl-2 and declined p53 level have been implicated in antagonizing the induction of apoptosis in tumor cells (46). Further, Bcl-2 also regulates HIF-1α protein stabilization in neoplastic cells (47). Moreover, suppression of TERT leads to inhibition of cell proliferation and promotion of cell cycle arrest and apoptosis induction (48). Furthermore, TERT is reported in apoptosis regulation *via* Bcl-2 and p53 (49, 50).

Another interesting finding of the present study is the lipid metabolism inhibitory ability of MJ. The reason behind examining the effect of MJ on lipid metabolism was due to its indispensable role in the cell proliferation. We observed the declined expression of lipid homeostasis regulating molecules like FASN, ACSS2, and SREBP1c in MJ exposed tumor cells. These molecules play a pivotal role in sustaining the *de novo* fatty acid production in neoplastic cells (51, 52). Nevertheless, HIF-1α and Hsp70 directly regulate apoptosis in neoplastic cells (33, 53) and govern the expression of FASN, ACSS 2, and SREBP1c (51, 54). The consequence of the inhibition of these crucial lipid homeostasis regulating molecules in MJ exposed tumor cells *in vivo* is reflected in increased osmotic fragility of tumor cells, indicating hampered membrane biogenesis (51). Indeed, Yousefi et al. reported that MJ increases breast cancer cell apoptosis by causing a decline in membrane fluidity (9). In turn, membrane fluidity is regulated by the membrane's lipid constituents (55). The declined membrane fluidity caused by MJ can also be associated with the hampered cell cycle progression (55).

It is mention-worthy that in one of our previous studies, curcumin, a well-established phytochemical with promising cancer therapeutic potential, also caused retardation of DL progression, implicating a modulation of the tumor growth-regulating constituents of the tumor microenvironment and induction of cell death by modulating the expression pattern of apoptosis, cell survival and chemoresistance regulatory molecules (56) as observed in the present investigation using MJ. Studies have also shown the role of anti-glycolytic and lipogenic inhibitory activity of curcumin in tumoricidal action (57, 58). Further, curcumin can alter mitochondrial membrane potential and the neoplastic cells' inflammatory state (59–61). Thus, in these respects, MJ seems to be similar to curcumin concerning some of its tumor progression inhibiting mechanisms. Therefore, to fully realize the therapeutic potential of MJ, it will be beneficial to study the cooperation of MJ and curcumin in retarding tumor progression in appropriate *in vitro* and *in vivo* settings of DL and other cancer cells. Our preliminary unpublished and ongoing experimental observations indicate that MJ has an adjuvant effect in potentiating

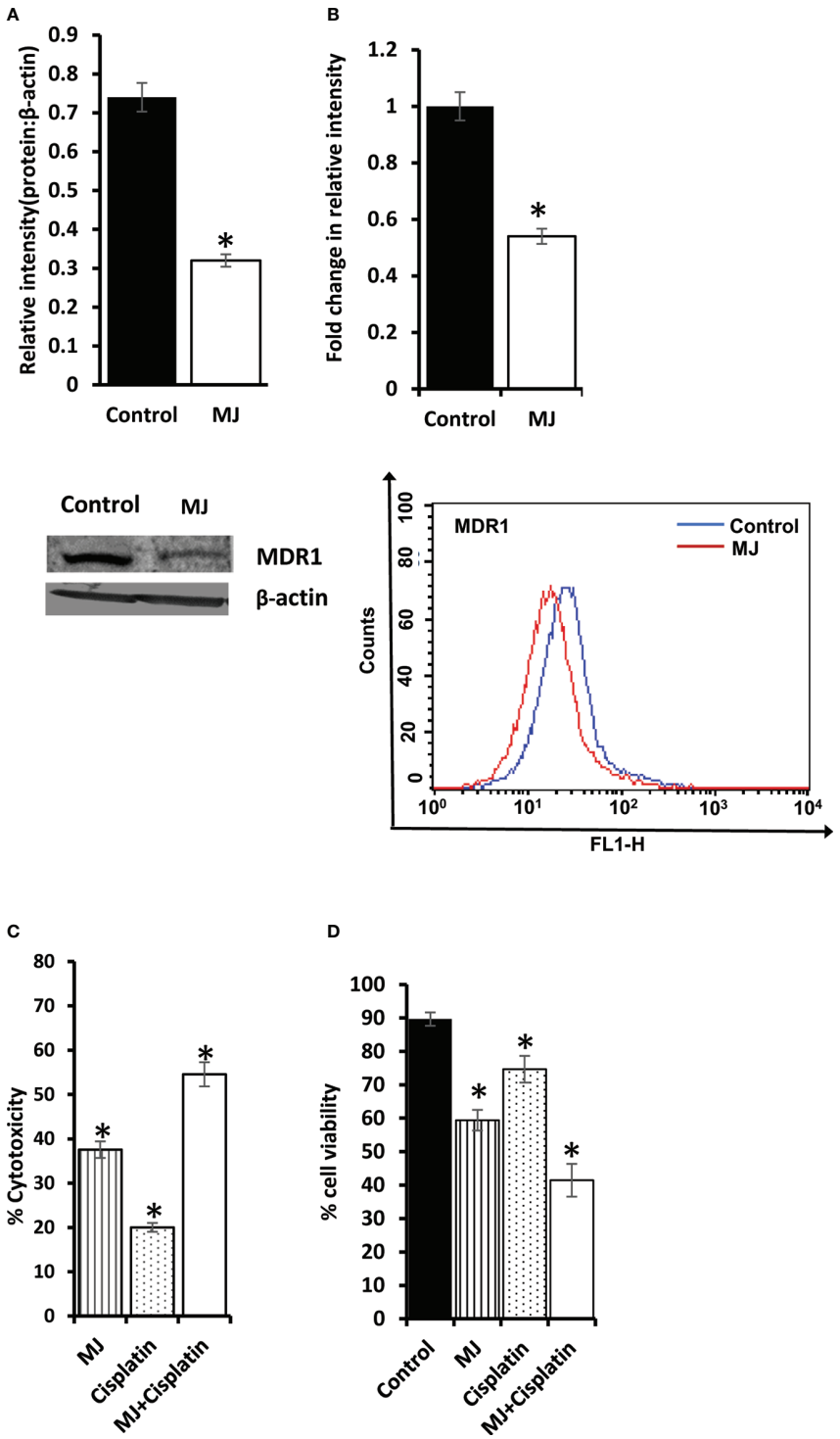

FIGURE 10 | Chemo-potentiating action of MJ *in vivo*. Tumor cells (1 x 10^6 cells/ml) harvested from control and MJ-administered tumor-bearing mice were examined for the expression of MDR1 by Western blotting **(A)** and flow cytometry **(B)**. Bands shown **(A)** and flow cytometric images **(B)** are from representative experiments out of three independent experiments with similar results. Values shown in bar diagrams are mean ± SD of three independent experiments. *$p < 0.05$ vs. respective control. To evaluate the chemo-potentiating effect of MJ administration, the tumor-bearing mice were administered with PBS with or without MJ (100 mg/kg body weight) or CP (5 mg/kg bodyweight) or both together on alternative days starting from day 4 to day 12 post tumor transplantation. Tumor cells harvested on day 14 from tumor-bearing mice of control and those administered with MJ, CP, and MJ plus CP were further examined for cytotoxicity by MTT assay **(C)** and survival by Trypan blue dye exclusion test **(D)** as described in materials and methods. Values shown are mean ± SD. *$p < 0.05$ vs. values for control.

curcumin's antitumor efficacy. Thus, there is a great potential to investigate the combined effect of these phytochemicals to optimize their successful application in anticancer regimens.

We also observed attenuated VEGF expression in tumor ascitic fluid and tumor cells of MJ-administered tumor-bearing mice. Indeed, VEGF is a well-defined target of HIF-1α (47). We also checked the pattern of blood flow in the ascitic tumor cavity using color doppler ultrasonographic imaging. Interestingly, we observed low mesenteric blood flow in MJ administered tumor-bearing mice. This observation indicates a declined blood flow in the tumor microenvironment, which could be responsible for tumor growth retardation. Moreover, diminished VEGF expression in tumor cells is also accompanied by augmented apoptosis (62). More so, inhibition of VEGF-dependent angiogenesis also induces tumor cell apoptosis (62). One report indicates the role of inhibited angiogenesis in MJ-induced cell death of endothelial and melanoma cells (63). However, the study used chick embryo angiogenesis as a model. The present study is the first of its kind to report the effect of *in vivo* administration of MJ on VEGF expression and blood flow in the tumor microenvironment of tumor-bearing mice. Further, we observed inhibition in the level of TGF-β in the ascitic fluid of MJ-administered tumor-transplanted mice, along with an increase in the level of IFN-ϒ and IL-6. The inhibited expression of HIF-1α could also be associated with the increased expression of proinflammatory cytokines like IFN-ϒ and IL-6 (17, 64). Both IFN-ϒ and IL-6 promote antitumor immunity (13, 45) and have shown the inhibitory effect on the expression of HIF-1α (17, 20). However, the increased level of TGF-β is very well reported in the uninterrupted tumor cell progression through attenuation of tumor cell death and antitumor immune response (65).

We also observed the increased tumoricidal ability of cisplatin in the presence of MJ. Although there could be multiple factors underlying MJ's action, we observed a declined expression of MDR1 in MJ exposed tumor cells. Indeed, MDR1 has been

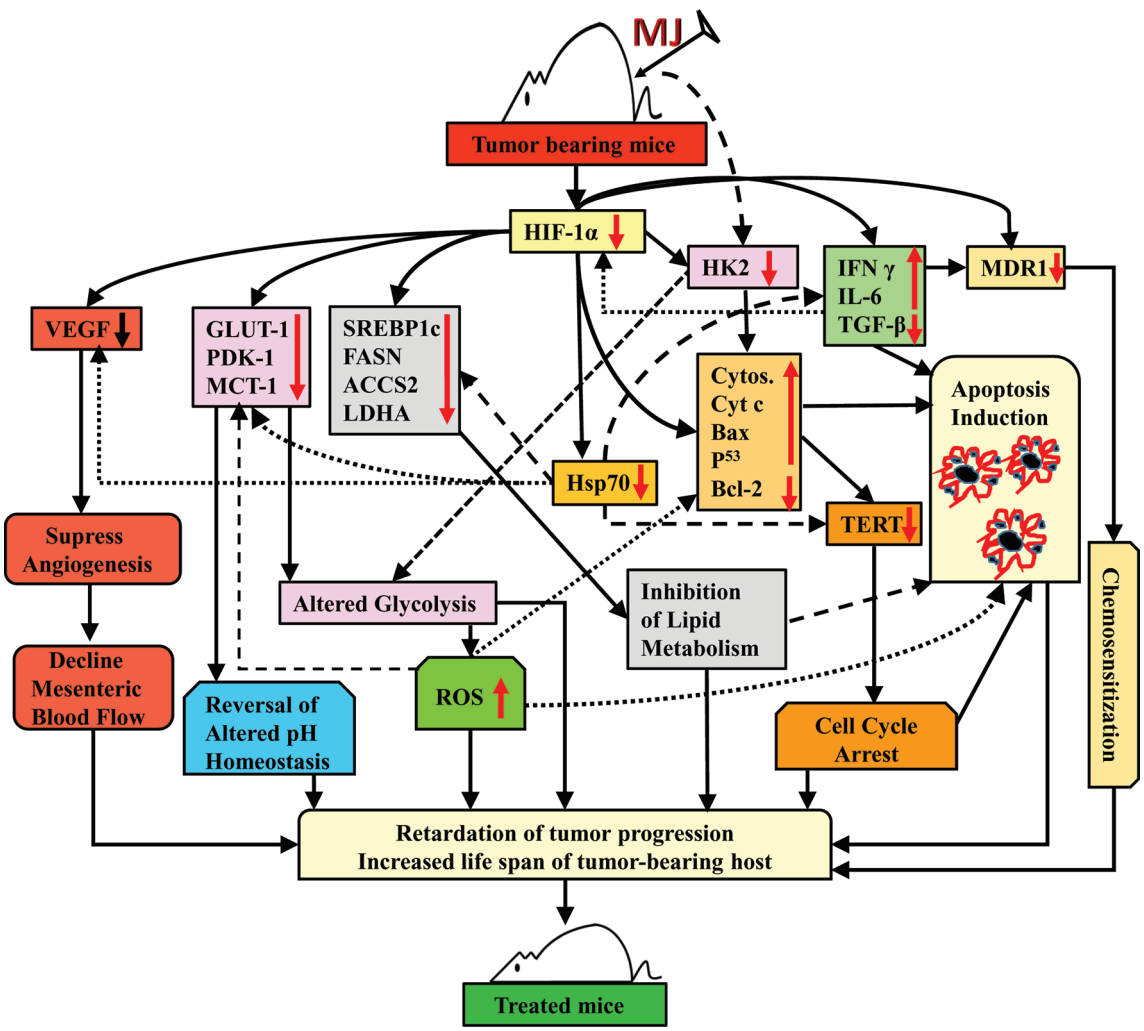

FIGURE 11 | Summary of the molecular mechanism underlying the tumor growth retarding and chemo-potentiating action of MJ.

reported to manifest drug resistance to cisplatin (66). Moreover, HIF-1α regulates the expression of MDR1 (17, 67). Further, IFN-ϒ has been shown to inhibit the expression of MDR1 (68). Numerous *in vitro* studies have shown the alteration in the expression of MDR1 by MJ (63). However, so far, no *in vivo* study had investigated the effect of MJ on MDR1 expression. The chemo-potentiating action of MJ has also not yet been evaluated in a progressively growing tumor. Hence, our study is the first to suggest MJ's chemo-potentiating action against hematological origin's malignancy and the plausible associated mechanisms.

Taken together, the results of this study indicate that the administration of MJ to T cell lymphoma bearing mice retards tumor progression by triggering induction of tumor cell death associated with interference with carbohydrate and lipid metabolism, pH homeostasis, angiogenesis, and drug resistance. These actions of MJ are mainly re-laid on altered levels of HK2, HIF-1α, SREBP 1c, and MDR1 (**Figure 11**). This preclinical study's findings will help to design the new anti-cancer therapeutic regimens against hematological origin malignancies.

DATA AVAILABILITY STATEMENT

The raw data supporting the conclusions of this article will be made available by the authors, without undue reservation.

ETHICS STATEMENT

The animal study was reviewed and approved by the Institutional Animal Ethical Committee, Institute of Science, Banaras Hindu University, Varanasi 221005, UP, India (Approval reference: BHU/DOZ/IAEC/2018-2019/019 dated January 01, 2019).

AUTHOR CONTRIBUTIONS

YG: conceiving the idea, performing of experiments, data generation, interpreting data, and writing of the manuscript. SY: interpreting data and writing of the manuscript. SP: interpreting data and writing of the manuscript. MT: interpreting data and writing of the manuscript. BM: ultrasonography, interpreting data, and writing of the manuscript. AV: ultrasonography, interpreting data, and writing of the manuscript. AK: interpreting data and writing of the manuscript. SS: conceiving the idea, interpreting data, and writing of the manuscript. All authors contributed to the article and approved the submitted version.

ACKNOWLEDGMENTS

We thankfully acknowledge fellowship support to YG [Award No. 3/1/3/JRF-2016/LS/HRD-10(80666)] from ICMR, New Delhi, SY. [Award No. 09/013(0577)/2015-EMR-I] from CSIR, New Delhi, SKP [Award No. 3/1/3/JRF-2015(2)HRD] from ICMR, New Delhi, and MKT [Award No. DBT/JRF/BET-18/I/2018/AL/154]. Infrastructural support from DBT, New Delhi, ISLS, DST-PURSE program, and UGC-UPE, Banaras Hindu University, is acknowledged. The work contained in this manuscript is a component of the Ph.D. dissertation of YG.

REFERENCES

1. Cesari IM, Carvalho E, Figueiredo Rodrigues M, Mendonça BDS, Amôedo ND, Rumjanek FD. Methyl jasmonate: putative mechanisms of action on cancer cells cycle, metabolism, and apoptosis. *Int J Cell Biol* (2014) 2014:1–25. doi: 10.1155/2014/572097
2. Sucu BO, Ipek OS, Kurtulus SO, Yazici BE, Karakas N, Guzel M. Synthesis of novel methyl jasmonate derivatives and evaluation of their biological activity in various cancer cell lines. *Bioorg Chem* (2019) 91:103146. doi: 10.1016/j.bioorg.2019.103146
3. Li J, Chen K, Wang F, Dai W, Li S, Feng J, et al. Methyl jasmonate leads to necrosis and apoptosis in hepatocellular carcinoma cells via inhibition of glycolysis and represses tumor growth in mice. *Oncotarget* (2017) 8:45965. doi: 10.18632/oncotarget.17469
4. Wang Y, Fan L, Cui C, Wang Y, Liang T. EZH2 inhibition promotes methyl jasmonate–induced apoptosis of human colorectal cancer through the Wnt/β–catenin pathway. *Oncol Lett* (2018) 16:1231–6. doi: 10.3892/ol.2018.8779
5. Goldin N, Arzoine L, Heyfets A, Israelson A, Zaslavsky Z, Bravman T, et al. Methyl jasmonate binds to and detaches mitochondria-bound hexokinase. *Oncogene* (2008) 27:4636–43. doi: 10.1038/onc.2008.108
6. Zhang M, Su L, Xiao Z, Liu X, Liu X. Methyl jasmonate induces apoptosis and pro-apoptotic autophagy via the ROS pathway in human non-small cell lung cancer. *Am J Cancer Res* (2016) 6:187.
7. Peng Z, Zhang Y. Methyl jasmonate induces the apoptosis of human colorectal cancer cells via downregulation of EZH2 expression by microRNA–101. *Mol Med Rep* (2017) 15:957–62. doi: 10.3892/mmr.2016.6061
8. Yeruva L, Elegbede JA, Carper SW. Methyl jasmonate decreases membrane fluidity and induces apoptosis via tumor necrosis factor receptor 1 in breast cancer cells. *Anticancer Drugs* (2008) 19:766. doi: 10.1097/CAD.0b013e32830b5894
9. Yousefi S, Darvishi P, Yousefi Z, Pourfathollah AA. Effect of methyl jasmonate and 3-bromopyruvate combination therapy on mice bearing the 4 T1 breast cancer cell line. *J Bioenerg Biomembr* (2020) 52:1–9. doi: 10.1007/s10863-019-09811-w
10. Klippel S, Jakubikova J, Delmore J, Ooi M, McMillin D, Kastritis E, et al. Methyljasmonate displays in vitro and in vivo activity against multiple myeloma cells. *Br J Haematol* (2012) 159:340–51. doi: 10.1111/j.1365-2141.2012.09253.x
11. Zhang M, Zhang MW, Zhang L, Zhang L. Methyl jasmonate and its potential in cancer therapy. *Plant Signaling Behav* (2015) 10:e1062199. doi: 10.1080/15592324.2015.1062199
12. Koiri R, Mehrotra A, Trigun S. Dalton's Lymphoma as a murine model for understanding the progression and development of t-cell lymphoma and its role in drug discovery. *Int J Immunother Cancer Res* (2017) 3:001–6. doi: 10.17352/2455-8591.000011
13. Yadav S, Kujur PK, Pandey SK, Goel Y, Maurya BN, Verma A, et al. Antitumor action of 3-bromopyruvate implicates reorganized tumor growth regulatory components of tumor milieu, cell cycle arrest and induction of mitochondria-dependent tumor cell death. *Toxicol Appl Pharmacol* (2018) 339:52–64. doi: 10.1016/j.taap.2017.12.004
14. Dunham LJ. A survey of transplantable and transmissible animal tumors. *Natl Inst Health* (1953) 50:1299–377.

15. Goldie H, Felix MD. Growth characteristics of free tumor cells transferred serially in the peritoneal fluid of the mouse. *Cancer Res* (1951) 11:73–80.
16. Samudrala PK, Augustine BB, Kasala ER, Bodduluru LN, Barua C, Lahkar M. Evaluation of antitumor activity and antioxidant status of Alternanthera brasiliana against Ehrlich ascites carcinoma in Swiss albino mice. *Pharmacognosy Res* (2015) 7:66. doi: 10.4103/0974-8490.147211
17. Yadav S, Pandey SK, Kumar A, Kujur PK, Singh RP, Singh SM. Antitumor and chemosensitizing action of 3-bromopyruvate: implication of deregulated metabolism. *Chem Biol Interact* (2017) 270:73–89. doi: 10.1016/j.cbi.2017.04.015
18. Mosmann T. Rapid colorimetric assay for cellular growth and survival: application to proliferation and cytotoxicity assays. *J Immunol Methods* (1983) 65:55–63. doi: 10.1016/0022-1759(83)90303-4
19. Vertosick FT, Selker RG, Randall MS, Kristofik MP, Rehn T. A comparison of the relative chemosensitivity of human gliomas to tamoxifen and n-desmethyltamoxifenin vitro. *J Neurooncol* (1994) 19:97–103. doi: 10.1007/BF01306450
20. Kant S, Kumar A, Singh SM. Tumor growth retardation and chemosensitizing action of fatty acid synthase inhibitor orlistat on T cell lymphoma: implication of reconstituted tumor microenvironment and multidrug resistance phenotype. *Biochim Biophys Acta (BBA)-General Subj* (2014) 1840:294–302. doi: 10.1016/j.bbagen.2013.09.020
21. Rieger AM, Nelson KL, Konowalchuk JD, Barreda DR. Modified annexin V/propidium iodide apoptosis assay for accurate assessment of cell death. *J Vis Exp* (2011) 50:e2597. doi: 10.3791/2597
22. Shen Y, Vignali P, Wang R. Rapid profiling cell cycle by flow cytometry using concurrent staining of DNA and mitotic markers. *Bio Protoc* (2017) 7:1–5. doi: 10.21769/BioProtoc.2517
23. Feller N, Kuiper C, Lankelma J, Ruhdal J, Scheper R, Pinedo H, et al. Functional detection of MDR 1/P170 and MRP/P190-mediated multidrug resistance in tumour cells by flow cytometry. *Br J Cancer* (1995) 72:543–9. doi: 10.1038/bjc.1995.371
24. Cook AD, Braine EL, Hamilton JA. The phenotype of inflammatory macrophages is stimulus dependent: implications for the nature of the inflammatory response. *J Immunol* (2003) 171:4816–23. doi: 10.4049/jimmunol.171.9.4816
25. Fido RJ, Tatham AS, Shewry PR. Applications of protein blotting in plant biochemistry and molecular biology, in *Methods in Plant Biochemistry*, vol 10, Molecular Biology (Bryant, J, ed), Academic, London (1995) pp 101–115.
26. Da Silva RJ, da Silva MG, Vilela LC, Fecchio D. Cytokine profile of Ehrlich ascites tumor treated with Bothrops jararaca venom. *Mediators Inflammation* (2002) 11:197–201. doi: 10.1080/0962935029000041
27. Gewies A, Rokhlin OW, Cohen MB. Cytochrome c is involved in Fas-mediated apoptosis of prostatic carcinoma cell lines. *Cancer Res* (2000) 60:2163–8.
28. Bradford MM. A rapid and sensitive method for the quantitation of microgram quantities of protein utilizing the principle of protein-dye binding. *Anal Biochem* (1976) 72:248–54. doi: 10.1016/0003-2697(76)90527-3
29. Furuta E, Pai SK, Zhan R, Bandyopadhyay S, Watabe M, Mo Y-Y, et al. Fatty acid synthase gene is up-regulated by hypoxia via activation of Akt and sterol regulatory element binding protein-1. *Cancer Res* (2008) 68:1003–11. doi: 10.1158/0008-5472.CAN-07-2489
30. Yadav S, Pandey SK, Goel Y, Kujur PK, Maurya BN, Verma A, et al. Protective and recuperative effects of 3-bromopyruvate on immunological, hepatic and renal homeostasis in a murine host bearing ascitic lymphoma: implication of niche dependent differential roles of macrophages. *Biomed Pharmacother* (2018) 99:970–85. doi: 10.1016/j.biopha.2018.01.149
31. van Harten AM, Buijze M, van der Mast R, Rooimans MA, Martens-de Kemp SR, Bachas C, et al. Targeting the cell cycle in head and neck cancer by Chk1 inhibition: a novel concept of bimodal cell death. *Oncogenesis* (2019) 8:1–16. doi: 10.1038/s41389-019-0147-x
32. Cohen S, Flescher E. Methyl jasmonate: a plant stress hormone as an anti-cancer drug. *Phytochemistry* (2009) 70:1600–9. doi: 10.1016/j.phytochem.2009.06.007
33. Cui X-G, Han Z-T, He S-H, Wu X-D, Chen T-R, Shao C-H, et al. HIF1/2α mediates hypoxia-induced LDHA expression in human pancreatic cancer cells. *Oncotarget* (2017) 8:24840. doi: 10.18632/oncotarget.15266
34. Martinez-Outschoorn UE, Peiris-Pages M, Pestell RG, Sotgia F, Lisanti MP. Cancer metabolism: a therapeutic perspective. *Nat Rev Clin Oncol* (2017) 14:11. doi: 10.1038/nrclinonc.2016.60
35. Nagao A, Kobayashi M, Koyasu S, Chow CC, Harada H. HIF-1-dependent reprogramming of glucose metabolic pathway of cancer cells and its therapeutic significance. *Int J Mol Sci* (2019) 20:238. doi: 10.3390/ijms20020238
36. Schulze A, Bensaad K, Harris AL. Cancer metabolism. In: *Oxford Textbook of Cancer Biology* Oxford, UK: Oxford University Press (2019). p. 221.
37. Garcia SN, Guedes RC, Marques MM. Unlocking the potential of HK2 in cancer metabolism and therapeutics. *Curr Med Chem* (2019) 26:7285–322. doi: 10.2174/0929867326666181213092652
38. Jiang Y, Wang X, Hu D. Furanodienone induces G0/G1 arrest and causes apoptosis via the ROS/MAPKs-mediated caspase-dependent pathway in human colorectal cancer cells: a study in vitro and in vivo. *Cell Death Dis* (2017) 8:e2815–e. doi: 10.1038/cddis.2017.220
39. Redza-Dutordoir M, Averill-Bates DA. Activation of apoptosis signalling pathways by reactive oxygen species. *Biochim Biophys Acta (BBA)-Molecular Cell Res* (2016) 1863:2977–92. doi: 10.1016/j.bbamcr.2016.09.012
40. Elena-Real CA, Díaz-Quintana A, González-Arzola K, Velázquez-Campoy A, Orzáez M, López-Rivas A, et al. Cytochrome c speeds up caspase cascade activation by blocking 14-3-3ε-dependent Apaf-1 inhibition. *Cell Death Dis* (2018) 9:1–12. doi: 10.1038/s41419-018-0408-1
41. Choi K, Ryu S, Song S, Choi H, Kang S, Choi C. Caspase-dependent generation of reactive oxygen species in human astrocytoma cells contributes to resistance to TRAIL-mediated apoptosis. *Cell Death Differ* (2010) 17:833–45. doi: 10.1038/cdd.2009.154
42. Pezzuto A, Carico E. Role of HIF-1 in cancer progression: Novel insights. A review. *Curr Mol Med* (2018) 18:343–51. doi: 10.2174/1566524018666181109121849
43. Peers C, Brahimi-Horn MC, Pouysségur J. Hypoxia in cancer cell metabolism and pH regulation. *Essays Biochem* (2007) 43:165–78. doi: 10.1042/bse0430165
44. Kumar A, Kant S, Singh SM. Novel molecular mechanisms of antitumor action of dichloroacetate against T cell lymphoma: Implication of altered glucose metabolism, pH homeostasis and cell survival regulation. *Chem Biol Interact* (2012) 199:29–37. doi: 10.1016/j.cbi.2012.06.005
45. Kumar A, Kant S, Singh SM. α-Cyano-4-hydroxycinnamate induces apoptosis in Dalton's lymphoma cells: role of altered cell survival-regulatory mechanisms. *Anticancer Drugs* (2013) 24:158–71. doi: 10.1097/CAD.0b013e3283586743
46. Campbell KJ, Tait SW. Targeting BCL-2 regulated apoptosis in cancer. *Open Biol* (2018) 8:180002. doi: 10.1098/rsob.180002
47. Ciccone V, Terzuoli E, Donnini S, Giachetti A, Morbidelli L, Ziche M. Stemness marker ALDH1A1 promotes tumor angiogenesis via retinoic acid/HIF-1α/VEGF signalling in MCF-7 breast cancer cells. *J Exp Clin Cancer Res* (2018) 37:311. doi: 10.1186/s13046-018-0975-0
48. Pestana A, Vinagre J, Sobrinho-Simões M, Soares P. TERT biology and function in cancer: beyond immortalisation. *J Mol Endocrinol* (2017) 58:R129–R46. doi: 10.1530/JME-16-0195
49. Del Bufalo D, Rizzo A, Trisciuoglio D, Cardinali G, Torrisi MR, Zangemeister-Wittke U, et al. Involvement of hTERT in apoptosis induced by interference with Bcl-2 expression and function. *Cell Death Differ* (2005) 12:1429–38. doi: 10.1038/sj.cdd.4401670
50. Yuan X, Larsson C, Xu D. Mechanisms underlying the activation of TERT transcription and telomerase activity in human cancer: old actors and new players. *Oncogene* (2019) 38:6172–83. doi: 10.1038/s41388-019-0872-9
51. Kant S, Kumar A, Singh SM. Fatty acid synthase inhibitor orlistat induces apoptosis in T cell lymphoma: role of cell survival regulatory molecules. *Biochim Biophys Acta (BBA)-Gen Subj* (2012) 1820:1764–73. doi: 10.1016/j.bbagen.2012.07.010
52. Frezza C. Metabolism and cancer: the future is now. *Br J Cancer* (2020) 122:133–5. doi: 10.1038/s41416-019-0667-3
53. Lazarev VF, Sverchinsky DV, Mikhaylova ER, Semenyuk PI, Komarova EY, Niskanen SA, et al. Sensitizing tumor cells to conventional drugs: HSP70 chaperone inhibitors, their selection and application in cancer models. *Cell Death Dis* (2018) 9:1–11. doi: 10.1038/s41419-017-0160-y

54. Ezzeddini R, Taghikhani M, Somi MH, Samadi N, Rasaee MJ. Clinical importance of FASN in relation to HIF-1α and SREBP-1c in gastric adenocarcinoma. *Life Sci* (2019) 224:169–76. doi: 10.1016/j.lfs.2019.03.056
55. Zalba S, ten Hagen TL. Cell membrane modulation as adjuvant in cancer therapy. *Cancer Treat Rev* (2017) 52:48–57. doi: 10.1016/j.ctrv.2016.10.008
56. Vishvakarma NK, Singh SM. Augmentation of myelopoiesis in a murine host bearing a T cell lymphoma following in vivo administration of proton pump inhibitor pantoprazole. *Biochimie* (2011) 93:1786–96. doi: 10.1016/j.biochi.2011.06.022
57. Das L, Vinayak M. Curcumin Modulates Glycolytic Metabolism and Inflammatory Cytokines via Nrf 2 in Dalton's Lymphoma Ascites Cells In Vivo. *Anticancer Agents Med Chem (Formerly Curr Med Chem Anticancer Agents)* (2018) 18:1779–91. doi: 10.2174/1871520618666180604093802
58. Naeini MB, Momtazi AA, Jaafari MR, Johnston TP, Barreto G, Banach M, et al. Antitumor effects of curcumin: A lipid perspective. *J Cell Physiol* (2019) 234:14743–58. doi: 10.1002/jcp.28262
59. Aggarwal BB, Harikumar KB. Potential therapeutic effects of curcumin, the anti-inflammatory agent, against neurodegenerative, cardiovascular, pulmonary, metabolic, autoimmune and neoplastic diseases. *Int J Biochem Cell Biol* (2009) 41:40–59. doi: 10.1016/j.biocel.2008.06.010
60. Wang M, Ruan Y, Chen Q, Li S, Wang Q, Cai J. Curcumin induced HepG2 cell apoptosis-associated mitochondrial membrane potential and intracellular free Ca2+ concentration. *Eur J Pharmacol* (2011) 650:41–7. doi: 10.1016/j.ejphar.2010.09.049
61. Fadus MC, Lau C, Bikhchandani J, Lynch HT. Curcumin: An age-old anti-inflammatory and anti-neoplastic agent. *J Tradit Complement Med* (2017) 7:339–46. doi: 10.1016/j.jtcme.2016.08.002
62. Peng N, Gao S, Guo X, Wang G, Cheng C, Li M, et al. Silencing of VEGF inhibits human osteosarcoma angiogenesis and promotes cell apoptosis via VEGF/PI3K/AKT signaling pathway. *Am J Trans Res* (2016) 8:1005.
63. Reischer D, Heyfets A, Shimony S, Nordenberg J, Kashman Y, Flescher E. Effects of natural and novel synthetic jasmonates in experimental metastatic melanoma. *Br J Pharmacol* (2007) 150:738–49. doi: 10.1038/sj.bjp.0707146
64. Braverman J, Sogi KM, Benjamin D, Nomura DK, Stanley SA. HIF-1α is an essential mediator of IFN-γ–dependent immunity to Mycobacterium tuberculosis. *J Immunol* (2016) 197:1287–97. doi: 10.4049/jimmunol.1600266
65. Dahmani A, Delisle J-S. TGF-β in T cell biology: implications for cancer immunotherapy. *Cancers* (2018) 10:194. doi: 10.3390/cancers10060194
66. Yi D, Xu L, Wang R, Lu X, Sang J. miR-381 overcomes cisplatin resistance in breast cancer by targeting MDR1. *Cell Biol Int* (2019) 43:12–21. doi: 10.1002/cbin.11071
67. Chen J, Ding Z, Peng Y, Pan F, Li J, Zou L, et al. HIF-1α inhibition reverses multidrug resistance in colon cancer cells via downregulation of MDR1/P-glycoprotein. *PloS One* (2014) 9:1–3. doi: 10.1371/journal.pone.0098882
68. Basingnaa A, Antwi-Baffour S, Nkansah DO, Afutu E, Owusu E. Plasma levels of cytokines (IL-10, IFN-γ and TNF-α) in multidrug resistant tuberculosis and drug responsive tuberculosis patients in Ghana. *Diseases* (2019) 7:2. doi: 10.3390/diseases7010002

Conflict of Interest: The authors declare that the research was conducted in the absence of any commercial or financial relationships that could be construed as a potential conflict of interest.

frontiers in Oncology

REVIEW
published: 22 July 2021
doi: 10.3389/fonc.2021.696705

The Role of Non-Coding RNAs in the Sorafenib Resistance of Hepatocellular Carcinoma

Xinyao Hu[1,2†], *Hua Zhu*[3†], *Yang Shen*[1,2], *Xiaoyu Zhang*[1,2], *Xiaoqin He*[1,2*] *and Ximing Xu*[1,2*]

[1] Department of Oncology, Renmin Hospital of Wuhan University, Wuhan, China, [2] Cancer Center, Renmin Hospital of Wuhan University, Wuhan, China, [3] Department of Neurosurgery, Renmin Hospital of Wuhan University, Wuhan, China

Hepatocellular carcinoma (HCC) is the second most common cause of cancer-related death. Sorafenib is approved by the U.S. Food and Drug Administration to be a first-line chemotherapy agent for patients with advanced HCC. A portion of advanced HCC patients can benefit from the treatment with sorafenib, but many patients ultimately develop sorafenib resistance, leading to a poor prognosis. The molecular mechanisms of sorafenib resistance are sophisticated and indefinite. Notably, non-coding RNAs (ncRNAs), which include long ncRNAs (lncRNAs), microRNAs (miRNAs) and circular RNAs (circRNAs), are critically participated in the occurrence and progression of tumors. Moreover, growing evidence has suggested that ncRNAs are crucial regulators in the development of resistance to sorafenib. Herein, we integrally and systematically summarized the molecular mechanisms and vital role of ncRNAs impact sorafenib resistance of HCC, and ultimately explored the potential clinical administrations of ncRNAs as new prognostic biomarkers and therapeutic targets for HCC.

Keywords: hepatocellular carcinoma, sorafenib resistance, microRNA, long non-coding RNA, circular RNA

OPEN ACCESS

Edited by:
Jiang-Jiang Qin, Institute of Cancer and Basic Medicine (CAS), China

Reviewed by:
Bernhard Biersack, University of Bayreuth, Germany
Eman Toraih, Tulane University, United States

****Correspondence:***
Xiaoqin He
whuhexq@aliyun.com
Ximing Xu
doctorxu120@aliyun.com

[†]These authors have contributed equally to this work

Specialty section:
This article was submitted to Pharmacology of Anti-Cancer Drugs, a section of the journal Frontiers in Oncology

Received: *17 April 2021*
Accepted: *28 June 2021*
Published: *22 July 2021*

Citation:
Hu X, Zhu H, Shen Y, Zhang X, He X and Xu X (2021) The Role of Non-Coding RNAs in the Sorafenib Resistance of Hepatocellular Carcinoma. Front. Oncol. 11:696705. doi: 10.3389/fonc.2021.696705

BACKGROUND

Hepatocellular carcinoma (HCC) is the paramount form of primary liver cancer, accounting for 75-85% (1). And it is deemed as the second leading cause of cancer-related deaths worldwide, with high probability of metastasis and lethality. Hepatitis B virus (HBV) or hepatitis C virus (HCV) infection, which stimulates chronic inflammation in the liver, is considered to be a dominating risk factor of HCC (2). Meaningfully, detecting early and taking treatment timely can obtain relatively long survival in HCC patients. However, patients are often diagnosed at an advanced stage because of the complex etiology, latent onset, difficulty in diagnosis and rapid progression of HCC. At this stage, chemotherapy is a major available palliative treatment (3), but chemotherapeutic drugs are prone to develop resistance during the course of HCC treatment.

Sorafenib is a first-line chemotherapeutic agent approval by the US Food and Drug Administration to treat the advanced HCC through inhibiting angiogenesis and cell proliferation (4).

As a kinase inhibitor of multiple targets, it is capable of blocking tumor cell multiplication *via* restraining the activation of Raf-1, B-RAF and kinases in Ras/Raf/MEK/ERK pathway. In addition, sorafenib inhibits the generation of tumor blood vessels *via* regulating platelet-derived growth factor receptor (PDGFR-β), Fms-like tyrosine kinase (FLT-3), hepatocyte factor receptor (C-Kit), vascular endothelial growth factor receptor (VEGFR) 2, VEGFR-3 and other tyrosine kinases (5). However, patients are vulnerable to develop resistance to sorafenib during treatment, resulting in poor outcomes, so further studies are needed to investigate the precise mechanisms of sorafenib resistance (6).

Only 2% of human genome is composed of protein-coding sequences, the rest are non-coding sequences (7). Non-coding RNAs (ncRNAs) principally consist of miRNAs, lncRNAs and circRNAs, which are widely associated with the transcription and post-transcription regulation, and also exert a critical action in the occurrence and development of cancer, as well as resistance of sorafenib (8). Herein, we discussed the molecular mechanisms of sorafenib resistance and the role of ncRNAs in this process (**Figure 1**), thus providing new ideas to antagonize sorafenib resistance, enhance the efficacy of sorafenib, and improve the outcome of HCC patients.

MECHANISMS OF SORAFENIB RESISTANCE IN HCC

Some individuals with HCC do not respond to sorafenib in clinical practice, and even if some patients do respond initially, they quickly become refractory (9), mainly due to the primary and acquired resistance to sorafenib. The primary mechanisms of the resistance to sorafenib are summarized here, more details are given in **Tables 1**, **2**.

Primary Resistance

The primary resistance of HCC to sorafenib, existing prior to drug treatment, is attributed mainly to the genetic heterogeneity (63), while the precise mechanism is still unclear. Epidermal growth factor receptor (EGFR), is the most well-studied target related to the primary resistance to sorafenib. EGFR, located at

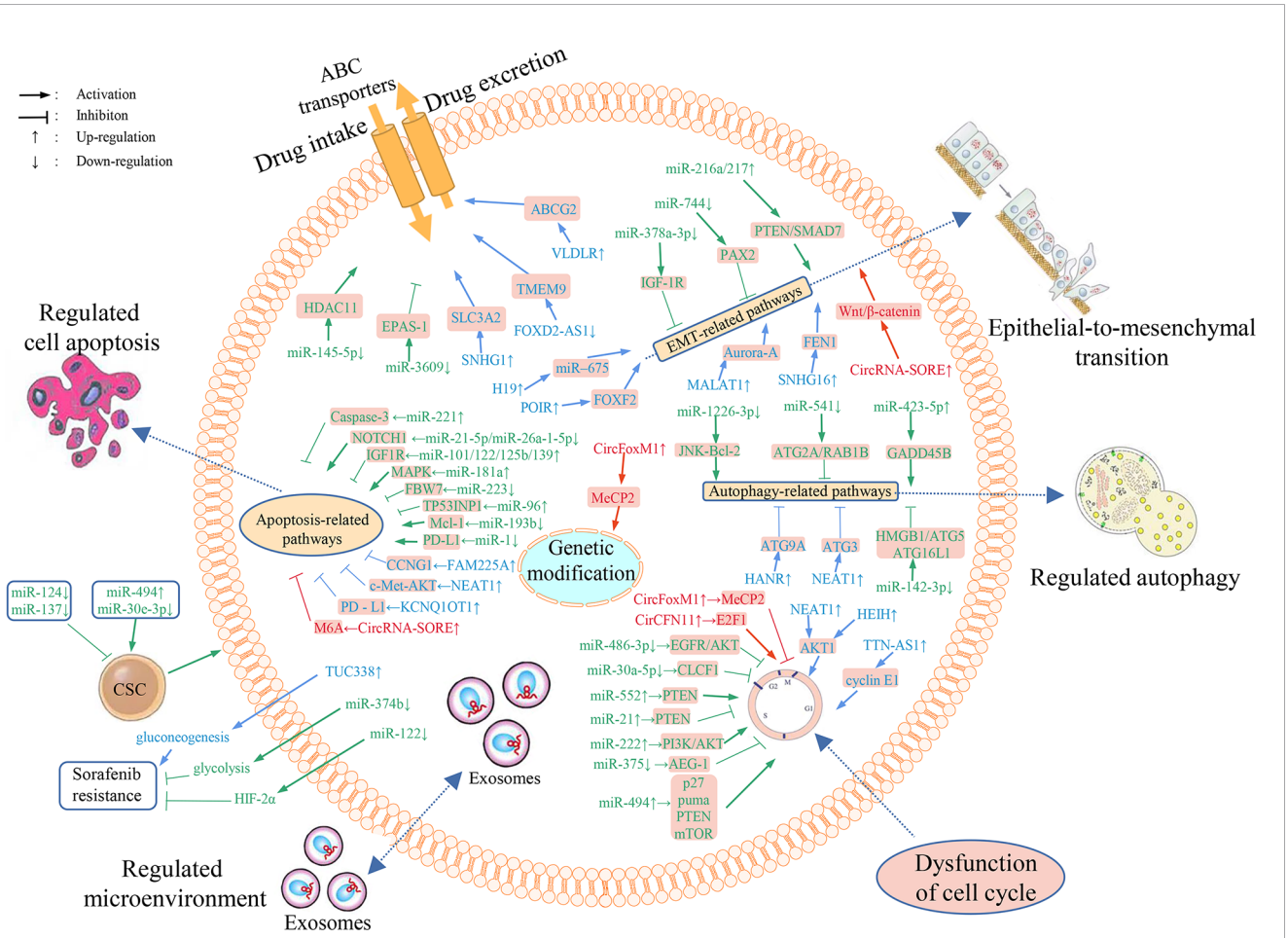

FIGURE 1 | Overview of the mechanisms of ncRNAs involved in HCC resistance to sorafenib and dysregulated ncRNAs' differential expression in sorafenib resistant HCC cells. Numerous miRNAs, lncRNAs and circRNAs are implicated in sorafenib resistance through regulating the expression of downstream target genes and affecting drug transport, metabolism, cell multiplication, autophagy, apoptosis, cell cycle, EMT, tumor microenvironment, and gene modifications.

TABLE 1 | miRNAs and sorafenib resistance in HCC.

miRNAs	Expression	Effects on sorafenib resistance	Target	Mechanism	References
miR-423-5p	up-regulated	Inhibiting	GADD45B	autophagy	(10, 11)
miR-142-3p	down-regulated	Promoting	HMGB1, ATG5, ATG16L1	autophagy	(12, 13)
miR-221	up-regulated	Promoting	Caspase-3	apoptosis	(14)
miR-541	down-regulated	Inhibiting	ATG2A/RAB1B	autophagy	(15)
miR-30e-3p	down-regulated	Promoting	TP53/MDM2, EpCAM, PTEN, p27	CSCs	(16)
miR-486-3p	down-regulated	Inhibiting	FGFR4, EGFR	AKT activation	(17)
miR-122	down-regulated	Inhibiting	SERPINB3	HIF-2α/CSCs	(18, 19)
miR-30a-5p	down-regulated	Inhibiting	CLCF1	AKT activation	(20)
miR-1226-3p	down-regulated	Inhibiting	DUSP4	JNK-Bcl-2 axis	(21)
miR-552	up-regulated	Promoting	PTEN	AKT activation	(22)
miR-124	down-regulated	Inhibiting	CAV1	CSCs	(23)
miR-181a	up-regulated	Promoting	RASSF1	MAPK	(24)
miR - 222	up-regulated	Promoting	PI3K/AKT	AKT activation	(25)
miR-378a-3p	down-regulated	Inhibiting	IGF-1R	EMT	(26)
miR-744	down-regulated	Inhibiting	PAX2	EMT	(27)
miR-374b	down-regulated	Inhibiting	hnRNPA1/PKM2	glycolysis	(28)
miR-21	up-regulated	Inhibiting	PTEN	AKT activation	(29, 30)
miR-375	down-regulated	Inhibiting	AEG-1	AKT activation	(31)
miR-223	down-regulated	Promoting	FBW7	apoptosis	(32)
miR-145-5p	down-regulated	Inhibiting	HDAC11	metabolism	(33)
miR-96	up-regulated	Promoting	TP53INP1	apoptosis	(34)
miR-494	up-regulated	Promoting	p27, puma, PTEN, mTOR	AKT, CSCs	(35, 36)
miR-21-5p	down-regulated	Inhibiting	EZH2	NOTCH1	(37)
miR-26a-1-5p	down-regulated	Inhibiting	EZH2	NOTCH1	(37)
miR-3609	down-regulated	Inhibiting	EPAS-1	metabolism	(38)
miR-101/122/125b/139	up-regulated	Promoting	IGF1R	apoptosis	(39)
miR-193b	down-regulated	Inhibiting	Mcl-1	apoptosis	(40)
miR-1	down-regulated	Inhibiting	PD-L1	apoptosis	(41)
miR-137	down-regulated	Inhibiting	ANT2	CSCs	(42)
miR-216a/217	up-regulated	Promoting	PTEN, SMAD7	EMT	(43)

the surface of epithelial cells, when bound to its ligands, can result in the activation of downstream pathways, thereby regulating cell proliferation (64). Over half of the patients diagnosed with HCC have aberrant EGFR/HER3 activation and over-expression of EGFR and its ligands (particularly the dual regulated ligands), which suppress the antitumor capacity of sorafenib. The efficacy of sorafenib can be improved when sorafenib combined with RNA interference agents inhibiting EGFR/HER-3 phosphorylation. Studies suggested that activated EGFR may be a promising predictor of primary sorafenib resistance in HCC cells, and overexpression of EGFR or its ligands may result in continuous activation of EGFR downstream pathways and subsequent resistance to sorafenib (65). Additionally, another downstream pathway of EGFR, the Ras/Raf/MEK/ERK pathway, is activated in sorafenib-resistant patients, further corroborating the vital action of EGFR in

TABLE 2 | lncRNAs and sorafenib resistance in HCC.

lncRNAs	Expression	Effects on sorafenib resistance	Interact with	Target	Mechanism	References
SNHG1	up-regulated	Promoting	miR-21	SLC3A2	transfer	(44)
HANR	up-regulated	Promoting	miR-29b	ATG9A	autophagy	(45)
FAM225A	up-regulated	Promoting	miR-130a-5p	CCNG1	apoptosis	(46)
NEAT1	up-regulated	Promoting	miR-149-5p	AKT1	Akt activation	(47)
HEIH	up-regulated	Promoting	miR-98-5p	PI3K/AKT	Akt activation	(48)
SNHG16	up-regulated	Promoting	miR-140-5p	FEN1	EMT	(49, 50)
KCNQ1OT1	up-regulated	Promoting	miR - 506	PD - L1	apoptosis	(51)
MALAT1	up-regulated	Promoting	miR-140-5p	Aurora-A	EMT	(52, 53)
H19	up-regulated	Promoting	miR-675	miR - 675	EMT	(54)
FOXD2-AS1	down-regulated	Inhibiting	miR-150-5p	TMEM9	transfer	(55)
TTN-AS1	up-regulated	Promoting	miR-16-5p	cyclin E1	Akt activation	(56)
NEAT1	up-regulated	Promoting	miR-204	ATG3	autophagy apoptosis	(57, 58)
			miR-335	c-Met-AKT	AKT activasion	
			miR-149-5p			
POIR	up-regulated	Promoting	miR-182-5p	FOXF2	EMT	(59)
TUC338	up-regulated	Promoting	/	RASAL1	gluconeogenesis	(60, 61)
VLDLR	up-regulated	Promoting	/	ABCG2	transfer	(62)

sorafenib resistance. The down-regulation of pERK may contribute to sorafenib resistance.

In addition, mitogen-activated protein kinase (MAPK) levels affect the susceptibility of HCC cells to sorafenib. Recent research has also demonstrated that c-Jun N-terminal kinase (JNK), another member of MAPK family, has great potential to predict the sorafenib sensitivity (65). Furthermore, sestrin2 (SESN2), an important component of the sestrin stress-inducible protein family, participates in tumorigenesis and development by regulating a variety of downstream pathways, among which MAPK and AKT are closely associated with cell multiplication and metabolism (66). Upregulation of SESN2 confers primary resistance to sorafenib in HCC cells by activating AKT (67). Additionally, HCC patients with overexpressed VEGFA are significantly susceptible to sorafenib. VEGFA can stimulate stromal cells to secrete hepatocyte growth factor to induce tumor progression, suggesting that VEGFA may be a promising predictor of response to sorafenib in patients with HCC (68).

In summary, it is highly prospective to further explore the mechanism of primary resistance to sorafenib, identify biomarkers that predict sorafenib sensitivity, and then personalize the therapy for patients with different sensitivities to save the economic and time costs of ineffective treatment. It is also helpful in seeking new therapeutic targets and exploring novel strategies to combine sorafenib with other targeted drugs for more effective treatment.

Acquired Resistance

Acquired sorafenib resistance can be induced under a variety of conditions, including reduced drug intake, enhanced intracellular drug metabolism, increased excretion, changes in molecular targets affecting the activation/inactivation of pathways, changes in DNA repair mechanisms, dysfunction of cell cycle-related proteins and tumor microenvironment regulation (69). Here we summarized several of the latest and most recognized mechanisms of acquired sorafenib resistance.

The Solute Carrier (SLC) Family

The human SLC superfamily transporter plays an important role in sorafenib uptake. Previous study has shown that SLC22 (organic cationic/anion transporter) is down-regulated in HCC and is closely related to sorafenib resistance. Moreover, down-regulated expression of SLC22A1 in human HCC is related to its DNA methylation (70). Therefore, demethylation agents targeting SLC22A1 methylation are promising for the treatment of patients resistant to sorafenib (71).

ATP Binding Box (ABC) Transporters Family

Removal of drugs from the cytoplasm is an important method of drug resistance. The ABC transporter is one of the largest family of membrane transporters. The genetic variants of ABC transporter genes, such as the ABCB family, the ABCC family and the ABCG2 family is related to clinical chemotherapy resistance (72). An *in vitro* research illustrated that the accumulation of sorafenib was lower in cells with ABCC2 overexpression than in cells with normal ABCC2 expression, suggesting that sorafenib resistance may be related to ABCC2 (MRP2) variation. Furthermore, downregulation of ABCC2 expression has the potential to restore sensitivity to sorafenib (73).

EGFR

EGFR/HER3 activation is associated with both primary and acquired drug resistance (74). The combination of gefitinib, which can down-regulate EGFR/HER3 expression, with sorafenib has been shown to increase tumor inhibition and prevent sorafenib resistance, demonstrating the role of EGFR/HER3 inhibition in the HCC treatment.

AKT Activation

The sustained action of sorafenib induces AKT activation, which further leads to resistance of HCC cells to sorafenib. AKT inhibition reverses sorafenib resistance by converting protective cellular autophagy into a cell-death mechanism. GDC0068, a new ATP competitive inhibitor of pan-AKT, acts synergistically with sorafenib in inhibiting the development of sorafenib-resistant HCC. Moreover, the combination of sorafenib with arsenic trioxide (ATO), an AKT-inhibited anti-cancer agent, enhances the anticancer activity of sorafenib against HCC (75). Furthermore, it has been found that the application of hepatocyte growth factor (HGF) in sorafenib treated HCC cells can activate the proto-oncogene MET, re-stimulate the downstream AKT and extracellular regulated protein kinases (ERK1/2) pathways, therefore inhibiting apoptosis. HCC cells treated by HGF can also induce the expression of early growth response protein (EGR1), which has strong correlation with sorafenib resistance. Taken together, HGF induced MET activation promotes the sorafenib resistance in HCC *via* AKT/ERK1/2-EGR1 pathway (76).

Hypoxia-Inducible Factors (HIF)

In patients continuously exposed to sorafenib, the anti-angiogenic effect of sorafenib causes a decrease in microvascular density, leading to intracellular hypoxia and favoring the selection of resistant cells adapted to the hypoxic microenvironment. Clinical studies suggest that overexpression of HIF-1 and HIF-2 in HCC patients is a reliable marker of poor prognosis (77). Therefore, sorafenib combined with HIF inhibitor therapy is a potential approach to overcome sorafenib resistance. It is important to note that HIF-1 and HIF-2 compensate for each other, and the removal of one HIF-subtype increases the expression of the other HIF-subtype. Hence, targeting both HIF-1 and HIF-2 is more effective.

Metallothionein (MT) -1G

Sorafenib activates the transcription factor nuclear factor erythrocyte 2-related factor 2, thus inducing the MT-1G expression. Downregulation of MT-1G was shown to improve the anticancer action of sorafenib both *in vitro* and *in vivo*. Knockdown of MT-1G by RNA interference increased the glutathione consumption and the lipid peroxidation, resulting in sorafenib-induced ferroptosis, which is a novel approach to regulate cell death (78). In summary, MT-1G may be a key regulator of sorafenib-resistant cells in human HCC and is a hopeful therapeutic target.

Cancer Stem Cells (CSC)

Tumorigenicity and chemoresistance of tumor cells can be increased by the acquisition of CSC characteristics. CD13, CD24, CD44, CD90, CD133 and EpCAM are potential markers for the enrichment of CSCs in HCC. $CD133^+$ cells activate the AKT/PKB axis and Bcl-2 cell survival response, thus promoting chemoresistance (79). CD44 also contributes to the formation of sorafenib resistance and can serve as a predictor of sorafenib efficacy. Moreover, Nanog is a gene essential for self-renewal of CSCs in HCC. It has been shown that in sorafenib-resistant HCC cells, Nanog expression is promoted by the destabilization and significant downregulation of the transactivation response element RNA binding protein 2, as a result of autophagy-lysosomal protein hydrolysis, promoting the sorafenib resistance of HCC cells (80). In addition, the interaction between cyclin-dependent kinases 1 (CDK1) and the pluripotent transcription factor octamer binding transcription factor 4 has a crucial action in differentiation of embryonic stem cells. It has revealed that blocking the CDK1/PDK1/β-catenin pathway by the CDK1 inhibitor RO3306 improves the therapeutic efficacy of sorafenib in a preclinical HCC model (81). Overall, CSCs-based studies are expected to reverse resistance to sorafenib and improve its efficacy.

Activator of Thyroid and Retinoic Acid Receptors (ACTR)

ACTR is a crucial oncogenic factor in HCC. It is also significantly elevated in sorafenib-resistant HCC cells in mice transplant models of HCC, increasing sorafenib resistance by modulating the Warburg effect. Cancer cells produce energy mainly through glycolysis. ACTR not only interacts with c-myc, a key regulator of the Warburg effect, to promote glycolysis to occur, but also promotes glucose uptake, ATP and lactate production, decreases extracellular acidification and oxygen consumption, thus inhibiting sorafenib sensitivity. Knockdown of ACTR decreases the expression of glycolytic enzyme and is associated with a better prognosis (17). Hence, ACTR is expected to be a prospective target for reversing sorafenib resistance.

Autophagy

Autophagy exerts a protective effect on tumor cells, and the EFGR/Ras/MAPK pathway, mammalian target of rapamycin (mTOR) pathway, p53 pathway and HIF-1 signaling pathway are several pathways that regulate autophagy in cancer cells (82). Inactivation of the mTOR pathway has been reported to induce resistance to sorafenib in HCC cells. P70S6K and 4E-BP1 are downstream proteins of mTORC1, and their activity can be inhibited by sorafenib in turn (83). The main upstream inducer of mTORC1 is the PI3K/AKT pathway, and inhibition of AKT reverses the acquired sorafenib resistance in HCC patients, converting protective autophagy into cell death. Moreover, PSMD10 translocates into nucleus and binds to heat shock transcription factor (HSF1), initiating ATG7 transcription, increasing autophagy, and promoting sorafenib resistance. This is a hallmark of poor outcome in HCC patients (84). In addition, N6-methyladenosine (M6A)-modified FoxO3 mRNA is downregulated in hypoxic environments, activating autophagy and promoting sorafenib resistance during HCC treatment (85). In conclusion, autophagy is a self-protective mode of HCC cells and a facilitator of sorafenib resistance. Regulating the upstream and downstream pathways of autophagy and converting protective autophagy into apoptosis may be effective approaches for HCC therapy.

Epithelial-Mesenchymal Transition (EMT)

EMT is known to be a key process in cancer development, promoting cell migration, and is also associated with resistance to sorafenib. There may be a negative correlation between EMT and the efficacy of sorafenib (86). Galactosin-1 induces EMT in HCC through activating FAK/PI3K/AKT signaling pathway to enhance sorafenib resistance and is a biomarker for predicting sorafenib sensitivity. Sorafenib inhibits the occurrence of EMT, which in turn impairs the efficacy of sorafenib. It has been shown that zinc finger protein 703 may be a promising target for cancer therapy by directly binding to and transfecting the CLDN4 promoter to activate the expression of CLDN4, inducing EMT and inhibiting the sensitivity of HCC cells to sorafenib (87).

The above-mentioned resistance mechanisms of sorafenib can help us to have a deeper understanding of the reasons for the poor chemotherapeutic effect of HCC, and to explore more targets to reverse the resistance of sorafenib for better therapeutic effect.

MiRNAs AND SORAFENIB RESISTANCE OF HCC

miRNAs are a category of short non-coding RNAs (about 20nt) that bind to the 3'-untranslated region (3' UTR) of mRNA, act as mRNA sponges to absorb mRNA and regulate the expression levels of downstream genes, participate in several physiological processes, influence cancer-associated pathways, and also contribute to the formation of the resistance to sorafenib (**Table 1**) (83).

Acting on Autophagy

MiR-423-5p is closely associated with treatment sensitivity. Statistical analysis revealed an increase in secretion of miR423-5p in 75% of patients after 6 months of sorafenib treatment. Further experiments has showed that the proportion of cells in the S phase of the cell cycle in HCC cells is markedly elevated after transfection with miR-423-5p (10). miR-423-5p has been revealed to promote autophagy and ultimately induce drug resistance by targeting growth arrest and DNA damage inducing β protein (GADD45B) (11). miR-142-3p is a tumor inhibitor miRNA that suppresses HCC cell invasion and migration by repressing the expression of the high mobility histone B1 (HMGB1) gene (12). It has also been shown to be an autophagy-regulating miRNA. miR-142-3p upregulation can decrease autophagy by targeting autophagy-related 5 (ATG5) and autophagy-related 16-like 1 (ATG16L1), thereby increasing the sensitivity of HCC cells to sorafenib and enhancing the apoptosis induced by sorafenib. PU.1 transcription factor can

up-regulate the miR-142-3p expression. Targeting the PU.1-miR-142-3p-ATG5/ATG16L1 axis may be an effective therapeutic strategy to reverse cytoprotective autophagy and overcome sorafenib resistance (12, 88).

Acting on Apoptosis

Overexpression of miR-221 activates caspase-3 thereby reversing the resistance of HCC cells to sorafenib and inducing apoptosis in HCC cells. In sorafenib-resistant cells, the activation of insulin-like growth factor 1 receptor (IGF-1R) triggered downstream EGFR pathway RAS/RAF/ERK signaling, resulting in the reduced miR-221 expression and poor therapeutic efficacy (14). Besides, miR−223 targets FBW7 to enhance the resistance of HCC cells to sorafenib and inhibit apoptosis. In addition, liver tumor-initiating cells (T-ICs) play a vital part in the occurrence, development, drug resistance and recurrence of HCC (32). In liver T-ICs, miR-96 down-regulates TP53INP1, inhibits HCC cell apoptosis, and promotes HCC cell resistance to sorafenib (34). Furthermore, enhancers of zeste 2 multimeric complex 2 subunit (EZH2) inhibit HCC cell apoptosis and promote sorafenib resistance by suppressing the expression of miR-101, miR-122, miR-125b and miR-139 thereby regulating insulin-like growth factor 1 receptor (IGF1R) levels (39). In HBV-positive HCC cells, MCL-1 level is elevated and miR-193b is markedly down-regulated. Upregulation of miR-193b can restore cellular sensitivity to sorafenib and promote sorafenib-induced apoptosis (40). Moreover, NRF-2/miR-1 axis-regulated programmed death ligand-1 (PD-L1) inhibits apoptosis of HCC cells, enhances sorafenib resistance and promotes tumor progression (39).

Acting on AKT Activation

MiR-30a-5p expression is decreased in HCC tissues, inhibits the PI3K/AKT axis, targets CLCF1, and then increases the sensitivity of HCC cells to sorafenib (20). MiR-375, which is also down-regulated in HCC, inhibits AKT activation by targeting AEG-1, suppresses tumor angiogenesis in HCC, and reverses the sorafenib resistance of HCC (31). miR-486-3p, similarly down-regulated, activates AKT by targeting FGFR4 and EGFR, leading to the sorafenib resistance in HCC patients (17). Down-regulation of miR-222 significantly inhibits the proliferation, migration and invasion of HepG2 cells (human hepatocellular cancer cell line, as HCC model) (89) and induces apoptosis. It regulates the expression of phosphorylated PI3K and AKT, thereby enhancing the sorafenib resistance of HCC (25). Moreover, miR-552 promotes hepatic T-IC amplification and decreases the sensitivity of HCC cells to sorafenib. It acts by targeting PTEN to affect AKT activation (22). Furthermore, exosome miR-21 modulates the TETS/PTENP1/PTEN pathway to facilitate the development of HCC, and also inhibits autophagy-mediated sorafenib resistance *via* the PTEN/AKT pathway (29, 30). Besides, miR-494 is related to stem cell phenotypes and promotes the progression of HCC. It enhances the sorafenib resistance of HCC cells *via* targeting PTEN, a crucial protein that inhibits the activation of AKT (35).

Other Pathways

MiR-30e-3p affects tumor development *via* the MDM2/TP53 axis, and EpCAM, PTEN and P27 are its additional targets that together exert miR-30e-3p's role in promoting tumor malignancy. In sorafenib-treated HCC patients, increased circulating miR-30e-3p levels predict the progression of sorafenib resistance (16). Likewise, miR-181a promote sorafenib resistance. Studies have reported that HepG2 cells are more sensitive to sorafenib than Hep3B cells and that miR-181a expression levels are lower in HepG2 cells. miR-181a directly targets and reduces the expression of MAPK signaling factor, RASSF1, an inhibitor of sorafenib resistance, thereby reducing sorafenib efficacy (24). Furthermore, miR-216a/217 expression level is increased in HCC and induces EMT *via* targeting PTEN and Smad7, leading to sorafenib resistance and cancer recurrence (43).

The above are miRNAs that promote sorafenib resistance, miRNAs that enhance sorafenib sensitivity is introduced in this paragraph. First, inhibitors of EZH2 can target Notch1 through Notch1-related miRNAs, such as miR-21-5p, miR-26a-1-5p, and act on the corresponding HCC stem cells to reduce sorafenib resistance (37). Second, in most HCC patients, miR-122 is down-regulated. It has been shown that miR-122 targets SERPINB3 and its low expression is related to SERPINB3 activity and CSC phenotype in HCC cells. Moreover, miR-122 have a crucial action in inhibiting sorafenib resistance by regulating the expression of HIF-2α (18). Third, miR-1226-3p is lowly expressed in HCC cells, and it promotes the sensitivity of HCC cells to sorafenib by downregulating DUSP4 and affecting the JNK-Bcl-2 pathway (21). Fourth, miR-124 acts on CAV1 to regulate HCC CSC proliferation, thereby inhibiting sorafenib resistance (23). Fifth, a study has found that LXR increases the sensitivity of sorafenib in HCC by activating miR-378a transcription. MiR-378a is downregulated in HCC, it targets IGF-1R and inhibits EMT, thereby suppressing sorafenib resistance (26). Sixth, miR-744 affects the expression of PAX2, thus inhibiting the multiplication of HCC cells and sorafenib resistance (27). Seventh, miR-374b inhibits the progression of HCC and re-sensitizes HCC cells to sorafenib through antagonizing the PKM2-related glycolysis pathways (28). Eighth, downregulation of miR-145-5p and promoter hypomethylation mediated HDAC11 overexpression affects the metabolism of HCC cells and tissues, and facilitates the metastasis of HCC cells and their resistance to sorafenib (33). Ninth, miR-3609 retards the sorafenib clearance in HCC cells through regulating EPAS-1 and inhibiting activation of the gestation hormone X receptor pathway (38). Last but not least, miR-137 upregulation reverses CSC phenotype and sorafenib resistance in HCC by degrading ANT2 (42).

LncRNAs AND SORAFENIB RESISTANCE OF HCC

LncRNA is a class of RNAs, over 200 nucleotides in length, with no protein-coding action. It can not only act as a sponge for a

variety of miRNAs, but also interact with one or more RNA-binding proteins (RBPs) to be involved in multiple biological processes by regulating cell proliferation, apoptosis, metastasis, and invasion (90, 91). In recent years, its effects on the occurrence, migration, prognosis, recurrence and chemoresistance of cancers have become a hotspot of research (**Table 2**).

Acting on Autophagy

LncHANR expression is increased in HCC. It serves as a sponge for miR-29b ang inhibits its expression, thus affecting the expression of autophagy-related protein 9A antibody (ATG9A), the target protein of miR-29b, and ultimately enhancing autophagy-associated sorafenib resistance (45). LncNEAT1 can promote the development of multiple cancers including HCC. lncNEAT1 serves as a sponge for miR-204, upregulates ATG3 expression, a target gene of miR-204, promotes autophagy, and facilitates the sorafenib resistance of HCC (57).

Acting on AKT Activation

LncSNHG1 is remarkably upregulated in HCC tissues and cells, promoting HCC invasion and leading to poor patient prognosis. Further mechanistic studies revealed that sorafenib can induce miR-21 translocation to the nucleus, which promotes lncSNHG1 expression, thereby upregulating solute carrier family 3 member 2 (SLC3A2) leading to AKT activation and ultimately to sorafenib resistance (92). Conversely, downregulation of SNHG1 enhances the effect of sorafenib. LncNEAT1, which also plays a pro-oncogenic role, is significantly increased in HCC cells. It inhibits the efficacy of sorafenib by targeting miR-149-5p and regulating the miR-149-5p/AKT1 axis (47). Furthermore, NEAT1 inhibits the sensitivity of HCC cells to sorafenib *via* modulating miR-335/c-Met (58). In addition, lncHEIH is also markedly upregulated in sorafenib-resistant HCC cells. HEIH acts as a sponge for miR-98-5p to activate the PI3K/AKT pathway, thereby enhancing sorafenib resistance (48). Besides, lncTTN-AS1 expression is upregulated in HCC cells, and lncTTN-AS1 acts as a sponge for miR-16-5p to inhibit its expression, thereby upregulating cyclinE1, the target protein of miR-16-5p, and activating the PTEM/AKT signaling pathway, ultimately leading to resistance of HCC cells to sorafenib (93).

Acting on Apoptosis

LncFAM225A is up-regulated in HCC tissues and sorafenib-resistant HepG2/SOR cells, and inhibition of FAM225A significantly inhibits the resistance of HepG2/SOR cells to sorafenib. Further studies have revealed that FAM225A interacts with miR-130a-5p to negatively regulate CNG1 expression, thereby inhibiting apoptosis and promoting sorafenib resistance of HCC cells (46). Besides, lncKCNQ1OT1 has been revealed to correlate with the sorafenib resistance and immune escape of HCC cells. In HCC tissues resistant to sorafenib, KCNQ1OT1 serves as a ceRNA for miR-506 and elevates the expression of PD-L1, leading to immune escape of HCC cells. Knockdown of KCNQ1OT1 could alter the tumor microenvironment, inhibit T-cell apoptosis and promote HCC cell apoptosis, thus inhibiting HCC cell resistance to sorafenib and cell metastasis (51). Furthermore, by restraining miR-335 expression, lncNCNEAT1 suppresses c-Met-AKT signaling pathway-mediated sorafenib resistance of HCC cells. In contrast, upregulation of miR-335 or knockdown of c-Met resists the antiapoptotic activity of NEAT1 in HCC cells (58).

Acting on EMT

LncSNHG16 is closely associated with HCC invasiveness and poor outcome of patients, and its expression is dramatically increased in HCC cells. Additionally, SNHG16 can serve as an endogenous sponge of miR-140-5p and up-regulate flap endonuclease 1 (FeN1), an oncogene in a range of cancers, which is also involved in the pathological process of HCC, thereby reducing the sensitivity of HCC cells to sorafenib and affecting the therapeutic effect (49). Previous study has confirmed that silencing FeN1 restrains the EMT of HCC cells, thereby suppressing HCC progression and metastasis (50). In summary, SNHG16 regulates the EMT of HCC cells through affecting the miR-140-5p/FeN1 axis, thereby promoting the sorafenib resistance of HCC.

The lncMALAT1 expression is increased in sorafenib-resistant HCC tissues, and enhances the multiplication, migration and EMT of HCC cells, thus affecting the development and progression of HCC. It has shown that MALAT1 as a sponge for miR-140-5p and promotes the expression of the serine/threonine protein kinase Aurora-A, which maintains genomic integrity and participate mitosis. Up-regulated Aurora-A is related to poor outcome of HCC patients and induces a variety of malignant phenotypes in HCC (52, 53). In addition, lncH19 expression is negatively related to sensitivity of HCC cells to sorafenib. Knockdown of lncH19 can improve the sensitivity of HCC cells to sorafenib by inhibiting EMT (54). Notably, H19 can upregulate the expression of miR-675 to promote EMT. What's more, through serving as a sponge for miR-182-5p, lncPOIR inhibits the expression of miR-182-5p and promotes EMT, thereby suppressing sorafenib sensitivity and promoting HCC development. Knockdown of lncPOIR reverses the EMT and the sorafenib resistance of HCC cells (59).

Acting on Other Pathways

It is shown that LncFOXD2-AS1 is significantly reduced in HCC cells. FOXD2-AS1 affects the transmembrane protein 9 (TMEM9) by suppressing miR-150-5p expression, thereby reversing sorafenib resistance in HCC (55). In contrast, lncTUC338 is highly expressed in HCC cells and tissues. Down-regulation of TUC338 suppresses tumor growth by increasing the expression of Rasal1, while enhancing the sensitivity of HCC cells to sorafenib *via* inhibiting gluconeogenesis (60, 61). Knockdown of lncVLDLR reduces the expression of ABCG2, an important transporter, thereby restraining drug efflux and enhancing sensitivity of HCC cells to sorafenib. lncVLDLR may be a novel target to improve the efficacy of sorafenib (62).

CircRNAs AND SORAFENIB RESISTANCE OF HCC

CircRNAs are a specific category of ncRNAs and a latest research hotspot in the field of RNA. Unlike linear RNAs, circRNAs, with a closed loop structure, cannot be sheared by RNA exonucleases

and are more stably expressed and less susceptible to degradation. They widely correlate with the regulation of cell multiplication, polarization and apoptosis *in vivo*, and also have significant effects on the development of various diseases, particularly on the pathogenesis, diagnosis, treatment and prognosis of tumors (94). However, studies on the role of circRNAs in the sorafenib resistance of HCC are still in the infancy. It has been found 582 differentially expressed circRNAs in HCC cells resistant to sorafenib (HUH7-S), of which 272 were up-regulated and 310 were down-regulated, with a statistically significant difference (0.05) (95). This suggests that circRNAs with different expression levels may exert a crucial role in sorafenib resistance of HCC.

N6-methyladenosine (M6A)-modified circRNA-SORE is expressed highly in sorafenib-resistant HCC cells. Further studies have shown that circRNA-SORE can induce EMT through serving as a sponge for miR-103a-2-5p and miR-660-3p to competitively activate Wnt/β-catenin pathway, thereby inducing sorafenib resistance in HCC cells (15). Furthermore, circRNA-SORE can bind to YBX1, a major oncogenic protein in cytoplasmic matrix, thereby preventing YBX1 from interacting with E3 ubiquitin ligase PRP19, blocking PRP19-mediated degradation of YBX1, stabilizing YBX1, and ultimately mediating sorafenib resistance in HCC cells and poor prognosis of patients (96).

CirCFN11 expression is increased in HCC cells, and its overexpression promotes the aggressiveness of HCC and is an independent risk factor for prognosis of HCC patients. It acts as a sponge of miR-1205 to upregulate the expression of oncogene E2F1 and finally mediates the resistance of HCC cells to sorafenib (97).

Moreover, circFoxM1, a newly discovered circRNA, significantly inhibits HCC development and enhances sorafenib efficacy *in vitro*. Interestingly, its expression is up-regulated in sorafenib-resistant HCC cells, suggesting that circFoxM1 may affect the development of HCC and sorafenib resistance, respectively, through different mechanisms. CircFOXM1 can serve as a sponge for miR-1324 and increase methyl-CpG-binding protein 2 (MeCP2) expression, thereby regulating sorafenib resistance in HCC. In addition, overexpression of miR-1324 reverses circFoxM1-induced sorafenib resistance and increases MeCP2 expression. This further confirms that circFOXM1 contribute to the regulation of sorafenib sensitivity in HCC cells through the miR-1324/MeCP2 axis (95).

CONCLUSIONS AND EXPECTATIONS

A growing number of ncRNAs have been identified to play critical regulatory roles in sorafenib resistance of HCC. MiRNAs exert regulatory effects by binding to the 3'-UTR of target mRNAs to regulate downstream proteins, while lncRNAs and circRNAs are mainly involved in modulating the resistance of sorafenib as sponges of miRNAs.

The underlying mechanisms of the role of sorafenib resistance-associated ncRNAs in HCC are summarized in **Figure 1**. Targeting these dysregulated ncRNAs may be a promising approach to reverse sorafenib resistance in HCC. Delivery of tumor suppressor ncRNAs directly or *via* suitable vectors to target cells to exogenously increase their expression, or designing small interfering RNA (siRNA) or short hairpin RNA (shRNA) to knock down oncogenic ncRNAs has been shown to be adaptable in reversing resistance to sorafenib in HCC patients. For example, gold nanoparticles-loaded anti-miR221 has been shown to enhance the effect of sorafenib by inhibiting HCC cell proliferation *via* inactivating miR-221/p27/DNMT1 pathway. In addition, the treatment with the combination of nanoparticles-loaded anti-miR221 and sorafenib is more efficient than with sorafenib alone (98). It has also been reported that miR-375 and sorafenib can be co-loaded into calcium carbonate nanoparticles with lipid coating to inhibit the resistance of sorafenib *via* exerting the anti-autophagic effect of miR-375, thus enhancing the anti-tumor effect of sorafenib (99). Matrine combined with sorafenib treatment also inhibits proliferation of HCC cells synergistically, partially by suppressing miRNA-21 expression and then inducing PTEN (100). Hence, targeting ncRNAs in combination with sorafenib against HCC is expected to conquer sorafenib resistance and represent a promising option for patients in advanced stage of HCC resistant to sorafenib. However, it is still a challenge to select key target ncRNAs from numerous candidate ncRNAs. In order to develop ncRNA-based therapeutics to benefit HCC patients, further additional translational research and clinical trials are warrant. We believe that targeting ncRNAs is promising to eventually overcome sorafenib resistance thus improving outcome of advanced HCC patients.

It is worth noting that the development of more reliable delivery systems is urgently required to improve the biological stability of ncRNAs and to improve their uptake, penetration, transport, distribution and retention. Meng et al. constructed 50 nm mesoporous silica nanoparticles to transport doxorubicin and Pgp siRNA, which are protected *via* a polyethyleneimine-polyethylene glycol copolymer, resulting in an 8% increase in doxorubicin and Pgp siRNA permeability by 8%, ultimately reversing the resistance of breast cancer to doxorubicin. This practice provides a rationale for ncRNAs-based therapy combined with sorafenib to against sorafenib resistance in HCC and improve patients' prognosis (101). Development of suitable transport vehicles for ncRNA/siRNA/shRNA and sorafenib is important to improve combination therapy to reverse sorafenib resistance and improve sorafenib efficacy.

AUTHOR CONTRIBUTIONS

All the authors made substantial contributions to this study. All authors contributed to the article and approved the submitted version.

FUNDING

This work was supported by the National Natural Science Foundation of China (no. 31971166 to XX).

REFERENCES

1. Zhou P, Zheng G, Li Y, Wu D, Chen Y. Construction of a Circrna-Mirna-Mrna Network Related to Macrophage Infiltration in Hepatocellular Carcinoma. *Front Genet* (2020) 11:1026. doi: 10.3389/fgene.2020.01026
2. Han TS, Ban HS, Hur K, Cho HS. The Epigenetic Regulation of HCC Metastasis. *Int J Mol Sci* (2018) 19(12):3978. doi: 10.3390/ijms19123978
3. Couri T, Pillai A. Goals and Targets for Personalized Therapy for HCC. *Hepatol Int* (2019) 13(2):125–37. doi: 10.1007/s12072-018-9919-1
4. Keating GM. Sorafenib: A Review in Hepatocellular Carcinoma. *Target Oncol* (2017) 12(2):243–53. doi: 10.1007/s11523-017-0484-7
5. Zhu YJ, Zheng B, Wang HY, Chen L. New Knowledge of the Mechanisms of Sorafenib Resistance in Liver Cancer. *Acta Pharmacol Sin* (2017) 38(5):614–22. doi: 10.1038/aps.2017.5
6. Fan G, Wei X, Xu X. Is the Era of Sorafenib Over? A Review of the Literature. *Ther Adv Med Oncol* (2020) 12:1758835920927602. doi: 10.1177/1758835920927602
7. Wong CM, Tsang FH, Ng IO. Non-Coding RNAs in Hepatocellular Carcinoma: Molecular Functions and Pathological Implications. *Nat Rev Gastroenterol Hepatol* (2018) 15(3):137–51. doi: 10.1038/nrgastro.2017.169
8. Ding B, Lou W, Xu L, Fan W. Non-Coding RNA in Drug Resistance of Hepatocellular Carcinoma. *Biosci Rep* (2018) 38(5):BSR20180915. doi: 10.1042/BSR20180915
9. Zhu AX. Beyond Sorafenib: Novel Targeted Therapies for Advanced Hepatocellular Carcinoma. *Expert Opin Investig Drugs* (2010) 19(5):663–72. doi: 10.1517/13543781003767426
10. Stiuso P, Potenza N, Lombardi A, Ferrandino I, Monaco A, Zappavigna S, et al. MicroRNA-423-5p Promotes Autophagy in Cancer Cells and Is Increased in Serum From Hepatocarcinoma Patients Treated With Sorafenib. *Mol Ther Nucleic Acids* (2015) 4:e233. doi: 10.1038/mtna.2015.8
11. Yu Z, Zhao H, Feng X, Li H, Qiu C, Yi X, et al. Long Non-Coding RNA FENDRR Acts as a miR-423-5p Sponge to Suppress the Treg-Mediated Immune Escape of Hepatocellular Carcinoma Cells. *Mol Ther Nucleic Acids* (2019) 17:516–29. doi: 10.1016/j.omtn.2019.05.027
12. Fu Y, Sun LQ, Huang Y, Quan J, Hu X, Tang D, et al. miR-142-3p Inhibits the Metastasis of Hepatocellular Carcinoma Cells by Regulating HMGB1 Gene Expression. *Curr Mol Med* (2018) 18(3):135–41. doi: 10.2174/1566524018666180907161124
13. Pratama MY, Pascut D, Massi MN, Tiribelli C. The Role of microRNA in the Resistance to Treatment of Hepatocellular Carcinoma. *Ann Transl Med* (2019) 7(20):577. doi: 10.21037/atm.2019.09.142
14. Fornari F, Pollutri D, Patrizi C, La Bella T, Marinelli S, Casadei Gardini A, et al. In Hepatocellular Carcinoma miR-221 Modulates Sorafenib Resistance Through Inhibition of Caspase-3-Mediated Apoptosis. *Clin Cancer Res* (2017) 23(14):3953–65. doi: 10.1158/1078-0432.CCR-16-1464
15. Xu WP, Liu JP, Feng JF, Zhu CP, Yang Y, Zhou WP, et al. miR-541 Potentiates the Response of Human Hepatocellular Carcinoma to Sorafenib Treatment by Inhibiting Autophagy. *Gut* (2020) 69(7):1309–21. doi: 10.1136/gutjnl-2019-318830
16. Gramantieri L, Pollutri D, Gagliardi M, Giovannini C, Quarta S, Ferracin M, et al. MiR-30e-3p Influences Tumor Phenotype Through MDM2/TP53 Axis and Predicts Sorafenib Resistance in Hepatocellular Carcinoma. *Cancer Res* (2020) 80(8):1720–34. doi: 10.1158/0008-5472.CAN-19-0472
17. Ma L, Liu W, Xu A, Ji Q, Ma Y, Tai Y, et al. Activator of Thyroid and Retinoid Receptor Increases Sorafenib Resistance in Hepatocellular Carcinoma by Facilitating the Warburg Effect. *Cancer Sci* (2020) 111(6):2028–40. doi: 10.1111/cas.14412
18. Turato C, Fornari F, Pollutri D, Fassan M, Quarta S, Villano G, et al. MiR-122 Targets SerpinB3 and Is Involved in Sorafenib Resistance in Hepatocellular Carcinoma. *J Clin Med* (2019) 8(2):171. doi: 10.3390/jcm8020171
19. Cannito S, Foglia B, Villano G, Turato C, Delgado TC, Morello E, et al. Serpinb3 Differently Up-Regulates Hypoxia Inducible Factors -1α and -2α in Hepatocellular Carcinoma: Mechanisms Revealing Novel Potential Therapeutic Targets. *Cancers (Basel)* (2019) 11(12):1933. doi: 10.3390/cancers11121933
20. Zhang Z, Tan X, Luo J, Yao H, Si Z, Tong JS. The miR-30a-5p/CLCF1 Axis Regulates Sorafenib Resistance and Aerobic Glycolysis in Hepatocellular Carcinoma. *Cell Death Dis* (2020) 11(10):902. doi: 10.1038/s41419-020-03123-3
21. Chen X, Tan W, Li W, Li W, Zhu S, Zhong J, et al. miR-1226-3p Promotes Sorafenib Sensitivity of Hepatocellular Carcinoma *Via* Downregulation of DUSP4 Expression. *J Cancer* (2019) 10(12):2745–53. doi: 10.7150/jca.31804
22. Han T, Zhang Y, Yang X, Han L, Li H, Chen T, et al. Mir-552 Regulates Liver Tumor-Initiating Cell Expansion and Sorafenib Resistance. *Mol Ther Nucleic Acids* (2020) 19:1073–85. doi: 10.1016/j.omtn.2019.12.043
23. Feng Y, Jiang W, Zhao W, Lu Z, Gu Y, Dong Y. miR-124 Regulates Liver Cancer Stem Cells Expansion and Sorafenib Resistance. *Exp Cell Res* (2020) 394(2):112162. doi: 10.1016/j.yexcr.2020.112162
24. Azumi J, Tsubota T, Sakabe T, Shiota G. miR-181a Induces Sorafenib Resistance of Hepatocellular Carcinoma Cells Through Downregulation of RASSF1 Expression. *Cancer Sci* (2016) 107(9):1256–62. doi: 10.1111/cas.13006
25. Liu K, Liu S, Zhang W, Ji B, Wang Y, Liu Y. miR−222 Regulates Sorafenib Resistance and Enhance Tumorigenicity in Hepatocellular Carcinoma. *Int J Oncol* (2014) 45(4):1537–46. doi: 10.3892/ijo.2014.2577
26. Lin Z, Xia S, Liang Y, Ji L, Pan Y, Jiang S, et al. LXR Activation Potentiates Sorafenib Sensitivity in HCC by Activating microRNA-378a Transcription. *Theranostics* (2020) 10(19):8834–50. doi: 10.7150/thno.45158
27. Wang G, Zhao W, Wang H, Qiu G, Jiang Z, Wei G, et al. Exosomal MiR-744 Inhibits Proliferation and Sorafenib Chemoresistance in Hepatocellular Carcinoma by Targeting PAX2. *Med Sci Monit* (2019) 25:7209–17. doi: 10.12659/MSM.919219
28. Zhang M, Zhang H, Hong H, Zhang Z. MiR-374b Re-Sensitizes Hepatocellular Carcinoma Cells to Sorafenib Therapy by Antagonizing PKM2-Mediated Glycolysis Pathway. *Am J Cancer Res* (2019) 9(4):765–78
29. He C, Dong X, Zhai B, Jiang X, Dong D, Li B, et al. MiR-21 Mediates Sorafenib Resistance of Hepatocellular Carcinoma Cells by Inhibiting Autophagy *Via* the PTEN/Akt Pathway. *Oncotarget* (2015) 6(30):28867–81. doi: 10.18632/oncotarget.4814
30. Cao LQ, Yang XW, Chen YB, Zhang DW, Jiang XF, Xue P. Exosomal miR-21 Regulates the TETs/PTENp1/PTEN Pathway to Promote Hepatocellular Carcinoma Growth. *Mol Cancer* (2019) 18(1):148. doi: 10.1186/s12943-019-1075-2
31. Li D, Wang T, Sun FF, Feng JQ, Peng JJ, Li H, et al. MicroRNA-375 Represses Tumor Angiogenesis and Reverses Resistance to Sorafenib in Hepatocarcinoma. *Cancer Gene Ther* (2021) 28(1):126–40. doi: 10.1038/s41417-020-0191-x
32. Tang X, Yang W, Shu Z, Shen X, Zhang W, Cen C, et al. MicroRNA−223 Promotes Hepatocellular Carcinoma Cell Resistance to Sorafenib by Targeting FBW7. *Oncol Rep* (2019) 41(2):1231–7. doi: 10.3892/or.2018.6908
33. Wang W, Ding B, Lou W, Lin S. Promoter Hypomethylation and miR-145-5p Downregulation- Mediated HDAC11 Overexpression Promotes Sorafenib Resistance and Metastasis of Hepatocellular Carcinoma Cells. *Front Cell Dev Biol* (2020) 8:724. doi: 10.3389/fcell.2020.00724
34. Huang Y, Zhang J, Li H, Peng H, Gu M, Wang H. miR-96 Regulates Liver Tumor-Initiating Cells Expansion by Targeting TP53INP1 and Predicts Sorafenib Resistance. *J Cancer* (2020) 11(22):6545–55. doi: 10.7150/jca.48333
35. Liu K, Liu S, Zhang W, Jia B, Tan L, Jin Z, et al. miR-494 Promotes Cell Proliferation, Migration and Invasion, and Increased Sorafenib Resistance in Hepatocellular Carcinoma by Targeting PTEN. *Oncol Rep* (2015) 34(2):1003–10. doi: 10.3892/or.2015.4030
36. Pollutri D, Patrizi C, Marinelli S, Giovannini C, Trombetta E, Giannone FA, et al. The Epigenetically Regulated miR-494 Associates With Stem-Cell Phenotype and Induces Sorafenib Resistance in Hepatocellular Carcinoma. *Cell Death Dis* (2018) 9(1):4. doi: 10.1038/s41419-017-0076-6
37. Wang S, Cai L, Zhang F, Shang X, Xiao R, Zhou H. Inhibition of EZH2 Attenuates Sorafenib Resistance by Targeting Notch1 Activation-Dependent Liver Cancer Stem Cells *Via* NOTCH1-Related MicroRNAs in Hepatocellular Carcinoma. *Transl Oncol* (2020) 13(3):100741. doi: 10.1016/j.tranon.2020.01.002
38. Shao QP, Wei C, Yang J, Zhang WZ. miR-3609 Decelerates the Clearance of Sorafenib in Hepatocellular Carcinoma Cells by Targeting EPAS-1 and Reducing the Activation of the Pregnane X Receptor Pathway. *Onco Targets Ther* (2020) 13:7213–27. doi: 10.2147/OTT.S246471
39. Hu J, Zhang J, Sun F, Qi M, Su P, Liu H, et al. Enhancer of Zeste 2 Polycomb Repressive Complex 2 Subunit Promotes Sorafenib Resistance of

Hepatocellular Carcinoma Though Insulin-Like Growth Factor 1 Receptor. *Anticancer Drugs* (2019) 30(7):e0746. doi: 10.1097/CAD.0000000000000746
40. Mao K, Zhang J, He C, Xu K, Liu J, Sun J, et al. Restoration of miR-193b Sensitizes Hepatitis B Virus-Associated Hepatocellular Carcinoma to Sorafenib. *Cancer Lett* (2014) 352(2):245–52. doi: 10.1016/j.canlet.2014.07.004
41. Li D, Sun FF, Wang D, Wang T, Peng JJ, Feng JQ, et al. Programmed Death Ligand-1 (PD-L1) Regulated by NRF-2/MicroRNA-1 Regulatory Axis Enhances Drug Resistance and Promotes Tumorigenic Properties in Sorafenib-Resistant Hepatoma Cells. *Oncol Res* (2020) 28(5):467–81. doi: 10.3727/096504020X15925659763817
42. Lu AQ, Lv B, Qiu F, Wang XY, Cao XH. Upregulation of miR-137 Reverses Sorafenib Resistance and Cancer-Initiating Cell Phenotypes by Degrading ANT2 in Hepatocellular Carcinoma. *Oncol Rep* (2017) 37(4):2071–8. doi: 10.3892/or.2017.5498
43. Xia H, Ooi LL, Hui KM. MicroRNA-216a/217-Induced Epithelial-Mesenchymal Transition Targets PTEN and SMAD7 to Promote Drug Resistance and Recurrence of Liver Cancer. *Hepatology* (2013) 58(2):629–41. doi: 10.1002/hep.26369
44. Li W, Dong X, He C, Tan G, Li Z, Zhai B, et al. LncRNA SNHG1 Contributes to Sorafenib Resistance by Activating the Akt Pathway and Is Positively Regulated by miR-21 in Hepatocellular Carcinoma Cells. *J Exp Clin Cancer Res* (2019) 38(1):183. doi: 10.1186/s13046-019-1177-0
45. Shi Y, Yang X, Xue X, Sun D, Cai P, Song Q, et al. HANR Enhances Autophagy-Associated Sorafenib Resistance Through miR-29b/ATG9A Axis in Hepatocellular Carcinoma. *Onco Targets Ther* (2020) 13:2127–37. doi: 10.2147/OTT.S229913
46. Liu YT, Liu GQ, Huang JM. FAM225A Promotes Sorafenib Resistance in Hepatocarcinoma Cells Through Modulating miR-130a-5p-CCNG1 Interaction Network. *Biosci Rep* (2020) 40(12):BSR20202054. doi: 10.1042/BSR20202054
47. Niu Y, Tang G, Wu X, Wu C. LncRNA NEAT1 Modulates Sorafenib Resistance in Hepatocellular Carcinoma Through Regulating the miR-149-5p/AKT1 Axis. *Saudi J Gastroenterol* (2020) 26(4):194–203. doi: 10.4103/sjg.SJG_4_20
48. Shen Q, Jiang S, Wu M, Zhang L, Su X, Zhao D. LncRNA HEIH Confers Cell Sorafenib Resistance in Hepatocellular Carcinoma by Regulating miR-98-5p/PI3K/AKT Pathway. *Cancer Manag Res* (2020) 12:6585–95. doi: 10.2147/CMAR.S241383
49. Ye J, Zhang R, Du X, Chai W, Zhou Q. Long Noncoding RNA SNHG16 Induces Sorafenib Resistance in Hepatocellular Carcinoma Cells Through Sponging miR-140-5p. *Onco Targets Ther* (2019) 12:415–22. doi: 10.2147/OTT.S175176
50. Li C, Zhou D, Hong H, Yang S, Zhang L, Li S, et al. TGFβ1- miR-140-5p Axis Mediated Up-Regulation of Flap Endonuclease 1 Promotes Epithelial-Mesenchymal Transition in Hepatocellular Carcinoma. *Aging (Albany NY)* (2019) 11(15):5593–612. doi: 10.18632/aging.102140
51. Zhang J, Zhao X, Ma X, Yuan Z, Hu M. KCNQ1OT1 Contributes to Sorafenib Resistance and Programmed Death–Ligand–1–Mediated Immune Escape *Via* Sponging miR–506 in Hepatocellular Carcinoma Cells. *Int J Mol Med* (2020) 46(5):1794–804. doi: 10.3892/ijmm.2020.4710
52. Yuan P, Cao W, Zang Q, Li G, Guo X, Fan J. The HIF-2α-MALAT1-miR-216b Axis Regulates Multi-Drug Resistance of Hepatocellular Carcinoma Cells *Via* Modulating Autophagy. *Biochem Biophys Res Commun* (2016) 478 (3):1067–73. doi: 10.1016/j.bbrc.2016.08.065
53. Zhang K, Wang T, Zhou H, Feng B, Chen Y, Zhi Y, et al. A Novel Aurora-a Inhibitor (MLN8237) Synergistically Enhances the Antitumor Activity of Sorafenib in Hepatocellular Carcinoma. *Mol Ther Nucleic Acids* (2018) 13:176–88. doi: 10.1016/j.omtn.2018.08.014
54. Xu Y, Liu Y, Li Z, Li H, Li X, Yan L, et al. Long Non–Coding RNA H19 Is Involved in Sorafenib Resistance in Hepatocellular Carcinoma by Upregulating miR–675. *Oncol Rep* (2020) 44(1):165–73. doi: 10.3892/or.2020.7608
55. Sui C, Dong Z, Yang C, Zhang M, Dai B, Geng L, et al. LncRNA FOXD2-AS1 as a Competitive Endogenous RNA Against miR-150-5p Reverses Resistance to Sorafenib in Hepatocellular Carcinoma. *J Cell Mol Med* (2019) 23 (9):6024–33. doi: 10.1111/jcmm.14465
56. Luo JF, Xu J, Zheng JZ. Long Non-Coding RNA TTN-AS1 Promotes Cell Proliferation and Inhibits Cell Apoptosis in Prostatic Cancer by Sponging miR-193a-5p. *Eur Rev Med Pharmacol Sci* (2019) 23(18):7816–25. doi: 10.26355/eurrev_201909_18991
57. Li X, Zhou Y, Yang L, Ma Y, Peng X, Yang S, et al. LncRNA NEAT1 Promotes Autophagy *Via* Regulating miR-204/ATG3 and Enhanced Cell Resistance to Sorafenib in Hepatocellular Carcinoma. *J Cell Physiol* (2020) 235(4):3402–13. doi: 10.1002/jcp.29230
58. Chen S, Xia X. Long Noncoding RNA NEAT1 Suppresses Sorafenib Sensitivity of Hepatocellular Carcinoma Cells Via Regulating miR-335-C-Met. *J Cell Physiol* (2019) 234:14999–5009. doi: 10.1002/jcp.27567
59. Chen BW, Zhou Y, Wei T, Wen L, Zhang YB, Shen SC, et al. lncRNA-POIR Promotes Epithelial-Mesenchymal Transition and Suppresses Sorafenib Sensitivity Simultaneously in Hepatocellular Carcinoma by Sponging miR-182-5p. *J Cell Biochem* (2021) 122(1):130–42. doi: 10.1002/jcb.29844
60. Jin W, Chen L, Cai X, Zhang Y, Zhang J, Ma D, et al. Long Non-Coding RNA TUC338 Is Functionally Involved in Sorafenib-Sensitized Hepatocarcinoma Cells by Targeting RASAL1. *Oncol Rep* (2017) 37(1):273–80. doi: 10.3892/or.2016.5248
61. Meng F, Zhang W, Wang Y. RASAL1 Inhibits HepG2 Cell Growth *Via* HIF-2α Mediated Gluconeogenesis. *Oncol Lett* (2017) 14(6):7344–52. doi: 10.3892/ol.2017.7123
62. Takahashi K, Yan IK, Wood J, Haga H, Patel T. Involvement of Extracellular Vesicle Long Noncoding RNA (linc-VLDLR) in Tumor Cell Responses to Chemotherapy. *Mol Cancer Res* (2014) 12(10):1377–87. doi: 10.1158/1541-7786.MCR-13-0636
63. De Mattia E, Cecchin E, Guardascione M, Foltran L, Di Raimo T, Angelini F, et al. Pharmacogenetics of the Systemic Treatment in Advanced Hepatocellular Carcinoma. *World J Gastroenterol* (2019) 25(29):3870–96. doi: 10.3748/wjg.v25.i29.3870
64. Sigismund S, Avanzato D, Lanzetti L. Emerging Functions of the EGFR in Cancer. *Mol Oncol* (2018) 12(1):3–20. doi: 10.1002/1878-0261.12155
65. Hagiwara S, Kudo M, Nagai T, Inoue T, Ueshima K, Nishida N, et al. Activation of JNK and High Expression Level of CD133 Predict a Poor Response to Sorafenib in Hepatocellular Carcinoma. *Br J Cancer* (2012) 106 (12):1997–2003. doi: 10.1038/bjc.2012.145
66. Dai J, Huang Q, Niu K, Wang B, Li Y, Dai C, et al. Sestrin 2 Confers Primary Resistance to Sorafenib by Simultaneously Activating AKT and AMPK in Hepatocellular Carcinoma. *Cancer Med* (2018) 7(11):5691–703. doi: 10.1002/cam4.1826
67. Dai J, Niu K, Wang B, Li Y, Xia C, Tao K, et al. Sestrin 2(SESN2) Promotes Primary Resistance to Sorafenib by Activating AKT in Hepatocellular Carcinoma Cells. *Xi Bao Yu Fen Zi Mian Yi Xue Za Zhi* (2018) 34(5):427–33.
68. Llovet JM. Focal Gains of VEGFA: Candidate Predictors of Sorafenib Response in Hepatocellular Carcinoma. *Cancer Cell* (2014) 25(5):560–2. doi: 10.1016/j.ccr.2014.04.019
69. Cabral LKD, Tiribelli C, Sukowati CHC. Sorafenib Resistance in Hepatocellular Carcinoma: The Relevance of Genetic Heterogeneity. *Cancers (Basel)* (2020) 12(6):1576. doi: 10.3390/cancers12061576
70. Schaeffeler E, Hellerbrand C, Nies AT, Winter S, Kruck S, Hofmann U, et al. DNA Methylation Is Associated With Downregulation of the Organic Cation Transporter OCT1 (SLC22A1) in Human Hepatocellular Carcinoma. *Genome Med* (2011) 3(12):82. doi: 10.1186/gm298
71. Seitz T, Stalmann R, Dalila N, Chen J, Pojar S, Dos Santos Pereira JN, et al. Global Genetic Analyses Reveal Strong Inter-Ethnic Variability in the Loss of Activity of the Organic Cation Transporter OCT1. *Genome Med* (2015) 7 (1):56. doi: 10.1186/s13073-015-0172-0
72. Amawi H, Sim HM, Tiwari AK, Ambudkar SV, Shukla S. ABC Transporter-Mediated Multidrug-Resistant Cancer. *Adv Exp Med Biol* (2019) 1141:549–80. doi: 10.1007/978-981-13-7647-4_12
73. Cascorbi I. Role of Pharmacogenetics of ATP-Binding Cassette Transporters in the Pharmacokinetics of Drugs. *Pharmacol Ther* (2006) 112(2):457–73. doi: 10.1016/j.pharmthera.2006.04.009
74. Tang W, Chen Z, Zhang W, Cheng Y, Zhang B, Wu F, et al. The Mechanisms of Sorafenib Resistance in Hepatocellular Carcinoma: Theoretical Basis and Therapeutic Aspects. *Signal Transduct Target Ther* (2020) 5(1):87. doi: 10.1038/s41392-020-0187-x
75. Sun T, Liu H, Ming L. Multiple Roles of Autophagy in the Sorafenib Resistance of Hepatocellular Carcinoma. *Cell Physiol Biochem* (2017) 44 (2):716–27. doi: 10.1159/000485285

76. Xiang QF, Zhan MX, Li Y, Liang H, Hu C, Huang YM, et al. Activation of MET Promotes Resistance to Sorafenib in Hepatocellular Carcinoma Cells *Via* the AKT/ERK1/2-EGR1 Pathway. *Artif Cells Nanomed Biotechnol* (2019) 47(1):83–9. doi: 10.1080/21691401.2018.1543195
77. Méndez-Blanco C, Fondevila F, García-Palomo A, González-Gallego J, Mauriz JL. Sorafenib Resistance in Hepatocarcinoma: Role of Hypoxia-Inducible Factors. *Exp Mol Med* (2018) 50(10):1–9. doi: 10.1038/s12276-018-0159-1
78. Sun X, Niu X, Chen R, He W, Chen D, Kang R, et al. Metallothionein-1G Facilitates Sorafenib Resistance Through Inhibition of Ferroptosis. *Hepatology* (2016) 64(2):488–500. doi: 10.1002/hep.28574
79. Shibue T, Weinberg RA. EMT, CSCs, and Drug Resistance: The Mechanistic Link and Clinical Implications. *Nat Rev Clin Oncol* (2017) 14(10):611–29. doi: 10.1038/nrclinonc.2017.44
80. Lai HH, Li CW, Hong CC, Sun HY, Chiu CF, Ou DL, et al. TARBP2-Mediated Destabilization of Nanog Overcomes Sorafenib Resistance in Hepatocellular Carcinoma. *Mol Oncol* (2019) 13(4):928–45. doi: 10.1002/1878-0261.12449
81. Wu CX, Wang XQ, Chok SH, Man K, Tsang SHY, Chan ACY, et al. Blocking CDK1/PDK1/β-Catenin Signaling by CDK1 Inhibitor RO3306 Increased the Efficacy of Sorafenib Treatment by Targeting Cancer Stem Cells in a Preclinical Model of Hepatocellular Carcinoma. *Theranostics* (2018) 8 (14):3737–50. doi: 10.7150/thno.25487
82. Li YJ, Lei YH, Yao N, Wang CR, Hu N, Ye WC, et al. Autophagy and Multidrug Resistance in Cancer. *Chin J Cancer* (2017) 36(1):52. doi: 10.1186/s40880-017-0219-2
83. Heqing Y, Bin L, Xuemei Y, Linfa L. The Role and Mechanism of Autophagy in Sorafenib Targeted Cancer Therapy. *Crit Rev Oncol Hematol* (2016) 100:137–40. doi: 10.1016/j.critrevonc.2016.02.006
84. Luo T, Fu J, Xu A, Su B, Ren Y, Li N, et al. PSMD10/Gankyrin Induces Autophagy to Promote Tumor Progression Through Cytoplasmic Interaction With ATG7 and Nuclear Transactivation of ATG7 Expression. *Autophagy* (2016) 12(8):1355–71. doi: 10.1080/15548627.2015.1034405
85. Lin Z, Niu Y, Wan A, Chen D, Liang H, Chen X, et al. RNA m(6) A Methylation Regulates Sorafenib Resistance in Liver Cancer Through FOXO3-Mediated Autophagy. *EMBO J* (2020) 39(12):e103181. doi: 10.15252/embj.2019103181
86. Du B, Shim JS. Targeting Epithelial-Mesenchymal Transition (EMT) to Overcome Drug Resistance in Cancer. *Molecules* (2016) 21(7):965. doi: 10.3390/molecules21070965
87. Wang H, Xu H, Ma F, Zhan M, Yang X, Hua S, et al. Zinc Finger Protein 703 Induces EMT and Sorafenib Resistance in Hepatocellular Carcinoma by Transactivating CLDN4 Expression. *Cell Death Dis* (2020) 11(4):225. doi: 10.1038/s41419-020-2422-3
88. Zhang K, Chen J, Zhou H, Chen Y, Zhi Y, Zhang B, et al. PU.1/microRNA-142-3p Targets ATG5/ATG16L1 to Inactivate Autophagy and Sensitize Hepatocellular Carcinoma Cells to Sorafenib. *Cell Death Dis* (2018) 9 (3):312. doi: 10.1038/s41419-018-0344-0
89. Costantini S, Di Bernardo G, Cammarota M, Castello G, Colonna G. Gene Expression Signature of Human HepG2 Cell Line. *Gene* (2013) 518(2):335–45. doi: 10.1016/j.gene.2012.12.106
90. Klingenberg M, Matsuda A, Diederichs S, Patel T. Non-Coding RNA in Hepatocellular Carcinoma: Mechanisms, Biomarkers and Therapeutic Targets. *J Hepatol* (2017) 67(3):603–18. doi: 10.1016/j.jhep.2017.04.009
91. Yuan L, Xu ZY, Ruan SM, Mo S, Qin JJ, Cheng XD. Long Non-Coding RNAs Towards Precision Medicine in Gastric Cancer: Early Diagnosis, Treatment, and Drug Resistance. *Mol Cancer* (2020) 19(1):96. doi: 10.1186/s12943-020-01219-0
92. Zhang M, Wang W, Li T, Yu X, Zhu Y, Ding F, et al. Long Noncoding RNA SNHG1 Predicts a Poor Prognosis and Promotes Hepatocellular Carcinoma Tumorigenesis. *BioMed Pharmacother* (2016) 80:73–9. doi: 10.1016/j.biopha.2016.02.036
93. Zheng QX, Wang J, Gu XY, Huang CH, Chen C, Hong M, et al. TTN-AS1 as a Potential Diagnostic and Prognostic Biomarker for Multiple Cancers. *BioMed Pharmacother* (2021) 135:111169. doi: 10.1016/j.biopha.2020.111169
94. Du WW, Zhang C, Yang W, Yong T, Awan FM, Yang BB. Identifying and Characterizing circRNA-Protein Interaction. *Theranostics* (2017) 7 (17):4183–91. doi: 10.7150/thno.21299
95. Wang M, Yu F, Chen X, Li P, Wang K. The Underlying Mechanisms of Noncoding RNAs in the Chemoresistance of Hepatocellular Carcinoma. *Mol Ther Nucleic Acids* (2020) 21:13–27. doi: 10.1016/j.omtn.2020.05.011
96. Xu J, Ji L, Liang Y, Wan Z, Zheng W, Song X, et al. CircRNA-SORE Mediates Sorafenib Resistance in Hepatocellular Carcinoma by Stabilizing YBX1. *Signal Transduct Target Ther* (2020) 5(1):298. doi: 10.1038/s41392-020-00375-5
97. Wei L, Wang X, Lv L, Liu J, Xing H, Song Y, et al. The Emerging Role of microRNAs and Long Noncoding RNAs in Drug Resistance of Hepatocellular Carcinoma. *Mol Cancer* (2019) 18(1):147. doi: 10.1186/s12943-019-1086-z
98. Cai H, Yang Y, Peng F, Liu Y, Fu X, Ji B. Gold Nanoparticles-Loaded anti-miR221 Enhances Antitumor Effect of Sorafenib in Hepatocellular Carcinoma Cells. *Int J Med Sci* (2019) 16(12):1541–8. doi: 10.7150/ijms.37427
99. Zhao P, Li M, Wang Y, Chen Y, He C, Zhang X, et al. Enhancing Anti-Tumor Efficiency in Hepatocellular Carcinoma Through the Autophagy Inhibition by miR-375/sorafenib in Lipid-Coated Calcium Carbonate Nanoparticles. *Acta Biomater* (2018) 72:248–55. doi: 10.1016/j.actbio.2018.03.022
100. Lin Y, Lin L, Jin Y, Wang D, Tan Y, Zheng C. Combination of Matrine and Sorafenib Decreases the Aggressive Phenotypes of Hepatocellular Carcinoma Cells. *Chemotherapy* (2014) 60(2):112–8. doi: 10.1159/000371736
101. Meng H, Mai WX, Zhang H, Xue M, Xia T, Lin S, et al. Codelivery of an Optimal Drug/siRNA Combination Using Mesoporous Silica Nanoparticles to Overcome Drug Resistance in Breast Cancer *In Vitro* and *In Vivo*. *ACS Nano* (2013) 7(2):994–1005. doi: 10.1021/nn3044066

Conflict of Interest: The authors declare that the research was conducted in the absence of any commercial or financial relationships that could be construed as a potential conflict of interest.

frontiers in Pharmacology

ORIGINAL RESEARCH
published: 22 December 2021
doi: 10.3389/fphar.2021.805499

Elevated N-Glycosylation Contributes to the Cisplatin Resistance of Non-Small Cell Lung Cancer Cells Revealed by Membrane Proteomic and Glycoproteomic Analysis

Wenjuan Zeng[1], Shanshan Zheng[1], Yonghong Mao[2], Shisheng Wang[1], Yi Zhong[1], Wei Cao[1], Tao Su[1], Meng Gong[1], Jingqiu Cheng[1], Yong Zhang[1,3] and Hao Yang[1,3]**

[1]NHC Key Laboratory of Transplant Engineering and Immunology, Institutes for Systems Genetics, National Clinical Research Center for Geriatrics, West China Hospital, Sichuan University, Chengdu, China, [2]Institute of Thoracic Oncology, West China Hospital, Sichuan University, Chengdu, China, [3]Sichuan Provincial Engineering Laboratory of Pathology in Clinical Application, West China Hospital, Sichuan University, Chengdu, China

OPEN ACCESS

Edited by:
Simona Rapposelli,
University of Pisa, Italy

Reviewed by:
Sumio Ohtsuki,
Kumamoto University, Japan
Mayank Saraswat,
Mayo Clinic, United States

***Correspondence:**
Hao Yang
yanghao@scu.edu.cn
Yong Zhang
nankai1989@foxmail.com

Specialty section:
This article was submitted to Pharmacology of Anti-Cancer Drugs, a section of the journal Frontiers in Pharmacology

Received: 30 October 2021
Accepted: 06 December 2021
Published: 22 December 2021

Citation:
Zeng W, Zheng S, Mao Y, Wang S, Zhong Y, Cao W, Su T, Gong M, Cheng J, Zhang Y and Yang H (2021) Elevated N-Glycosylation Contributes to the Cisplatin Resistance of Non-Small Cell Lung Cancer Cells Revealed by Membrane Proteomic and Glycoproteomic Analysis. Front. Pharmacol. 12:805499. doi: 10.3389/fphar.2021.805499

Chemoresistance is the major restriction on the clinical use of cisplatin. Aberrant changes in protein glycosylation are closely associated with drug resistance. Comprehensive study on the role of protein glycosylation in the development of cisplatin resistance would contribute to precise elucidation of the complicated mechanism of resistance. However, comprehensive characterization of glycosylated proteins remains a big challenge. In this work, we integrated proteomic and N-glycoproteomic workflow to comprehensively characterize the cisplatin resistance-related membrane proteins. Using this method, we found that proteins implicated in cell adhesion, migration, response to drug, and signal transduction were significantly altered in both protein abundance and glycosylation level during the development of cisplatin resistance in the non-small cell lung cancer cell line. Accordingly, the ability of cell migration and invasion was markedly increased in cisplatin-resistant cells, hence intensifying their malignancy. In contrast, the intracellular cisplatin accumulation was significantly reduced in the resistant cells concomitant with the down-regulation of drug uptake channel protein, LRRC8A, and over-expression of drug efflux pump proteins, MRP1 and MRP4. Moreover, the global glycosylation was elevated in the cisplatin-resistant cells. Consequently, inhibition of N-glycosylation reduced cell resistance to cisplatin, whereas promoting the high-mannose or sialylated type of glycosylation enhanced the resistance, suggesting that critical glycosylation type contributes to cisplatin resistance. These results demonstrate the high efficiency of the integrated proteomic and N-glycoproteomic workflow in discovering drug resistance-related targets, and provide new insights into the mechanism of cisplatin resistance.

Keywords: cisplatin resistance, membrane proteins, N-glycosylation, proteomics, N-glycoproteomics

INTRODUCTION

Cisplatin, a representative anticancer drug, is one of the most widely used chemotherapeutic agents for the clinical treatment of various solid tumors including ovarian, testicular, colorectal, bladder and non-small cell lung cancers (Dilruba and Kalayda, 2016; Rottenberg et al., 2021). Unfortunately, despite the initial effectiveness, the clinical use of cisplatin is dramatically restricted by the development of chemoresistance of cancer cells. The underlying mechanisms of cisplatin resistance are multifactorial and complicated. It has been demonstrated that many pathways are involved in the development of cisplatin resistance, including reduced cellular drug accumulation (Kuo et al., 2012), increased drug detoxification (De Luca et al., 2019), enhanced DNA repair and defective apoptosis signal transduction (Michaud et al., 2009; Ray Chaudhuri et al., 2016). However, these mechanisms are still insufficient to account for the complicated chemoresistance due to the heterogeneous nature of tumor cells and the complexity of cellular responses to cisplatin.

Cell membrane holds multiple membrane carrier proteins (e.g., solute carrier family 22 A1/2/3/4/5, copper transporter 1, volume-regulated anion channels, ATP-binding cassette superfamily), which control the cisplatin uptake and efflux, thereby determining the intracellular drug concentration (Ishida et al., 2002; Wen et al., 2014; Harrach and Ciarimboli, 2015; Planells-Cases et al., 2015; Jia et al., 2021). Importantly, most of these membrane proteins undergo post-translational modifications, particularly with various glycans (Maryon et al., 2007; Voss et al., 2014). Aberrant changes in glycosylation will cause dysfunction of the glycoproteins, consequently giving rise to numerous pathophysiological events, especially those associated with cancer cell growth, invasion, and metastasis (Lau and Dennis, 2008; Christiansen et al., 2014; Zhang et al., 2014). Intriguingly, some recent studies have revealed a correlation between protein glycosylation and chemoresistance, including multidrug resistance in gastric cancer cells, Adriamycin resistance in leukemia cells, and cisplatin resistance in ovarian cancer cells (Li et al., 2013; Sun et al., 2014; Ji et al., 2017; Lin et al., 2020). N-glycans with α2,3-linked sialic structures have been found remarkably higher in cisplatin-resistant ovarian cancer cells and may act as biomarkers to monitor the dynamic process of the acquisition of platinum resistance (Lin et al., 2020). Although protein glycosylation has been expected to provide additional targets for current cancer theranostics (Ferreira et al., 2016; Mereiter et al., 2019; Costa et al., 2020), accurately decoding the site-specific glycosylation profile of the drug resistance-related proteome remains a big challenge (Kolli et al., 2015; Ruhaak et al., 2018), which largely impedes the progress of cancer drug discovery in this field.

Generally, glycoproteomics studies involve the analysis of glycoproteins and site-specific glycans, including the identification of protein, glycopeptide and glycosite, as well as the characterization of site-specific glycan composition and structure (Shah et al., 2015; Gao et al., 2019; Zhang et al., 2020). However, in these previous studies, glycoproteins and glycans were investigated separately. Namely, glycans were released from glycopeptides using N-glycosidase, and either the obtained glycans or deglycopeptides were subjected to mass spectrometry (MS) analysis. Hence, comprehensive information on the role of both glycoproteins and site-specific glycans in chemoresistance remains unavailable. Accordingly, there is still a lack of characterization of cisplatin resistance-associated membrane proteins in both expression and glycosylation profile.

In this work, we integrated a workflow based on high-resolution MS to simultaneously identify glycoprotein, glycopeptide, glycosite, and glycan composition/structure in a single run. Employing this workflow, we analyzed the membrane proteins associated with cisplatin resistance in non-small cell lung

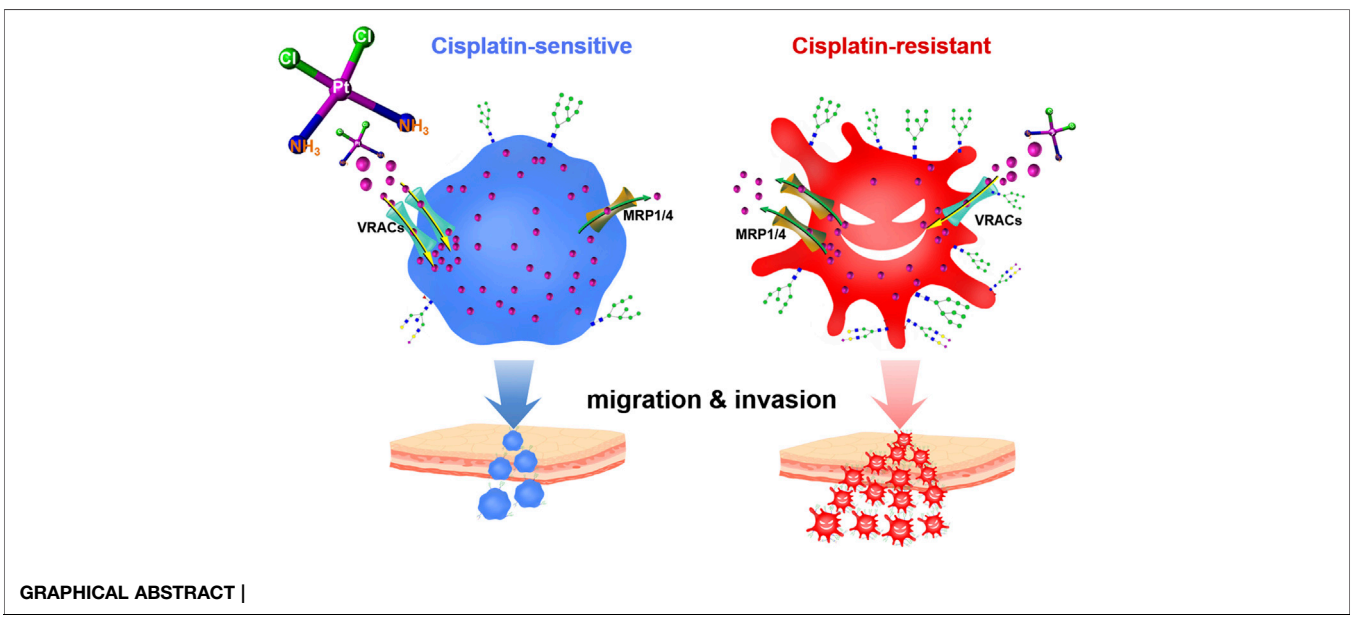

GRAPHICAL ABSTRACT |

cancer cells. We found that critical membrane proteins were altered in abundance and glycosylation during the development of cisplatin resistance, which was related to cell migration, invasion, and cisplatin accumulation. Our results demonstrated that elevated high-mannose or sialylated type of glycosylation attenuated the sensitivity of non-small cell lung cancer cells to cisplatin and contributed to the resistant phenotype. These findings provide new insights into the mechanisms underlying cisplatin resistance.

MATERIALS AND METHODS

Materials and Chemicals

Cisplatin, dithiothreitol (DTT), iodoacetamide (IAA), formic acid (FA), trifluoroacetic acid (TFA), concanavalin A (Con A) and horseradish peroxidase (HRP) were obtained from Sigma (St. Louis, MO, United States). Acetonitrile (ACN) was purchased from Merck (Darmstadt, Germany). Sequencing-grade trypsin was obtained from Enzyme and Spectrum (Beijing, China). Minute™ Plasma Membrane Protein Isolation and Cell Fractionation Kit (SM-005) was obtained from Invent Biotechnologies (Eden Prairie, MN, United States). The rabbit monoclonal anti-human Na/K ATPase antibody (ab76020), anti-human Lamin-B1 antibody (ab133741), anti-human Tomm20 antibody (ab186735), anti-human α-1,2-mannosidase IA (MAN1A1) antibody (ab140613), anti-human sialidase-1 (Neu1) antibody (ab197020), anti-human leucine-rich repeat-containing 8A (LRRC8A) antibody (ab157489), and anti-human multidrug resistance-associated protein 1 (MRP1) antibody (ab180960) were purchased from Abcam (Cambridge, MA, United States). Rabbit monoclonal anti-human β-actin antibody (AC026) was purchased from Abclonal (Wuhan, China), and goat anti-rabbit horseradish peroxidase-conjugated secondary antibody (511,203) was purchased from Zen Bioscience (Chengdu, China). The glycosylation inhibitors, Tunicamycin and Kifunensine, were obtained from Abcam (Cambridge, MA, United States), Oseltamivir phosphate from SelleckChem (Houston, TX, United States), and Castanospermine from MedChemExpress (United States). Zwitterionic hydrophilic interaction liquid chromatography (Zic-HILIC) materials were obtained from Fresh Bioscience (Shanghai, China). Deionized water was prepared using a Milli-Q system (Millipore, Bedford, MA, United States). All other chemicals and reagents of the best available grade were purchased from Sigma-Aldrich or Thermo Fisher Scientific.

Cell Culture and Drug Treatment

Human non-small cell lung cancer cell line, A549, and its cisplatin-resistant counterpart, A549/DDP, were obtained from KeyGen Biotech (Nanjing, China) with the authentication by short tandem repeat (STR) detection. The cisplatin-resistance of A549/DDP cells was acquired by continuously exposing A549 cells to cisplatin of progressive concentrations until the final concentration reached 1.0 μg/ml. A549 cells were cultured in RPMI-1640 (Gibco) supplemented with 10% fetal bovine serum (FBS, Gibco) and 100 U/ml penicillin-streptomycin (Hyclone). The same medium with 1.0 μg/ml cisplatin was used to culture A549/DDP cells. However, to avoid the influence of cisplatin, A549/DDP cells were cultured in a drug-free medium for 3 days prior to subsequent experimentation. All cells were grown at 5% CO_2 in a humidified incubator at 37°C. Cisplatin was dissolved in phosphate buffered saline (PBS) to prepare a 1.0 mM stock solution and further diluted with culture medium to desired concentration.

Cell Fractionation, Protein Extraction, and Protein Characterization

A549 and A549/DDP cells were washed and harvested using a cell scraper when reaching 80% confluence, followed by wash and centrifugation with PBS for three times. Cells were fractionated into four parts, the cell membrane (CM), organelle (CO), nucleus (CN), and cytosol (CC) using the Minute™ Plasma Membrane Protein Isolation and Cell Fractionation Kit following the manufacturer's instructions. Intact cells and the obtained CM, CO and CN fractions were lysed using UA buffer (8 M urea, 0.1 M Tris, pH 8.5) with sonication at 4°C for protein extraction. The protein concentration was determined using bicinchoninic acid assay (BCA) kit (Thermo Fisher Scientific, United States). Proteins from the CM, CO, CN, and CC fraction, along with the whole cell lysate (WP) were boiled with gel-loading buffer, and then loaded onto a 4–20% gradient gel (Genscript, Nanjing, China) for sodium dodecyl sulfate polyacrylamide gel electrophoresis (SDS-PAGE). The gel was stained with Coomassie brilliant blue for 10 min, washed with water overnight, and imaged. For Western blot (WB) analysis, the separated proteins were transferred to a polyvinylidene fluoride (PVDF) membrane (Millipore, United States). The membrane was blocked in 5% skimmed milk in Tris-buffered saline (TBS) with 0.1% Tween20 (TBST) at room temperature for 1 h, and then incubated with primary antibodies of human Na/K ATPase, Lamin-B1, Tomm20, and β-actin in appropriate dilutions at 4°C overnight. The blots were washed four times with TBST for 5 min each and incubated with HRP-conjugated secondary antibody at room temperature for 1 h. After being washed with TBST, the protein bands were visualized by enhanced chemiluminescence (ECL, Thermo Fisher Scientific, United States) and imaged using an image analyzer (Tanon 4600SF, China).

Sample Preparation for MS Analysis

Cell membrane proteins were prepared in three biological replicates for each cell line from the cell culture step. The membrane proteins were prepared for MS analysis using a modified filter-aided sample preparation (FASP) protocol. In brief, 100 μg of proteins were loaded onto a 30-kDa filter and centrifuged at 13,000 g for 15 min. After being reduced by DTT (20 mM) for 4 h at 37°C and alkylated with IAA (50 mM) for 30 min at 25°C in the dark, the protein mixture was washed once with 200 μl UA buffer and three times with 200 μl of 50 mM ammonium bicarbonate by centrifugation at 13,000 g for 15 min at room temperature. Then 200 μl of 50 mM ammonium bicarbonate containing 2.0 μg trypsin was added to each filter

and incubated for 16 h at 37°C. Finally, the filter tubes were washed three times with 100 µl water by centrifugation at 13,000 g for 10 min. The concentration of these collected peptides was determined using a peptide assay kit (Thermo Fisher Scientific, United States) based on the absorbance measured at 480 nm. The peptide mixtures were freeze-dried and then stored at −80°C.

Enrichment of Intact N-Glycopeptides

Intact N-glycopeptides were enriched by the Zic-HILIC method. Specifically, the peptide mixtures were re-dissolved in 100 µl equilibration buffer (80% ACN/0.2% TFA), and 2 mg processed Zic-HILIC materials were added and rotated for 2 h at 37°C. Finally, the mixture was transferred to a 200-µl pipette tip packed with a C8 membrane and washed twice with 70 µl equilibration buffer. Intact N-glycopeptides were then eluted three times with 70 µl elution buffer (0.1% TFA in water) and were freeze-dried for further analysis.

LC-MS/MS Analysis

All samples were analyzed by LC-MS/MS in the data-dependent acquisition mode using an Orbitrap FusionLumos mass spectrometer (Thermo Fisher Scientific). In brief, peptides and intact N-glycopeptides of membrane proteins were dissolved in water with 0.1% FA and separated on a column (ReproSil-Pur C18-AQ, 1.9, 75 µm inner diameter, length 20 cm; Dr Maisch) over a 78-min gradient (solvent A, 0.1% FA in water; solvent B, 0.1% FA in 80% ACN) at a flow rate of 300 nl/min (0–8 min, 5–8% B; 8–58 min, 8–22% B; 58–70 min, 22–32% B; 70–71 min, 32–90% B; and 71–78 min, 90% B).

MS parameters for the detection of peptides were as follows. 1) MS1: orbitrap resolution = 120,000; scan range (m/z) = 350–1,550; RF lens = 30%; AGC target = $1.0\,e^6$; maximum injection time = 50 ms; included charge state = 2–6; exclusion duration = 15 s; exclusion after n times, n = 1; each selected precursor ion was subjected to one high-energy collision dissociation MS/MS (HCD-MS/MS); 2) MS2: isolation window (m/z) = 2.0; HCD collision energy = 35%; detector type = orbitrap; orbitrap resolution = 15,000; first mass (m/z) = 120; AGC target = $5.0\,e^4$; maximum injection time = 80 ms.

MS parameters for the detection of intact N-glycopeptides were as follows. 1) MS1: orbitrap resolution = 120,000; scan range (m/z) = 800–2000; RF lens = 30%; AGC target = $2.0\,e^5$; maximum injection time = 100 ms; included charge state = 2–6; exclusion duration = 15 s; exclusion after n times, n = 1; each selected precursor ion was subjected to one stepped collision energy high-energy collision dissociation MS/MS (SCE-HCD-MS/MS); 2) MS2: isolation window (m/z) = 2.0; detector type = orbitrap; orbitrap resolution = 15,000; first mass (m/z) = 120; AGC target = $5.0\,e^5$; maximum injection time = 250 ms; HCD collision energy = 30%; stepped collision energy mode on, energy difference of ± 10% (20–30–40%).

Data Processing

For the identification and quantification of cell membrane protein, the raw peptide data files were searched against the human uniprot database (v. 2020_08; 20,368 entries) with MaxQuant (v. 1.5.3.8; Max Planck Gesellschaft, Munich, Germany). Label-free quantification (LFQ) analysis of the proteins was performed. Two missed cleavage sites were allowed for trypsin digestion. Cysteine carbamidomethylation (+57.02 Da) was set as the fixed modification. Oxidation of methionine (+15.99 Da), deamidation of asparagine (+0.98 Da), and acetylation of the protein N-terminal (+42.01 Da) were set as variable modifications. Match between runs was used for the alignment of retention time across the six individual LC-MS/MS runs. The false discovery rates (FDR) of the peptide spectrum matches (PSMs) and proteins were set to <1%.

For the identification of the intact N-glycopeptides, the raw data files were searched using Byonic software (version 3.6.1, Protein Metrics, Inc.), with the mass tolerance for precursors and fragment ions set at ± 6 ppm and ±20 ppm, respectively. Two missed cleavage sites were allowed for trypsin digestion. The fixed modification was carbamidomethyl (C), and variable modifications included oxidation (M), acetylation (protein N-term), and deamidation (N). In addition, 182 human N-glycans were specified as N-glycan modifications. All other parameters were set as the default values, and the protein groups were filtered to a 1% FDR based on the number of hits obtained for searches against these databases. Stricter quality control methods for intact N-glycopeptide identification were implemented, requiring a score of no less than 300 and identification of at least six amino acids. Furthermore, all of these PSMs and glycopeptide-spectrum matches (GPSMs) were examined manually and filtered using the following criteria: PSMs were accepted if there were at least 3 b/y ions identified in the peptide backbone, and GPSMs were accepted if there were at least three glycan oxonium ions identified and at least three 3 b/y ions identified in the peptide backbone.

Bioinformatics Analysis

We performed the bioinformatics analysis using an R language-based in-house freely available platform called "Wu Kong" (https://wkomics.omicsolution.com/wkomics/main/) (Wang et al., 2020). For quantitative analysis of the proteomics data, the LFQ intensities of cell membrane proteins from A549 and A549/DDP cells were extracted from the MaxQuant result file to represent the expression level of corresponding protein in six samples. Proteins with the number of missing LFQ intensity accounting for 50% or more across all samples were filtered, after which the intensity was normalized to the median and then the missing value was filled using k-nearest neighbors (KNN) imputation. To get precise quantitation results, proteins with a coefficient of variation of the intensities larger than 0.3 were filtered. After filtering, a 1,360 × 6 protein expression matrix was generated for subsequent statistical analysis. Unpaired Student's t-test was performed to screen the differentially expressed proteins (DEPs) between A549 cell membrane (ACM) and A549/DDP cells membrane (DCM) with a Benjamini-Hochberg (BH) adjusted p value <0.05 and a fold change >2.00. Biological function of the DEPs was analyzed through Gene Ontology (GO) enrichment analysis and Kyoto Encyclopedia of Genes and Genomes (KEGG) pathway enrichment analysis using the "Wu Kong" platform. For quantitative analysis of the intact

N-glycopeptides, the intensities of intact N-glycopeptides were extracted from the Byonic result files to represent the abundance of corresponding intact N-glycopeptides in the six samples. Glycopeptides having more than 50% missing data were excluded. The intensity was normalized to the median and then the missing values were filled using KNN imputation. Moreover, glycopeptides with a coefficient of variation of the intensities larger than 0.5 were filtered. Unpaired Student's *t*-test was performed to screen the differentially expressed glycopeptides (DEGs) between ACM and DCM groups with a BH adjusted p value <0.05 and a fold change >2.00. In particular, we reserved the intact N-glycopeptides that were identified in all the three biological replicates within one group while completely missing in all replicates of the other.

WB Analysis and Glycoprotein Detection

Proteins extracted from ACM and DCM, or the whole cell lysate of A549 and A549/DDP were transferred to PVDF membrane after SDS-PAGE separation. For the detection of high-mannose glycosylated protein, the membrane was blocked with TBST at room temperature for 1 h, followed by the incubation with 25 μg/ml Con A in TBST containing 1 mM $CaCl_2$ and 1 mM $MnCl_2$ (TBSTS) at 4°C overnight. The blots were washed four times with TBSTS for 5 min each, and then incubated with 0.5 μg/ml HRP at room temperature for 1 h. After being washed with TBSTS, the protein bands were visualized by ECL and imaged using an image analyzer (Tanon 4600SF, China). For the detection of MAN1A1, Neu1, LRRC8A and MRP1 proteins, the PVDF membrane was blocked with 5% skimmed milk in TBST at room temperature for 1 h, followed by the incubation with corresponding primary antibodies in appropriate dilutions at 4°C overnight. The blots were washed with TBST and incubated with HRP-conjugated secondary antibody at room temperature for 1 h. The protein bands were also visualized by ECL and imaged by the image analyzer. Na/K ATPase was used as the internal standard for the detection of cell membrane proteins LRRC8A, MRP1 and the global high-mannose glycosylated membrane proteins. In particular, for the detection of MRP1, the samples were not boiled before loading onto the SDS-PAGE gel to reduce protein aggregation. β-actin was used as the internal standard for the detection of MAN1A1 and Neu1 from the whole cell lysates.

Inductively Coupled Plasma Mass Spectrometry (ICP-MS) Detection

A549 and A549/DDP cells with a density of 1×10^6 were cultured for 24 h, and then treated with 30 μM cisplatin for 24 h. After rinsing with PBS twice, the cells were collected, further washed three times with PBS, and counted. Subsequently, the cells were lysed with 250 μl of 4% SDS via repeated freeze-thaw cycles in liquid nitrogen followed by sonication. Then, the cell lysate was diluted to 1 ml with water, filtered through a 0.22 μm filter, and injected into the ICP mass spectrometer (7,700, Agilent, United States) to determine the concentration of platinum (Pt). A standard curve was generated using a certified platinum standard solution. The amount of Pt in cells was calculated from the standard curve and reported in nanogram per million cells (Pt ng/10E6 cells). All samples were prepared and detected in quadruplicate to obtain the average and standard deviation (SD).

Methyl Thiazolyl Tetrazolium (MTT) Assay

Cytotoxicity of cisplatin alone or the co-administration of cisplatin and glycosylation inhibitors was evaluated in A549 and A549/DDP cells using MTT assay. Cells (5×10^3) were seeded in a 96-well plate and incubated at 37°C overnight. For the individual administration of cisplatin or the glycosylation inhibitor (Tunicamycin, Kifunensine, Castanospermine or Oseltamivir phosphate), 200 μl of culture medium with different concentrations of cisplatin (1–100 μM) or glycosylation inhibitor (2–200 μM) were added to each well followed by incubation for 48 h. For the co-administration of cisplatin and glycosylation inhibitor, 200 μl of medium with inhibitor and different concentrations of cisplatin were added to each well and incubated for 48 h. The medium was removed, and 100 μl of 0.5 mg/ml solution of MTT in RPMI-1640 medium were added to each well and incubated for another 3.5 h. Then, the medium was fully aspirated, and 150 μl DMSO were added to dissolve the purple formazan. Absorbance at 562 nm was determined, and cell viability or death was calculated.

Transwell Migration and Invasion Assays

Cell migration assay was conducted using a 24-well Transwell chamber with a polycarbonate membrane filter of 8 μm pore size (Corning). A549 or A549/DDP cells (5×10^5) suspended in 200 μl serum-free RPMI-1640 media were seeded in the upper compartment of the chamber, and 500 μl RPMI-1640 with 2.5% FBS were added to the lower compartment of the chamber. Cells were incubated at 37°C with 5% CO_2 for 24 h to allow migration, after which the cells were fixed with 4% paraformaldehyde for 20 min and stained with hematoxylin for 20 min at room temperature. After being washed three times with PBS, the non-migrating cells in the upper chamber were carefully removed using a cotton swab. The migrated cells on the lower surface of the membrane were imaged and photographed with an inverted microscope (Olympus IX83) at 200× magnification in five randomly selected visual fields, and the migrated cells were counted using Image J software with manual inspection. Each assay was performed in triplicate, and the number of migrated cells was shown as means ± SD. Cell invasion assay was performed similarly, except that the FBS concentration in the lower compartment of the chamber was increased to 8%, and the incubation time was extended to 48 h.

Molecular Modeling

The molecular model of the glycosylated human volume-regulated anion channel (VRAC) protein was constructed using the Sybyl X 2.0 program (Tripos Inc.) running on a Dual-core Intel(R) E5300 CPU, 2.60 GHz, 4 GB RAM, under the Windows 10 operating system. Crystal structure of the human VRAC protein was obtained from the Protein Data Bank (PDB code: 6DJB). The oligosaccharide was constructed using Sybyl 2.0 program and docked onto the protein's binding site (Asn66 at Chain A) via the formation of C-N glycosidic bond between the C-1 atom of the terminal N-acetylglucosamine and the N atom of the sidechain amide of the asparagine residue. The initial covalent

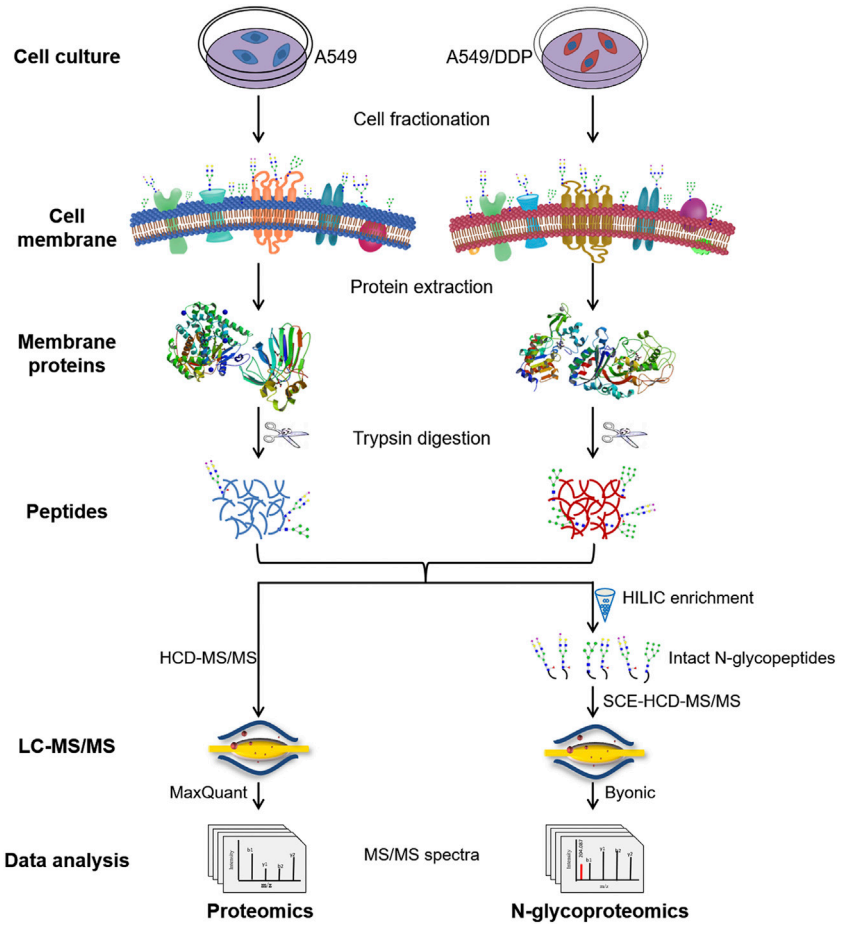

FIGURE 1 | Schematic illustration of the workflow for the integrated proteomic and N-glycoproteomic method designed to comprehensively profile cisplatin-resistance-related cell membrane proteins, N-glycoproteins, and N-glycans of the non-small cell lung cancer cell line.

bond distance of C-N was set to 1.4 Å, and all the hydrogen atoms were added to define the correct configuration and tautomeric states. Then Amber7 FF99 charges were added to the biopolymer and all the atoms were set as Amber7 FF99 type, followed by stepwise energy minimization under standard set parameters using the Amber7 FF99 force field with the Powell energy minimization algorithm, a distance dependent dielectric function, and current charges with the 0.05 kcal·mol^{-1} constringent energy gradient to generate the molecular model. The final schematic diagrams were created using PyMOL. The calculation of the solvent accessible area (SAA, Å^2) of the NH_2 group on the sidechain of Asn66 residue before and after glycosylation was performed using the VEGA ZZ module of PyMOL program.

RESULTS AND DISCUSSION

Workflow for the Integrated Proteome and Glycoproteome Analytical Method

The integrated proteome and glycoproteome analytical workflow was composed of four major steps, including cell culture and fractionation, membrane protein extraction and digestion, proteomic analysis, and N-glycoproteomic analysis (**Figure 1**).

The cisplatin-resistant A549/DDP cell line was established by continuously exposing the parental A549 cell line to cisplatin of increasing concentrations till 1.0 μg/ml. The resistance factor was determined to be 8.36 by measuring the cytotoxicity of cisplatin to A549 and A549/DDP cells (**Supplementary Figure S1**), verifying the cisplatin-resistance of A549/DDP cells. A549 and A549/DDP cell fractionation was performed using a membrane extraction kit. Cell membrane proteins, the proteins from other fractions, and the whole cell lysate were analyzed by SDS-PAGE and WB to examine the purity of membrane proteins (**Supplementary Figures S2A,B**). WB analysis showed that the cell membrane marker, Na/K ATPase, was significantly enriched in the cell membrane fraction, validating the high purity of the obtained cell membrane. Then, the membrane proteins were denatured, reduced, alkylated and digested into peptides, which were further divided in half for subsequent proteomic and N-glycoproteomic analysis. For proteomic analysis, the peptides were detected by HCD-MS/MS, and quantified by LFQ method. For

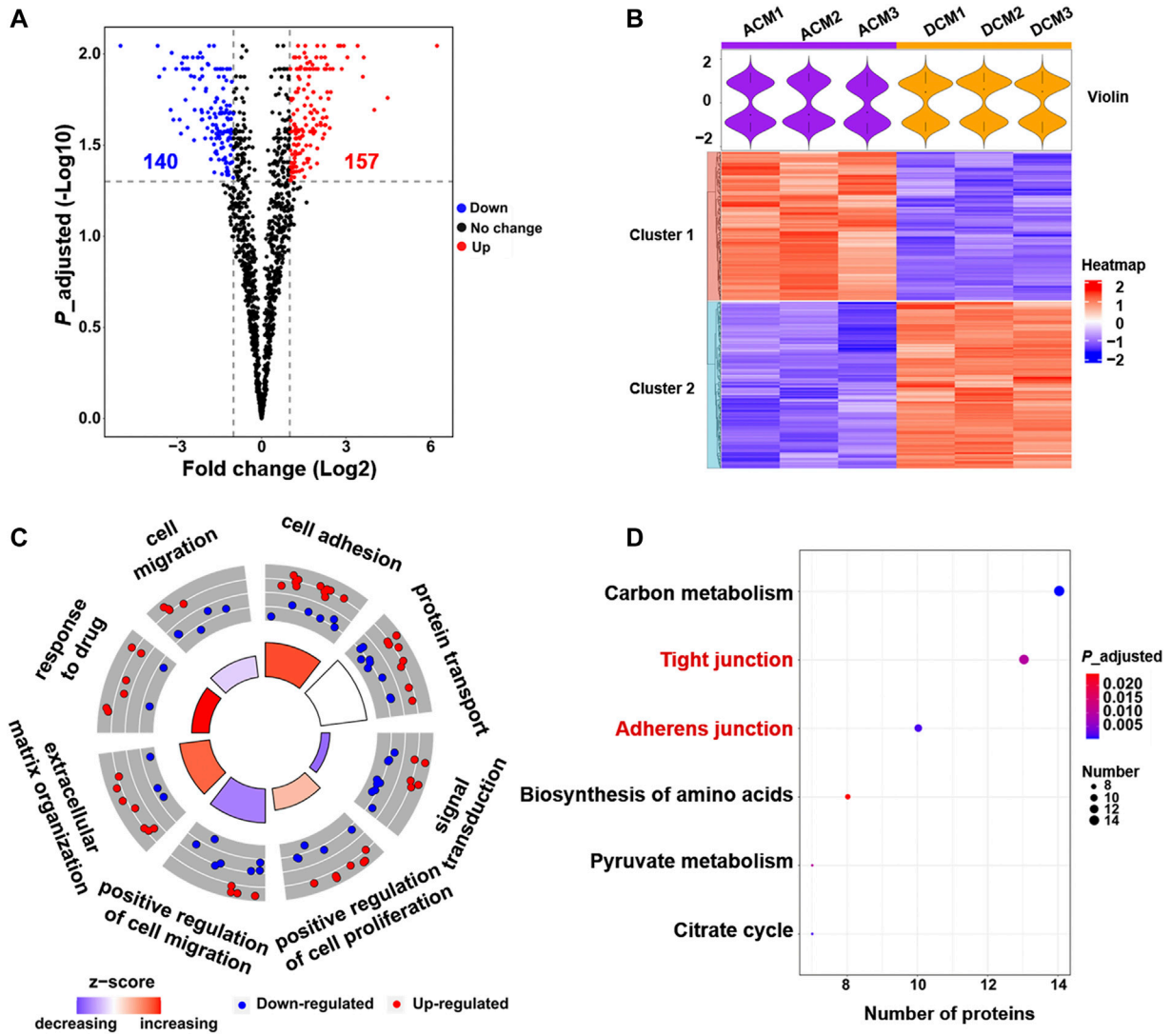

FIGURE 2 | Quantitative proteomic analysis of cell membrane proteins. **(A)** Volcano plot of proteomic data constructed using fold changes (DCM/ACM) and adjusted *p* values. Red dots: significantly up-regulated proteins (fold change >2.00, $p < 0.05$). Blue dots: significantly down-regulated proteins (fold change <0.50, $p < 0.05$). Black dots: proteins with no significant changes. **(B)** Heat map generated from the normalized intensity of the 297 DEPs across ACM and DCM groups. The upper violin plot shows the intensity distribution of proteins in each sample. **(C)** GOCircle plot of the top eight enriched biological processes of the 297 DEPs. The up-regulated (red dots) and down-regulated (blue dots) proteins in each process are distributed in the outer circle of the plot. The inner circle displays the z-score, calculated as the number of up-regulated proteins minus the number of down-regulated proteins divided by the square root of the total count. The larger z-score represents more up-regulated proteins enriched in the process. **(D)** Top six enriched KEGG pathways of the DEPs.

N-glycoproteomic analysis, the intact N-glycopeptides were enriched by HILIC beads, and then directly analyzed by SCE-HCD-MS/MS with flexible collision energy settings (20–30–40%). In this manner, abundant and informative fragment ions from both the glycan and the peptide can be produced and detected within one spectrum, allowing the simultaneous identification of glycoproteins, glycopeptides, glycosites, and glycan composition/structure in a single run. This integrated method is able to simultaneously analyze membrane proteins and N-glycoproteins as well as N-glycans by intact glycopeptide analysis in a single process, making it suitable to comprehensively characterize the alterations in both abundance and glycosylation of membrane proteins involved in the development of cisplatin-resistance.

Proteomic Screening of the Resistance-Related Cell Membrane Proteins

Comparative proteomic analysis was performed to characterize the abundance changes of membrane proteins in A549/DDP cells compared with parental A549 cells. The experiments were conducted in triplicate and a total of 2,906 proteins were identified. GO enrichment analysis showed that these proteins

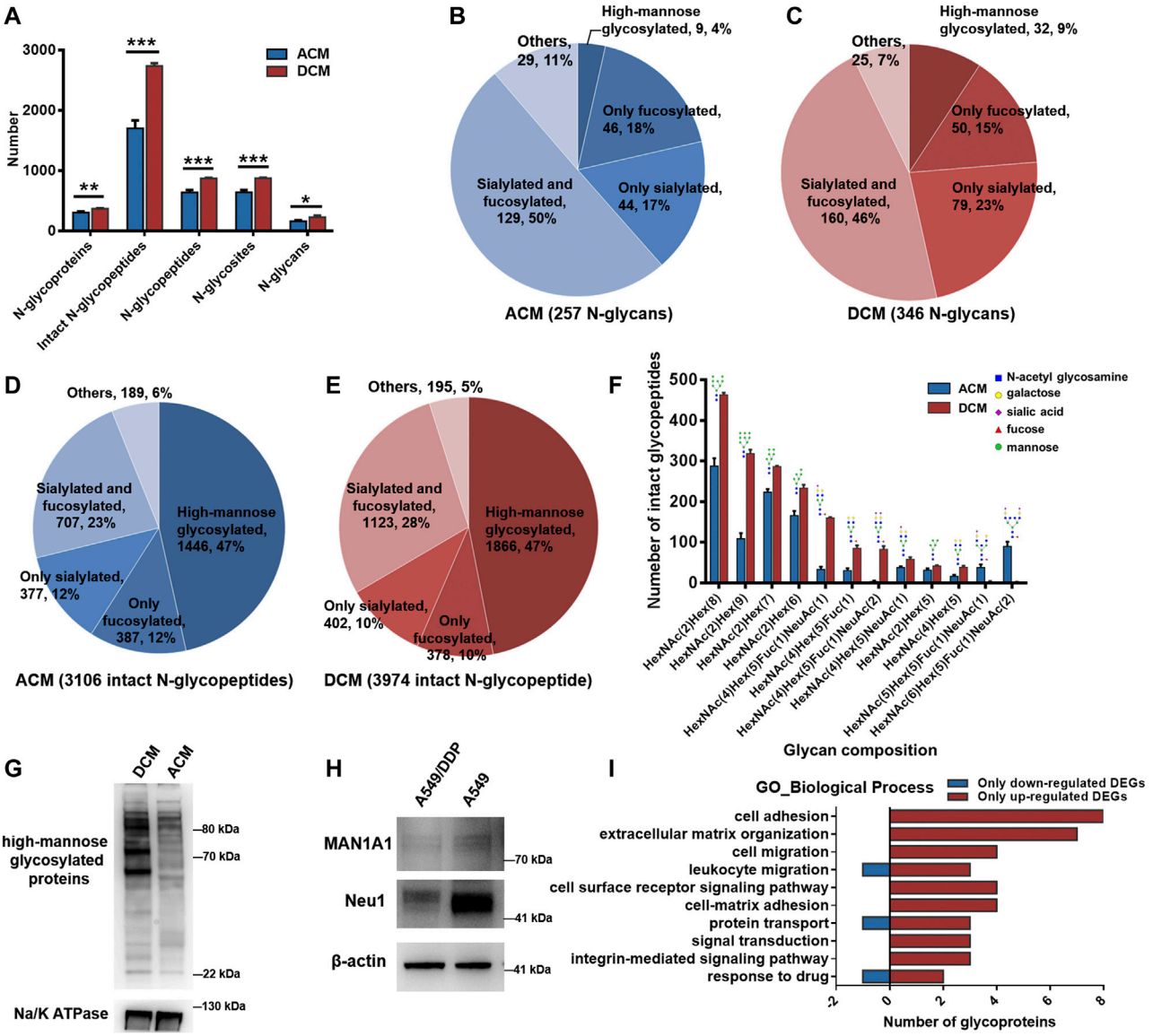

FIGURE 3 | N-glycoproteomic analysis of cell membrane proteins and WB verification of the results. **(A)** Number of identified N-glycoproteins, intact N-glycopeptides, N-glycopeptides, N-glycosites, and N-glycans in ACM and DCM groups. **(B,C)** Number of N-glycans of each type in ACM **(B)** and DCM **(C)** groups. **(D,E)** Number of intact glycopeptides modified with different types of glycans in ACM **(D)** and DCM **(E)** groups. **(F)** Compositions and structures of the top ten glycans detected on the intact glycopeptides from ACM and DCM groups. **(G)** WB detection of global high-mannose glycosylated proteins in ACM and DCM groups. Na/K ATPase was used as an internal standard. **(H)** WB detection of MAN1A1 and Neu1 in A549 and A549/DDP cells. β-actin was used as an internal standard. **(I)** Main biological processes involving the 82 differentially glycosylated proteins and the number of glycoproteins containing only down- or up-regulated glycopeptides implicated in these processes. Error bars represent mean ± SD; *$p < 0.05$, **$p < 0.01$, ***$p < 0.001$, Student's *t*-test.

were mainly enriched in the membrane component (**Supplementary Figure S2C**), further confirming the purity of the extracted proteins. To identify the proteins associated with cisplatin resistance, we carried out the quantitative proteomic analysis based on LFQ method, and the quantitation results were shown as the fold change of DCM/ACM. A total of 297 cell membrane DEPs were screened out, among which 157 proteins were up-regulated with a fold change >2.00, and 140 were down-regulated with a fold change <0.50 (**Figure 2A**). The abundance of these membrane proteins was significantly altered in drug-resistant A549/DDP cells, suggesting their involvement in the development of cisplatin resistance. The DEPs could be classified into two distinct clusters between ACM and DCM groups, and the normalized intensities of the same protein were similar in the three biological replicates, indicating good reproducibility and reliability of the results (**Figure 2B**).

To explore the functions of these DEPs, the biological processes and pathways they participate in were analyzed through GO enrichment analysis and KEGG pathway enrichment analysis. The GO analysis results were further

integrated with the fold changes of these proteins to generate the GOCircle plot (**Figure 2C**), which could clearly present the major enriched biological processes and the composition of up- and down-regulated proteins in each process, facilitating the comparison of biological functions amongst these DEPs. As shown in **Figure 2C**, the biological processes involving more up-regulated proteins mainly included cell adhesion and response to drug, which were expected to enhance cell adhesion and the tolerance to cisplatin, thereby contributing to drug resistance. In contrast, most of the down-regulated membrane proteins were implicated in signal transduction and cell migration, implying the deficient signal transduction and reduced migration of A549/DDP cells.

GO analysis revealed that cell adhesion and response to drug were enhanced, while signal transduction and cell migration appeared to be impaired in the cisplatin-resistant cells (**Figure 2C**, **Supplementary Figure S3**). Moreover, KEGG pathway analysis indicated that the 297 DEPs mainly functioned in the cell junction and metabolism pathways (**Figure 2D**). In particular, the up-regulated proteins were concentrated on the tight junction and adherens junction pathways (**Supplementary Figures S4, S5**), which supported the result of GO analysis that cell adhesion was increased in the resistant cells. Altogether, proteomic screening highlights that some critical membrane proteins implicated in cell adhesion, response to drug, cell migration and some signal pathways are altered in the abundance during the development of cisplatin resistance.

N-Glycoproteomic Profiling of Resistance-Related Membrane Glycoproteins and Glycans

N-glycoproteomic analysis was employed to comprehensively study the alteration of membrane protein glycosylation in multiple aspects, including proteins, glycopeptides, glycosites, and glycans. By virtue of SCE-HCD-MS/MS, simultaneous identification of N-glycoproteins and N-glycans can be achieved in a single run. N-glycoproteome profiling of whole cell lysate was also performed and compared with that of membrane proteins. The identified intact N-glycopeptides, N-glycopeptides (peptide backbones without glycans), and N-glycosites were significantly elevated in the membrane protein groups (**Supplementary Figure S6**), which contributed to the identification of N-glycoproteins with higher confidence.

All the experiments were carried out in triplicate for the membrane proteins from each cell line, and the number of identified N-glycoproteins, intact N-glycopeptides, N-glycopeptides, N-glycosites, and N-glycans of each biological replicate were displayed in **Supplementary Figure S7**. In the ACM group, we identified a total of 3,106 unique intact glycopeptides composed of 257 glycan compositions, 908 glycosites, and 902 unique glycopeptides from 405 glycoproteins. In the DCM group, a total of 3,974 unique intact glycopeptides were identified, which consisted of 346 glycan compositions, 1,079 glycosites, and 1,075 unique glycopeptides from 449 glycoproteins. ACM and DCM groups overlapped across 284 proteins, 1,206 intact glycopeptides, 631 glycopeptides, 633 glycosites and 135 glycan compositions (**Supplementary Figure S8**). Furthermore, the membrane protein glycosylation were systematically compared between A549 and A549/DDP cells. Evidently, the number of N-glycoproteins, intact N-glycopeptides, N-glycopeptides, N-glycosites, and N-glycans identified in the DCM group were all significantly higher than those in ACM group (**Figure 3A**), indicating an increase of global glycosylation in the cisplatin-resistant cells. Based on the glycan compositions, the identified N-glycans were classified into five types: high-mannose glycosylated, only fucosylated (but not sialylated), only sialylated (but not fucosylated), fucosylated and sialylated, and others. The dually fucosylated and sialylated type accounted for the highest proportion of diversity (50% for ACM, 46% for DCM) regardless of their abundance, and the high-mannose type contributed only 4 and 9% of diversity, respectively (**Figures 3B,C**). Moreover, the N-glycan compositions of DCM had larger diversity than those of ACM in high-mannose, fucosylated, or sialylated types of N-glycans. Although the high-mannose type was less diverse, nearly half of glycopeptides were modified with high-mannose glycans for both the ACM and DCM samples (**Figures 3D,E**). Approximately one third of the glycopeptides were fucosylated or silaylated. Similar to the N-glycans, the number of glycopeptides modified with high-mannose, fucosylated, or sialylated glycans in DCM group were all greater than those in ACM group. In addition, the top ten glycopeptides (the number of peptides containing the same glycan) and the deduced structure of each glycan were shown in **Figure 3F**. Likewise, the high-mannose glycosylated peptides were proven to have the largest population with those containing HexNAc(2)Hex(8) being the most abundant. These top high-mannose glycosylated peptides were notably increased in A549/DDP cells.

To validate the elevated high-mannose glycosylation in A549/DDP cells revealed by the N-glycoproteomic analysis, the global high-mannose glycosylation level of ACM and DCM groups were detected by WB assay using the lectin Con A as a specific mannose-binding partner. As shown in **Figure 3G**, the abundance of high-mannose glycosylated proteins was markedly higher in the DCM group, confirming the result of N-glycoproteomic analysis. Furthermore, we examined the expression of two proteins, MAN1A1 and Neu1, which play critical roles in protein glycosylation. MAN1A1 is involved in the maturation of Asn-linked oligosaccharides, and progressively trims α-1,2-linked mannose residues from $Man_9GlcNAc_2$ (Man: mannose, GlcNAc: N-acetylglucosamine) to produce $Man_5GlcNAc_2$ (Ogen-Shtern et al., 2016). WB assay showed that MAN1A1 was down-regulated in A549/DDP cells (**Figure 3H**). The low expression of MAN1A1 may hamper the processing of N-glycans thereby promoting the accumulation of $Man_9GlcNAc_2$ high-mannose glycosylation in A549/DDP cells, which was also uncovered by the glycoproteomic analysis as peptide modified with the $Man_9GlcNAc_2$ chain [i.e., HexNAc(2)Hex(9)] was one of the most abundant glycopeptides and was markedly increased in A549/DDP cells (**Figure 3F**). Neu1 functions in sialic acid metabolism and catalyzes the removal of sialic acid moiety

TABLE 1 | Identities and abundance changes of the 9 $DEGs_w$ (fold change >2.00 or <0.50) and corresponding proteins.

N-glycopeptide	Glycosite	Glycan	Gene name	Intact N-glycopeptide		Protein	
				Fold change	Expression	Fold change	Expression
LPADCIDCTTN#FSCTYGK	87	HexNAc(2)Hex(8)	TM2D3	47.061	Up	NA[a]	NA
DAVNN#ITAK	324	HexNAc(2)Hex(8)	CACNA2D1	6.936	Up	NA	NA
LN#SSTIK	275	HexNAc(5)Hex(6)	LAMP2	6.845	Up	0.613	No change
N#MSFVNDLTVTQDGRK	196	HexNAc(2)Hex(8)	APMAP	5.204	Up	2.982	Up
N#YTADYDK	106	HexNAc(2)Hex(8)	ERLIN1	4.164	Up	3.328	Up
YHYN#GTLLDGTLFDSSYSR	286	HexNAc(2)Hex(9)	FKBP9	2.075	Up	0.627	No change
IAPASN#VSHTVVLRPLK	88	HexNAc(2)Hex(9)	SSR2	0.004	Down	NA	NA
TQN#FTLLVQGSPELK	439	HexNAc(2)Hex(6)	BCAM	0.304	Down	0.249	Down
DTCTQECSYFN#ITK	669	HexNAc(4)Hex(5)Fuc (2)	ITGB1	0.379	Down	3.142	Up

[a]*NA: not quantified in the proteomic analysis.*

from glycoproteins (Bonten et al., 1996). The expression of Neu1 was substantially decreased in the resistant cells (**Figure 3H**). In view of this, our results suggest that the degradation of sialic acid from glycoproteins is retarded in A549/DDP cells, in turn leading to the accumulation of sialylated glycoproteins in cisplatin-resistant cells.

We also conducted quantitative analysis of the intact N-glycopeptides to detect the abundance changes of glycopeptides between ACM and DCM groups. The DEGs were classified into two types, DEGs with fold changes ($DEGs_w$) and DEGs without fold changes ($DEGs_{w/o}$). $DEGs_{w/o}$ included those special glycopeptides that were identified in all the three biological replicates within one group while completely missing in all replicates of the other. Overall nine $DEGs_w$ derived from nine glycoproteins were screened out, including six up-regulated (fold change >2.00) and three down-regulated (fold change <0.50) intact glycopeptides (**Supplementary Figure S9**). The identities and abundance changes of these $DEGs_w$ and corresponding proteins were shown in **Table 1**; **Supplementary Figures S10–S18**. Besides $DEGs_w$, a total of 1,010 $DEGs_{w/o}$ were screened out, among which 833 were exclusively identified in DCM group as up-regulated glycopeptides and 177 were unique in ACM group as down-regulated glycopeptides. Hence, the number of up-regulated glycopeptides was much larger than the down-regulated, confirming the elevated global glycosylation in cisplatin-resistant cells. The top 10 up- and down-regulated $DEGs_{w/o}$ in intensity as well as corresponding glycoproteins were listed in **Supplementary Tables S1, S2**. Most of the top up-regulated $DEGs_{w/o}$ were derived from cell adhesion molecules, integrins, while the top down-regulated $DEGs_{w/o}$ mainly stemmed from folate receptor.

The 1,019 DEGs including $DEGs_w$ and $DEGs_{w/o}$ were derived from 254 glycoproteins, among which 129 were also quantified at the proteomic level. Particularly, we further focused on the differentially glycosylated proteins that contained DEGs but were not changed in protein abundance. A total of 82 differentially glycosylated proteins were screened out containing 54 down-regulated glycopeptides and 302 up-regulated glycopeptides. Specifically, 56 out of 82 glycoproteins contained only the up-regulated glycopeptides while six glycoproteins contained only the down-regulated glycopeptides (**Supplementary Figure S19**). GO enrichment analysis disclosed that the 82 glycoproteins were primarily implicated in the biological processes of cell adhesion, extracellular matrix (ECM) organization, signal transduction, cell migration, protein transport, and response to drug (**Supplementary Figure S20**), which are known to be the functions of membrane proteins. Moreover, these biological processes mainly attributed from the glycoproteins containing up-regulated glycopeptides (**Figure 3I**), suggesting the increased glycosylation of proteins associated with these processes in A549/DDP cells. Additionally, KEGG pathway analysis of the 82 proteins showed that many glycoproteins containing up-regulated DEGs were annotated as cell adhesion molecules (**Supplementary Figure S21**) and functioned in the ECM-receptor interaction (**Supplementary Figure S22**), being in good consistency with the findings of GO analysis.

In summary, N-glycoproteomic analysis indicated that the glycosylation of membrane proteins in A549/DDP cells was elevated in terms of the number of identified N-glycoproteins, intact N-glycopeptides, N-glycopeptides, N-glycosites, N-glycans as well as the up-regulated glycopeptides. Moreover, the high-mannose, fucosylated, or sialylated glycosylation levels were increased in the cisplatin-resistant cells. The glycosylation of proteins participating in cell adhesion, ECM organization, signal transduction, cell migration, protein transport, and response to drug was enhanced in the resistant cells, which was closely related to the development of cisplatin resistance.

Biological Verification of the Results of Proteomic and N-Glycoproteomic Study

Proteomic study of the membrane proteins revealed that the proteins involved in cell adhesion, response to drug, cell migration, and signal transduction were associated with cisplatin resistance. Meanwhile, N-glycoproteomic analysis indicated that the glycosylation of proteins implicated in these biological processes was also altered in the development of cisplatin resistance. Inspired by these findings, we further investigated the cell migration and invasion, as well as the cisplatin uptake and efflux in A549 and A549/DDP cells. In addition, we explored the specific glycosylation type most relevant to cisplatin resistance.

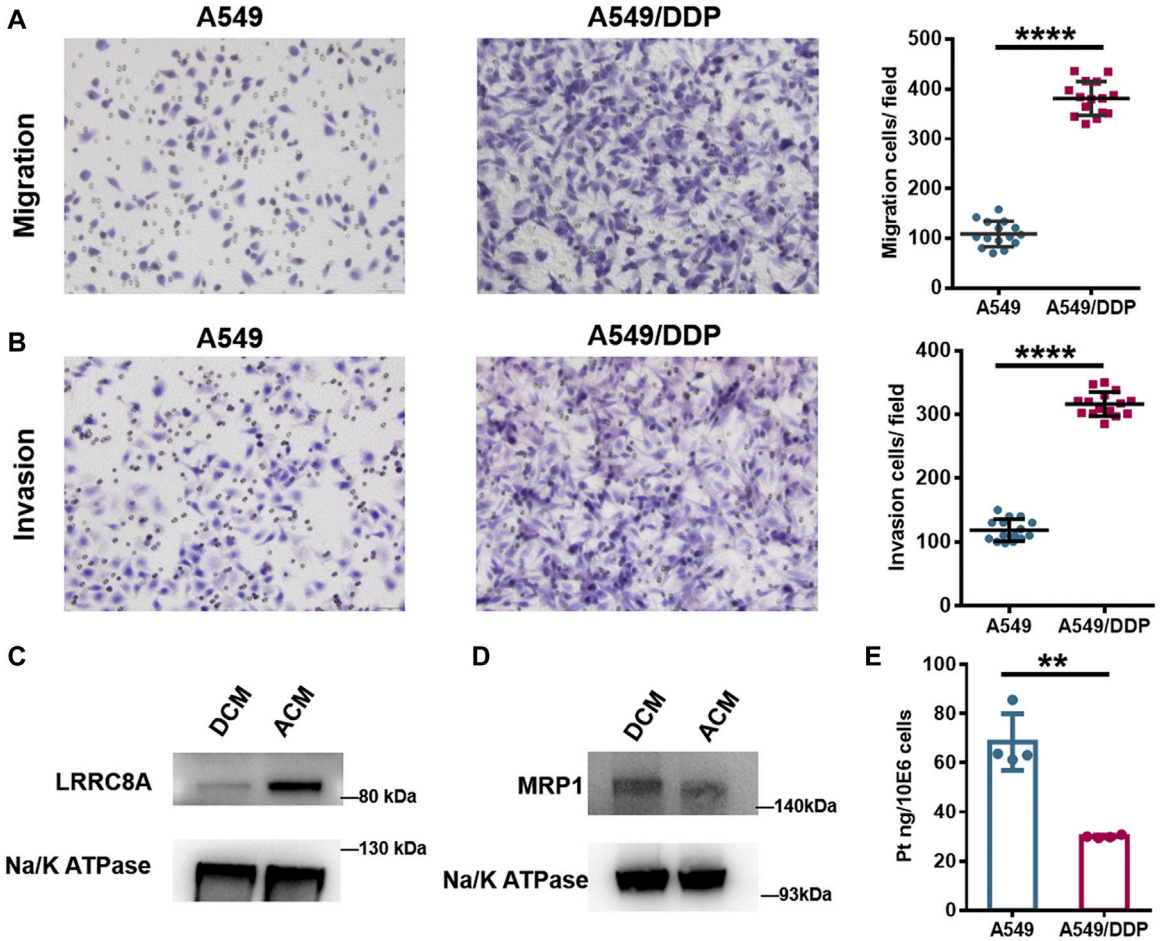

FIGURE 4 | Biological verification of the results of proteomic and N-glycoproteomic study. **(A,B)** Representative images of the Transwell migration **(A)** and invasion assay **(B)** of A549 and A549/DDP cells, and the quantitative number of migration and invasion cells. **(C,D)** WB assay of LRRC8A **(C)** and MRP1 **(D)** in ACM and DCM groups. **(E)** The amount of Pt in A549 and A549/DDP cells measured by ICP-MS. Error bars represent the mean ± SD; $^{**}p < 0.01$, $^{****}p < 0.0001$, Student's *t*-test.

Cell Migration and Invasion

Proteomic analysis showed that the proteins required for cell migration were reduced in the cisplatin-resistant cells, implying the defective migration of A549/DDP cells. Interestingly, the glycosylation of proteins involved in cell migration was increased; for example, the number of identified intact glycopeptides, glycopeptides, glycosites, or glycans of integrin β1 (ITGB1), a key participant in cell adhesion and migration (Leavesley et al., 1993), was increased in DCM group (**Supplementary Figures S23A,B**), and for most glycosites, the number of modified glycans on each site was also increased (**Supplementary Figure S23C**). Further assessment using the Transwell system found that the number of migration and invasion A549/DDP cells was much higher than that of A549 cells (**Figures 4A,B**), indicating that the resistant cells have stronger ability of migration and invasion. This observation revealed that although some proteins involved in the cell migration were down-regulated in the A549/DDP cells, the ability of migration was not impaired and even increased, which was thought to be attributed, at least in part, to the elevated glycosylation of membrane proteins associated with cell adhesion and migration. These results also demonstrate the necessity for integrating proteomic and glycoproteomic detection to comprehensively and accurately study the mechanism of cisplatin resistance.

Cisplatin Uptake and Efflux

Cell membrane proteins play key roles in the response to drug as there are multiple carriers controlling the uptake and efflux of various drugs. Many carriers have been proposed to function in the accumulation of cisplatin in cells, among which the VRACs are key players. VRACs consist of six LRRC8 subunits (Kefauver et al., 2018). It has been demonstrated that about 50% of cisplatin uptake relies on LRRC8A and LRRC8D under isotonic conditions (Planells-Cases et al., 2015). In the genome-wide screening for Pt drug resistance, loss of LRRC8 subunits of VRACs was found to increase the resistance to cisplatin (Planells-Cases et al., 2015; He et al., 2018). Thus, the LRRC8 subunits play crucial roles in cisplatin accumulation and drug resistance (Planells-Cases et al., 2015; Sørensen et al., 2016; He et al., 2018). Through the quantitative proteomic analysis, we found that LRRC8A was down-regulated in the A549/DDP cells, and WB assay also confirmed the decrease of

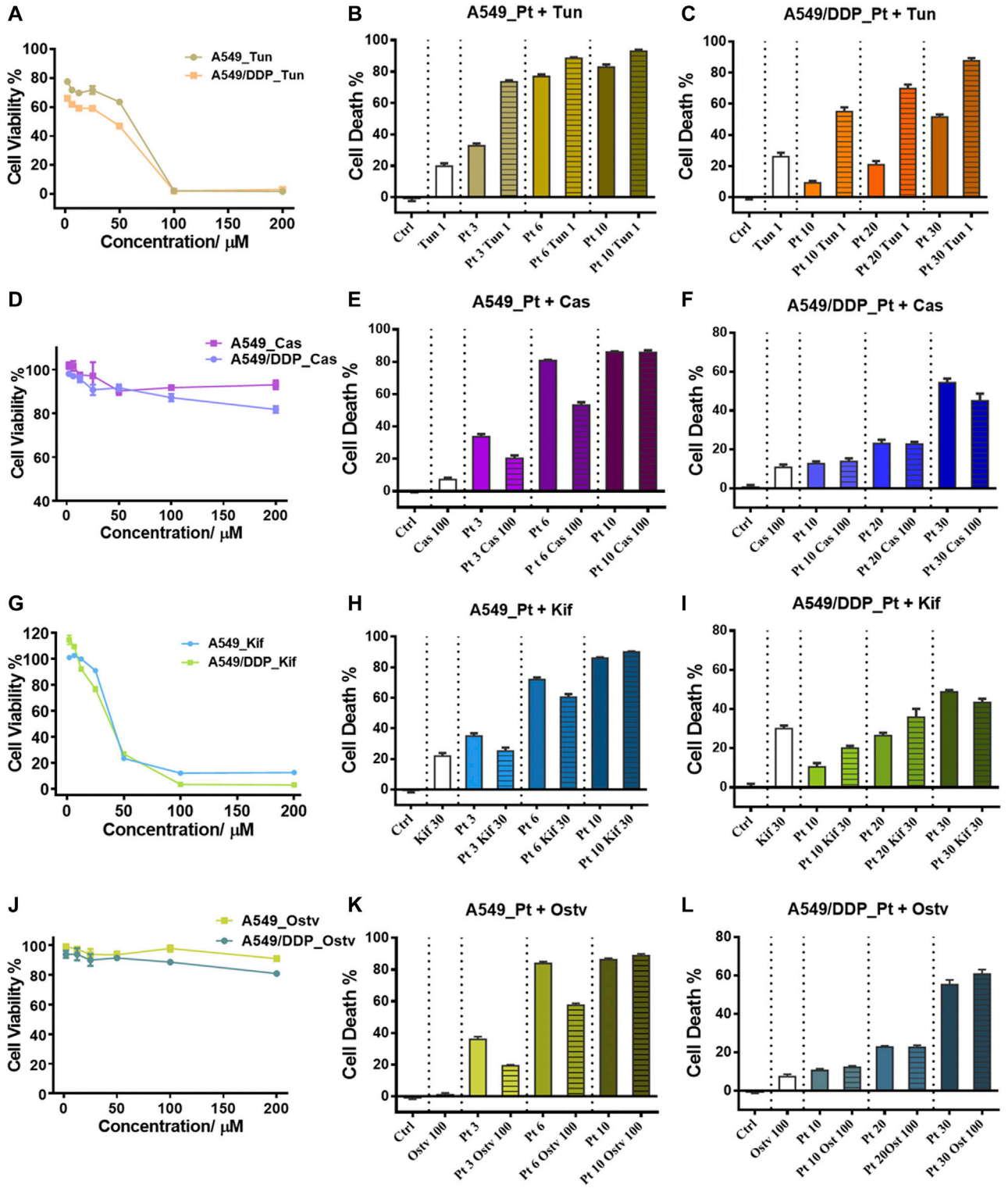

FIGURE 5 | Inhibition of N-glycosylation by small molecule inhibitors. **(A)** Cytotoxicity of Tunicamycin to A549 and A549/DDP cells. **(B,C)** Cytotoxicity of the combination treatment of Tunicamycin (1 μM) and cisplatin to A549 **(B)** and A549/DDP cells **(C)**. **(D)** Cytotoxicity of Castanospermine to A549 and A549/DDP cells. **(E,F)** Cytotoxicity of the combination treatment of Castanospermine (100 μM) and cisplatin to A549 **(E)** and A549/DDP cells **(F)**. **(G)** Cytotoxicity of Kifunensine to A549 and A549/DDP cells. **(H,I)** Cytotoxicity of the combination treatment of Kifunensine (30 μM) and cisplatin to A549 **(H)** and A549/DDP cells **(I)**. **(J)** Cytotoxicity of Oseltamivir to A549 and A549/DDP cells. **(K,L)** Cytotoxicity of the combination treatment of Oseltamivir (100 μM) and cisplatin to A549 **(K)** and A549/DDP cells **(L)**. Concentrations of cisplatin used in the combination treatment are 3, 6 and 9 μM for A549 cells, and 10, 20 and 30 μM for A549/DDP cells. Error bars represent the mean ± SD.

LRRC8A in the resistant cells (**Figure 4C**). Moreover, the N-glycoproteomic study showed that the LRRC8A in DCM group was modified with $Man_8GlcNAc_2$ chain at the site of Asn66, whereas no glycosylation was identified in ACM group. Asn66 was located on the extracellular loop of LRRC8A (**Supplementary Figure S24A**). Molecular modeling showed that the SAA of Asn66 was increased from 21.377 $Å^2$ to 29.407 $Å^2$ after the modification of $Man_8GlcNAc_2$ oligosaccharide (**Supplementary Figures S24B,C**). The increased solvent accessibility may affect the channel structure and activity to carry cisplatin into cells (Planells-Cases et al., 2015; Singh et al., 2018). Collectively, the low expression and elevated glycosylation of LRRC8A may cause a reduction in cisplatin uptake by A549/DDP cells, therefore bringing about the resistance to cisplatin.

Apart from the carriers responsible for cisplatin uptake, some transporters mediate the drug efflux out of cells. ATP-binding cassette (ABC) transporters are well-known drug efflux pumps capable of extruding numerous drugs from the cytoplasm (Robey et al., 2018). The ABC superfamily members, multidrug resistance protein 1 (MDR1), MRPs, and breast cancer resistance protein (BCRP), have been proposed to regulate cisplatin sensitivity in various cancer cells, including breast cancer (Yi et al., 2019), lung cancer (Fang et al., 2018; Wu et al., 2019), oesophageal squamous cell carcinoma (Yamasaki et al., 2011), and ovarian carcinoma (Guminski et al., 2006). The role of ABC transporters in cisplatin resistance may vary among the ABC subfamily members and depend on the cancer type. Proteome screening in this study found that MRP1 and MRP4 were slightly over-expressed in A549/DDP cells, and the result of WB assay displayed the same tendency (**Figure 4D**). Notably, the increased expression of MRP1 and MRP4 has also been reported to correlate with the platinum-based drug resistance in the ovarian carcinoma cells (Beretta et al., 2010). The over-expression of MRP1/4 may increase the export of cisplatin from A549/DDP cells and reduce the intracellular drug concentration. To validate the influence of the alteration of LRRC8A and MRP1/4 on cisplatin accumulation, we used ICP-MS to determine the amount of cisplatin in A549 and A549/DDP cells. For A549 cells, there was 68.5 ng cisplatin in per million cells, while the amount decreased to 30.0 ng for A549/DDP cells (**Figure 4E**). Thus, the accumulation of cisplatin was significantly reduced in the drug resistant cells due to the low expression and glycosylation of LRRC8A as well as a concomitant increased expression of MRP1/4, thereby conferring cisplatin resistance.

High-Mannose and Sialylated Glycosylation Contribute to Cisplatin Resistance

N-glycoproteomic analysis indicated the increased glycosylation of membrane proteins in A549/DDP cells. To further determine the specific glycosylation type most relevant to cisplatin resistance, we used several well-established glycosylation inhibitors that could block N-glycan synthesis at different stages to treat the A549 and A549/DDP cells in combination with cisplatin.

Tunicamycin (Tun), a potent protein glycosylation inhibitor, inhibits protein N-glycosylation entirely at the first step of glycan synthesis (Wu et al., 2018). Tun has been reported to enhance the suppressive effects of cisplatin on cancer cell growth (Noda et al., 1999; Hou et al., 2013; Ahmmed et al., 2019). In this study, we found that Tun exerts cytotoxicity on both A549 and A549/DDP cells with higher toxicity to the resistant cells (**Figure 5A**). When co-administered with cisplatin, Tun worked synergistically with cisplatin and potentiated its efficacy on A549 and A549/DDP cells, especially at low cisplatin concentrations (**Figures 5B,C**). The synergistic effect was more apparent on the resistant cells.

Two alkaloids, Castanospermine (Cas) and Kifunensine (Kif), were employed to alter the protein glycosylation in A549 and A549/DDP cells, respectively. Cas and Kif block the trimming reaction of nascent $Glc_3Man_9GlcNAc_2$ (Glc: glucose) oligosaccharide on glycoproteins by inhibiting the glycosidases involved in the trimming process (Zhong et al., 2020). Cas preferentially inhibits α-glucosidases I and II, causing the accumulation of fully glucosylated high-mannose chains (Pili et al., 1995). Cas did not significantly suppress the proliferation of the 2 cell lines (**Figure 5D**). In contrast to Tun, Cas increased the tolerance to cisplatin of A549 cells (at the low dosage of cisplatin) and A549/DDP cells (at the high dosage of cisplatin) as the cell death of combinatorial administration was lower than that of individual treatment with cisplatin (**Figures 5E,F**). Kif selectively inhibits the α-mannosidase I, resulting in the accumulation of $Man_{7-9}GlcNAc_2$ high-mannose type oligosaccharides on glycoproteins (Zhou et al., 2008), which were also the top three abundant glycans identified in ACM and DCM groups (**Figure 3F**). Although being cytotoxic to A549 and A549/DDP cells (**Figure 5G**), Kif also increased the cell survival in a similar way to Cas when working in combination with cisplatin (**Figures 5H,I**).

Oseltamivir phosphate (Ostv) is an efficient small-molecule inhibitor of neuraminidase that prevents the cleavage of sialic acid from glycan chains and increases the level of sialylated glycosylation (de Oliveira et al., 2015). Ostv alone did not have a strong suppressive effect on cell proliferation (**Figure 5J**). When treated with a combination of Ostv and cisplatin, A549/DDP cells showed no significant difference in cell death from those treated with cisplatin alone, while A549 cells survived more compared with the individual treatment (**Figures 5K,L**).

Collectively, these findings suggest that inhibition of protein N-glycosylation could enhance the anticancer activity of cisplatin on both A549 and A549/DDP cells. However, promoting the high-mannose or sialylated type of glycosylation attenuated the sensitivity of A549 cells to cisplatin. Therefore, the increased high-mannose or sialylated glycosylation play critical roles in the development of cisplatin resistance and contribute to the resistant phenotype.

CONCLUSION

In this work, we have integrated proteomic and N-glycoproteomic detection for the comprehensive characterization of the membrane proteins associated with cisplatin resistance in non-small cell lung cancer cells. Based on this method, we found that the proteins involved in cell adhesion, cell migration, response to drug, and signal transduction were significantly altered in abundance and glycosylation in the development of cisplatin resistance. Consequently, the ability of migration and invasion was substantially increased in cisplatin-resistant cells, further aggravating their malignancy. On the other hand, the concentration of cisplatin was

significantly reduced in the resistant cells, concomitant with the down-regulation of LRRC8A and over-expression of MRP1 and MRP4, thereby decreasing the amount of cellular cisplatin and conferring the resistance. In addition, the global glycosylation of membrane proteins was significantly elevated in the cisplatin-resistant cells, and inhibition of protein N-glycosylation potentiated the anticancer efficacy of cisplatin. Particularly, increasing the high-mannose or sialylated type of glycosylation promoted the cell resistance to cisplatin, revealing the key glycosylation type associated with cisplatin-resistance. These results give new insights into the mechanism of cisplatin resistance. It is also worth noting that the integrated method is versatile and highly efficient for obtaining multilevel and comprehensive information on the expression and glycosylation of proteins in a single experiment. We anticipate its broad application in the study on the mechanisms of drug resistance.

DATA AVAILABILITY STATEMENT

The datasets presented in this study can be found in online repositories. The names of the repository/repositories and accession number(s) can be found below: http://www.proteomexchange.org/, PXD028691.

AUTHOR CONTRIBUTIONS

YoZ, YH, and JC directed and designed the research; WZ, YM, SZ, MG, and WC performed the biological experiments; YM, SZ, YiZ, and TS performed the sample preparation and MS detection; WZ, YoZ, and SW conducted the data processing and bioinformatics analysis; WZ, YoZ, JC, and HY discussed the results; WZ, YoZ, and HY wrote and reviewed the manuscript.

FUNDING

We thank The National Natural Science Foundation of China (31901038), the 1.3.5 Project for Disciplines of Excellence (ZYGD18014) and the National Clinical Research Center for Geriatrics (Z20201014), West China Hospital, Sichuan University for financial support.

ACKNOWLEDGMENTS

We thank Dr. Wei Zheng from Peking University for performing the molecular modeling and Dr. Yang Zhou from the Institute of Chemistry, Chinese Academy of Sciences for conducting the ICP-MS detection.

SUPPLEMENTARY MATERIAL

The Supplementary Material for this article can be found online at: https://www.frontiersin.org/articles/10.3389/fphar.2021.805499/full#supplementary-material

REFERENCES

Ahmmed, B., Khan, M. N., Nisar, M. A., Kampo, S., Zheng, Q., Li, Y., et al. (2019). Tunicamycin Enhances the Suppressive Effects of Cisplatin on Lung Cancer Growth through PTX3 Glycosylation via AKT/NF-κB Signaling Pathway. *Int. J. Oncol.* 54 (2), 431–442. doi:10.3892/ijo.2018.4650

Beretta, G. L., Benedetti, V., Cossa, G., Assaraf, Y. G., Bram, E., Gatti, L., et al. (2010). Increased Levels and Defective Glycosylation of MRPs in Ovarian Carcinoma Cells Resistant to Oxaliplatin. *Biochem. Pharmacol.* 79 (8), 1108–1117. doi:10.1016/j.bcp.2009.12.002

Bonten, E., van der Spoel, A., Fornerod, M., Grosveld, G., and d'Azzo, A. (1996). Characterization of Human Lysosomal Neuraminidase Defines the Molecular Basis of the Metabolic Storage Disorder Sialidosis. *Genes Dev.* 10 (24), 3156–3169. doi:10.1101/gad.10.24.3156

Chaudhuri, A. R., Callen, E., Ding, X., Gogola, E., Duarte, A. A., Lee, J. E., et al. (2016). Erratum: Replication fork Stability Confers Chemoresistance in BRCA-Deficient Cells. *Nature* 539 (7612), 456–387. doi:10.1038/nature1832510.1038/nature19826

Christiansen, M. N., Chik, J., Lee, L., Anugraham, M., Abrahams, J. L., and Packer, N. H. (2014). Cell Surface Protein Glycosylation in Cancer. *Proteomics* 14 (4-5), 525–546. doi:10.1002/pmic.201300387

Costa, A. F., Campos, D., Reis, C. A., and Gomes, C. (2020). Targeting Glycosylation: A New Road for Cancer Drug Discovery. *Trends Cancer* 6 (9), 757–766. doi:10.1016/j.trecan.2020.04.002

De Luca, A., Parker, L. J., Ang, W. H., Rodolfo, C., Gabbarini, V., Hancock, N. C., et al. (2019). A Structure-Based Mechanism of Cisplatin Resistance Mediated by Glutathione Transferase P1-1. *Proc. Natl. Acad. Sci. U. S. A.* 116 (28), 13943–13951. doi:10.1073/pnas.1903297116

de Oliveira, J. T., Santos, A. L., Gomes, C., Barros, R., Ribeiro, C., Mendes, N., et al. (2015). Anti-influenza Neuraminidase Inhibitor Oseltamivir Phosphate Induces Canine Mammary Cancer Cell Aggressiveness. *PLoS One* 10 (4), e0121590. doi:10.1371/journal.pone.0121590

Dilruba, S., and Kalayda, G. V. (2016). Platinum-based Drugs: Past, Present and Future. *Cancer Chemother. Pharmacol.* 77 (6), 1103–1124. doi:10.1007/s00280-016-2976-z

Fang, Z., Chen, W., Yuan, Z., Liu, X., and Jiang, H. (2018). LncRNA-MALAT1 Contributes to the Cisplatin-Resistance of Lung Cancer by Upregulating MRP1 and MDR1 via STAT3 Activation. *Biomed. Pharmacother.* 101, 536–542. doi:10.1016/j.biopha.2018.02.130

Ferreira, J. A., Peixoto, A., Neves, M., Gaiteiro, C., Reis, C. A., Assaraf, Y. G., et al. (2016). Mechanisms of Cisplatin Resistance and Targeting of Cancer Stem Cells: Adding Glycosylation to the Equation. *Drug Resist. Updat* 24, 34–54. doi:10.1016/j.drup.2015.11.003

Gao, W., Li, H., Liu, L., Huang, P., Wang, Z., Chen, W., et al. (2019). An Integrated Strategy for High-Sensitive and Multi-Level Glycoproteome Analysis from Low Micrograms of Protein Samples. *J. Chromatogr. A.* 1600, 46–54. doi:10.1016/j.chroma.2019.04.041

Guminski, A. D., Balleine, R. L., Chiew, Y. E., Webster, L. R., Tapner, M., Farrell, G. C., et al. (2006). MRP2 (ABCC2) and Cisplatin Sensitivity in Hepatocytes and Human Ovarian Carcinoma. *Gynecol. Oncol.* 100 (2), 239–246. doi:10.1016/j.ygyno.2005.08.046

Harrach, S., and Ciarimboli, G. (2015). Role of Transporters in the Distribution of Platinum-Based Drugs. *Front. Pharmacol.* 6 (85), 85. doi:10.3389/fphar.2015.00085

He, Y. J., Meghani, K., Caron, M. C., Yang, C., Ronato, D. A., Bian, J., et al. (2018). DYNLL1 Binds to MRE11 to Limit DNA End Resection in BRCA1-Deficient Cells. *Nature* 563 (7732), 522–526. doi:10.1038/s41586-018-0670-5

Hou, H., Sun, H., Lu, P., Ge, C., Zhang, L., Li, H., et al. (2013). Tunicamycin Potentiates Cisplatin Anticancer Efficacy through the DPAGT1/Akt/ABCG2 Pathway in Mouse Xenograft Models of Human Hepatocellular Carcinoma. *Mol. Cancer Ther.* 12 (12), 2874–2884. doi:10.1158/1535-7163.MCT-13-0201

Ishida, S., Lee, J., Thiele, D. J., and Herskowitz, I. (2002). Uptake of the Anticancer Drug Cisplatin Mediated by the Copper Transporter Ctr1 in Yeast and Mammals. *Proc. Natl. Acad. Sci. U. S. A.* 99 (22), 14298–14302. doi:10.1073/pnas.162491399

Ji, Y., Wei, S., Hou, J., Zhang, C., Xue, P., Wang, J., et al. (2017). Integrated Proteomic and N-Glycoproteomic Analyses of Doxorubicin Sensitive and Resistant Ovarian Cancer Cells Reveal Glycoprotein Alteration in Protein Abundance and Glycosylation. *Oncotarget* 8 (8), 13413–13427. doi:10.18632/oncotarget.14542

Kefauver, J. M., Saotome, K., Dubin, A. E., Pallesen, J., Cottrell, C. A., Cahalan, S. M., et al. (2018). Structure of the Human Volume Regulated Anion Channel. *eLife* 7, e38461. doi:10.7554/eLife.38461

Kolli, V., Schumacher, K. N., and Dodds, E. D. (2015). Engaging Challenges in Glycoproteomics: Recent Advances in MS-based Glycopeptide Analysis. *Bioanalysis* 7 (1), 113–131. doi:10.4155/bio.14.272

Kuo, M. T., Fu, S., Savaraj, N., and Chen, H. H. (2012). Role of the Human High-Affinity Copper Transporter in Copper Homeostasis Regulation and Cisplatin Sensitivity in Cancer Chemotherapy. *Cancer Res.* 72 (18), 4616–4621. doi:10.1158/0008-5472.CAN-12-0888

Lau, K. S., and Dennis, J. W. (2008). N-glycans in Cancer Progression. *Glycobiology* 18 (10), 750–760. doi:10.1093/glycob/cwn071

Leavesley, D. I., Schwartz, M. A., Rosenfeld, M., and Cheresh, D. A. (1993). Integrin Beta 1- and Beta 3-mediated Endothelial Cell Migration Is Triggered through Distinct Signaling Mechanisms. *J. Cel Biol* 121 (1), 163–170. doi:10.1083/jcb.121.1.163

Li, K., Sun, Z., Zheng, J., Lu, Y., Bian, Y., Ye, M., et al. (2013). In-depth Research of Multidrug Resistance Related Cell Surface Glycoproteome in Gastric Cancer. *J. Proteomics* 82, 130–140. doi:10.1016/j.jprot.2013.02.021

Lin, G., Zhao, R., Wang, Y., Han, J., Gu, Y., Pan, Y., et al. (2020). Dynamic Analysis of N-Glycomic and Transcriptomic Changes in the Development of Ovarian Cancer Cell Line A2780 to its Three Cisplatin-Resistant Variants. *Ann. Transl. Med.* 8 (6), 289. doi:10.21037/atm.2020.03.12

Maryon, E. B., Molloy, S. A., and Kaplan, J. H. (2007). O-linked Glycosylation at Threonine 27 Protects the Copper Transporter hCTR1 from Proteolytic Cleavage in Mammalian Cells. *J. Biol. Chem.* 282 (28), 20376–20387. doi:10.1074/jbc.M701806200

Mereiter, S., Balmaña, M., Campos, D., Gomes, J., and Reis, C. A. (2019). Glycosylation in the Era of Cancer-Targeted Therapy: Where Are We Heading?. *Cancer Cell* 36 (1), 6–16. doi:10.1016/j.ccell.2019.06.006

Michaud, W. A., Nichols, A. C., Mroz, E. A., Faquin, W. C., Clark, J. R., Begum, S., et al. (2009). Bcl-2 Blocks Cisplatin-Induced Apoptosis and Predicts Poor Outcome Following Chemoradiation Treatment in Advanced Oropharyngeal Squamous Cell Carcinoma. *Clin. Cancer Res.* 15 (5), 1645–1654. doi:10.1158/1078-0432.CCR-08-2581

Noda, I., Fujieda, S., Seki, M., Tanaka, N., Sunaga, H., Ohtsubo, T., et al. (1999). Inhibition of N-Linked Glycosylation by Tunicamycin Enhances Sensitivity to Cisplatin in Human Head-And-Neck Carcinoma Cells. *Int. J. Cancer* 80 (2), 279–284. doi:10.1002/(sici)1097-0215(19990118)80:2<279:aid-ijc18>3.0.co;2-n

Ogen-Shtern, N., Avezov, E., Shenkman, M., Benyair, R., and Lederkremer, G. Z. (2016). Mannosidase IA Is in Quality Control Vesicles and Participates in Glycoprotein Targeting to ERAD. *J. Mol. Biol.* 428 (16), 3194–3205. doi:10.1016/j.jmb.2016.04.020

Pili, R., Chang, J., Partis, R. A., Mueller, R. A., Chrest, F. J., and Passaniti, A. (1995). The Alpha-Glucosidase I Inhibitor Castanospermine Alters Endothelial Cell Glycosylation, Prevents Angiogenesis, and Inhibits Tumor Growth. *Cancer Res.* 55 (13), 2920–2926.

Planells-Cases, R., Lutter, D., Guyader, C., Gerhards, N. M., Ullrich, F., Elger, D. A., et al. (2015). Subunit Composition of VRAC Channels Determines Substrate Specificity and Cellular Resistance to Pt-Based Anti-cancer Drugs. *EMBO J.* 34 (24), 2993–3008. doi:10.15252/embj.201592409

Robey, R. W., Pluchino, K. M., Hall, M. D., Fojo, A. T., Bates, S. E., and Gottesman, M. M. (2018). Revisiting the Role of ABC Transporters in Multidrug-Resistant Cancer. *Nat. Rev. Cancer* 18 (7), 452–464. doi:10.1038/s41568-018-0005-8

Rottenberg, S., Disler, C., and Perego, P. (2021). The Rediscovery of Platinum-Based Cancer Therapy. *Nat. Rev. Cancer* 21 (1), 37–50. doi:10.1038/s41568-020-00308-y

Ruhaak, L. R., Xu, G., Li, Q., Goonatilleke, E., and Lebrilla, C. B. (2018). Mass Spectrometry Approaches to Glycomic and Glycoproteomic Analyses. *Chem. Rev.* 118 (17), 7886–7930. doi:10.1021/acs.chemrev.7b00732

Shah, P., Wang, X., Yang, W., Toghi Eshghi, S., Sun, S., Hoti, N., et al. (2015). Integrated Proteomic and Glycoproteomic Analyses of Prostate Cancer Cells Reveal Glycoprotein Alteration in Protein Abundance and Glycosylation. *Mol. Cel. Proteomics* 14 (10), 2753–2763. doi:10.1074/mcp.M115.047928

Singh, A., Singh, A., Grover, S., Pandey, B., Kumari, A., and Grover, A. (2018). Wild-type Catalase Peroxidase vs G279D Mutant Type: Molecular Basis of Isoniazid Drug Resistance in *Mycobacterium tuberculosis*. *Gene* 641, 226–234. doi:10.1016/j.gene.2017.10.047

Sørensen, B. H., Dam, C. S., Stürup, S., and Lambert, I. H. (2016). Dual Role of LRRC8A-Containing Transporters on Cisplatin Resistance in Human Ovarian Cancer Cells. *J. Inorg. Biochem.* 160, 287–295. doi:10.1016/j.jinorgbio.2016.04.004

Sun, Z., Dong, J., Zhang, S., Hu, Z., Cheng, K., Li, K., et al. (2014). Identification of Chemoresistance-Related Cell-Surface Glycoproteins in Leukemia Cells and Functional Validation of Candidate Glycoproteins. *J. Proteome Res.* 13 (3), 1593–1601. doi:10.1021/pr4010822

Voss, F. K., Ullrich, F., Münch, J., Lazarow, K., Lutter, D., Mah, N., et al. (2014). Identification of LRRC8 Heteromers as an Essential Component of the Volume-Regulated Anion Channel VRAC. *Science* 344(6184), 634–638. doi:doi:doi:10.1126/science.1252826

Wang, F., Luo, Q., Zhang, Y., Zhao, Y., Wu, K., and Wang, F. (2021). The Disturbance of Anticancer Drug Cisplatin to Cellular Homeostasis of Trace Elements Revealed by ICP-MS and ToF-SIMS. *At.Spectrosc.* 42 (3), 9. doi:10.46770/as.2021.106

Wang, S., Li, W., Hu, L., Cheng, J., Yang, H., and Liu, Y. (2020). NAguideR: Performing and Prioritizing Missing Value Imputations for Consistent Bottom-Up Proteomic Analyses. *Nucleic Acids Res.* 48 (14), e83. doi:10.1093/nar/gkaa498

Wen, X., Buckley, B., McCandlish, E., Goedken, M. J., Syed, S., Pelis, R., et al. (2014). Transgenic Expression of the Human MRP2 Transporter Reduces Cisplatin Accumulation and Nephrotoxicity in Mrp2-Null Mice. *Am. J. Pathol.* 184 (5), 1299–1308. doi:10.1016/j.ajpath.2014.01.025

Wu, J., Chen, S., Liu, H., Zhang, Z., Ni, Z., Chen, J., et al. (2018). Tunicamycin Specifically Aggravates ER Stress and Overcomes Chemoresistance in Multidrug-Resistant Gastric Cancer Cells by Inhibiting N-Glycosylation. *J. Exp. Clin. Cancer Res.* 37 (1), 272. doi:10.1186/s13046-018-0935-8

Wu, Y., Jin, D., Wang, X., Du, J., Di, W., An, J., et al. (2019). UBE2C Induces Cisplatin Resistance via ZEB1/2-dependent Upregulation of ABCG2 and ERCC1 in NSCLC Cells. *J. Oncol.* 2019, 8607859. doi:10.1155/2019/8607859

Yamasaki, M., Makino, T., Masuzawa, T., Kurokawa, Y., Miyata, H., Takiguchi, S., et al. (2011). Role of Multidrug Resistance Protein 2 (MRP2) in Chemoresistance and Clinical Outcome in Oesophageal Squamous Cell Carcinoma. *Br. J. Cancer* 104 (4), 707–713. doi:10.1038/sj.bjc.6606071

Yi, D., Xu, L., Wang, R., Lu, X., and Sang, J. (2019). miR-381 Overcomes Cisplatin Resistance in Breast Cancer by Targeting MDR1. *Cell Biol. Int.* 43 (1), 12–21. doi:10.1002/cbin.11071

Zhang, Y., Jiao, J., Yang, P., and Lu, H. (2014). Mass Spectrometry-Based N-Glycoproteomics for Cancer Biomarker Discovery. *Clin. Proteomics* 11 (1), 18. doi:10.1186/1559-0275-11-18

Zhang, Y., Mao, Y., Zhao, W., Su, T., Zhong, Y., Fu, L., et al. (2020). Glyco-CPLL: An Integrated Method for In-Depth and Comprehensive N-Glycoproteome Profiling of Human Plasma. *J. Proteome Res.* 19 (2), 655–666. doi:10.1021/acs.jproteome.9b00557

Zhong, C., Li, P., Argade, S., Liu, L., Chilla', A., Liang, W., et al. (2020). Inhibition of Protein Glycosylation Is a Novel Pro-angiogenic Strategy that Acts via Activation of Stress Pathways. *Nat. Commun.* 11 (1), 6330. doi:10.1038/s41467-020-20108-0

Zhou, Q., Shankara, S., Roy, A., Qiu, H., Estes, S., McVie-Wylie, A., et al. (2008). Development of a Simple and Rapid Method for Producing Non-fucosylated Oligomannose Containing Antibodies with Increased Effector Function. *Biotechnol. Bioeng.* 99 (3), 652–665. doi:10.1002/bit.21598

Conflict of Interest: The authors declare that the research was conducted in the absence of any commercial or financial relationships that could be construed as a potential conflict of interest.

Publisher's Note: All claims expressed in this article are solely those of the authors and do not necessarily represent those of their affiliated organizations, or those of the publisher, the editors and the reviewers. Any product that may be evaluated in this article, or claim that may be made by its manufacturer, is not guaranteed or endorsed by the publisher.

frontiers in Pharmacology

ORIGINAL RESEARCH
published: 18 March 2022
doi: 10.3389/fphar.2022.862504

Mechanistic Insights Into Co-Administration of Allosteric and Orthosteric Drugs to Overcome Drug-Resistance in T315I BCR-ABL1

Hao Zhang[1,2†], Mingsheng Zhu[3†], Mingzi Li[1†], Duan Ni[4], Yuanhao Wang[4], Liping Deng[1], Kui Du[1], Shaoyong Lu[4]*, Hui Shi[6]* and Chen Cai[5]**

[1]School of Chemistry and Chemical Engineering, Shaoxing University, Shaoxing, China, [2]Department of Plastic and Reconstructive Surgery, Shanghai Ninth People's Hospital, Shanghai Jiao Tong University, School of Medicine, Shanghai, China, [3]Department of Anesthesiology, Huashan Hospital Affiliated to Fudan University, Shanghai, China, [4]Medicinal Chemistry and Bioinformatics Center, Shanghai Jiao Tong University, School of Medicine, Shanghai, China, [5]Department of VIP Clinic, Changhai Hospital, Navy Medical University, Shanghai, China, [6]Department of Respiratory and Critical Care Medicine, Changhai Hospital, Navy Medical University, Shanghai, China

OPEN ACCESS

Edited by:
Simona Rapposelli,
University of Pisa, Italy

Reviewed by:
Ruth Nussinov,
National Cancer Institute (NIH), United States
Jinan Wang,
University of Kansas, United States

***Correspondence:**
Shaoyong Lu
lushaoyong@sjtu.edu.cn
Kui Du
dkui@usx.edu.cn
Hui Shi
pooh_shi@163.com
Chen Cai
Cai_chen1978@163.com

[†]These authors have contributed equally to this work

Specialty section:
This article was submitted to Pharmacology of Anti-Cancer Drugs, a section of the journal Frontiers in Pharmacology

Received: 26 January 2022
Accepted: 28 February 2022
Published: 18 March 2022

Citation:
Zhang H, Zhu M, Li M, Ni D, Wang Y, Deng L, Du K, Lu S, Shi H and Cai C (2022) Mechanistic Insights Into Co-Administration of Allosteric and Orthosteric Drugs to Overcome Drug-Resistance in T315I BCR-ABL1. Front. Pharmacol. 13:862504. doi: 10.3389/fphar.2022.862504

Chronic myeloid leukemia (CML) is a myeloproliferative neoplasm, driven by the BCR-ABL1 fusion oncoprotein. The discovery of orthosteric BCR-ABL1 tyrosine kinase inhibitors (TKIs) targeting its active ATP-binding pocket, such as first-generation Imatinib and second-generation Nilotinib (NIL), has profoundly revolutionized the therapeutic landscape of CML. However, currently targeted therapeutics still face considerable challenges with the inevitable emergence of drug-resistant mutations within BCR-ABL1. One of the most common resistant mutations in BCR-ABL1 is the T315I gatekeeper mutation, which confers resistance to most current TKIs in use. To resolve such conundrum, co-administration of orthosteric TKIs and allosteric drugs offers a novel paradigm to tackle drug resistance. Remarkably, previous studies have confirmed that the dual targeting BCR-ABL1 utilizing orthosteric TKI NIL and allosteric inhibitor ABL001 resulted in eradication of the CML xenograft tumors, exhibiting promising therapeutic potential. Previous studies have demonstrated the cooperated mechanism of two drugs. However, the conformational landscapes of synergistic effects remain unclear, hampering future efforts in optimizations and improvements. Hence, extensive large-scale molecular dynamics (MD) simulations of wide type (WT), WT-NIL, T315I, T315I-NIL, T315I-ABL001 and T315I-ABL001-NIL systems were carried out in an attempt to address such question. Simulation data revealed that the dynamic landscape of NIL-bound BCR-ABL1 was significantly reshaped upon ABL001 binding, as it shifted from an active conformation towards an inactive conformation. The community network of allosteric signaling was analyzed to elucidate the atomistic overview of allosteric regulation within BCR-ABL1. Moreover, binding free energy analysis unveiled that the affinity of NIL to BCR-ABL1 increased by the induction of ABL001, which led to its favorable binding and the release of drug resistance. The findings uncovered the in-depth structural mechanisms underpinning dual-targeting towards T315I BCR-ABL1 to

overcome its drug resistance and will offer guidance for the rational design of next generations of BCR-ABL1 modulators and future combinatory therapeutic regimens.

Keywords: chronic myelogenous leukemia (CML), BCR-ABL1, tyrosine kinase inhibitors (TKIs), nilotinib, drug resistance, ABL001, allosteric drug, combinatory treatment

INTRODUCTION

Targeted drug therapy strikes specifically at defined carcinogenic targets representing a therapeutic breakthrough in human cancer treatments (Bozic et al., 2013). Kinase, one of the largest gene families, is a class of critical drug targets (Manning et al., 2002; Qiu et al., 2021a; Wang et al., 2021), and kinase inhibitors have revolutionized cancer therapeutics. Traditionally, most kinases inhibitors target the ATP-binding site, also known as orthosteric site. Prolonged administration of inhibitors often leads to inevitable emergence of resistant mutations, which subsequently results in diminished therapeutic efficacy (Nussinov et al., 2017, 2021; Agnello et al., 2019), posing a huge challenge to drug development and threatening global public health (Holohan et al., 2013). Compared to orthosteric ligands bounding to conserved orthosteric sites, allosteric modulators bind to structurally diverse allosteric sites (Lu et al., 2021) and yield pivotal advantages in terms of high specificity and selectivity in the paradigm of precision medicine (Guarnera and Berezovsky, 2016; Lu et al., 2019c; Lu and Zhang, 2019). In addition, allosteric drugs could act together with orthosteric inhibitors to exert synergistic and allosteric effects on a protein, potentially restoring or even boosting the efficacy of orthosteric inhibitors (Ma et al., 2016; Huang et al., 2021). Hence, co-administration of allosteric and orthosteric inhibitors offers a revolutionary strategy to conquer the notorious problem of drug resistance (Al-Lazikani et al., 2012; Nussinov et al., 2017; Ni et al., 2020a; Zhang et al., 2020).

The most recent successful example of combining allosteric and orthosteric drugs to circumvent drug resistance is the treatment of chronic myeloid leukemia (CML) by targeting Breakpoint Cluster Region-Abelson1 (BCR-ABL1) kinase (Heisterkamp et al., 1985). CML is driven by the reciprocal translocation between chromosomes 9 and 22, leading to the fusion of the Breakpoint Cluster Region (BCR) and Abelson1 (ABL1) genes on the Philadelphia chromosome (Ph) (Apperley, 2015). The expression of BCR-ABL1 which has a constitutively active ABL1 kinase domain leads to aberrant activation of numerous signaling pathways finally resulting in the dysregulated differentiation, growth, and survival of leukemic cells (Melo, 1996). In recent years, the prognosis of CML patients has been improved due to the promotion of tyrosine kinase inhibitors (TKIs), including imatinib, dasatinib, nilotinib (NIL) and ponatinib, inhibiting the kinase activity of BCR-ABL1 by targeting its adenosine triphosphate (ATP) -binding site (Jabbour and Kantarjian, 2016). More than 80% of patients treated with TKI had improved survival rates of more than 10 years (Kalmanti et al., 2015). However, some patients suffer from loss of response to TKIs, usually associated with drug resistance generated by BCR-ABL1 kinase mutations that impede drug binding (Pophali and Patnaik, 2016). In particular, the T315I gatekeeper mutation with a frequency up to 30% in BCR-ABL1 (Chahardouli et al., 2013), is resistant to first- and second-generation TKIs except ponatinib whose dosing is limited by adverse events (Quintás-Cardama et al., 2007; Miller et al., 2014). To tackle the notorious problem of drug resistance, researchers have proposed the possibility of combinatorial treatments with allosteric and orthosteric drugs to against drug resistance.

Here we characterize Asciminib (ABL001), the first allosteric BCR-ABL1 inhibitor successfully entering phase III clinical trial and marketed (Deeks, 2022), which synergistically inhibits the BCR-ABL1 mutant with orthosteric drugs. Remarkably, previous studies have confirmed that the dual targeting towards BCR-ABL1 utilizing ABL001 and NIL resulted in complete disease control and eradication of the CML xenograft tumours without recurrence after discontinuation of treatment (Wylie et al., 2017), highlighting the great potential of the combinatory therapeutics of orthosteric and allosteric molecules. Previous studies have described the mechanism of BCR-ABL allosteric drugs and how they working conjointly with orthosteric drugs (Adrián et al., 2006; Zhang et al., 2010). Nevertheless, the detailed mechanism in conformational ensembles of their cooperative inhibition remains unclear.

Therefore, we applied extensive large-scale molecular dynamics (MD) simulations of wide type (WT), WT-NIL, T315I, T315I-NIL, T315I-ABL001 and T315I-ABL001-NIL systems to unravel the detailed molecular mechanistic of dual-targeting therapeutics to overcome drug resistance. Among these complexes, T315I, and T315-NIL are considered as resistant systems whose enzymatic activities were not successfully inhibited; whereas WT-NIL, T315I-ABL001, and T315I-ABL001-NIL are considered as sensitive systems, where the kinases within were successfully inactivated. Dissection of conformation landscapes of these systems found that the dynamic conformation of the ternary complex is the most stable. ABL001 could shift NIL-bound active BCR-ABL1 to inactive conformation by modulating the conformation of key structural domains utilizing Markov state model (MSM) analysis. The binding free energy analysis showed that the affinity of NIL to BCR-ABL1 was strengthened upon ABL001 binding, thus exerting concerted effects on improving the overall therapeutic efficacy. The community network of allosteric signaling was described, to gain an atomistic view of allosteric regulation within BCR-ABL1. Moreover, the allosteric crosstalk between the allosteric site and ATP-binding pocket was investigated utilizing energetic dynamics computations.

Collectively, the findings uncovered the in-depth structural mechanisms underpinning dual-targeting towards BCR-ABL1. This will help offer guidance for the rational design of future generations of BCR-ABL1 modulators and provide novel insights

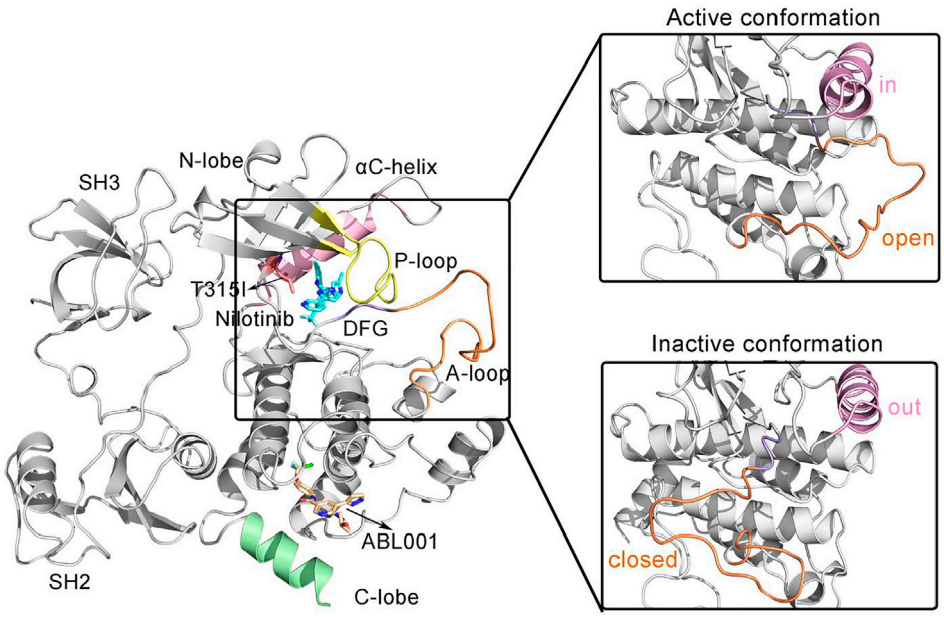

FIGURE 1 | The overall structure of the allosteric drug ABL001 (off-white) bound to the myristoyl pocket and the second generation TKI NIL (cyan) bound to the ATP-pocket in a ternary complex with BCR-ABL1 fusion protein (PDB ID: 5mo4). The backbone of BCR-ABL1 structure is represented in gray. Key structural elements are highlighted in orange (A-loop), yellow (P-loop), pink (αC-helix), and purple (DFG motif), respectively.

into the regulation of receptor tyrosine kinase (Nussinov et al., 2014). The cooperative targeting of orthosteric and allosteric inhibitors to address drug resistance provides proof of exemplifying for clinical optimization of co-administration therapy in the future.

RESULTS

Overview of the Ternary Complex Structure

The structural domain of BCR-ABL1 protein is organized similarly to Src family kinases, with contiguous Src homolog 2 (SH2) and SH3 domains, an SH2/kinase linker, and a bilobal kinase domain (**Figure 1**) (Panjarian et al., 2013).

SH3 and SH2 domains are among the most common modular protein-protein interaction domains in human proteins (Sherbenou et al., 2010). Structurally, the SH3 domain consists of two short antiparallel β-sheets forming a barrel-shaped structure, and the SH2 domain comprises a central antiparallel β-sheet flanked by α-helices. Deletion or mutations of the SH3 and SH2 structural domains results in upregulation of ABL1 kinase activity, suggesting that the SH3 and SH2 structural domains together inhibit kinase activation (Mayer and Baltimore, 1994).

The core catalytic domain of kinase adopts a bilobed architecture, consisting of a small N-terminal lobe (N-lobe) followed by a large C-terminal lobe (C-lobe), which is in charge of catalyzing the transfer of γ-phosphate from ATP to tyrosine residues of substrate proteins. The N-lobe consists of β1-β5 sheets and an important αC-helix. A glycine-rich loop (or Wolker loop) connects the β1 and β2 strands, also known as the P-loop that is critical for binding ATP. The P-loop is highly flexible, so it can be interspersed between the β- and γ-phosphates of the substrate ATP to facilitate phosphoryl transfer reactions. Whereas the C-lobe consists mainly of α-helices. Within the C-lobe, the activation loop (A-loop), the most flexible part of BCR-ABL1, is a principal regulatory structure for modulating kinase activity (Schindler et al., 2000; Sonti et al., 2018). A conserved "DFG" motif (D381-F382-G383) motif implicated in ATP binding is located at the N-terminus of A-loop (Lovera et al., 2012). In the active conformation of Abl1 kinase, the A-loop is in an "open" or "extended" conformation. In this conformation, the body of the A loop does not block the C-lobe, enabling the C-lobe to be available for binding the substrate. The D381 within the DFG conserved motif is oriented toward the ATP binding pocket, also known as DFG-in active conformation, and its carboxylic acid functional group binds the Mg coordinated to ATP in active kinases. While in the "closed" form, the A-loop could block substrate binding to the C-lobe. The Abl kinase domain switches from an active from to an inactive form, resulting in a conformational change at the start of the A loop. This flips the orientation of the DFG motif by 180°, termed DFG-out conformation (Shan et al., 2009). With the Asp side chain is flipped away from the ATP binding site, Mg coordination (with the Mg-ATP complex) is prevented. Additional conformational changes upon the ABL1 activity transition include the rotation orthogonal to main axis of αC-helix (Fajer et al., 2017). In the active ABL1 kinase, the αC helix is rotated inward, also known as the "in" position, allowing a salt bridge to form between E286 and K271 in the β-III sheet lining the ATP binding pocket. This salt bridge between two highly conserved residues is considered to be critical for a catalytically competent kinase active site. In the

inactive state, E286 along the αC-helix points away from the binding pocket, adopting the "out" conformation. E286 whereas interacts with Arg386 in the A-loop and the salt bridge breaks (Paul et al., 2020). Furthermore, there is a "myristate binding pocket" located in the C-lobe. The myristoyl group covalently attached to the N-terminal end of ABL1 prior to fusion with BCR and induced an assembly inactive state (Nagar et al., 2003). However, this natural autoregulation mechanism disappears after the BCR fragment replaces the N-terminal cap region of ABL1 containing the myristoylation site, resulting in structural activation of BCR-ABL1.

The N-lobe and C-lobe of the kinase are connected by a hinge domain, which contains several conserved residues that provide the catalytic machinery and make up an essential part of the ATP binding pocket, also participating in substrate binding. The catalytic pocket situates at the interface between the N-lobe and C-lobe where the substrate binds. TKIs currently approved for the treatment of CML were designed to target the catalytic ATP binding site of BCR-ABL1, whose efficacy tends to be compromised due to resistance mutations. Especially, there is a "gatekeeper" residue Thr315 within this pocket involved in ATP binding that plays a critical role in stabilizing the active conformation of BCR-ABL1 (Liu et al., 1998). The T315I gatekeeper mutation always leads to recalcitrant resistance to TKIs, with a frequency up to 30% in BCR-ABL1 (Gorre et al., 2001).

NIL, a second-generation TKI, was computationally designed to overcome BCR-ABL1's resistance to the first-generation TKI imatinib (Kantarjian et al., 2011). Although NIL is effective in suppressing most mutations within BCR-ABL1, it still failed to counteract the T315I gatekeeper mutation. However, recent research has shown that the notorious T315I resistance could be tamed by the combination of ABL001 and NIL without recurrence after the cessation of treatment. In contrast to catalytic-site ABL1 kinase inhibitors, ABL001 was developed using fragment-based NMR screening X-ray for the myristate pocket of ABL1 that is normally occupied by the myristoylated N-terminal of ABL1—a motif that serves as an allosteric negative regulatory element lost upon fusion of ABL1 to BCR (Schoepfer et al., 2018). Structural analysis showed that ABL001 forms hydrophobic interactions mainly with BCR-ABL1, and induces an inactive kinase conformation. To explore the mechanism underlying cooperatively double targeting of ABL001 and NIL towards BCR-ABL1, MD simulations were carried out for six systems, WT, WT-NIL, T315I, T315I-NIL, T315I-ABL001, and T315I-ABL001-NIL, in an attempt to pursue deeper insight into the drug combinations to overcome T135I resistance.

Allosteric Drug Enhanced System Stability

We calculated the Cα atoms root-mean-square deviation (RMSD) of each system versus initial structures to interrogate the dynamic conformational alterations during simulations. RMSD data indicated that all six systems began to reach equilibrium after 600 ns of simulations (**Supplementary Figure S1A**), and our further analyses focused on the trajectories under equilibrium states. The RMSD values for the six systems were 3.35 ± 0.43(WT), 2.90 ± 0.6(WT-NIL), 3.13 ± 0.33(T315I), 3.20 ± 0.45(T315I-NIL), 3.10 ± 0.48(T315I-ABL001) and 2.67 ± 0.39 Å (T315I-ABL001-NIL), respectively. They were not significantly different among the systems, implying that the single mutation T315I did not affect the overall protein stability. The RMSD value of the T35I-ABL001-NIL system was the lowest, suggesting this system might exhibit the most stable conformational dynamics.

To quantify the local conformation dynamics of BCR-ABL1, the atomic root-mean-square fluctuations (RMSFs) of Cα atoms around its original position were calculated for each residue (**Supplementary Figure S1B**), which was projected onto the structure of ABL1 in each system for visualization (**Figure 2**). The RMSF values for the six systems were 1.30 ± 0.71(WT), 1.35 ± 0.80(WT-NIL), 1.28 ± 0.72(T315I), 1.30 ± 0.63(T315I-NIL), 1.26 ± 0.61(T315I-ABL001) and 1.17 ± 0.64 Å (T315I-ABL001-NIL), respectively. Analysis of the RMSF profiles of the six systems showed that the T35I-ABL001-NIL system typically displayed a lower RMSF, suggesting that this system was relatively more stable. Notably, the functional domains such as αC-helix and A-loop, which played critical roles in the binding of TKIs, displayed relatively higher RMSFs in each system, demonstrating their elasticity and critical implication in TKI drugging. We thus mainly focused on these domains in following analysis.

Principal component analysis (PCA) was next conducted to identify the predominant overall conformational transitions of BCR-ABL1 (Amadei et al., 1993). Porcupine diagrams were constructed where PC1 was projected onto initiation structure of each system to graphically visualize the dominant motions of different regions in BCR-ABL1 throughout the simulation (**Figure 3**).

The principal dynamic motions of BCR-ABL1 system mainly resided on its A loop and αC-helix, which is in accordance with the RMSF data. Particularly, systems exhibited the most prominent differences in the motion vectors of A-loop. We observed that NIL relieved the downward movement of the A-loop in the WT system and conversely induced an upward motion. It thus locked the kinase in an inactive conformation. In contrast, in the T315I-NIL system, the A-loop remained a downward opening orientation possibly due to the hindrance from the resistant T315I mutation towards NIL. Furthermore, in the T315I-ABL001 and T315I-ABL001-NIL systems, ABL001 inhibited kinase activity by allosteric regulation during which the A-loop, readout of kinase activity, exhibited elevat motion.

Overall, in the WT, T315I and T315I-NIL systems where BCR-ABL1 was in active state, the global movement trends of the protein were large. While the overall kinase movement tendency was smaller and the global structures were more stabilized in the WT-NIL, T315I-ABL001 and T315I-ABL001-NIL systems, which were in accordance with their successful inhibition by different drugs respectively, especially in the dual-targeting ternary system.

Drug Combination Limited Correlated Motions Between Domains

To explore the intra-chain correlation within all systems, residue interactions in each system were quantified through dynamic

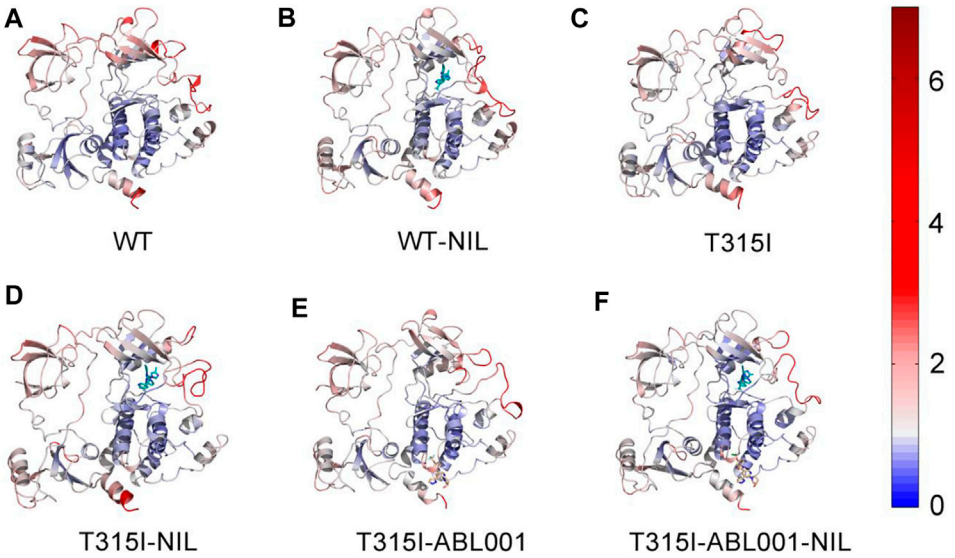

FIGURE 2 | The Cα RMSFs of WT **(A)**, WT-NIL **(B)**, T315I **(C)**, T315I-NIL **(D)**, T315I-ABL001 **(E)** and T315I-ABL001-NIL **(F)** systems along 3,000 ns MD simulations were projected onto the structure of BCR-ABL1.

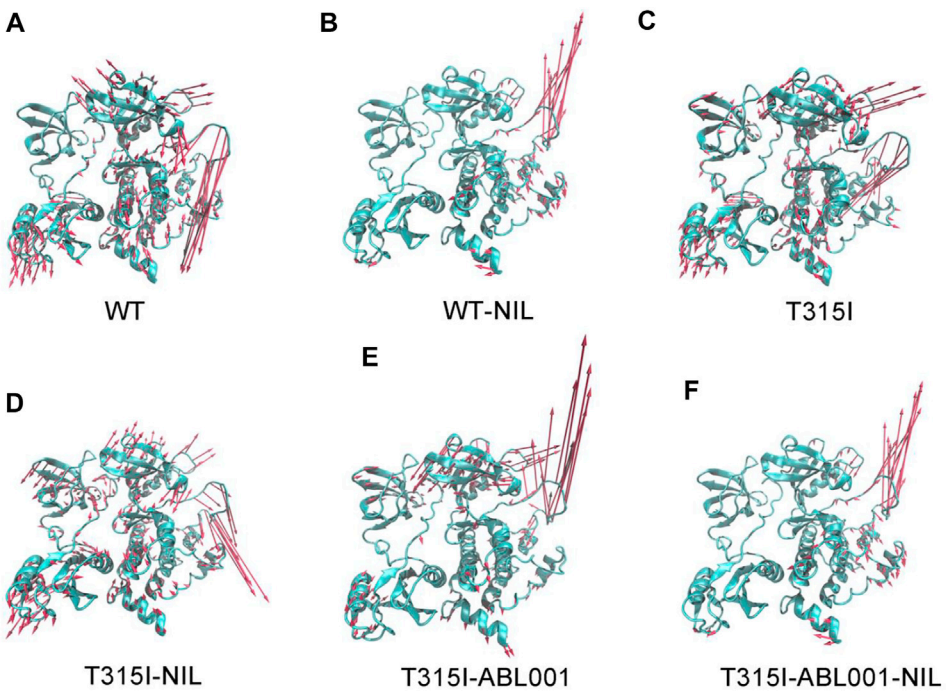

FIGURE 3 | Comparison of principal mode of motion along PC1 in WT **(A)**, WT-NIL **(B)**, T315I **(C)**, T315I-NIL **(D)**, T315I-ABL001 **(E)** and T315I-ABL001-NIL **(F)** systems. Red arrows depict the directions of protein motions, while the length of the arrows represents the magnitude of the movements.

cross-correlation matrices (DCCMs) (**Figure 4**). The dynamic correlated motions of the WT-NIL system were markedly reduced compared with the WT system, indicating that NIL might stabilize the residual interactions within BCR-ABL1, conferring its inhibitory activity. However, compared with the T315I system, the T315I-NIL system exhibited a slight elevation of correlated motions in the T315I-NIL system, which may be related to the inability of NIL to suppress T315I mutation. In contrast, the T315I-ABL001 system exhibit a lower value of DCCM globally. Overall, in the T315I-ABL001-NIL system, the dynamic correlated motion amplitude was the lowest (**Figure 4F**), indicating that the residue interactions within this

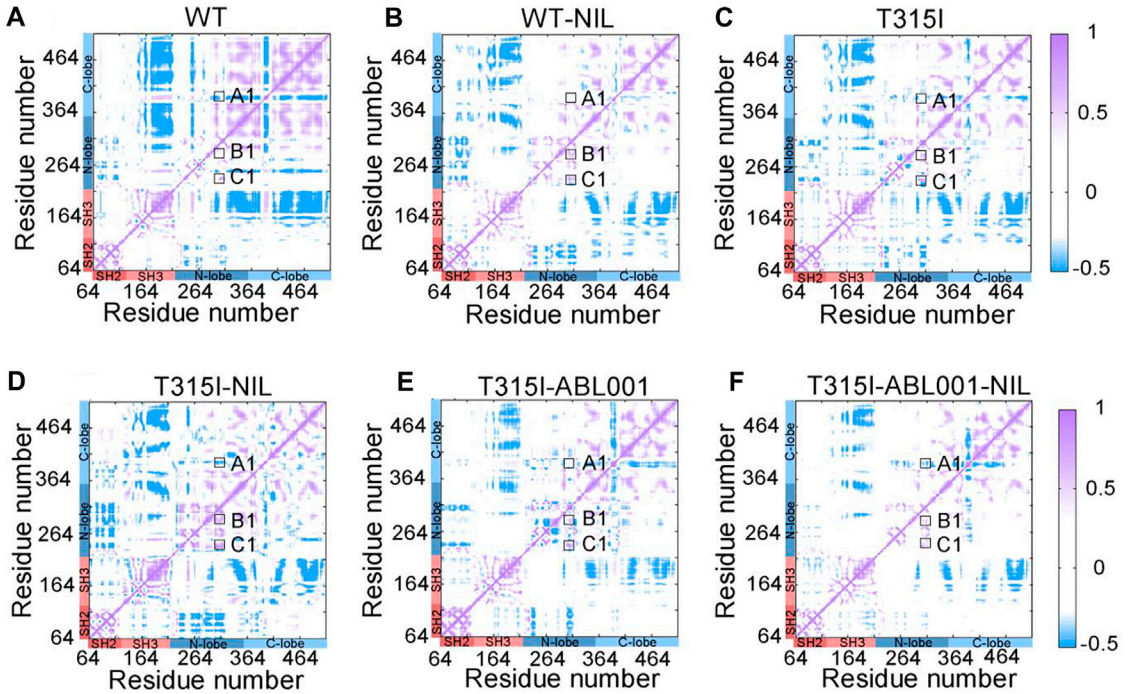

FIGURE 4 | DCCM plots of WT **(A)**, WT-NIL **(B)**, T315I **(C),** T315I-NIL **(D)**, T315I-ABL001 **(E)**, and T315I-ABL001-NIL **(F)** systems. Positive areas (purple) represent correlated motion, while negative areas (blue) stand for anti-correlated motion. Correlation motions with absolute values less than 0.3 are ignored and displayed in white.

system were the most stable, which was consistent with the RMSF and PCA analysis.

In particular, we observed that DCCM was weakened in A-loop (A1) and enhanced in the αC-helix (B1) and P-loop (C1) in the T315I system, compared with WT system, implying that the T315I mutation was anti-correlated with A-loop whereas positively associated with the movements of αC-helix and P-loop. In the T315I system, the binding of NIL failed to suppress the mutation, and A1, B1, C1 all became larger, enhancing the coupling between the mutated residue T315I and A-loop, αC-helix and P-loop. While A1, B1, and C1 were slightly reduced in the T315I-ABL001 complex compared with T315I system, implying ABL001 led to weakened coupling. Furthermore, in the co-administered T315I-ABL001-NIL system, A1, B1, and C1 were the weakest, indicating the weakest coupling between T315I and important structural domains mentioned above. The outcome is consistent with the clinical fact that the combination of TKI and ABL001 can successfully inhibit T315I BCR-ABL1, while TKI alone failed to inhibit T315I.

Co-Administration of NIL and ABL001 Reprogrammed Structural Community and Allosteric Signal Network Within BCR-ABL1

We next explored the propagation pathways of the allosteric signal through community analysis based on the Girvan-Newman algorithm, and quantitatively estimated the variational coupling among the communities. Throughout the trajectory, residues within a cut-off distance of 4.5 Å for at least 75% of simulation time were classified in the same community, which were considered as a synergistic functional unit within the overall structure. The visualized community network graphs clearly depicted the paths and the corresponding intensity of allosteric crosstalk, allowing visual comparison of the allosteric network within BCR-ABL1 among different systems (**Figure 5**).

In the WT system, community one was composed of SH3, while the majority of SH2 formed community 4, except for the connection between SH3 and SH2 that constituted community 12. Community three consisted of the majority of the C-lobe, including the P-loop. The αC-helix constituted community 8, and the rest of the C-lobe, A-loop, made up community 5. The N-lobe contained communities 2, 6, 7, and 10, where communities 2, 6, 7 enclosed the allosteric cavity of ABL001. Compared with WT (**Figure 5A**), upon NIL loading, community eight of was incorporated into community 2, indicating that the inhibitor strengthened the association within BCR-ABL1 N-lobe and might thereby capture the kinase in an inactive state (**Figure 5B**). When NIL was loaded into the T315I system (**Figure 5D**), community 11, representing the myristoyl pocket within the C-lobe, was independent from community six and had diminished signal linkage to surrounding residues as NIL failed to inhibit T315I BCR-ABL1 kinase activity. And the connection between community one and community three becomes weaker in T315I-ABL001 system compared with T315I system,

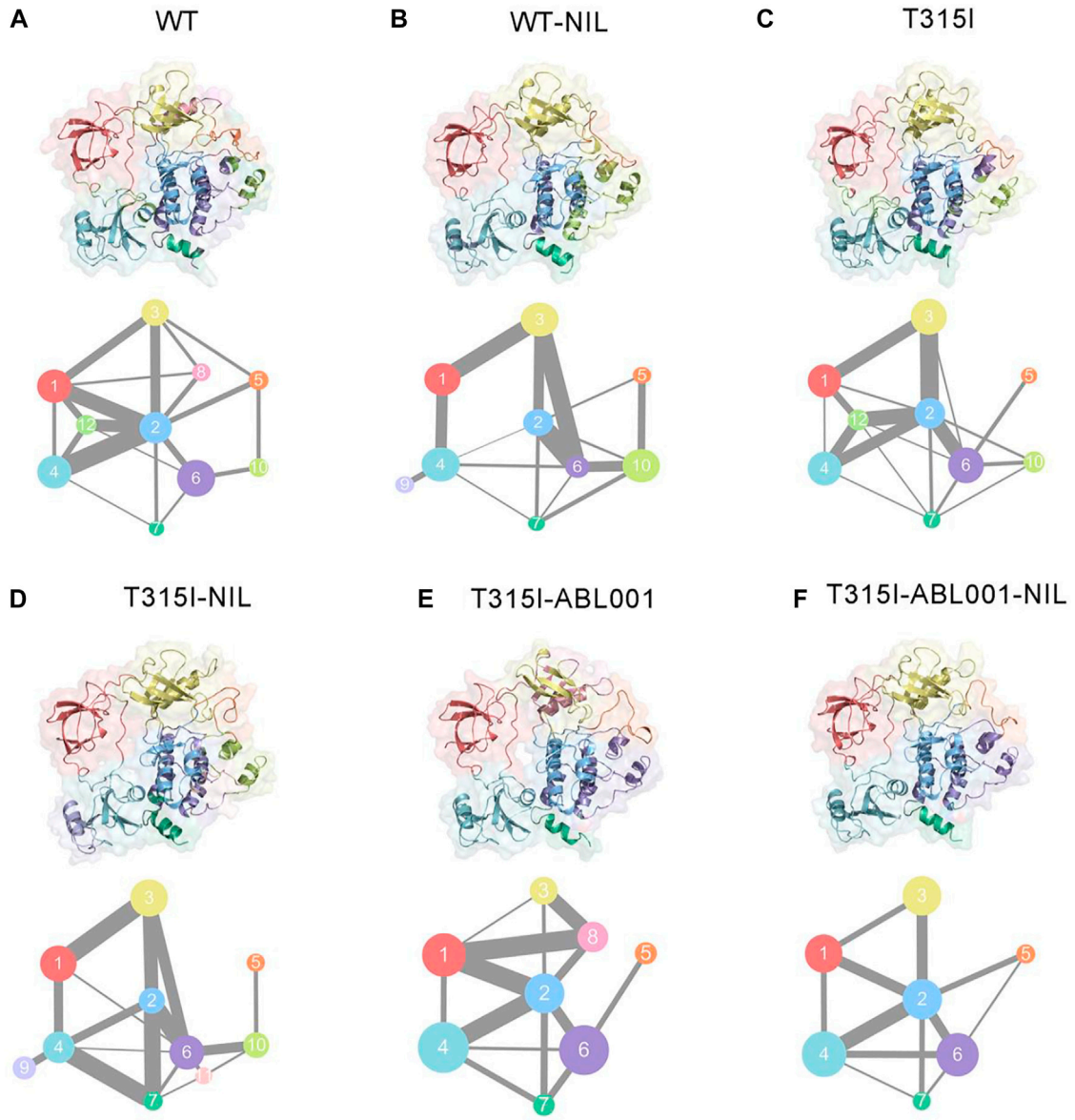

FIGURE 5 | Colored community networks of WT **(A)**, WT-NIL **(B)**, T315I **(C),** T315I-NIL **(D)**, T315I-ABL001 **(E)**, and T315I-ABL001-NIL **(F)**. Each sphere stands for an individual community with an area proportional to the number of residues it contains. While the lines connecting different spheres visualize the inter-community connections, and the thickness of these lines is proportional to the corresponding edge connectivity.

suggesting that ABL001 could induce a reduction in the perturbation of SH3 and N-lobe (**Figure 5E**). In the T315I-NIL-ABL001 system, distinct alterations were observed for the topologic characteristics and the inter-community communications within the BCR-ABL1 allosteric network compared with T315I-NIL system. Communities 10 and 11 that are close to the allosteric site are incorporated into community 6, indicating an enhanced signal transduction near the allosteric site, possibly explaining the allosteric effect in distant regions. The incorporation of community nine into community four within SH2 implies that the allosteric effect promoted the internal signal of the SH2 region. In addition, the connection between Community two and Community five was strengthened upon ABL001 binding, indicating an enhanced allosteric signal flow between them. This implied that some less important connections were quenched upon inhibitor binding, but specific signaling pathways were promoted to transmit the effects of the ligands.

Overall, there were 10 communities and 15 pathways in the T315I-NIL complex, 9 communities and 14 pathways in the T315I-AB001, and 8 communities and 11 pathways in the T315I-ABL001-NIL complex (**Figure 5F**). The reduction in the number of communities and the overall complexity of community connectivity following drug binding implied that

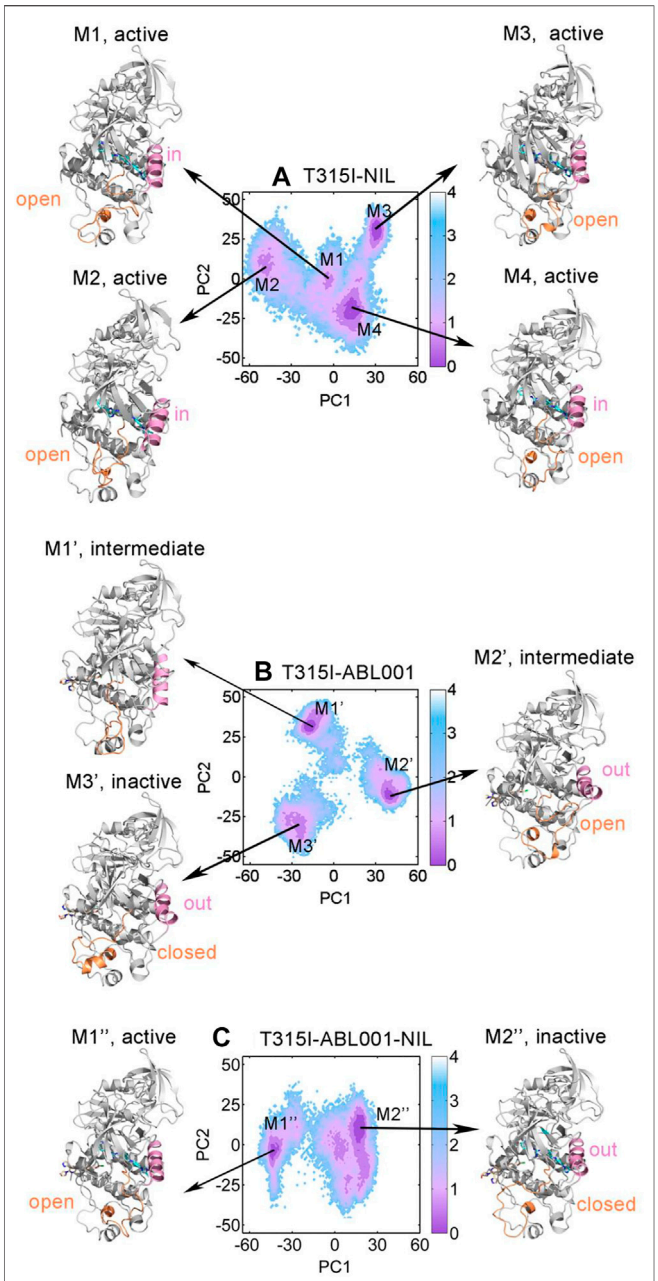

FIGURE 6 | Conformational landscapes of T315I-NIL **(A)**, T315I-ABL001 **(B)** and T315I-ABL001-NIL **(C)** were generated using PCA. Structural comparison of dominant intermediate state of T315I-NIL (M1, M2, M3, and M4), T315I-ABL001 (M1′, M2′, and M3′) and T315I-ABL001-NIL (M1″ and M2″), with the A-loop colored in orange and αC-helix in pink.

the co-binding of inhibitors significantly remodeled the topology of communities, possibly accounting for their inhibition.

Co-Binding of NIL and ABL001 Shifted BCR-ABL1 Towards Inactive State

Based on the results above, T315I-NIL, T315I-ABL001 and T315I-ABL001-NIL systems were selected to perform PCA to interrogate the overall free energy landscapes of the three relevant systems. The two most dominant collective principal components (PC1 and PC2) were used to project the overall conformation ensembles onto two dimensions (2D) plots to elaborate the conformational dynamics of the BCR-ABL1 during simulations. As shown in **Figure 6A**, T315I-NIL system exhibited four dominant conformations. The conformational ensembles of BCR-ABL1 were significantly changed upon ABL001 binding regardless of the presence or absence of NIL (**Figures 6B,C**). The T315I-ABL001 system had three major conformational clusters, whose global basin slightly shifted along the positive X-axis compared to the T315I-NIL system. The T315I-ABL001-NIL ternary complex, which contained two major structural clusters, had the lowest overall PCA values compared to the other two systems, indicating that the system had the least volatility.

To investigate their key conformational states during simulation, we applied PyEMMA (see Materials and Methods) for our complex systems to construct MSMs for analyses, which is powerful to probe into the protein conformations, unraveling unprecedented dynamic details (Lu et al., 2019b). Our models were first confirmed to be Markovian by the implied time scale tests (**Supplementary Figure S2**) and the Chapman-Kolmogorov tests (**Supplementary Figure S3**). Conformational ensembles for T315I-NIL, T315I-ABL001 and T315I-ABL001-NIL were then clustered into 4 (M1, M2, M3, and M4), 3 (M1', M2' and M3') and 2 (M1" and M2") MSM metastable states, respectively (**Figures 6A–C**). Comparative analysis of these dominant conformations showed that the whole backbone structure of BCR-ABL1 was

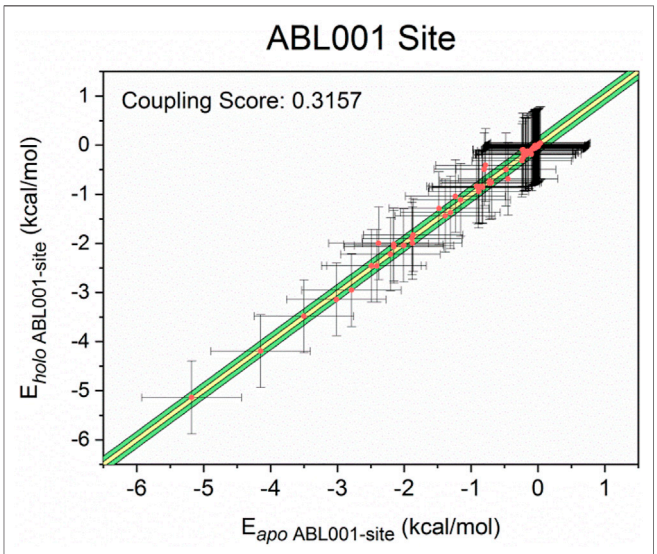

FIGURE 7 | Energy coupling analysis for the ABL001 site in *apo-(unbound)* and *holo- (NIL-bound)* BCR-ABL1. Each dot stands for a residue pair, and its intersection indicates the corresponding standard deviation. The yellow region indicated minor energy differences (one standard deviation, group a), the green regions indicated moderate energy differences (three standard deviations, group b), and the area beyond the green area represented major energy differences (greater than three standard deviations, group c).

TABLE 1 | Binding free energy analysis (kcal/mol) for the interactions between NIL and T315I BCR-ABL1 in T315I-NIL system and T315I-ABL001-NILsystem[a].

Energy component (kcal/mol)	T315I-NIL	T315I-ABL001-NIL
ΔG_{gas}	−101.34 (1.10)	−102.82 (1.39)
ΔG_{solv}	92.22 (1.14)	89.71 (1.44)
$\Delta G_{binding}$	−9.12 (1.42)	−13.11 (1.12)

[a]*Numbers in the parentheses are the standard deviations.*

stable during simulations, regardless of whether the kinase was successfully inhibited by drug.

The conformations of M1, M2, M3 and M4 in the T315I-NIL system all exhibited an A-loop open conformation and the αC-helix of M1, M2 and M4 showed a in conformation, implying their activated statuses. In the T315I-ABL001 system, the A-loop and αC-helix of M1' are in an intermediate state, and the A-loop of M2' exhibited an open state but αC-helix showed a distinct out conformation, implying that M1' and M2' were in an intermediate state. In contrast, the dominant conformation of M2', which accounted for about 54.6% of the structural cluster, showed an A-loop closed and αC-helix out conformation, revealing that ABL001 allosterically regulated the global conformation of T315I-ABL001 complex shifted towards an inactive state. Significantly, in the T315I-ABL001-NIL system, the dominant conformation of M2", which accounted for 75.5% of the overall structural ensemble, exhibited an inactive A-loop closed and αC-helix out conformation. The highest proportion of inactive conformation in the ensemble of the ternary complex system suggested that the co-binding of NIL and ABL001 might be the most effective in BCR-ABL1 inhibition, highlighting the synergistic effects between them.

Overall, conformational landscape analyses through MSMs unraveled that the combinatory regimen of NIL and ABL001 might function through trapping BCR-ABL1 in an inactive topology, suppressing its kinase activity.

Energetic Insights for Overcoming Drug Resistance

To investigate in-depth detailed mechanism by which ABL001 restores the action of NIL, the binding free energy ($\Delta G_{binding}$) between NIL and T315I BCR-ABL1 upon ABL001 binding or not was calculated using molecular mechanics/Poisson-Boltzmann surface area (MM/PBSA) methods. As shown in **Table 1**, the $\Delta G_{binding}$ of NIL to BCR-ABL1 kinase in T315I-NIL system was -9.12 ± 1.42 kcal/mol, while for the T315I-ABL001-NILsystem, the result was -13.11 ± 1.12 kcal/mol. For the ternary complex, the $\Delta G_{binding}$ was lower, implying the favorable binding of NIL and its higher affinity in this system, which could be the explanation for co-administration to overcome resistance in T315I mutation. Hence, dual-targeting overcomes drug resistance not only by stabilizing the dynamic conformation of BCR-ABL1, but also by enhancing the binding of NIL to kinase through the induction of ABL001.

Finally, for more insight into the synergistic effect of NIL and ABL001 to inhibit BCR-ABL1, a computational scheme was established to confirm the coupling between the orthosteric and allosteric sites (Ma et al., 2016). Previous studies have modeled residue-residue interactions in which a number of residue pairs within the allosteric sites displayed massive interaction energy alters upon ligand binding (Ni et al., 2020b; Zhang et al., 2021). On the basis of this model, we yielded a quantitative model that all residue pairs within the allosteric pocket were classified into three groups based on the difference in interaction energy before and after orthosteric binding: minor energy difference a), moderate energy difference b) and major energy difference c). The energy differences between residue pairs in the minor energy difference a) group were within one standard deviation of the mean (in the yellow area), while those in the moderate energy difference b) group were within three standard deviations (in the green area). In the major energy difference group c), the energy differences between residue pairs are distributed at least three standard deviations beyond the mean interaction energy change (outside the green area). We calculated the ratio of the number of residue pairs in group c) to the number of residue pairs in groups b) and c) as the energy coupling fraction, which represents the coupling between the orthosteric and allosteric sites. The energy coupling fraction threshold was 0.25, which was chosen based on a previous study. The energy coupling score for the allosteric ABL001 site is 0.3157 (**Figure 7**), which surpassed the threshold of 0.25. The residue-residue interaction free energy of a portion of the residue pairs within the ABL001 site changed considerably before and after NIL loading, suggesting that the orthosteric drug NIL perturbation leads to a reversal allosteric communication. The energy coupling fraction deciphered the crosstalk between orthosteric perturbations and allosteric pockets in an energetic perspective, reflecting the synergistic effect of orthosteric NIL and allosteric ABL001.

DISCUSSION

In the era of modern medicine, drug resistance is one of the leading challenges, posing great threats towards effective therapeutics, especially in infections and cancers (Beyer et al., 2018; Li et al., 2021). The development of new therapies to circumvent such conundrum are therefore urgently needed. Accumulating evidence suggests that allosteric drugs can target structurally diverse allosteric sites of the resistant orthosteric target, resensitizing the resistant target and thus restoring the efficacy of the orthosteric drug (Guarnera and Berezovsky, 2020). In addition, dual-targeting at allosteric and orthosteric sites could improve pharmacological effectiveness and cover a broader therapeutic spectrum than monotherapy. Hence, combinatory treatments are emerging as a novel trend, representing a revolutionary strategy to tackle drug resistance (Qiu et al., 2021b).

One of the quintessential examples of harnessing both orthosteric and allosteric drugs to overcome drug resistance is dual-targeting BCR-ABL1, one of the most crucial anti-cancer targets within tyrosine kinase family, for CML treatments. The

co-administration of allosteric drug ABL001 and classical TKIs targeting BCR-ABL1, (including imatinib, NIL, and dasatinib) for the therapy of CML achieved persistent and complete regression of the malignancy and addressed historically notorious resistance. Importantly, a recent clinical trial (Clinical Trial Number: NCT02081378) confirmed the efficacy of ABL001 in combination with TKIs for the treatment of CML. Such regimen was later approved for marketing by the FDA, highlighting its great therapeutic potential. However, the specific conformational landscapes mechanism of combination drug use to overcome T315I resistance mutation is unclear and needs to be studied in depth.

Here, based on computational biology system method, we illustrated the mechanism of dual-targeting therapy with BCR-ABL1. To gain an atomic structural view, a comparative MD simulation study and relevant analysis were conducted in the WT, WT-NIL, T315I, T315I-NIL, T315I-ABL001 and T315I-ABL001-NIL BCR-ABL1 systems for in-depth investigations on drug combinations to overcome T135I resistance. RMSD and RMSF analyses unveiled that the T3I5I-ABL001-NIL system had the lowest deviation and fluctuation values, indicating the dual-targeting system had the most stable conformational dynamics. DCCMs were carried out to reveal correlated motions in BCR-ABL1. The residue interactions within T315I-ABL001-NIL system were the most stable, suggesting that the drug combination limited the correlated motions between structural domains. Furthermore, The visualized community network clearly depicted the path and intensity of the allosteric crosstalk in each system, unveiling double targeting at allosteric and orthosteric sites could reduce the signal flow within BCR-ABL1. Conformational landscapes were also analyzed by MSM. The dominant MSM metastable state of T315I-ABL001-NIL system elucidated that the overall conformation of T315I-ABL001-NIL complex is preferred to be inactive compared to the conformation of T315I-NIL which tends to be in the activated state. Energetic analysis showed that the binding free energy between NIL and BCR-ABL1 was lower in the T315I-ABL001-NIL system, compared with T315I-NIL system, indicating the favorable binding of NIL and its higher affinity in the ternary complex. In conclusion, allo-loading could shift NIL-bound active form of BCR-ABL1 to a more stable inactive conformation by modulating the conformation of key structural domains such as A-loop and αC-helix through allosteric communication and induce stronger binding of NIL to BCR-ABL1, thus exerting concerted effects on improving the overall therapeutic efficacy.

Hence, our research revealed allosteric communication mechanism underlying dual-targeting at allosteric and orthosteric sites. The findings serve as proof of the concept for future clinical strategies to overcoming drug resistance that the appropriate combination of orthosteric and allosteric inhibitors could resolve drug-resistance as well as synergistically improve the efficacy of both drugs. According to our study, ABL001 could re-sensitize resistant TKI drugs by allosterically modulating the conformation of A-loop and C-helix. In the future, we can develop drug molecules to induce such conformational changes to restore recalcitrant drug-resistant kinases. And based on the identified allosteric pathways, it may be possible that drug allosteric potency could be enhanced by enhancing internal signal transduction within the C-lobe or SH2 or by strengthening he connection between Community two and the A-loop. And resistance residues outside the drug pocket could be predicted as mutations on the allosteric pathway may lead to resistance to allosteric drugs (Lu et al., 2019a, 2020). Moreover, based on reversed allosteric communication theory, we validated the coupling between the ATP-binding pocket and the allosteric site by energetic dynamics calculations. The residue-residue interaction free energy of a portion of the residue pairs within the ABL001 site changed considerably before and after NIL loading, suggesting that the orthosteric drug NIL perturbation leads to a reversal allosteric communication. The results supported the intrinsic linkage between topologically distinct sites, providing theoretical basis for future approaches using orthosteric modulators binding to predict allosteric pockets (Fan et al., 2021). Future research is expected to provide a more comprehensive insight into orthosteric ligands to fine-tune BCR-ABL1 and enable the mining of allosteric pockets with superior affinity and potency (Ni et al., 2021). The ABL001 pocket was also detected in Cyclin-dependent kinase 2 (CDK2), thus the investigation of BCR-ABL1 dual-targeting mechanism is useful to guide combination therapies with other kinases.

MATERIALS AND METHODS

Construction of Stimulation Systems

In this study, six systems (WT, WT-NIL, T315I, T315I-NIL, T315I-ABL001 and T315I-ABL001-NIL) were constructed. The initial structure for T315I BCR-ABL in complex with NIL and NIL was obtained from Protein Data Bank (PDB ID: 5MO4) (Wylie et al., 2017). The missing residues (Thr277, Met278, and Gly383-Lys400) in the original crystal profile were modeled using available X-ray structures of relevant homologs (PDB ID: 3XOZ) by Discover Studio 3.1. Based on the T315-ABL001-NIL structure, the structures of T315I-ABL001, T315I-NIL and T315I were extracted from the T315I-ABL001-NIL complex. The I315 was mutated back to T in the WT and WT-NIL systems using Discovery Studio.

MD Simulations Settings

MD simulations were performed for the six systems. We prepared the initial parameter files for minimizations and simulations utilizing Amber ff14SB force field (Maier et al., 2015) and general amber force field (GAFF) (Wang et al., 2004). A transferable intermolecular potential three-point (TIP3P) truncated octahedral water box (10 Å) was employed for solvation, and then the counterions were added for neutralization (Jorgensen et al., 1983). Subsequently, 0.15 mol L^{-1} NaCl was added into each system to attain the physiological conditions for proteins.

After the preparation, each system underwent two rounds of energy minimization with the steepest descent and conjugate gradient algorithm. Next, every system was heated from 0 to 300 K in 300 ps in a canonical ensemble (NVT), with an equilibrium runs of 700 ps. Finally, three independent rounds of 3 μs conventional MD simulations were conducted with random velocities for all systems under isothermal isobaric ensemble (NPT) condition and periodic boundary condition. During the MD simulation, the Particle Mesh Ewald (PME) method was performed to model the long-range electrostatic interactions (Darden et al., 1993), while a cutoff of 10 Å was set for the short-range electrostatic interactions and van der Waals force calculations. Furthermore, the SHAKE algorithm was performed to constrain covalent bonds involving hydrogens (Ryckaert et al., 1977).

Dynamic Cross-Correlation Matrix Analysis

Using the CPPTRAJ plugin, the DCCM of all protein Cα atoms, which represents the fluctuations in Cα atom coordinates, was calculated to reflect the inter-residue correlations in each system (Hünenberger et al., 1995). The cross-correlation coefficient Cij was calculated according to the following **Eq. 1**:

$$C(i,j) = \frac{c(i,j)}{c(i,i)^{1/2} c(j,j)^{1/2}} \quad (1)$$

where *i* and *j* represent the *i*th and *j*th Cα atoms, respectively.

Community Network Analysis

Utilizing the NetworkView plugin in VMD (Eargle and Luthey-Schulten, 2012), the community organizations of each system were calculated based on the correlation coefficient matrix C_{ij}. The whole ABL1 of each system was recognized as a group of nodes (assigned to the Cα atom of each residue) connected by edges, which were drawn between nodes that remained within a cut-off distance of 4.5 Å for at least 75% of the simulation process (Sethi et al., 2009). We calculated the edge connections between certain nodes by **Eq. 2**:

$$d_{i,j} = -log\left(\left|C_{i,j}\right|\right) \quad (2)$$

where i and j represent two nodes and Cij was calculated by **Eq. 1**.

Then, optimal pathways between all pairs of nodes were calculated with Floyd–Warshall algorithm. The gncommunities program was employed to get the substructure of the communities, which embedded the Girvan-Newman divisive algorithm and applied edge betweenness defined as the number of paired optimal paths. To acquire the optimal substructure of the network, edges with the highest betweenness would be iteratively removed from the network, and the remaining edges would be recomputed until each node represents an isolated community. Communities with residues less than three were discarded. Connectivity between communities was measured by the betweenness value.

Energy Coupling Score Calculation

The molecular mechanisms generalized Born surface area (MM-GBSA) energy decomposition calculation was applied for the allosteric pockets on ABL^{T315I} in both NIL-bound (apo) and NIL-unbound (holo) systems to compare the residue-residue interactions, based on MD simulation trajectories. The interaction free energy for residues pairs separated by at least three amino acids in the sequence of the cavity was calculated by **Eq. 3**:

$$E = E_{\text{int}} + E_{eel} + E_{vdw} + G_{pol} + G_{sas} \quad (3)$$

where E_{int} denotes internal energy, E_{eel} indicates electrostatic energy, E_{vdw} indicates van der Waals energy, G_{pol} represents the polar solvation free energy, and G_{sas} is the solvent accessible surface energy.

The energy coupling scores were assessed using the energy differences between the allosteric pockets in the holo and apo systems.

CONSTRUCTION OF MARKOV STATE MODEL

Based on the coordinates of T315I-NIL and T315I-ABL001-NIL, the PCA of overall protein backbone during the simulation of the two systems was calculated. and then taken as input for PyEMMA MSM analysis. The Python library PyEMMA (http://www.emma-project.org/latest/) was employed to estimate and validate Markov state models (MSM) based on MD simulation data (Scherer et al., 2015). By implied timescale validation, we confirmed that the T315I-ABL001-NIL and T315I-NIL systems were Markovian (**Supplementary Figure S1**) and reliable with a 100 microstate model with a lag time of 60 ns and a maximum k-means iteration number of 100. Next, based on the Perron cluster analysis (PCCA+) algorithm, the microstates were clustered into three macrostates in T315I-ABL001-NIL system and four macrostates in T315I-NIL system, respectively, which was further validated by the Chapman–Kolmogorov test (**Supplementary Figure S2**) (Prinz et al., 2011).

In each transferable state, we extracted trajectories that include more than 50% snapshots of the corresponding state using the "coordinates.save_traj" algorithm. The mdtraj package was used to extract the structures near the microstate cluster centers of each macrostate into the trajectories of corresponding macrostates. The representative conformation of each macrostate was selected based on the similarity score S_{ij}.

$$S_{ij} = e^{-d_{ij}/d_{scale}} \quad (4)$$

In **Eq. 4**, the structure with the highest S_{ij} among the trajectories was considered as the most representative conformation of the macrostate. The d_{ij} represents the RMSD between the conformations i and j, while dscale is the standard deviation of d.

DATA AVAILABILITY STATEMENT

The original contributions presented in the study are included in the article/**Supplementary Material**, further inquiries can be directed to the corresponding authors.

AUTHOR CONTRIBUTIONS

Conceptualization, SL, KD, SH, and CC; methodology, HZ, MZ, ML, and DN; validation, HZ, MZ, DN, YW, and LD; formal analysis, HZ; investigation, HZ and MZ; resources, SL; data curation, HZ; writing—original draft preparation, HZ; writing—review and editing, SL and DN; visualization, SL; supervision, SL and KD; project administration, SL; funding acquisition, SL and CC.

FUNDING

This research was funded by the Natural Science Foundation of China (No. 22077082).

SUPPLEMENTARY MATERIAL

The Supplementary Material for this article can be found online at: https://www.frontiersin.org/articles/10.3389/fphar.2022.862504/full#supplementary-material

REFERENCES

Adrián, F. J., Ding, Q., Sim, T., Velentza, A., Sloan, C., Liu, Y., et al. (2006). Allosteric Inhibitors of Bcr-abl-dependent Cell Proliferation. *Nat. Chem. Biol.* 2, 95–102. doi:10.1038/nchembio760

Agnello, S., Brand, M., Chellat, M. F., Gazzola, S., and Riedl, R. (2019). A Structural View on Medicinal Chemistry Strategies against Drug Resistance. *Angew. Chem. Int. Ed. Engl.* 58, 3300–3345. doi:10.1002/anie.201802416

Al-Lazikani, B., Banerji, U., and Workman, P. (2012). Combinatorial Drug Therapy for Cancer in the post-genomic Era. *Nat. Biotechnol.* 30, 679–692. doi:10.1038/nbt.2284

Amadei, A., Linssen, A. B., and Berendsen, H. J. (1993). Essential Dynamics of Proteins. *Proteins* 17, 412–425. doi:10.1002/prot.340170408

Apperley, J. F. (2015). Chronic Myeloid Leukaemia. *Lancet* 385, 1447–1459. doi:10.1016/S0140-6736(13)62120-0

Beyer, P., Moorthy, V., Paulin, S., Hill, S. R., Sprenger, M., Garner, S., et al. (2018). The Drugs Don't Work: WHO's Role in Advancing New Antibiotics. *Lancet* 392, 264–266. doi:10.1016/S0140-6736(18)31570-8

Bozic, I., Reiter, J. G., Allen, B., Antal, T., Chatterjee, K., Shah, P., et al. (2013). Evolutionary Dynamics of Cancer in Response to Targeted Combination Therapy. *Elife* 2, e00747. doi:10.7554/eLife.00747

Chahardouli, B., Zaker, F., Mousavi, S. A., Kazemi, A., Ostadali, M., Nadali, F., et al. (2013). Evaluation of T315I Mutation Frequency in Chronic Myeloid Leukemia Patients after Imatinib Resistance. *Hematology* 18, 158–162. doi:10.1179/1607845412Y.0000000050

Darden, T., York, D., and Pedersen, L. (1993). Particle Mesh Ewald: AnN·Log(N) Method for Ewald Sums in Large Systems. *J. Chem. Phys.* 98, 10089–10092. doi:10.1063/1.464397

Deeks, E. D. (2022). Asciminib: First Approval. *Drugs* 82, 219–226. doi:10.1007/s40265-021-01662-3

Eargle, J., and Luthey-Schulten, Z. (2012). NetworkView: 3D Display and Analysis of Protein·RNA Interaction Networks. *Bioinformatics* 28, 3000–3001. doi:10.1093/bioinformatics/bts546

Fajer, M., Meng, Y., and Roux, B. (2017). The Activation of C-Src Tyrosine Kinase: Conformational Transition Pathway and Free Energy Landscape. *J. Phys. Chem. B* 121, 3352–3363. doi:10.1021/acs.jpcb.6b08409

Fan, J., Liu, Y., Kong, R., Ni, D., Yu, Z., Lu, S., et al. (2021). Harnessing Reversed Allosteric Communication: A Novel Strategy for Allosteric Drug Discovery. *J. Med. Chem.* 64, 17728–17743. doi:10.1021/acs.jmedchem.1c01695

Gorre, M. E., Mohammed, M., Ellwood, K., Hsu, N., Paquette, R., Rao, P. N., et al. (2001). Clinical Resistance to STI-571 Cancer Therapy Caused by BCR-ABL Gene Mutation or Amplification. *Science* 293, 876–880. doi:10.1126/science.1062538

Guarnera, E., and Berezovsky, I. N. (2020). Allosteric Drugs and Mutations: Chances, Challenges, and Necessity. *Curr. Opin. Struct. Biol.* 62, 149–157. doi:10.1016/j.sbi.2020.01.010

Guarnera, E., and Berezovsky, I. N. (2016). Allosteric Sites: Remote Control in Regulation of Protein Activity. *Curr. Opin. Struct. Biol.* 37, 1–8. doi:10.1016/j.sbi.2015.10.004

Heisterkamp, N., Stam, K., Groffen, J., de Klein, A., and Grosveld, G. (1985). Structural Organization of the Bcr Gene and its Role in the Ph' Translocation. *Nature* 315, 758–761. doi:10.1038/315758a0

Holohan, C., Van Schaeybroeck, S., Longley, D. B., and Johnston, P. G. (2013). Cancer Drug Resistance: an Evolving Paradigm. *Nat. Rev. Cancer* 13, 714–726. doi:10.1038/nrc3599

Huang, J., Yuan, Y., Zhao, N., Pu, D., Tang, Q., Zhang, S., et al. (2021). Orthosteric-allosteric Dual Inhibitors of PfHT1 as Selective Antimalarial Agents. *Proc. Natl. Acad. Sci. USA* 118, e2017749118. doi:10.1073/pnas.2017749118

Hünenberger, P. H., Mark, A. E., and van Gunsteren, W. F. (1995). Fluctuation and Cross-Correlation Analysis of Protein Motions Observed in Nanosecond Molecular Dynamics Simulations. *J. Mol. Biol.* 252, 492–503. doi:10.1006/jmbi.1995.0514

Jabbour, E., and Kantarjian, H. (2016). Chronic Myeloid Leukemia: 2016 Update on Diagnosis, Therapy, and Monitoring. *Am. J. Hematol.* 91, 252–265. doi:10.1002/ajh.24275

Jorgensen, W. L., Chandrasekhar, J., Madura, J. D., Impey, R. W., and Klein, M. L. (1983). Comparison of Simple Potential Functions for Simulating Liquid Water. *J. Chem. Phys.* 79, 926–935. doi:10.1063/1.445869

Kalmanti, L., Saussele, S., Lauseker, M., Müller, M. C., Dietz, C. T., Heinrich, L., et al. (2015). Safety and Efficacy of Imatinib in CML over a Period of 10 years: Data from the Randomized CML-Study IV. *Leukemia* 29, 1123–1132. doi:10.1038/leu.2015.36

Kantarjian, H. M., Baccarani, M., Jabbour, E., Saglio, G., and Cortes, J. E. (2011). Second-Generation Tyrosine Kinase Inhibitors: The Future of Frontline CML Therapy. *Clin. Cancer Res.* 17, 1674–1683. doi:10.1158/1078-0432.CCR-10-2922

Li, X., Wang, C., Peng, T., Chai, Z., Ni, D., Liu, Y., et al. (2021). Atomic-scale Insights into Allosteric Inhibition and Evolutional rescue Mechanism of Streptococcus Thermophilus Cas9 by the Anti-CRISPR Protein AcrIIA6. *Comput. Struct. Biotechnol. J.* 19, 6108–6124. doi:10.1016/j.csbj.2021.11.010

Liu, Y., Shah, K., Yang, F., Witucki, L., and Shokat, K. M. (1998). A Molecular Gate Which Controls Unnatural ATP Analogue Recognition by the Tyrosine Kinase V-Src. *Bioorg. Med. Chem.* 6, 1219–1226. doi:10.1016/S0968-0896(98)00099-6

Lovera, S., Sutto, L., Boubeva, R., Scapozza, L., Dölker, N., and Gervasio, F. L. (2012). The Different Flexibility of C-Src and C-Abl Kinases Regulates the Accessibility of a Druggable Inactive Conformation. *J. Am. Chem. Soc.* 134, 2496–2499. doi:10.1021/ja210751t

Lu, S., Chen, Y., Wei, J., Zhao, M., Ni, D., He, X., et al. (2021). Mechanism of Allosteric Activation of SIRT6 Revealed by the Action of Rationally Designed Activators. *Acta Pharm. Sin. B* 11, 1355–1361. doi:10.1016/j.apsb.2020.09.010

Lu, S., He, X., Ni, D., and Zhang, J. (2019a). Allosteric Modulator Discovery: From Serendipity to Structure-Based Design. *J. Med. Chem.* 62, 6405–6421. doi:10.1021/acs.jmedchem.8b01749

Lu, S., Qiu, Y., Ni, D., He, X., Pu, J., and Zhang, J. (2020). Emergence of Allosteric Drug-Resistance Mutations: New Challenges for Allosteric Drug Discovery. *Drug Discov. Today* 25, 177–184. doi:10.1016/j.drudis.2019.10.006

Lu, S., Shen, Q., and Zhang, J. (2019c). Allosteric Methods and Their Applications: Facilitating the Discovery of Allosteric Drugs and the Investigation of Allosteric Mechanisms. *Acc. Chem. Res.* 52, 492–500. doi:10.1021/acs.accounts.8b00570

Lu, S., and Zhang, J. (2019). Small Molecule Allosteric Modulators of G-Protein-Coupled Receptors: Drug-Target Interactions. *J. Med. Chem.* 62, 24–45. doi:10.1021/acs.jmedchem.7b01844

Lu, S., Ni, D., Wang, C., He, X., Lin, H., Wang, Z., et al. (2019b). Deactivation Pathway of Ras GTPase Underlies Conformational Substates as Targets for Drug Design. *ACS Catal.* 9, 7188–7196. doi:10.1021/acscatal.9b02556

Ma, X., Meng, H., and Lai, L. (2016). Motions of Allosteric and Orthosteric Ligand-Binding Sites in Proteins Are Highly Correlated. *J. Chem. Inf. Model.* 56, 1725–1733. doi:10.1021/acs.jcim.6b00039

Maier, J. A., Martinez, C., Kasavajhala, K., Wickstrom, L., Hauser, K. E., and Simmerling, C. (2015). ff14SB: Improving the Accuracy of Protein Side Chain and Backbone Parameters from ff99SB. *J. Chem. Theor. Comput.* 11, 3696–3713. doi:10.1021/acs.jctc.5b00255

Manning, G., Whyte, D. B., Martinez, R., Hunter, T., and Sudarsanam, S. (2002). The Protein Kinase Complement of the Human Genome. *Science* 298, 1912–1934. doi:10.1126/science.1075762

Mayer, B. J., and Baltimore, D. (1994). Mutagenic Analysis of the Roles of SH2 and SH3 Domains in Regulation of the Abl Tyrosine Kinase. *Mol. Cell. Biol.* 14, 2883–2894. doi:10.1128/mcb.14.5.2883-2894.1994

Melo, J. V. (1996). The Diversity of BCR-ABL Fusion Proteins and Their Relationship to Leukemia Phenotype. *Blood* 88, 2375–2384. doi:10.1182/blood.V88.7.2375.bloodjournal8872375

Miller, G. D., Bruno, B. J., and Lim, C. S. (2014). Resistant Mutations in CML and Ph(+)ALL - Role of Ponatinib. *Biologics* 8, 243–254. doi:10.2147/BTT.S50734

Nagar, B., Hantschel, O., Young, M. A., Scheffzek, K., Veach, D., Bornmann, W., et al. (2003). Structural Basis for the Autoinhibition of C-Abl Tyrosine Kinase. *Cell* 112, 859–871. doi:10.1016/S0092-8674(03)00194-6

Ni, D., Li, Y., Qiu, Y., Pu, J., Lu, S., and Zhang, J. (2020a). Combining Allosteric and Orthosteric Drugs to Overcome Drug Resistance. *Trends Pharmacol. Sci.* 41, 336–348. doi:10.1016/j.tips.2020.02.001

Ni, D., Wei, J., He, X., Rehman, A. U., Li, X., Qiu, Y., et al. (2020b). Discovery of Cryptic Allosteric Sites Using Reversed Allosteric Communication by a Combined Computational and Experimental Strategy. *Chem. Sci.* 12, 464–476. doi:10.1039/d0sc05131d

Ni, D., Chai, Z., Wang, Y., Li, M., Yu, Z., Liu, Y., et al. (2021). Along the Allostery Stream: Recent Advances in Computational Methods for Allosteric Drug Discovery. *Wires Comput. Mol. Sci.*, 1–30. doi:10.1002/wcms.1585

Nussinov, R., Jang, H., and Tsai, C. J. (2014). The Structural Basis for Cancer Treatment Decisions. *Oncotarget* 5, 7285–7302. doi:10.18632/oncotarget.2439

Nussinov, R., Tsai, C. J., and Jang, H. (2017). A New View of Pathway-Driven Drug Resistance in Tumor Proliferation. *Trends Pharmacol. Sci.* 38, 427–437. doi:10.1016/j.tips.2017.02.001

Nussinov, R., Tsai, C. J., and Jang, H. (2021). Anticancer Drug Resistance: An Update and Perspective. *Drug Resist. Updat.* 59, 100796. doi:10.1016/j.drup.2021.100796

Panjarian, S., Iacob, R. E., Chen, S., Engen, J. R., and Smithgall, T. E. (2013). Structure and Dynamic Regulation of Abl Kinases. *J. Biol. Chem.* 288, 5443–5450. doi:10.1074/jbc.R112.438382

Paul, F., Meng, Y., and Roux, B. (2020). Identification of Druggable Kinase Target Conformations Using Markov Model Metastable States Analysis of Apo-Abl. *J. Chem. Theor. Comput.* 16, 1896–1912. doi:10.1021/acs.jctc.9b01158

Pophali, P. A., and Patnaik, M. M. (2016). The Role of New Tyrosine Kinase Inhibitors in Chronic Myeloid Leukemia. *Cancer J.* 22, 40–50. doi:10.1097/PPO.0000000000000165

Prinz, J. H., Wu, H., Sarich, M., Keller, B., Senne, M., Held, M., et al. (2011). Markov Models of Molecular Kinetics: Generation and Validation. *J. Chem. Phys.* 134, 174105. doi:10.1063/1.3565032

Qiu, Y., Wang, Y., Chai, Z., Ni, D., Li, X., Pu, J., et al. (2021a). Targeting RAS Phosphorylation in Cancer Therapy: Mechanisms and Modulators. *Acta Pharm. Sin. B* 11, 3433–3446. doi:10.1016/j.apsb.2021.02.014

Qiu, Y., Yin, X., Li, X., Wang, Y., Fu, Q., Huang, R., et al. (2021b). Untangling Dual-Targeting Therapeutic Mechanism of Epidermal Growth Factor Receptor (Egfr) Based on Reversed Allosteric Communication. *Pharmaceutics* 13, 747. doi:10.3390/pharmaceutics13050747

Quintás-Cardama, A., Kantarjian, H., and Cortes, J. (2007). Flying under the Radar: the New Wave of BCR-ABL Inhibitors. *Nat. Rev. Drug Discov.* 6, 834–848. doi:10.1038/nrd2324

Ryckaert, J.-P., Ciccotti, G., and Berendsen, H. J. C. (1977). Numerical Integration of the Cartesian Equations of Motion of a System with Constraints: Molecular Dynamics of N-Alkanes. *J. Comput. Phys.* 23, 327–341. doi:10.1016/0021-9991(77)90098-5

Scherer, M. K., Trendelkamp-Schroer, B., Paul, F., Pérez-Hernández, G., Hoffmann, M., Plattner, N., et al. (2015). PyEMMA 2: A Software Package for Estimation, Validation, and Analysis of Markov Models. *J. Chem. Theor. Comput.* 11, 5525–5542. doi:10.1021/acs.jctc.5b00743

Schindler, T., Bornmann, W., Pellicena, P., Miller, W. T., Clarkson, B., and Kuriyan, J. (2000). Structural Mechanism for STI-571 Inhibition of Abelson Tyrosine Kinase. *Science* 289, 1938–1942. doi:10.1126/science.289.5486.1938

Schoepfer, J., Jahnke, W., Berellini, G., Buonamici, S., Cotesta, S., Cowan-Jacob, S. W., et al. (2018). Discovery of Asciminib (ABL001), an Allosteric Inhibitor of the Tyrosine Kinase Activity of BCR-ABL1. *J. Med. Chem.* 61, 8120–8135. doi:10.1021/acs.jmedchem.8b01040

Sethi, A., Eargle, J., Black, A. A., and Luthey-Schulten, Z. (2009). Dynamical Networks in tRNA:protein Complexes. *Proc. Natl. Acad. Sci. U. S. A.* 106, 6620–6625. doi:10.1073/pnas.0810961106

Shan, Y., Seeliger, M. A., Eastwood, M. P., Frank, F., Xu, H., Jensen, M. Ø., et al. (2009). A Conserved Protonation-dependent Switch Controls Drug Binding in the Abl Kinase. *Proc. Natl. Acad. Sci. U. S. A.* 106, 139–144. doi:10.1073/pnas.0811223106

Sherbenou, D. W., Hantschel, O., Kaupe, I., Willis, S., Bumm, T., Turaga, L. P., et al. (2010). BCR-ABL SH3-SH2 Domain Mutations in Chronic Myeloid Leukemia Patients on Imatinib. *Blood* 116, 3278–3285. doi:10.1182/blood-2008-10-183665

Sonti, R., Hertel-Hering, I., Lamontanara, A. J., Hantschel, O., and Grzesiek, S. (2018). ATP Site Ligands Determine the Assembly State of the Abelson Kinase Regulatory Core via the Activation Loop Conformation. *J. Am. Chem. Soc.* 140, 1863–1869. doi:10.1021/jacs.7b12430

Wang, J., Wolf, R. M., Caldwell, J. W., Kollman, P. A., and Case, D. A. (2004). Development and Testing of a General Amber Force Field. *J. Comput. Chem.* 25, 1157–1174. doi:10.1002/jcc.20035

Wang, Y., Ji, D., Lei, C., Chen, Y., Qiu, Y., Li, X., et al. (2021). Mechanistic Insights into the Effect of Phosphorylation on Ras Conformational Dynamics and its Interactions with Cell Signaling Proteins. *Comput. Struct. Biotechnol. J.* 19, 1184–1199. doi:10.1016/j.csbj.2021.01.044

Wylie, A. A., Schoepfer, J., Jahnke, W., Cowan-Jacob, S. W., Loo, A., Furet, P., et al. (2017). The Allosteric Inhibitor ABL001 Enables Dual Targeting of BCR-ABL1. *Nature* 543, 733–737. doi:10.1038/nature21702

Zhang, J., Adrián, F. J., Jahnke, W., Cowan-Jacob, S. W., Li, A. G., Iacob, R. E., et al. (2010). Targeting Bcr-Abl by Combining Allosteric with ATP-Binding-Site Inhibitors. *Nature* 463, 501–506. doi:10.1038/nature08675

Zhang, M., Jang, H., and Nussinov, R. (2020). PI3K Inhibitors: Review and New Strategies. *Chem. Sci.* 11, 5855–5865. doi:10.1039/d0sc01676d

Zhang, Q., Chen, Y., Ni, D., Huang, Z., Wei, J., Feng, L., et al. (2022). Targeting a Cryptic Allosteric Site of SIRT6 with Small-Molecule Inhibitors that Inhibit the Migration of Pancreatic Cancer Cells. *Acta Pharmaceutica Sinica B* 12, 876–889. doi:10.1016/j.apsb.2021.06.015

Conflict of Interest: The authors declare that the research was conducted in the absence of any commercial or financial relationships that could be construed as a potential conflict of interest.

Publisher's Note: All claims expressed in this article are solely those of the authors and do not necessarily represent those of their affiliated organizations, or those of the publisher, the editors and the reviewers. Any product that may be evaluated in this article, or claim that may be made by its manufacturer, is not guaranteed or endorsed by the publisher.

frontiers | Frontiers in Pharmacology

CASE REPORT
published: 06 April 2022
doi: 10.3389/fphar.2022.838247

Acquired Concurrent EGFR T790M and Driver Gene Resistance From EGFR-TKIs Hampered Osimertinib Efficacy in Advanced Lung Adenocarcinoma: Case Reports

*Yue Zeng[1], Yuanqing Feng[2], Guihua Fu[2], Junlan Jiang[3], Xiaohan Liu[1], Yue Pan[1], Chunhong Hu[1,4], Xianling Liu[1] and Fang Wu[1,4,5,6]**

[1]Department of Oncology, The Second Xiangya Hospital, Central South University, Changsha, China, [2]Department of Oncology, Xiangtan Central Hospital, Xiangtan, China, [3]Jiangnan Hospital, Xiangtan, China, [4]Hunan Cancer Mega-Data Intelligent Application and Engineering Research Centre, Changsha, China, [5]Hunan Key Laboratory of Tumor Models and Individualized Medicine, The Second Xiangya Hospital, Central South University, Changsha, China, [6]Hunan Key Laboratory of Early Diagnosis and Precision Therapy in Lung Cancer, The Second Xiangya Hospital, Central South University, Changsha, China

OPEN ACCESS

Edited by:
Francesco Bertoni,
Institute of Oncology Research (IOR), Switzerland

Reviewed by:
Lizhen Huang,
South China University of Technology, China
Patrizia Froesch,
Oncology Institute of Southern Switzerland (IOSI), Switzerland

***Correspondence:**
Fang Wu
wufang4461@csu.edu.cn
orcid.org/0000-0002-6627-3437

Specialty section:
This article was submitted to Pharmacology of Anti-Cancer Drugs, a section of the journal Frontiers in Pharmacology

Received: 17 December 2021
Accepted: 11 March 2022
Published: 06 April 2022

Citation:
Zeng Y, Feng Y, Fu G, Jiang J, Liu X, Pan Y, Hu C, Liu X and Wu F (2022) Acquired Concurrent EGFR T790M and Driver Gene Resistance From EGFR-TKIs Hampered Osimertinib Efficacy in Advanced Lung Adenocarcinoma: Case Reports. Front. Pharmacol. 13:838247. doi: 10.3389/fphar.2022.838247

The acquired resistance of epidermal growth factor receptor tyrosine kinase inhibitors (EGFR-TKIs) is inevitable and heterogeneous. The strategies to overcome acquired resistance are significant. For patients with secondary T790M-positive after early generation EGFR-TKIs, osimertinib is the standard second-line therapy. In patients resistant to prior early generation EGFR-TKIs, the acquired T790M mutation overlaps with other driver gene resistance, such as HER2-and MET amplification, accounting for 4–8%. The efficacy of osimertinib is unclear in patients with concurrent multiple driver gene resistance. We here report a patient who acquired EGFR T790M, STRN-ALK fusion, and EGFR amplification after gefitinib progression and subsequent MET amplification acquired from osimertinib. The other patient acquired EGFR T790M and MET amplification post-dacomitinib and acquired CCDC6-RET fusion after osimertinib treatment. Besides, subsequent new bypass activations were the possible resistance mechanisms to second-line osimertinib. Both patients had progression-free survival (PFS) less than 4 months and limited benefits from osimertinib second-line therapy. The T790M accompanying driver gene resistance will be a new subtype after EGFR-TKIs progression, needing effective treatment options.

Keywords: non-small-cell lung cancer, EGFR-TKI acquired resistance, T790M, diver gene resistance, ALK fusion, MET amplification, RET fusion

INTRODUCTION

The resistance mechanisms to epidermal growth factor receptor tyrosine kinase inhibitors (EGFR-TKIs) are inevitable and heterogeneous, which restricts the clinical benefits (Piper-Vallillo et al., 2020). The most frequent acquired resistance mechanism of early generation EGFR-TKIs is secondary T790M mutation, and osimertinib is the standard second-line therapy (Mok et al., 2017; Westover et al., 2018). Some oncogene alterations like ALK, ROS1, and RET are increasingly observed in resistance mechanisms (Piper-Vallillo et al., 2020). Concurrent driver gene alteration as a

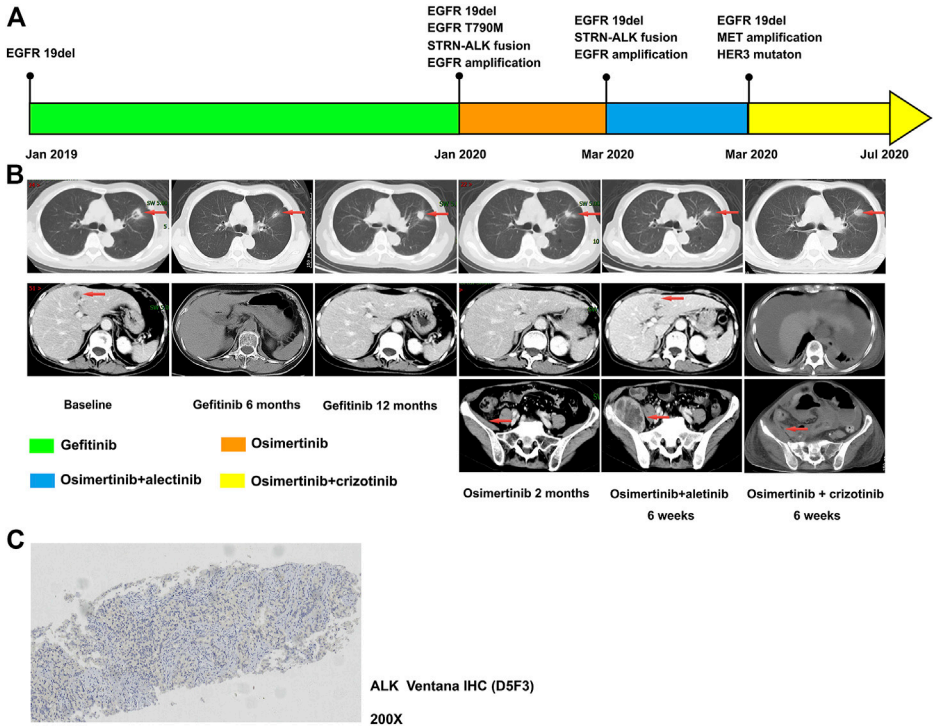

FIGURE 1 | (A): Timer shaft of gene testing and treatment measurement of case 1; **(B)**: Computed tomographic images of primary lung lesion, liver, and iliopsoas mass metastases; **(C)**: ALK Ventana immunohistochemistry (D5F3) as negative.

resistance mechanism occurs in lung adenocarcinoma with a low incidence rate. However, no good consensus was formulated when EGFR T790M mutation was combined with other driver gene resistance. Herein, we reported two cases that developed T790M-positive and driver gene resistance after receiving EGFR-TKIs, which provide valuable suggestions for clinical decisions. Further, extensive literature reviews were made to summarize the reported cases with T790M mutation and driver gene resistance in NSCLC patients and to analyze the prognosis and efficacy of osimertinib.

CASE REPORT

Case 1

Case 1 reports a 75-year-old non-smoking woman suffering from cough and pain in her upper limbs and back. Computed tomography (CT) identified a nodule in the left superior lung and metastasis in the liver in October 2018 (**Figure 1B**). Single-photon emission computed tomography bone imaging showed multiple bone metastases. The pathology was confirmed as lung adenocarcinoma and ALK Ventana immunohistochemistry (D5F3) was negative (**Figure 1C**). Besides, genotype by amplification-refractory mutation system polymerase chain reaction (RT-PCR) revealed an EGFR 19 exon in-frame deletion (19del) (**Supplementary Table S1**). She started on gefitinib at 250 mg daily in December 2018 (**Figure 1A**). Partial response was obtained in the patient with liver metastasis disappearing. The disease progressed with lung lesion enlargement and bone metastases after 12 months. Plasma-based next-generation sequencing (NGS, 168-gene panel, Burning Rock, Guangzhou) in December 2019 showed an EGFR 19del, EGFR T790M, STRN-ALK fusion, TP53 mutation, and EGFR amplification. Then she began osimertinib at 80 mg daily, which controlled her lung mass within 2 months. Alectinib was combined with osimertinib since plasma-based NGS showed that the STRN-ALK frequency was increasing. The STRN-ALK frequency disappeared after 3 weeks of treatment. However, new liver and right iliopsoas metastases were identified after 7 weeks of combination treatment. The CT-guided needle biopsy of the right iliopsoas lesion revealed metastatic lung adenocarcinoma, and tissue-based NGS showed an EGFR 19del, MET amplification, and HER3 mutation (425 gene-panel, Geneseeq Technology Inc., Nanjing). Crizotinib combined with osimertinib was administrated. Due to gastrointestinal toxicity, crizotinib was reduced to 250 mg daily. The patient showed remission of the right iliopsoas mass after 2 months of treatment, but her clinical conditions worsened, and she eventually died 1 week later.

Case 2

A 72-years woman was diagnosed with lung adenocarcinoma by percutaneous left lung biopsy in August 2019. The patient had multiple bone metastases with clinical disease stage Ⅳ. The gene testing showed an EGFR 19del by plasma-based ARMS-PCR (EGFR gene mutation assay). She started dacomitinib at 45 mg daily in

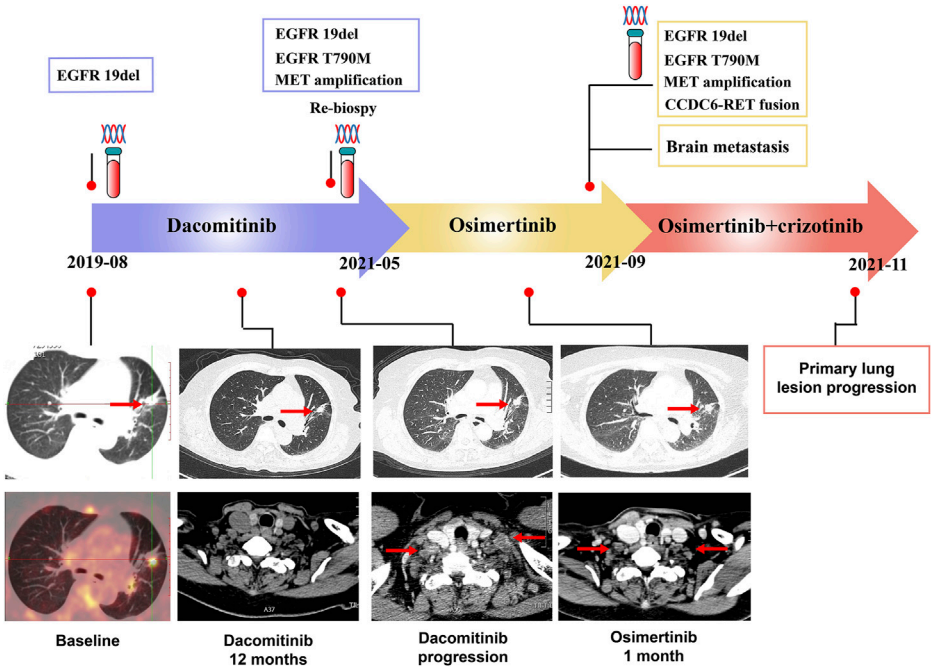

FIGURE 2 | Timer shaft of gene testing and treatments measurement, and the computed tomographic images of primary lung lesion and lymph nodes metastases of case 2.

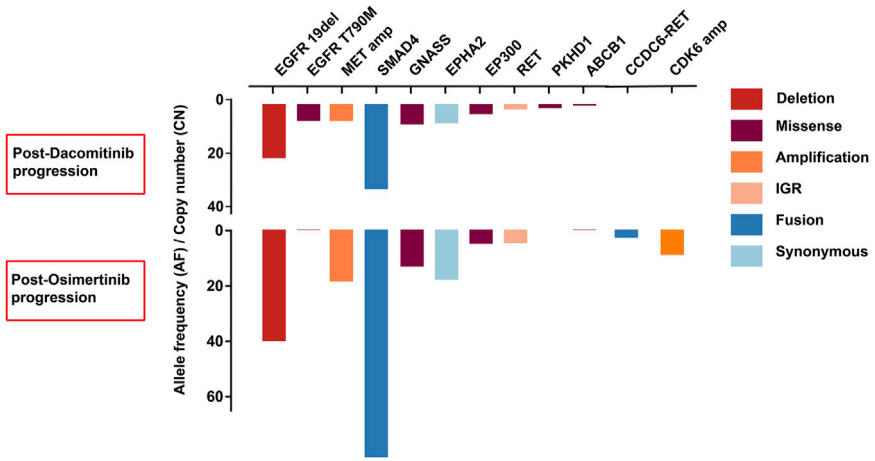

FIGURE 3 | The comparison of resistance mechanisms of genetic alterations between dacomitinib progression and osimertini progression in case 2.

August 2019. The tumor shrank with a duration of response (DOR) of 19 months (**Figure 2**). The patient had progression on the right supraclavicular and cervical lymph nodes. The ultrasound-guided percutaneous biopsy of the right supraclavicular lymph node showed metastatic lung adenocarcinoma. Besides, tissue- and plasma-based NGS (425 gene-panel, Geneseeq Technology Inc., Nanjing) revealed an EGFR 19del, T790M mutation in both, and MET amplification (CN:4.7) in plasma. Second-line osimertinib was administrated in May 2021. The patient's lesion shrank in the first month of osimertinib therapy. However, the supraclavicular lymph nodes enlarged and new brain metastases appeared in September 2021 with progression-free survival (PFS) of less than 4 months. The plasma-based NGS (437 gene-panel, Geneseeq Technology Inc., Nanjing) revealed an EGFR 19del, T790M mutation, MET amplification (CN:14.2), and CCDC6-RET fusion (**Supplementary Table S2**, **Figure 3**). The patient received radiotherapy for brain and subsequent osimertinib and crizotinib combination therapy in October 2021. She showed mild gastrointestinal toxicity of nausea and vomiting to the combination. The brain metastatic lesion was controlled but the primary lung lesion progressed after a 1-month

TABLE 1 | Clinicopathological characteristics of concurrent EGFR-T790M and driver gene-resistant NSCLC patients.

Case no	Age	Sex	Smoking History	Pathology	Staging	Baseline Driver Gene	First-Line Therapy	Resistance Mechanisms	Second-Line Therapy	Best Response	PFS (mo)[a]
1 (Ralki et al., 2019)	60	M	Never	ADC	IV	EGFR L858R, HER2 amp	Gefitinib	EGFR T790M, HER2 S310Y mutation, HER2 amp	Osimertinib and trastuzumab	SD	4
2 (Zhang et al., 2018)	57	M	Yes	ADC	IV	EGFR L858R	Icotinib	EGFR T790M, HER2 V777L mutation, HER2 amp	Osimertinib	PD	1
3 (Meedendorp et al., 2018)	62	M	N/A	ADC	IV	EGFR L858R	Gefitinib, afatinib	EGFR T790M, HER2 amp	Osimertinib	SD	3
4 (Xiang et al., 2015)	69	M	Yes	ADC	IV	EGFR L858R	Gefitinib	EGFR T790M, KRAS G12V	Chemotherapy	PD	2[b]
5 (Fu et al., 2021)	72	M	N/A	ADC	IV	EGFR 19del	Gefitinib	EGFR T790M, KRAS G12V	Osimertinib	PD	3
6	76	F	Yes	ADC	IV	EGFR 19del	Gefitinib	EGFR T790M, STRN-ALK, EGFR amp	Osimertinib and alectinib	SD	4
7	72	F	Never	ADC	IV	EGFR 19del	Dacomitinib	EGFR T790M, MET amp	Osimertinib	SD	3

[a]*The PFS, of second-line therapy.*

[b]*The patients had an OS, of 2 months*

AbbreviationsM, male; F, female; ADC, adenocarcinoma; N/A, not available; PR, partial response; SD, stable disease; PD, progression disease; PFS, progression-free survival; mo, months.

combination. The patient had a poor performance status and severe symptoms of dyspnea.

DISCUSSION

The mechanisms of resistance were heterogeneous and the remaining unknown mechanisms need to be discovered. The acquired secondary EGFR T790M mutation could be overcome by second-line osimertinib with a median PFS of 10.1 months in the AURA3 study (Mok et al., 2017; Westover et al., 2018). The driver gene acquired resistance, such as MET, ALK, and RET alterations, are increasingly reported (Zeng et al., 2022). It is unclear if osimertinib will exert its efficacy in patients with concurrent T790M-positive and driver gene resistance.

For the first time, we reported cases harboring concurrent alterations of EGFR T790M with ALK fusion and MET amplification after EGFR-TKIs. Both patients had a PFS of less than 4 months under osimertinib second-line therapy. The presented cases showed concurrent EGFR T790M and that driver gene resistance could not benefit from osimertinib monotherapy. Besides, the two patients developed MET amplification and RET fusions after osimertinib, which indicated that subsequent new bypass activations were possible resistance mechanisms to second-line osimertinib in patients with EGFR T790M and driver gene resistance.

Further, we conducted extensive literature reviews to identify the incidence rate and prognosis of concurrent driver gene resistance. EGFR secondary T790M, accompanying ALK, ROS1, MET, RET, HER2, KRAS, or NTRK gene alterations, were included. The incidence of T790M mutation overlapping with driver gene mutation, such as HER2-and MET amplification, was 4–8% after prior EGFR-TKIs treatment (Yu et al., 2013; Gou et al., 2016; Fu et al., 2021). Wang and coworkers reported a T790M lative allele frequency less than 20% was more likely concurrent driver gene resistance, like MET and HER2-amplification in EGFR-TKIs progression patients, who had a lower objective response rate and disease control rate to osimertinib (Wang et al., 2020). Besides, the reported cases of concurrent EGFR T790M and driver gene resistance are summarized in **Table 1**. The patients with T790M and KRAS G12V mutation coexistence did not respond to osimertinib therapy (Xiang et al., 2015; Fu et al., 2021). The patients harboring acquired EGFR T790M, HER2 mutation, and HER2 amplification from first-generation EGFR-TKIs did not respond to osimertinib and the combination of trastuzumab with a frustrating PFS (Meedendorp et al., 2018; Zhang et al., 2018; Ralki et al., 2019). The statistics also presented the poor efficacy of osimertinib on T790M and driver gene resistance.

EGFR-TKIs combined with bypass targeted therapy showed potent antitumor activity. Osimertinib plus savolitinib showed an acceptable risk-benefit in NSCLC patients with acquired MET amplification from pretreated EGFR-TKIs in a phase Ib study (Sequist et al., 2020). crizotinib combined with osimertinib also demonstrated improved PFS in a real-world study (Liu et al., 2021). Patients with acquired ALK fusions resistant to EGFR-TKIs, such as EML4-ALK and STRN-ALK, may benefit from EGFR plus ALK inhibitors (Offin et al., 2018; Zhou et al., 2019). RET fusion appearance post-osimertinib progression responded to osimertinib and pralsetinib, the selective RET-TKI (Piotrowska et al., 2018). trastuzumab emtansine (T-DM1) and trastuzumab deruxtecan were available targeted agents with activity against the HER2 alterations, however, strategies against acquired HER2 alterations await more clinical evidence (Zeng et al., 2022).

Hence, strategies to rival multiple driver gene resistance are urgently needed. Firstly, the plasma assay of EGFR T790M single-point is insufficient to identify the resistance of EGFR-TKIs, since concurrent driver gene resistance impairs osimertinib's efficacy.

Osimertinib combined with bypass TKIs is a promising treatment for concurrent EGFR T790M and driver gene resistance. The circulating tumor DNA (ctDNA) genomic profile was an effective tool to observe the resistance mechanisms (Del Re et al., 2019). ctDNA monitoring may allow the timely combination of osimertinib and bypass inhibitors. When EGFR T790M is accompanied with ALK/MET/ROS1 resistance, osimertinib and crizotinib with AEs observation could be taken into consideration since crizotinib may prevent the activation of the other two mechanisms.

CONCLUSION

We firstly reported lung cancer patients harboring concurrent alterations of EGFR T790M with ALK fusion, MET amplification, and RET fusions as mechanisms of resistance after EGFR-TKIs. Both patients had poor outcomes from osimertinib. Additionally, subsequent new bypass activations were possible resistance mechanisms to second-line osimertinib. T790M accompanying driver gene resistance will be a new subtype after EGFR-TKI progression and needs effective treatment options.

DATA AVAILABILITY STATEMENT

The original contributions presented in the study are included in the article/**Supplementary Material**, further inquiries can be directed to the corresponding author.

ETHICS STATEMENT

Written informed consent was obtained from the minor(s)' legal guardian/next of kin for the publication of any potentially identifiable images or data included in this article.

AUTHOR CONTRIBUTIONS

YZ collected and analyzed data, and wrote the draft of the paper. FW conceptualized the study and revised the paper. YF, GF, and JJ provided data. XlL and CH provided guidance. YP and XhL collected data. All authors critically reviewed and revised the final manuscript.

ACKNOWLEDGMENTS

We sincerely thank the multidisciplinary team (MDT) of thoracic oncology, the Second Xiangya Hospital, Central South University, for their guidance in clinical work.

SUPPLEMENTARY MATERIAL

The Supplementary Material for this article can be found online at: https://www.frontiersin.org/articles/10.3389/fphar.2022.838247/full#supplementary-material

REFERENCES

Del Re, M., Crucitta, S., Gianfilippo, G., Passaro, A., Petrini, I., Restante, G., et al. (2019). Understanding the Mechanisms of Resistance in EGFR-Positive NSCLC: From Tissue to Liquid Biopsy to Guide Treatment Strategy. *Int. J. Mol. Sci.* 20 (16). doi:10.3390/ijms20163951

Fu, Y., Wang, A., Zhou, J., Feng, W., Shi, M., Xu, X., et al. (2021). Advanced NSCLC Patients with EGFR T790M Harboring TP53 R273C or KRAS G12V Cannot Benefit from Osimertinib Based on a Clinical Multicentre Study by Tissue and Liquid Biopsy. *Front. Oncol.* 11, 621992. doi:10.3389/fonc.2021.621992

Gou, L. Y., Li, A. N., Yang, J. J., Zhang, X. C., Su, J., Yan, H. H., et al. (2016). The Coexistence of MET Over-expression and an EGFR T790M Mutation Is Related to Acquired Resistance to EGFR Tyrosine Kinase Inhibitors in Advanced Non-small Cell Lung Cancer. *Oncotarget* 7 (32), 51311–51319. doi:10.18632/oncotarget.9697

Liu, L., Qu, J., Heng, J., Zhou, C., Xiong, Y., Yang, H., et al. (2021). A Large Real-World Study on the Effectiveness of the Combined Inhibition of EGFR and MET in EGFR-Mutant Non-small-cell Lung Cancer after Development of EGFR-TKI Resistance. *Front. Oncol.* 11, 722039. doi:10.3389/fonc.2021.722039

Meedendorp, A. D., Ter Elst, A., 't Hart, N. A., Groen, H. J. M., Schuuring, E., and van der Wekken, A. J. (2018). Response to HER2 Inhibition in a Patient with Brain Metastasis with EGFR TKI Acquired Resistance and an HER2 Amplification. *Front. Oncol.* 8, 176. doi:10.3389/fonc.2018.00176

Mok, T. S., Wu, Y-L., Ahn, M-J., Garassino, M. C., Kim, H. R., Ramalingam, S. S., et al. (2017). Osimertinib or Platinum-Pemetrexed in EGFR T790M-Positive Lung Cancer. *N. Engl. J. Med.* 376 (7), 629–640. doi:10.1056/NEJMoa1612674

Offin, M., Somwar, R., Rekhtman, N., Benayed, R., Chang, J. C., Plodkowski, A., et al. (2018). Acquired ALK and RET Gene Fusions as Mechanisms of Resistance to Osimertinib in EGFR-Mutant Lung Cancers. *JCO Precis Oncol.* 2. doi:10.1200/po.18.00126

Piotrowska, Z., Isozaki, H., Lennerz, J. K., Gainor, J. F., Lennes, I. T., Zhu, V. W., et al. (2018). Landscape of Acquired Resistance to Osimertinib in EGFR-Mutant NSCLC and Clinical Validation of Combined EGFR and RET Inhibition with Osimertinib and BLU-667 for Acquired RET Fusion. *Cancer Discov.* 8 (12), 1529–1539. doi:10.1158/2159-8290.Cd-18-1022

Piper-Vallillo, A. J., Sequist, L. V., and Piotrowska, Z. (2020). Emerging Treatment Paradigms for EGFR-Mutant Lung Cancers Progressing on Osimertinib: A Review. *Jco* 38–2936. doi:10.1200/jco.19.03123

Ralki, M., Maes, B., Pat, K., Wynants, J., and Cuppens, K. (2019). Triple Trouble: A Case of Multiple Resistance Mechanisms after First Generation EGFR-TKI in NSCLC. *Case Rep. Oncol.* 12 (2), 625–630. doi:10.1159/000502214

Sequist, L. V., Han, J. Y., Ahn, M. J., Cho, B. C., Yu, H., Kim, S. W., et al. (2020). Osimertinib Plus Savolitinib in Patients with EGFR Mutation-Positive, MET-Amplified, Non-small-cell Lung Cancer after Progression on EGFR Tyrosine Kinase Inhibitors: Interim Results from a Multicentre, Open-Label, Phase 1b Study. *Lancet Oncol.* 21 (3), 373–386. doi:10.1016/s1470-2045(19)30785-5

Wang, Y., He, Y., Tian, P., Wang, W., Wang, K., Chuai, S., et al. (2020). Low T790M Relative Allele Frequency Indicates Concurrent Resistance Mechanisms and Poor Responsiveness to Osimertinib. *Transl Lung Cancer Res.* 9 (5), 1952–1962. doi:10.21037/tlcr-20-915

Westover, D., Zugazagoitia, J., Cho, B. C., Lovly, C. M., and Paz-Ares, L. (2018). Mechanisms of Acquired Resistance to First- and Second-Generation EGFR Tyrosine Kinase Inhibitors. *Ann. Oncol.* 29 i10–i9. doi:10.1093/annonc/mdx703

Xiang, X., Yu, J., Lai, Y., He, W., Li, S., Wang, L., et al. (2015). L858R-positive Lung Adenocarcinoma with KRAS G12V, EGFR T790M and EGFR L858R Mutations: A Case Report. *Oncol. Lett.* 10 (3), 1293–1296. doi:10.3892/ol.2015.3435

Yu, H. A., Arcila, M. E., Rekhtman, N., Sima, C. S., Zakowski, M. F., Pao, W., et al. (2013). Analysis of Tumor Specimens at the Time of Acquired Resistance to EGFR-TKI Therapy in 155 Patients with EGFR-Mutant Lung Cancers. *Clin. Cancer Res.* 19 (8), 2240–2247. doi:10.1158/1078-0432.Ccr-12-2246

Zeng, Y., Yu, D., Tian, W., and Wu, F. (2022). Resistance Mechanisms to Osimertinib and Emerging Therapeutic Strategies in Nonsmall Cell Lung Cancer. *Curr. Opin. Oncol.* 34 (1), 54–65. doi:10.1097/CCO.0000000000000805

Zhang, P., Nie, X., Wang, B., and Li, L. (2018). Combined Therapy with Osimertinib and Afatinib in a Lung Adenocarcinoma Patient with EGFR T790M Mutation and Multiple HER2 Alterations after Resistance to Icotinib: A Case Report. *Thorac. Cancer* 9 (12), 1774–1777. doi:10.1111/1759-7714.12889

Zhou, C., Zeng, L., Zhang, Y., and Yang, N. (2019). Responder of Gefitinib Plus Crizotinib in Osimertinib Failure EGFR-Mutant NSCLC-Resistant with Newly Identified STRN-ALK by Next-Generation Sequencing. *J. Thorac. Oncol.* 14 (7), e143–e4. doi:10.1016/j.jtho.2019.02.014

Conflict of Interest: The authors declare that the research was conducted in the absence of any commercial or financial relationships that could be construed as a potential conflict of interest.

Publisher's Note: All claims expressed in this article are solely those of the authors and do not necessarily represent those of their affiliated organizations, or those of the publisher, the editors and the reviewers. Any product that may be evaluated in this article, or claim that may be made by its manufacturer, is not guaranteed or endorsed by the publisher.

frontiers | Frontiers in Pharmacology

ORIGINAL RESEARCH
published: 19 April 2022
doi: 10.3389/fphar.2022.873131

Induced Cell Cycle Arrest in Triple-Negative Breast Cancer by Combined Treatment of Itraconazole and Rapamycin

Hua-Tao Wu[1,2†], *Chun-Lan Li*[2,3†], *Ze-Xuan Fang*[2,3], *Wen-Jia Chen*[2,3], *Wen-Ting Lin*[4] *and Jing Liu*[2,3*]

[1]Department of General Surgery, The First Affiliated Hospital of Shantou University Medical College, Shantou, China, [2]Guangdong Provincial Key Laboratory for Diagnosis and Treatment of Breast Cancer, Cancer Hospital of Shantou University Medical College, Shantou, China, [3]Department of Physiology/Changjiang Scholar's Laboratory, Shantou University Medical College, Shantou, China, [4]Department of Pathology, Shantou University Medical College, Shantou, China

Triple-negative breast cancer (TNBC) is the aggressive molecular type of breast carcinoma, with a high metastasis/relapse incidence and cancer-related death rate, due to lack of specific therapeutic targets in the clinic. Exploring potential therapeutic targets or developing novel therapeutic strategies are the focus of intense research to improve the survival and life quality of patients with TNBC. The current study focused on drugs targeting the mTOR signaling pathway by investigating the potential utilization of itraconazole (ITZ) combined with rapamycin in the treatment of TNBC. CCK-8, colony formation and transwell assays were conducted to evaluate the effect of ITZ with rapamycin in combination on MDA-MB-231 and BT-549 TNBC cells. Synergistic inhibition was found in terms of proliferation and motility of TNBC cells. However, apoptosis was not enhanced by the combined treatment of ITZ and rapamycin. Flow cytometry analysis showed that ITZ and/or rapamycin arrested cells in G0/G1 phase and prevented G1/S phase transition. Reduced cyclin D1 protein levels were consistent with G0/G1 phase arrest, especially when resulting from the combination of ITZ with rapamycin. In conclusion, the combination of ITZ with rapamycin is a promising therapeutic strategy for patients with TNBC through synergistically arresting cells in the G0/G1 phase of the cell cycle, rather than inducing apoptosis.

Keywords: itraconazole, rapamycin, triple-negative breast cancer, cell cycle, apoptosis

OPEN ACCESS

Edited by:
Simona Rapposelli, University of Pisa, Italy

Reviewed by:
Zhuo-Xun Wu, St. John's University, United States
Paula Rezende-Teixeira, University of São Paulo, Brazil

***Correspondence:**
Jing Liu
jliu12@stu.edu.cn

†These authors have contributed equally to this work

Specialty section:
This article was submitted to Pharmacology of Anti-Cancer Drugs, a section of the journal Frontiers in Pharmacology

Received: *10 February 2022*
Accepted: *24 March 2022*
Published: *19 April 2022*

Citation:
Wu H-T, Li C-L, Fang Z-X, Chen W-J, Lin W-T and Liu J (2022) Induced Cell Cycle Arrest in Triple-Negative Breast Cancer by Combined Treatment of Itraconazole and Rapamycin. Front. Pharmacol. 13:873131. doi: 10.3389/fphar.2022.873131

INTRODUCTION

Itraconazole (ITZ), a broad-spectrum antifungal agent, has recently been verified as an anti-cancer drug in preclinical and clinical research (Pantziarka et al., 2015). ITZ exerts its antifungal activity through decreasing ergosterol synthesis, which is required for the membrane integrity of fungal cells (Poulsen et al., 2021). Based on its antifungal effects, ITZ is used as a safe and effective long-tern prophylaxis for fungal infections in immunocompromised cancer patients with neutropenia (Muhldorfer and Konig, 1990).

The effects and mechanisms of action for ITZ's anti-cancer activities have been reported in different types of cancer *in vitro* and *in vivo*. Its anti-cancer potential to reverse multi-drug resistance (MDR) has been shown in daunorubicin-resistant P388 leukemia cells (Gupta et al., 1991),

adriamycin-resistant K562 leukemia cells (Kurosawa et al., 1996), human breast cancer resistance protein-expressing HEK cells resistant to topotecan (Gupta et al., 2007), P-glycoprotein (MDR1)-overexpressing, multidrug-resistant HeLa cells (Iida et al., 2001), bevacizumab-resistant gastrointestinal cancer (Hara et al., 2016) and metastatic castration-resistant prostate cancer (Antonarakis et al., 2013). It has also been reported that ITZ inhibits tumor growth and angiogenesis or induces apoptosis and autophagy in non-small cell lung cancer (NSCLC) (Aftab et al., 2011; Gerber et al., 2020), gastric cancer (Hu et al., 2017; Lan et al., 2018), cervical cancer (Rojo-Leon et al., 2019), and skin cancer (Liang et al., 2017; Carbone et al., 2018). Importantly, the underlying molecular mechanism of ITZ's anti-cancer effect has been reported *via* inhibiting hedgehog signaling, Wnt pathway and/or reducing mTOR expression, recognized as an mTOR inhibitor (Head et al., 2015; Wang et al., 2020).

Growing evidence demonstrates that combined therapeutic strategies with ITZ are promising for cancer patients. Chemotherapy with ITZ has been reported as a promising treatment for patients with unresectable gastric cancer (Sawasaki et al., 2020). A prospective randomized controlled study found that the utilization of ITZ in patients with NSCLC significantly benefits patients in terms of 1-year progression-free survival and overall response rate, although no improvement was found in terms of 1-year overall survival (Mohamed et al., 2021). As arsenic trioxide and ITZ antagonize the hedgehog pathway, Ally *et al.* proposed a sequential arsenic trioxide and ITZ treatment for metastatic basal cell carcinoma and found that the combined treatment is a feasible strategy for metastatic basal cell carcinoma patients (Ally et al., 2016). For colorectal cancer, ITZ synergistically increases the therapeutic effect of paclitaxel and ^{99m}Tc-methoxyisobutylisonitrile accumulation in an HT-29 human colorectal tumor-bearing animal model (Ghadi et al., 2021).

Breast cancer, the most common female malignant tumor, threatens the patients' health worldwide (Siegel et al., 2021). Among the different molecular types of breast cancer, triple-negative breast cancer (TNBC) is highly aggressive and has a high incidence of metastasis/relapse and increased mortality due to the absence of the estrogen receptor (ER), progesterone receptor (PR) and human epidermal growth factor receptor 2 (HER2) expression, hindering the ability to employ targeted therapy (Cao et al., 2021). Interestingly, for heavily treated patients with TNBC, especially patients with recurring tumors, chemotherapy with ITZ has shown a promising effect in the clinic (Tsubamoto et al., 2014). To evoke drug repurposing and drug combinations, a screening of the most promising drugs with verapamil and ITZ was conducted and identified the combination of ITZ and 5-fluorouracil as the most effective by decreasing cell viability and proliferation (Correia et al., 2018). Recently, El-Sheridy *et al.* used miltefosine-modified lipid nanocapsules to develop an ITZ nanoformulation, with a relatively small size and high entrapment efficiency, to enhance the chemotherapeutic efficacy of ITZ, regarding inhibition of tumor growth and cellular proliferation (El-Sheridy et al., 2021). Based on the above evidence, ITZ shows promise as an anti-cancer drug in the treatment of patients with TNBC.

Head *et al.* focused on the molecular mechanism of ITZ and found the suppressive function of ITZ on the AMPK/Mtor signaling axis (Head et al., 2015). The mTOR signaling pathway is essential for cell proliferation and survival, and in many types of cancers, mTOR is typically abnormally activated due to metabolic changes or mutations in upstream regulatory factors. Not surprisingly, inhibition of the mTOR pathway is a promising strategy for the development of anticancer drugs and has been demonstrated in clinical studies (Ferrari et al., 2022). Rapamycin, another antifungal drug extracted from Streptomyces hygroscopicus, is currently considered as a potent immunosuppressant in clinical and a target for mTOR, a serine/threonine protein kinase (Sabatini, 2017), exerting cytotoxicity against various kinds of cancers (Jelonek et al., 2021). However, Lee *et al.* demonstrated that rapamycin did not inhibit the activation of downstream effectors of mTOR completely (Lee et al., 2021), leading to the compensatory up-regulation of AKT activity and chemotherapy, limiting the utilization of rapamycin as an independent therapy (Mossmann et al., 2018).

So, the current study targets the AKT/mTOR signaling pathway, downstream of ITZ (Head et al., 2015), investigates the anti-cancer effect of monotherapy using ITZ and another drug each, as well as the two in combination, in TNBC cells. Also, the potential molecular mechanism of the therapeutic effect was also evaluated to provide potential drug combinations for patients with TNBC.

MATERIALS AND METHODS

Chemical Reagents

ITZ (HY-17514) and rapamycin (HY-10219) were purchased from MedChemExpress (United States).

Cell Culture

The human triple-negative breast cancer cell lines MDA-MB-231 and BT-549 were from the cell bank of the Chinese Academy of Sciences (Shanghai). MDA-MB-231 cells were cultured in Dulbecco's modified Eagle's medium plus 10% fetal bovine serum (FBS, GIBCO, Brazil) and 1% penicillin-streptomycin antibiotics (Beyotime, China). BT-549 cells were cultured in RPMI 1640 medium (GIBCO, Brazil) plus 10% FBS and 1% penicillin-streptomycin. All cells were cultured in a 37°C incubator containing 5% carbon dioxide.

CCK-8 Assay

Determination of IC50 concentration: 5×10^3 cells were inoculated into each well of a 96-well plate. After 24 h, culture medium containing a series of drug dilutions was changed and cells were further cultured for 48 h. Then, 10 μL CCK-8 reagent (Invigentech, United States) and 100 μL culture medium were added to each well and cells were cultured an additional 2 h before absorbance was measured at 450 nm. Growth inhibition was calculated as Inhibition rate% = (OD value of control group-OD value of experimental group)/(OD value of control group-OD value of the blank) × 100%. The SPSS 19.0 software was used

for statistical analysis of data to obtain half maximal growth inhibitory concentration (IC50) value of drugs, each experiment was repeated for three times.

Quantitation of cell proliferation: cells were inoculated at 1×10^3 cells per well into 96-well plates and cultured at 37C, 5% CO_2 and allowed to attach for 24 h. Drugs at their half maximal growth inhibitory concentration (IC50) concentrations were added. After 24, 48, 72, 96, and 120 h, 10 μL CCK-8 reagent and 100 μL medium were added for 2 h at 37°C. Then absorbance of each well was measured at 450 nm using a spectrophotometer.

Colony Formation

Cells were inoculated into a 60 mm dish with drug at the IC50 concentration for 48 h. Then, cells were resuspended and seeded at 1×10^3 cells per well in 6-well plates and cultured for 14 days. Cells were fixed with methanol and stained with 0.1% crystal violet. Count the size and number of cell colonies in each group.

Transwell Assay

Chambers with 8-μM pore membranes were used for migration assays. Cells were initially cultured for 48 h in media without and with different concentrations of drugs. Then, cells were digested with pancreatin and diluted in serum-free medium and inoculate into the upper transwell chambers at a density of 2×10^4 cells per chamber. Complete medium was added to the bottom chamber. After 24 or 48 h, migrated cells were stained with 0.1% crystal violet.

Flow Cytometry

For quantitation of apoptosis, Annexin V-FITC Detection Kit (C1063, Beyotime, China) was used and cells were inoculated into a 60 mm dish with drugs at IC50 concentrations for 48 h. After washing the cells twice with PBS, the cells were digested and resuspended in binding buffer containing 5 μL of an Annexin V-FITCAfter incubation at room temperature for 20 min, 10 μL PI was added to the suspension and incubated for another 10 min. Then the degree of apoptosis was detected by flow cytometry (Accuri C6, Becton-Dickinson, United States).

For quantitation of cell cycle phases, Cell cycle Detection Kit (BestBio, China) was applied and cells were incubated with drugs for 24 h, then digested and collected into 70% ethanol at -20°C and allowed to fix for 2 h. The fixed cells were centrifuged at 1000 rpm and then washed with PBS, resuspended in staining buffer (0.5 ml) containing PI (25 μL) and RNase A (10 μL), and incubated at 37°C for 30 min in the dark. Finally, the DNA level was measured by flow cytometry.

Western Blotting

Cell cultures were incubated in 60 mm dishes with different concentrations of drug for 48 h and then washed twice with PBS for digestion and cell collection. The cells were lysed for 30 min in ice-cold RIPA buffer with phenylmethylsulfonyl fluoride and Protein phosphatase inhibitor (Solarbio, China). Then, lysates were ultrasonicated three times (4 s each) and centrifuged at 12,000 rpm for 15 min to remove the precipitate, and the protein concentration was determined using a bicinchoninic acid assay (BCA) kit (GenStar, China). After denaturation, 30 μg of protein was subjected to SDS-polyacrylamide gel electrophoresis, transferred to a polyvinylidene fluoride membrane, and blocked with 5% milk. The PVDF membrane was incubated with primary antibodies overnight to detect the expression of mTOR pathway-related proteins and cycle-related proteins. Primary antibodies and diluted concentration were followed: Akt (1:1000, #4691, CST, United States), p-Akt (1:1000, #4060, CST, United States), mTOR (1:1000, #2983, CST, United States), p-mTOR (1:1000, #5536, CST, United States), p70S6K (1:1000, #9202, CST, United States), p-p70S6K (1:1000, #9205, CST, United States), cyclin D1 (1:1000, #2978, CST, United States), GAPDH (1:1000, #TA309157, ZSGB-BIO, China), p21 (1:1000, #2947, CST, United States), β-Actin (1:1000, #TA-09, ZSGB-BIO, China). After incubation with primary antibody, membranes were washed, then incubated with HRP-conjugated secondary antibody (1:2000) at room temperature for 120 min. Enhanced chemiluminescence chemicals were used to visualize target proteins and chemiluminescence western blotting detection system (Bio-Rad ChemiDoc XRS+, United States) was used for protein detection.

RESULTS

Itraconazole Inhibits the Proliferation and Motility of Triple-Negative Breast Cancer Cells Through Suppressing the AKT/mTOR Pathway

To investigate the potential function and mechanism of ITZ in TNBC, the concentration of ITZ required for treating TNBC cells was determined by CCK-8 assay to identify IC50 for MDA-MB-231 and BT-549 cells. Results showed that with increasing concentration of ITZ, the survival rate of TNBC cells decreased in a dose-dependent manner (**Figure 1A**), with IC50s of 4.917 μM for MDA-MB-231 and 4.367 μM for BT-549 obtained.

The anti-cancer activities of ITZ were examined by measuring the effects of ITZ on the proliferation and motility of TNBC cells. In the CCK-8 assay, TNBC cells were exposed with or without ITZ at the IC50 concentration for 24, 48, 72, 96, and 120 h. ITZ treatment inhibited the proliferation of both MDA-MB-231 and BT-549 cells (**Figure 1B**). Colony formation was also decreased by ITZ, compared with the control group, in both MDA-MB-231 and BT-549 cells (**Figure 1C**). Furthermore, transwell assays suggested that treatment with ITZ suppressed the migratory ability of MDA-MB-231 and BT-549 cells (**Figure 1D**).

To explore the underlying mechanism of ITZ in TNBC cells, protein levels of AKT/mTOR signaling pathway components were examined by western blotting. Interestingly, the activated forms of AKT and mTOR were decreased with ITZ treatment, while the expression levels of AKT and mTOR were not suppressed in the ITZ-treated groups. To confirm the

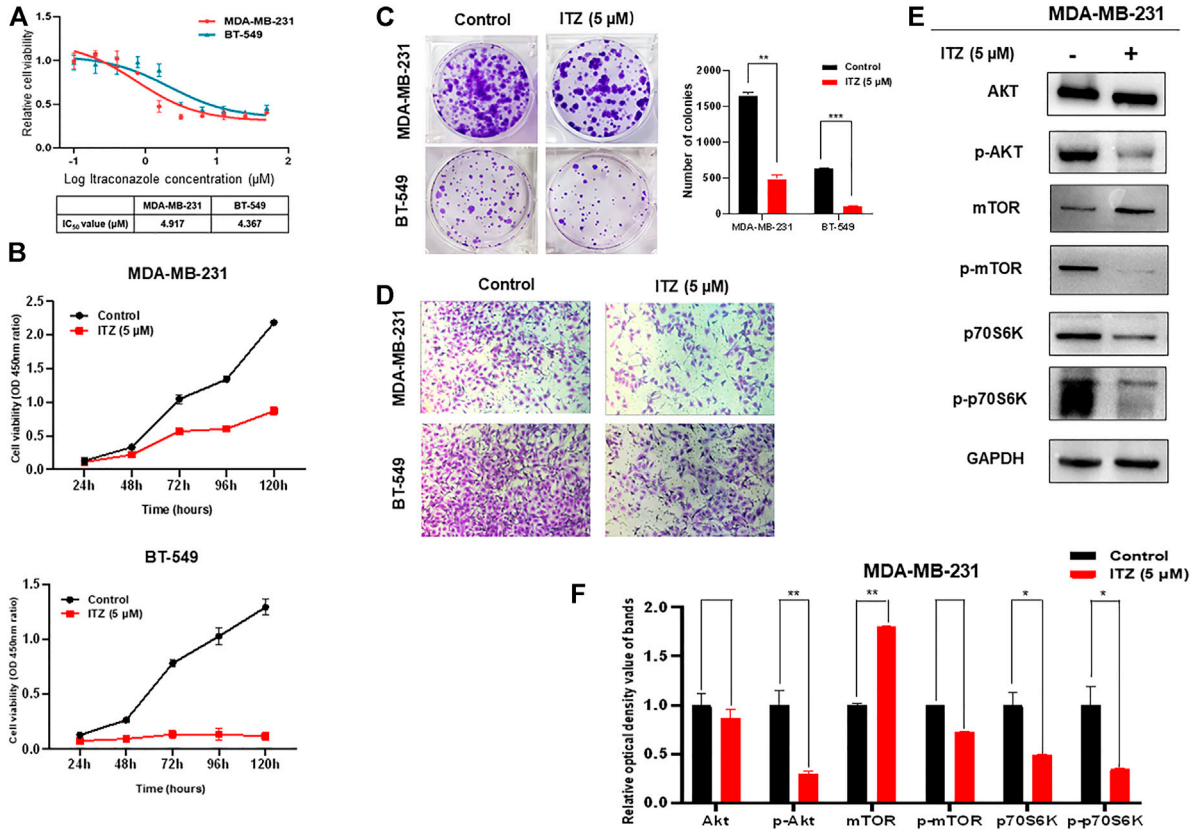

FIGURE 1 | Effect of ITZ on TNBC cells. **(A)** Proliferation of TNBC cells was dose-dependently inhibited by varying concentrations of ITZ **(B)** The proliferation rate of TNBC cells was suppressed by ITZ in time-dependent manner **(C)** Colony formation assay showing ITZ treatment reduces both the number and size of colonies formed by both MDA-MB-231 and BT-549 cells, quantified and analyzed in histogram **(D)** Transwell assay showing the motility of MDA-MB-231 and BT-549 cells was dramatically inhibited by ITZ treatment **(E,F)** Activity of the AKT/mTOR signaling pathway was decreased by ITZ treatment. The quantified results from Western blot **(E)** were analyzed with statistical significance in histogram **(F)**. $^{*}p < 0.05$, $^{**}p < 0.01$, $^{***}p < 0.001$.

involvement of the AKT/mTOR signaling pathway, phosphorylation of the mTOR downstream target p70S6K was also examined. Phosphorylation of p70S6K was inhibited in the ITZ-treated groups, consistent with reduced p-AKT and p-mTOR levels (**Figures 1E,F**).

Inhibition of the AKT/mTOR Pathway by Rapamycin Inhibits the Proliferation and Motility of Triple-Negative Breast Cancer Cells

The ability of rapamycin to inhibit growth of TNBC cells was also determined by CCK-8 assay, which showed IC50s of 12.2 μM for MDA-MB-231 and 15.9 μM for BT-549 cells (**Figure 2A**). Not surprisingly, the proliferation and colony formation of both MDA-MB-231 and BT-549 cells were suppressed by rapamycin treatment at the IC50 concentration (**Figures 2B,C**). The number of migratory cells in the transwell assay was lower in the rapamycin-treated group than that in the control (**Figure 2D**). As an mTOR inhibitor, rapamycin treatment of TNBC cells resulted in low activity of the AKT/mTOR signaling pathway, as demonstrated by decreased expression of p-AKT, p-mTOR, and p-p70S6K (**Figures 2E,F**).

Combined Treatment of Itraconazole and Rapamycin Suppresses Triple-Negative Breast Cancer Cells Synergistically

To investigate the potential function of combined ITZ with rapamycin in TNBC cells, CCK-8, colony formation and transwell assays were used to evaluate the malignant behavior of TNBC cells. In **Figure 3A**, the proliferation of both MDA-MB-231 and BT-549 cells was suppressed in both the ITZ- and rapamycin-treated groups, compared with the control groups, while the combined treatment inhibited the proliferation of TNBC cells dramatically compared to treatment with either drug alone. Consistently, colony formation was decreased by ITZ or rapamycin treatment alone, but the decline was even greater in the combined treatment groups than that in the groups treated with either drug alone (**Figures 3B,C**). Regarding the migratory ability of TNBC cells, transwell assays showed that the inhibition of TNBC cell motility was the most obvious in the

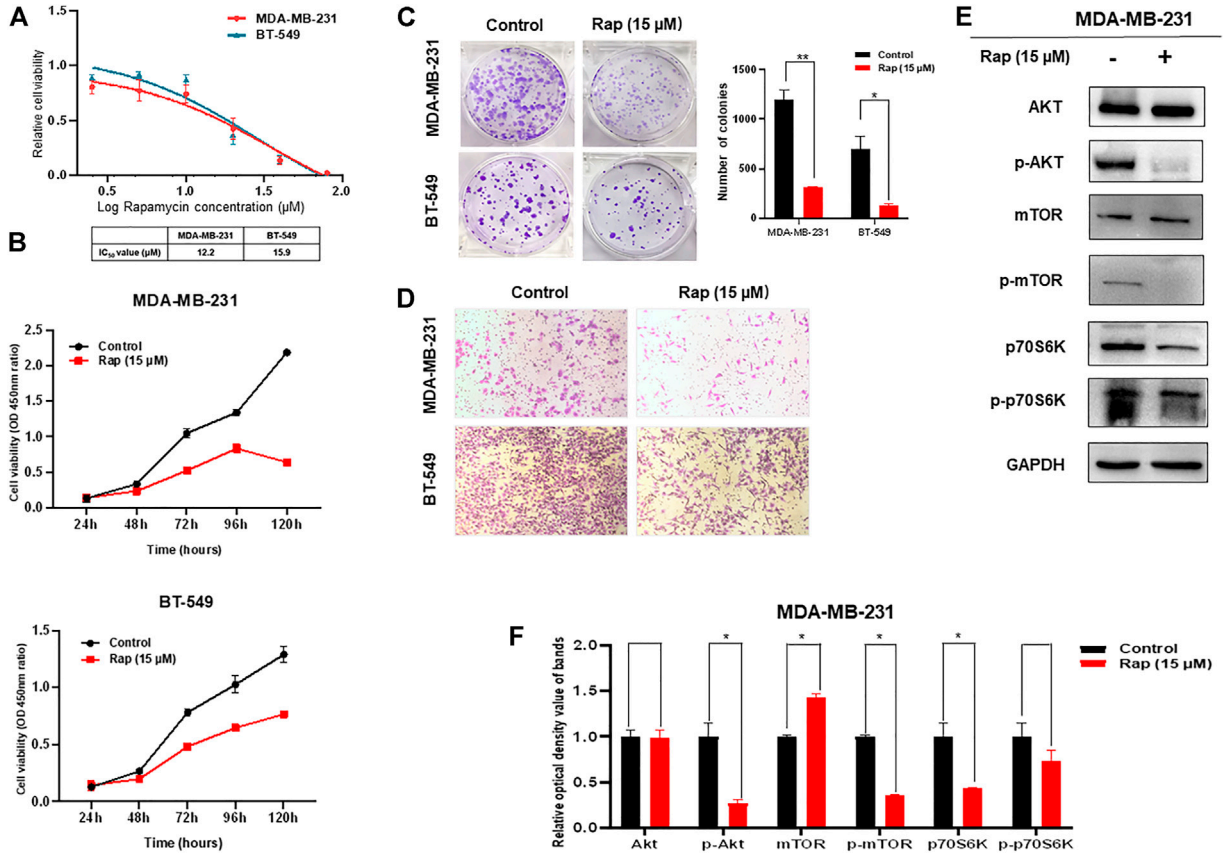

FIGURE 2 | Effect of rapamycin on TNBC cells. **(A)** Viability of TNBC cells treated with varying concentrations of rapamycin **(B)** Proliferation of TNBC cells was inhibited by rapamycin in time-dependent manner **(C)** Colony formation of both MDA-MB-231 and BT-549 cells were suppressed by rapamycin treatment, analyzing in histogram **(D)** Motility of MDA-MB-231 and BT-549 cells was dramatically inhibited by rapamycin treatment **(E,F)** Rapamycin treatment decreased the activity of the AKT/mTOR signaling pathway. The quantified results from Western blot **(E)** were analyzed with statistical significance in histogram (F). $^{*}p < 0.05$, $^{**}p < 0.01$, $^{***}p < 0.001$.

combined treatment of ITZ and rapamycin rather than treatment with ITZ or rapamycin alone (**Figure 3D**).

The activity of the AKT/mTOR signaling pathway was also evaluated by the expression of biomarkers. In **Figures 3E,F**, although the expression level of AKT, mTOR, and p70S6K was not decreased following treatment with ITZ and rapamycin alone or in combination, their activated forms, i.e. p-mTOR, and p-p70S6K, were decreased in the single drug-treated groups, and were even lower in the combined treatment group.

Itraconazole and Rapamycin Induce Triple-Negative Breast Cancer Cell Apoptosis Seperately

In order to investigate the combined effect of ITZ and rapamycin in TNBC, the percentage of apoptotic cells was evaluated by flow cytometry after ITZ and rapamycin treatment. Apoptosis was induced by ITZ treatment and rapamycin treatment alone in MDA-MB-231 cells (**Figure 4A**), whereas for BT-549 cells, ITZ but not rapamycin induced apoptosis (**Figure 4A**).

For the combined treatment of ITZ and rapamycin, the cells were collected after a 48 h treatment and analyzed by flow cytometry. Although in the ITZ-treated group, apoptosis was induced accordingly, the percentage of apoptotic cells in the combined treatment group was not increased compared with the single drug groups (**Figure 4B**), indicating that the synergistic inhibition of ITZ and rapamycin on TNBC cells was not through inducing apoptosis.

Synergistic Inhibition of Itraconazole in Combination With Rapamycin Is due to Cell Cycle Arrest

As apoptosis was not synergistically induced by ITZ and rapamycin in combination, the question arose as to how the proliferation and motility of TNBC cells was inhibited. Cell cycle analysis of TNBC cells was conducted to investigate the underlying mechanism. Interestingly, the proportion of TNBC cells in G0/G1 phase increased with ITZ and rapamycin treatment alone, but was especially high in the combined treatment group (**Figure 5A**).

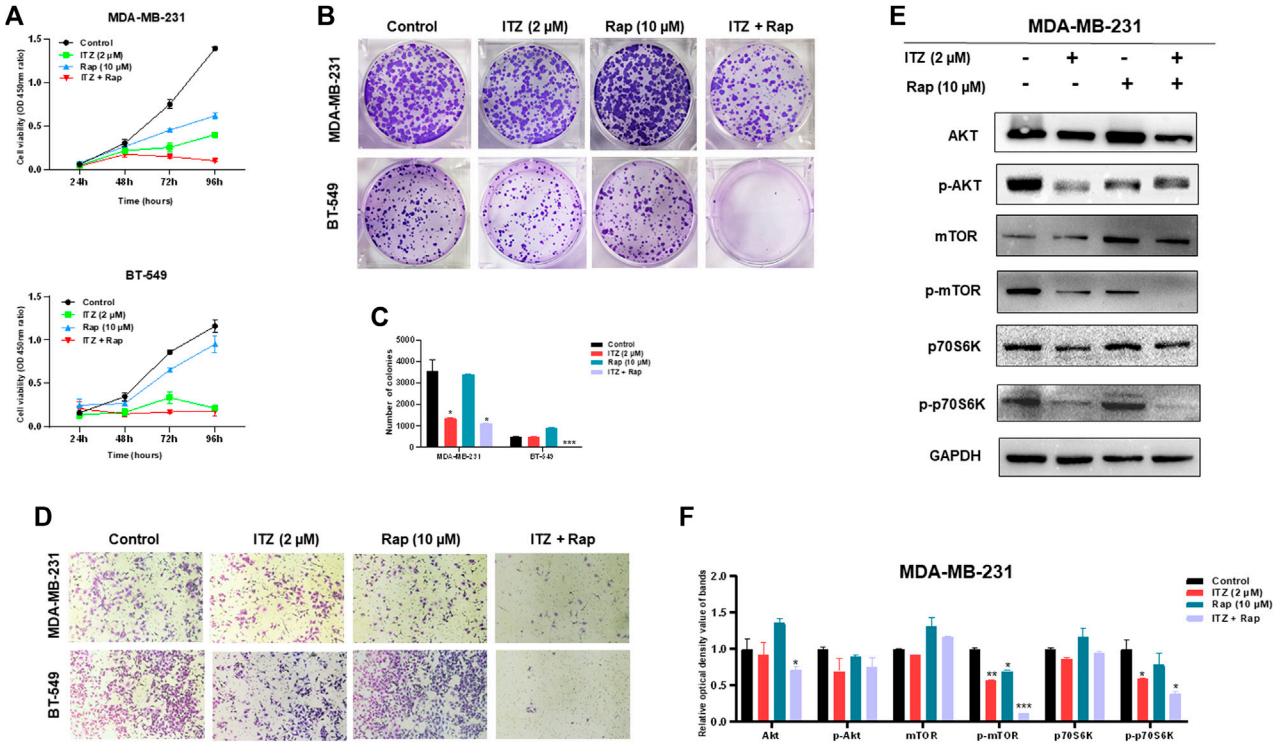

FIGURE 3 | Combined effect of ITZ and rapamycin in TNBC cells. **(A,B)** Proliferation (A) and colony formation (B) of both MDA-MB-231 and BT-549 cells were suppressed by treatment with ITZ, rapamycin and ITZ + rapamycin **(C)** The quantified results of colony formation in TNBC cell treated with control, monotherapy and combined therapy **(D)** Motility of MDA-MB-231 and BT-549 cells was dramatically inhibited by treatment with ITZ, rapamycin and ITZ + rapamycin **(E)** AKT/mTOR signaling pathway activity was decreased by treatment with ITZ and rapamycin alone and combined **(F)** The quantified results from Western blot were analyzed with statistical significance in histogram. $^{*}p < 0.05$, $^{**}p < 0.01$, $^{***}p < 0.001$.

Concomitant with cell cycle arrest in G0/G1 phase, the number of TNBC cells entering S and G2 phases was decreased accordingly. To confirm the synergistic effect of ITZ and rapamycin on blocking cell cycling, cell cycle-related proteins were detected by western blotting, which showed that treatment with ITZ (5 μM) or rapamycin (15 μM) alone suppressed the expression of cyclin D1, an indicator of G1/S phase transition (**Figures 5B,C**). Importantly, upon combined treatment with ITZ (2 μM) and rapamycin (10 μM), the expression of cyclin D1 was the lowest compared with control and single drug-treated groups (**Figures 5D,E**).

DISCUSSION

For patients with TNBC, chemotherapy has been the main therapeutic strategy due to the lack of targeted therapy. However, chemo-resistance, distant metastasis and relapse seriously affect the quality of life and survival of patients with TNBC (Shi et al., 2018). Drug combinations or drug repurposing have the potential to treat TNBC and/or reduce the amount of drug and related toxicity. Important signaling pathways, such as NF-κB, PI3K/Akt/mTOR, Notch 1, Wnt/β-catenin, and YAP, have been considered as therapeutic targets for patients with cancer (Lee et al., 2020). The current study proposes a novel combination of ITZ and rapamycin, both of which target the mTOR signaling pathway.

First, the optimal concentration used for TNBC cells was evaluated by CCK-8 assay. Interestingly, although both MDA-MB-231 and BT-549 cells are TNBC cell lines, the tolerance to ITZ and rapamycin are quite different with different IC50 values. For other types of breast cancer cell lines, the sensitivity to ITZ and rapamycin can be different based on the exposure time (Tengku Din et al., 2014; Ozates et al., 2021). Our results show that at the IC50 concentrations for ITZ and rapamycin, the proliferation and motility of both MDA-MB-231 and BT-549 cells are inhibited.

Cai *et al.* investigated the influence of different triazole antifungal drugs on the pharmacokinetics of cyclophosphamide, and all tested triazoles, including ITZ, increased the pharmacokinetics of cyclophosphamide in cancer patients, as well as the area under the plasma concentration-time curve of cyclophosphamide (Cai et al., 2020). Importantly, it has been reported that combination with ITZ treatment enhanced the toxicity due to chemotherapy in patients with Hodgkin's lymphoma, causing severe myelosuppression and neurotoxicity after concurrent administration (Bashir et al., 2006). However, our combined treatment used lower concentrations of ITZ and rapamycin than the IC50, with the hypothesis that ITZ would enhance the cytotoxicity of rapamycin in TNBC cells. As expected, synergistic inhibition was observed to occur through suppressing the AKT/mTOR signaling pathway.

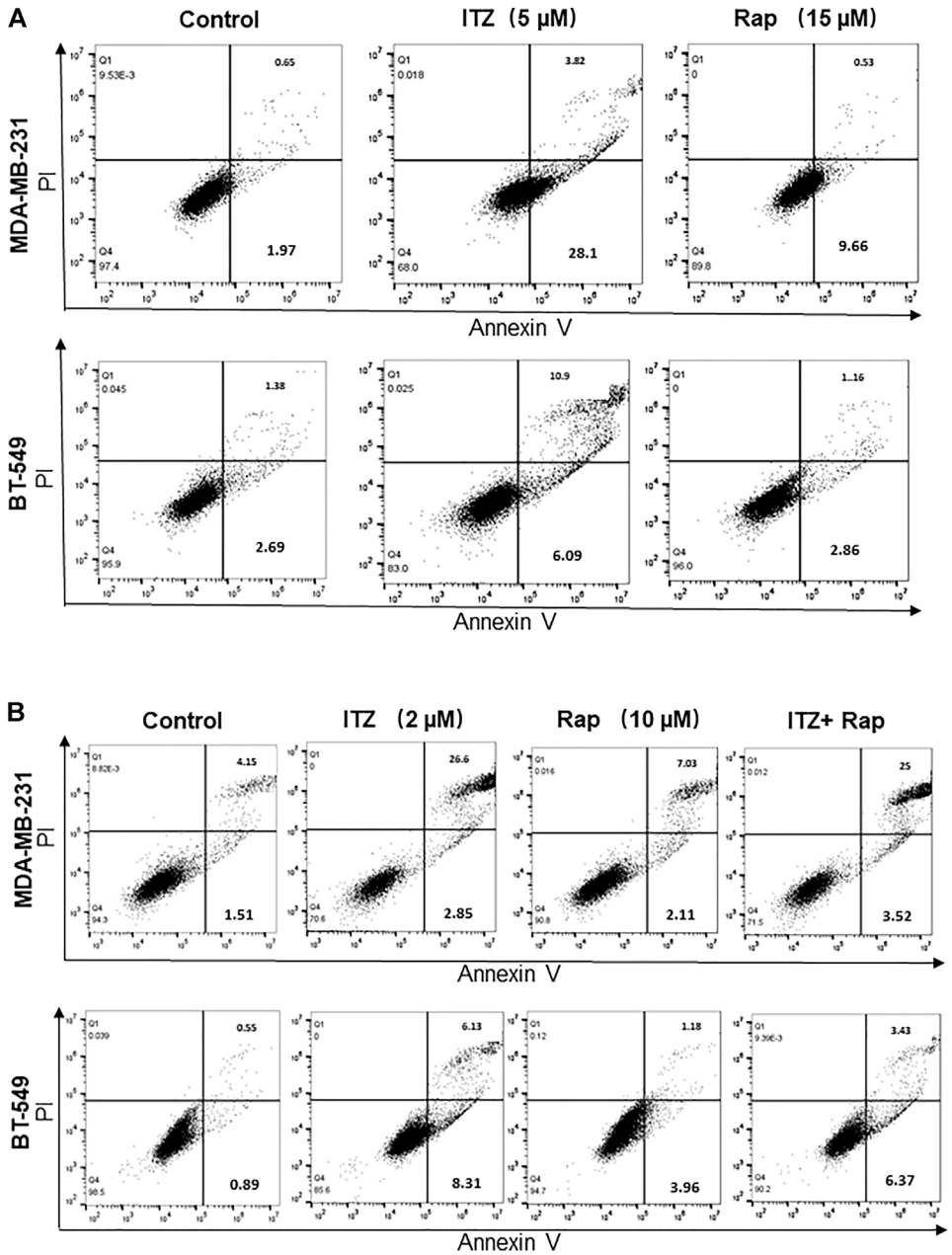

FIGURE 4 | Apoptosis induced by ITZ and/or rapamycin in TNBC cells. **(A)** The percentage of apoptotic cells with or without ITZ or rapamycin treatment **(B)** The combined treatment of TNBC cells induced apoptosis without a synergistic effect.

Further investigation focused on the mechanism of synergism in TNBC cells. Both apoptosis and cell cycle arrest are involved in this process. Flow cytometric analyses were conducted in this study. Interestingly, no enhanced induction of apoptosis was found upon combined treatment, indicating other mechanisms are involved in the inhibition of malignant behavior. Buczacki *et al.* demonstrated that ITZ could cause cycling and dormant cells to switch to global senescence in CRC models (Buczacki et al., 2018). Consistent with this, either ITZ or rapamycin treatment induced cell cycle arrest. Moreover, combined treatment with ITZ and rapamycin enhanced cell cycle arrest in TNBC cells through or partially p21 protein and decreasing cyclin D1 levels.

Nevertheless, attention also should be paid to side effects due to ITZ-enhanced toxicity of other compounds. In adult acute lymphoblastic leukemia, ITZ was found to enhance vindesine neurotoxicity (Chen et al., 2007). Recently, Foroughinia *et al.* reported vincristine-induced seizures potentiated by ITZ following chemotherapy of diffuse large B-cell lymphoma (Foroughinia et al., 2012), calling for

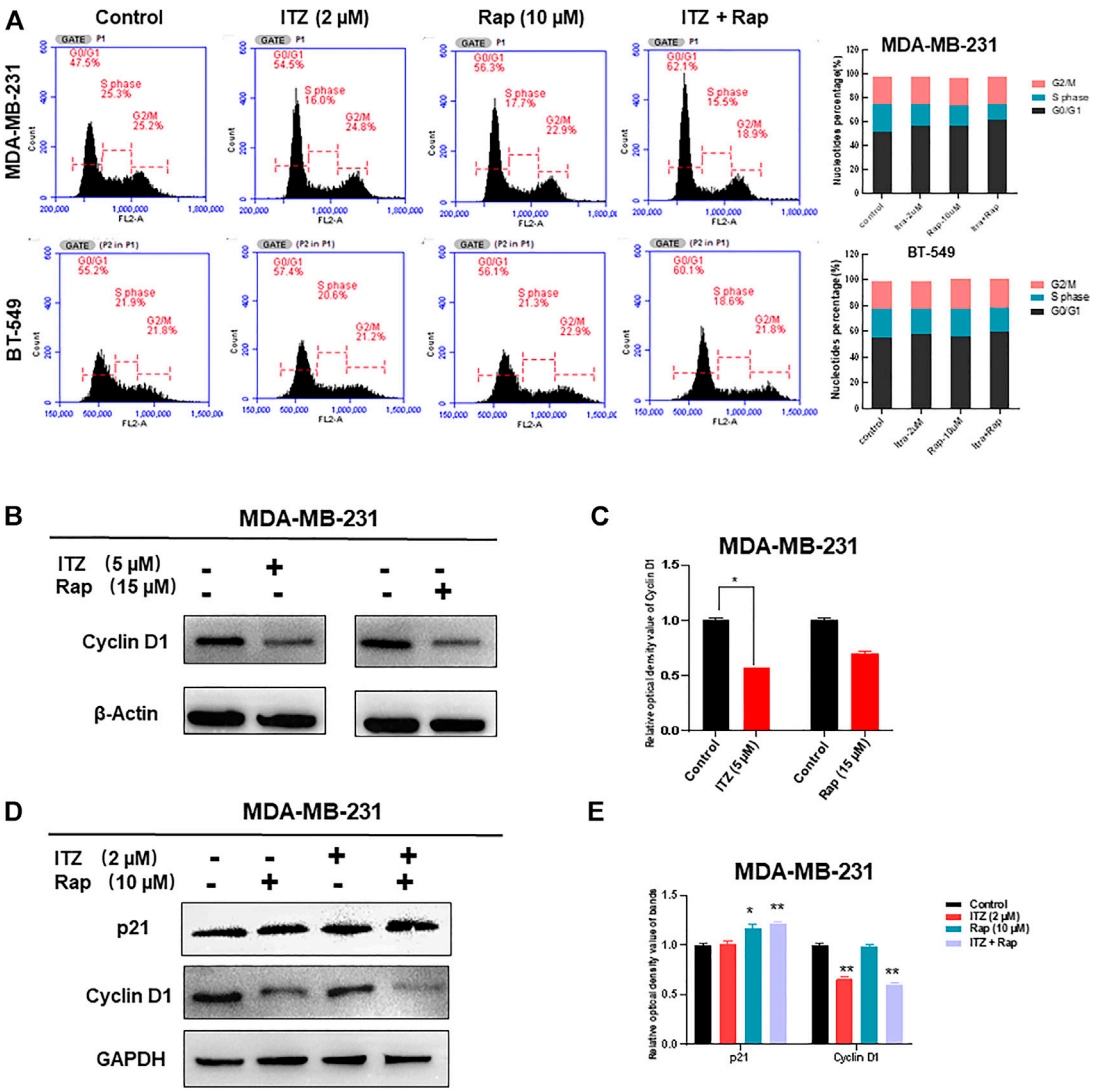

FIGURE 5 | Cell cycle arrest caused by synergism between ITZ and rapamycin in TNBC cells. **(A)** ITZ and rapamycin caused cell cycle arrest in G0/G1 phase to inhibit the malignant behavior of TNBC cells **(B,C)** Expression of cyclin D1 was suppressed by ITZ (5 μM) or rapamycin (15 μM) treatment, analyzed in histogram (C) **(D,E)** Expression of cyclin D1 was decreased by the synergistic effect of ITZ (2 μM) combined with rapamycin (10 μM) in TNBC cells, whereas p21 accumulated in the combined group, analyzed in histogram (E). $^{*}p < 0.05$, $^{**}p < 0.01$, $^{***}p < 0.001$.

attention to the need to evaluate the benefits and risks of patients before clinical use.

CONCLUSION

Combination of ITZ with rapamycin exerts an antitumor effect on TNBC cells through arresting cell cycling in G0/G1 phase, rather than synergistically inducing apoptosis.

DATA AVAILABILITY STATEMENT

The raw data supporting the conclusion of this article will be made available by the authors, without undue reservation.

AUTHOR CONTRIBUTIONS

JL and W-JC: conceptualization. H-TW, C-LL, Z-XF, and W-TL: organization of the database. H-TW, and C-LL: performance of most of the experiments. Z-XF, W-JC, and W-TL: performance of some of the experiments. H-TW and C-LL: writing–original draft preparation. JL: writing–review and editing. JL: supervision and project administration. JL and H-TW: funding acquisition. All authors have read and agreed to the published version of the manuscript.

FUNDING

This work was supported by the National Natural Science Foundation of China (No. 81501539), the Natural Science

Foundation of Guangdong Province (Nos. 2021A1515012180 and 2016A030312008), 2021 Science and Technology Special Project of Guangdong Province, China (No. 210715216902829), Special Grant for Key Area Programs of Guangdong Department of Education (No. 2021ZDZX2004), and "Dengfeng Project" for the construction of high-level hospital in Guangdong Province—The First Affiliated Hospital of Shantou University College Supporting Funding (No. 202003-10).

REFERENCES

Aftab, B. T., Dobromilskaya, I., Liu, J. O., and Rudin, C. M. (2011). Itraconazole Inhibits Angiogenesis and Tumor Growth in Non-small Cell Lung Cancer. *Cancer Res.* 71, 6764–6772. doi:10.1158/0008-5472.CAN-11-0691

Ally, M. S., Ransohoff, K., Sarin, K., Atwood, S. X., Rezaee, M., Bailey-Healy, I., et al. (2016). Effects of Combined Treatment with Arsenic Trioxide and Itraconazole in Patients with Refractory Metastatic Basal Cell Carcinoma. *JAMA Dermatol.* 152, 452–456. doi:10.1001/jamadermatol.2015.5473

Antonarakis, E. S., Heath, E. I., Smith, D. C., Rathkopf, D., Blackford, A. L., Danila, D. C., et al. (2013). Repurposing Itraconazole as a Treatment for Advanced Prostate Cancer: a Noncomparative Randomized Phase II Trial in Men with Metastatic Castration-Resistant Prostate Cancer. *Oncologist* 18, 163–173. doi:10.1634/theoncologist.2012-314

Bashir, H., Motl, S., Metzger, M. L., Howard, S. C., Kaste, S., Krasin, M. P., et al. (2006). Itraconazole-enhanced Chemotherapy Toxicity in a Patient with Hodgkin Lymphoma. *J. Pediatr. Hematol. Oncol.* 28, 33–35. doi:10.1097/01.mph.0000196452.91823.f9

Buczacki, S. J. A., Popova, S., Biggs, E., Koukorava, C., Buzzelli, J., Vermeulen, L., et al. (2018). Itraconazole Targets Cell Cycle Heterogeneity in Colorectal Cancer. *J. Exp. Med.* 215, 1891–1912. doi:10.1084/jem.20171385

Cai, T., Liao, Y., Chen, Z., Zhu, Y., and Qiu, X. (2020). The Influence of Different Triazole Antifungal Agents on the Pharmacokinetics of Cyclophosphamide. *Ann. Pharmacother.* 54, 676–683. doi:10.1177/1060028019896894

Cao, Y., Chen, C., Tao, Y., Lin, W., and Wang, P. (2021). Immunotherapy for Triple-Negative Breast Cancer. *Pharmaceutics* 13, 2003. doi:10.3390/pharmaceutics13122003

Carbone, C., Martins-Gomes, C., Pepe, V., Silva, A. M., Musumeci, T., Puglisi, G., et al. (2018). Repurposing Itraconazole to the Benefit of Skin Cancer Treatment: A Combined Azole-DDAB Nanoencapsulation Strategy. *Colloids Surf. B Biointerfaces* 167, 337–344. doi:10.1016/j.colsurfb.2018.04.031

Chen, S., Wu, D., Sun, A., Qiu, H., Jin, Z., Tang, X., et al. (2007). Itraconazole-enhanced Vindesine Neurotoxicity in Adult Acute Lymphoblastic Leukaemia. *Am. J. Hematol.* 82, 942. doi:10.1002/ajh.20918

Correia, A., Silva, D., Correia, A., Vilanova, M., Gärtner, F., and Vale, N. (2018). Study of New Therapeutic Strategies to Combat Breast Cancer Using Drug Combinations. *Biomolecules* 8, 175. doi:10.3390/biom8040175

El-Sheridy, N. A., El-Moslemany, R. M., Ramadan, A. A., Helmy, M. W., and El-Khordagui, L. K. (2021). Enhancing the *In Vitro* and *In Vivo* Activity of Itraconazole against Breast Cancer Using Miltefosine-Modified Lipid Nanocapsules. *Drug Deliv.* 28, 906–919. doi:10.1080/10717544.2021.1917728

Ferrari, P., Scatena, C., Ghilli, M., Bargagna, I., Lorenzini, G., and Nicolini, A. (2022). Molecular Mechanisms, Biomarkers and Emerging Therapies for Chemotherapy Resistant TNBC. *Int. J. Mol. Sci.* 23, 1665. doi:10.3390/ijms23031665

Foroughinia, F., Baniasadi, S., Seifi, S., and Fahimi, F. (2012). Vincristine-induced Seizure Potentiated by Itraconazole Following RCHOP Chemotherapy for Diffuse Large B-Cell Lymphoma. *Curr. Drug Saf.* 7, 372–374. doi:10.2174/157488612805076633

Gerber, D. E., Putnam, W. C., Fattah, F. J., Kernstine, K. H., Brekken, R. A., Pedrosa, I., et al. (2020). Concentration-dependent Early Antivascular and Antitumor Effects of Itraconazole in Non-small Cell Lung Cancer. *Clin. Cancer Res.* 26, 6017–6027. doi:10.1158/1078-0432.CCR-20-1916

Ghadi, M., Hosseinimehr, S. J., Amiri, F. T., Mardanshahi, A., and Noaparast, Z. (2021). Itraconazole Synergistically Increases Therapeutic Effect of Paclitaxel and 99mTc-MIBI Accumulation, as a Probe of P-Gp Activity, in HT-29 Tumor-Bearing Nude Mice. *Eur. J. Pharmacol.* 895, 173892. doi:10.1016/j.ejphar.2021.173892

Gupta, S., Kim, J., and Gollapudi, S. (1991). Reversal of Daunorubicin Resistance in P388/ADR Cells by Itraconazole. *J. Clin. Invest.* 87, 1467–1469. doi:10.1172/JCI115154

Gupta, A., Unadkat, J. D., and Mao, Q. (2007). Interactions of Azole Antifungal Agents with the Human Breast Cancer Resistance Protein (BCRP). *J. Pharm. Sci.* 96, 3226–3235. doi:10.1002/jps.20963

Hara, M., Nagasaki, T., Shiga, K., and Takeyama, H. (2016). Suppression of Cancer-Associated Fibroblasts and Endothelial Cells by Itraconazole in Bevacizumab-Resistant Gastrointestinal Cancer. *Anticancer Res.* 36, 169–177.

Head, S. A., Shi, W., Zhao, L., Gorshkov, K., Pasunooti, K., Chen, Y., et al. (2015). Antifungal Drug Itraconazole Targets VDAC1 to Modulate the AMPK/mTOR Signaling axis in Endothelial Cells. *Proc. Natl. Acad. Sci. U S A.* 112, E7276–E7285. doi:10.1073/pnas.1512867112

Hu, Q., Hou, Y. C., Huang, J., Fang, J. Y., and Xiong, H. (2017). Itraconazole Induces Apoptosis and Cell Cycle Arrest via Inhibiting Hedgehog Signaling in Gastric Cancer Cells. *J. Exp. Clin. Cancer Res.* 36, 50. doi:10.1186/s13046-017-0526-0

Iida, N., Takara, K., Ohmoto, N., Nakamura, T., Kimura, T., Wada, A., et al. (2001). Reversal Effects of Antifungal Drugs on Multidrug Resistance in MDR1-Overexpressing HeLa Cells. *Biol. Pharm. Bull.* 24, 1032–1036. doi:10.1248/bpb.24.1032

Jelonek, K., Zajdel, A., Wilczok, A., Kaczmarczyk, B., Musiał-Kulik, M., Hercog, A., et al. (2021). Comparison of PLA-Based Micelles and Microspheres as Carriers of Epothilone B and Rapamycin. The Effect of Delivery System and Polymer Composition on Drug Release and Cytotoxicity against MDA-MB-231 Breast Cancer Cells. *Pharmaceutics* 13, 1881. doi:10.3390/pharmaceutics13111881

Kurosawa, M., Okabe, M., Hara, N., Kawamura, K., Suzuki, S., Sakurada, K., et al. (1996). Reversal Effect of Itraconazole on Adriamycin and Etoposide Resistance in Human Leukemia Cells. *Ann. Hematol.* 72, 17–21. doi:10.1007/BF00663011

Lan, K., Yan, R., Zhu, K., Li, W., Xu, Z., Dang, C., et al. (2018). Itraconazole Inhibits the Proliferation of Gastric Cancer Cells *In Vitro* and Improves Patient Survival. *Oncol. Lett.* 16, 3651–3657. doi:10.3892/ol.2018.9072

Lee, Y. T., Chuang, Y. M., and Chan, M. W. Y. (2020). Combinatorial Epigenetic and Immunotherapy in Breast Cancer Management: A Literature Review. *Epigenomes* 4, 27. doi:10.3390/epigenomes4040027

Lee, B. J., Boyer, J. A., Burnett, G. L., Thottumkara, A. P., Tibrewal, N., Wilson, S. L., et al. (2021). Selective Inhibitors of mTORC1 Activate 4EBP1 and Suppress Tumor Growth. *Nat. Chem. Biol.* 17, 1065–1074. doi:10.1038/s41589-021-00813-7

Liang, G., Liu, M., Wang, Q., Shen, Y., Mei, H., Li, D., et al. (2017). Itraconazole Exerts its Anti-melanoma Effect by Suppressing Hedgehog, Wnt, and PI3K/mTOR Signaling Pathways. *Oncotarget* 8, 28510–28525. doi:10.18632/oncotarget.15324

Mohamed, A. W., Elbassiouny, M., Elkhodary, D. A., Shawki, M. A., and Saad, A. S. (2021). The Effect of Itraconazole on the Clinical Outcomes of Patients with Advanced Non-small Cell Lung Cancer Receiving Platinum-Based Chemotherapy: a Randomized Controlled Study. *Med. Oncol.* 38, 23. doi:10.1007/s12032-021-01475-0

Mossmann, D., Park, S., and Hall, M. N. (2018). mTOR Signalling and Cellular Metabolism Are Mutual Determinants in Cancer. *Nat. Rev. Cancer* 18, 744–757. doi:10.1038/s41568-018-0074-8

Muhldorfer, S. M., and Konig, H. J. (1990). Prophylaxis of Fungal Infections with Itraconazole in Immunocompromised Cancer Patients. *Mycoses* 33, 291–295. doi:10.1111/myc.1990.33.6.291

Ozates, N. P., Soğutlu, F., Lerminoglu, F., Demir, B., Gunduz, C., Shademan, B., et al. (2021). Effects of Rapamycin and AZD3463 Combination on Apoptosis, Autophagy, and Cell Cycle for Resistance Control in Breast Cancer. *Life Sci.* 264, 118643. doi:10.1016/j.lfs.2020.118643

Pantziarka, P., Sukhatme, V., Bouche, G., Meheus, L., and Sukhatme, V. P. (2015). Repurposing Drugs in Oncology (ReDO)-Itraconazole as an Anti-cancer Agent. *Ecancermedicalscience* 9, 521. doi:10.3332/ecancer.2015.521

Poulsen, J. S., Madsen, A. M., White, J. K., and Nielsen, J. L. (2021). Physiological Responses of Aspergillus niger Challenged with Itraconazole. *Antimicrob. Agents Chemother.* 65, e02549. doi:10.1128/AAC.02549-20

Rojo-Leon, V., García, C., Valencia, C., Méndez, M. A., Wood, C., and Covarrubias, L. (2019). The E6/E7 Oncogenes of Human Papilloma Virus and Estradiol Regulate Hedgehog Signaling Activity in a Murine Model of Cervical Cancer. *Exp. Cel Res.* 381, 311–322. doi:10.1016/j.yexcr.2019.05.024

Sabatini, D. M. (2017). Twenty-five Years of mTOR: Uncovering the Link from Nutrients to Growth. *Proc. Natl. Acad. Sci. U S A.* 114, 11818–11825. doi:10.1073/pnas.1716173114

Sawasaki, M., Tsubamoto, H., Nakamoto, Y., Kakuno, A., and Sonoda, T. (2020). S-1, Oxaliplatin, Nab-Paclitaxel and Itraconazole for Conversion Surgery for Advanced or Recurrent Gastric Cancer. *Anticancer Res.* 40, 991–997. doi:10.21873/anticanres.14033

Shi, L., Tang, X., Qian, M., Liu, Z., Meng, F., Fu, L., et al. (2018). A SIRT1-Centered Circuitry Regulates Breast Cancer Stemness and Metastasis. *Oncogene* 37, 6299–6315. doi:10.1038/s41388-018-0370-5

Siegel, R. L., Miller, K. D., Fuchs, H. E., and Jemal, A. (2021). Cancer Statistics, 2021. *CA Cancer J. Clin.* 71, 7–33. doi:10.3322/caac.21654

Tengku Din, T. A., Seeni, A., Khairi, W. N., Shamsuddin, S., and Jaafar, H. (2014). Effects of Rapamycin on Cell Apoptosis in MCF-7 Human Breast Cancer Cells. *Asian Pac. J. Cancer Prev.* 15, 10659–10663. doi:10.7314/apjcp.2014.15.24.10659

Tsubamoto, H., Sonoda, T., and Inoue, K. (2014). Impact of Itraconazole on the Survival of Heavily Pre-treated Patients with Triple-Negative Breast Cancer. *Anticancer Res.* 34, 3839–3844.

Wang, W., Dong, X., Liu, Y., Ni, B., Sai, N., You, L., et al. (2020). Itraconazole Exerts Anti-liver Cancer Potential through the nt, PI3K/AKT/mTOR, and ROS Pathways. *Biomed. Pharmacother.* 131, 110661. doi:10.1016/j.biopha.2020.110661

Conflict of Interest: The authors declare that the research was conducted in the absence of any commercial or financial relationships that could be construed as a potential conflict of interest.

Publisher's Note: All claims expressed in this article are solely those of the authors and do not necessarily represent those of their affiliated organizations, or those of the publisher, the editors and the reviewers. Any product that may be evaluated in this article, or claim that may be made by its manufacturer, is not guaranteed or endorsed by the publisher.

frontiers | Frontiers in Pharmacology

ORIGINAL RESEARCH
published: 20 April 2022
doi: 10.3389/fphar.2022.862125

CXCR2 Small-Molecule Antagonist Combats Chemoresistance and Enhances Immunotherapy in Triple-Negative Breast Cancer

Alaa M. Ghallab[1], *Reda A. Eissa*[2] *and Hend M. El Tayebi*[1]*

[1]The Molecular Pharmacology Research Group, Department of Pharmacology, Toxicology and Clinical Pharmacy, Faculty of Pharmacy and Biotechnology, German University in Cairo, Cairo, Egypt, [2]Department of Surgery, Faculty of Medicine, Ain Shams University, Cairo, Egypt

Triple-negative breast cancer (TNBC) is the most malignant subtype of breast cancer as the absence of cell surface receptors renders it more difficult to be therapeutically targeted. Chemokine receptor 2 (CXCR2) has been suggested not only to promote therapy resistance and suppress immunotherapy but it also to possess a positive cross-talk with the multifunctional cytokine transforming growth factor beta (TGF-β). Here, we showed that CXCR2 and TGF-β signaling were both upregulated in human TNBC biopsies. CXCR2 inhibition abrogated doxorubicin-mediated TGF-β upregulation in 3D *in vitro* TNBC coculture with PBMCs and eliminated drug resistance in TNBC mammospheres, suggesting a vital role for CXCR2 in TNBC doxorubicin-resistance *via* TGF-β signaling regulation. Moreover, CXCR2 inhibition improved the efficacy of the immunotherapeutic drug "atezolizumab" where the combined inhibition of CXCR2 and PDL1 in TNBC *in vitro* coculture showed an additive effect in cytotoxicity. Altogether, the current study suggests CXCR2 inhibitors as a promising approach to improve TNBC treatment if used in combination with chemotherapy and/or immunotherapy.

Keywords: triple-negative breast cancer, chemoresistance, CXCR2 inhibition, doxorubicin, atezolizumab, AZD5069

OPEN ACCESS

Edited by:
Simona Rapposelli, University of Pisa, Italy

Reviewed by:
Yuning Hou, Emory University, United States
Zhe Yang, The University of Queensland, Australia

***Correspondence:**
Hend M. El Tayebi
hend.saber@guc.edu.eg

Specialty section:
This article was submitted to Pharmacology of Anti-Cancer Drugs, a section of the journal Frontiers in Pharmacology

Received: *25 January 2022*
Accepted: *11 March 2022*
Published: *20 April 2022*

Citation:
Ghallab AM, Eissa RA and El Tayebi HM (2022) CXCR2 Small-Molecule Antagonist Combats Chemoresistance and Enhances Immunotherapy in Triple-Negative Breast Cancer. Front. Pharmacol. 13:862125. doi: 10.3389/fphar.2022.862125

1 INTRODUCTION

Breast cancer (BC) is the most common cancer and one of the leading causes of death in women (Momenimovahed and Salehiniya, 2019). Triple-negative breast cancer (TNBC) is the most lethal subtype of BC characterized by lack of expression of hormonal estrogen (ER+) and progesterone receptors (PR+) and the human epidermal growth factor receptor 2 (HER2+) receptor (Pal et al., 2011). TNBC is thought to be more immunogenic than hormonal subtypes (Rody et al., 2011), and it is consistently associated with poorer survival than non-TNBC (Dent et al., 2007). The major obstacle hindering TNBC effective therapy is the acquired resistance to chemotherapeutics after repetitive and long-term chemotherapeutic administration (Nedeljković and Damjanović, 2019; Gottesman, 2002). Chemoresistance in TNBC is a multifactorial process based on the particular interplay of the tumor microenvironment, drug efflux, cancer stem cells, and bulk tumor cells, where the alterations of multiple signaling pathways govern these interactions (Nedeljković and Damjanović, 2019).

Doxorubicin is one of the anthracycline antibiotics (Barrett-Lee et al., 2009). Presently, it is the most powerful chemotherapeutic agent used to treat breast cancer (Shi et al., 2018).

Unfortunately, it has been shown that doxorubicin can cause drug resistance, resulting in poor prognosis and survival in patients since the onset of multidrug resistance in cancer cells usually leads to chemotherapy failure (Li et al., 2005; Lee et al., 2006; Shukla et al., 2010). Studies reported that the interplay between signaling pathways can promote drug resistance through the initiation of proliferation, cell cycle progression, and inhibition of apoptosis (Lee et al., 2006; Abrams et al., 2010). Previous data showed that knockdown of CXCR2 enhances doxorubicin-mediated toxicity in mammary tumor cells. Furthermore, CXCL1, "a CXCR2 ligand," was found to be overexpressed in doxorubicin-treated mammary tumor cells, which was inhibited following CXCR2 knockdown (Sharma et al., 2013a).

A new weapon against cancer that has elicited durable clinical advances is cancer immunotherapy that inhibits immune-checkpoints; cytotoxic T-lymphocyte–associated protein 4 (CTLA4) or programmed death 1 (PD1) and its ligand, and programmed death 1 ligand (PDL1) has changed the landscape of anticancer treatment (Smyth et al., 2016). Specifically, inhibitors targeting PD1 and PDL1 have shown remarkable clinical efficacy in more than 15 cancer types, including TNBC (Sharma and Allison, 2015; Thomas et al., 2021). This unprecedented success prompted FDA approval of the anti-PDL1 monoclonal antibody (mAb), atezolizumab, for the treatment of TNBC (FDA, 2019). Although, the efficacy of immune checkpoint inhibitors was unusual, many patients did not respond to it. Recent data showed that some patients, who demonstrate encouraging primary responses to immunotherapy, can acquire resistance gradually. Currently, there is an urgent need to predict targets for combination therapy to inhibit or treat resistant tumors (O'Donnell et al., 2017).

Chemokine receptor 2 (CXCR2) is a typical G protein–coupled cell surface chemokine receptor (Wise et al., 2002), which has been found to be highly expressed in various cancers, including breast cancer (Koch et al., 1992). Various studies have observed the role of CXCR2 receptor in tumor aggressiveness, resistance, and immunosuppressive properties (Infanger et al., 2013; Wang et al., 2016; Zhang et al., 2017; Wang et al., 2018). CXCR2 is involved in therapy resistance by maintaining and promoting the migration of cancer stem cells (CSCs), and it is not only suggested as a novel cancer stem-like cell marker for TNBC (Wang et al., 2018) but also known to regulate TGF-β signaling, which is known to promote chemotherapy resistance (Mohammad et al., 2015). Furthermore, there is emerging evidence that the myeloid-derived suppressor cells (MDSCs), recruited to the tumor microenvironment through CXCR2 signaling, play a crucial role in protecting tumors from the cytotoxic T cell–mediated antitumor effect and in suppressing the efficacy of immune checkpoint blockade (ICB) (Talmadge, 2007; Gabrilovich et al., 2012). The blockade of CXCR2 significantly reduced the infiltration of MDSCs and improved the function of cytotoxic T cells in bladder and prostate cancer (Wang et al., 2016; Zhang et al., 2017). In a pancreatic ductal adenocarcinoma model, CXCR2 inhibition was found to augment PD1-inhibition (Steele et al., 2016). CXCR2 inhibition has been proposed as an attractive antitumor treatment not only to enhance immunotherapy but also to intensify the cytotoxicity of chemotherapeutic drugs (Gao et al., 2015).

In an attempt to puzzle out a clinically oriented approach to boost the effect of conventional chemotherapy and immunotherapy in TNBC, we selected a novel, potent, selective, and clinically relevant CXCR2 small-molecule inhibitor "AZD5069." AZD5069 was developed with the aim of being selective for CXCR2. When measured in a similar system expressing recombinant CXCR1, it was apparent that this drug is around 100-fold more potent against CXCR2 than CXCR1. Furthermore, this drug has recently shown safety and tolerability in patients with chronic obstructive pulmonary disease (COPD) and advanced malignancies (Kirsten et al., 2015; Nicholls et al., 2015). Moreover, AZD5069 has shown rapid absorption in healthy volunteers (Cullberg et al., 2018).

Our study aims at evaluating the impact of targeting CXCR2 in combination with standard chemotherapy and immunotherapy on several outcomes in TNBC using "AZD5069″ as a selective small-molecule antagonist of the human CXCR2.

2 MATERIALS AND METHODS

2.1 Patient Sample Collection

In total, 22 pairs of breast cancer tissues and adjacent nonbreast cancer tissues were collected from patients undergoing tumor resection surgery. All tissues are of invasive (Infiltrative) ductal carcinoma (IDC); any other type of breast cancer was excluded. The tissues were kept at −80°C for further use. The blood samples were collected from the same pool of patients where peripheral blood mononuclear cells (PBMCs) were isolated from TNBC patients' whole blood and were preserved at −80°C for further use. All human materials were obtained with informed consent after the approval of the German University in Cairo and Ain Shams University Ethical Review Committees. The study followed the ethical guidelines of the 1975 Declaration of Helsinki. Patient clinical parameters are presented in **Table 1**.

2.1.1 Blood Collection Procedure

A total of 8 ml blood was drawn from each patient. The blood was stored in EDTA blood collection tubes at 4°C for few hours. Afterward, 6 ml fresh blood was used for isolating PBMCs using the Ficoll separation method. PBMCs of each patient were stored at −80°C for further use. The PBMCs were pooled together during the preparation of the coculture (**Section 2.2.1**). Plasma was isolated from 2 ml fresh blood by centrifugation and then stored at −80°C for further use.

2.2 Cell Culture and Reagents

MDA-MB-231 cells were purchased from Vacsera tissue bank, Egypt. The cells were cultured in DMEM high glucose media

TABLE 1 | Patient characteristics.

Patients (*n* = 22)	Percentage (%)
Sex	
Male (1/22)	5
Female (21/22)	95
Age (years)	
<50 (1/22)	5
>50 (21/22)	95
Subtype	
Invasive ductal carcinoma (IDC) (22/22)	100
Grade	
Grade 2 (15/22)	68
Grade 3 (6/22)	27
Grade 4 (1/22)	5
ER	
ER +ve (14/22)	64
ER –ve (8/22)	36
PR	
PR +ve (13/22)	59
PR –ve (9/22)	41
HER 2/NEU	
HER 2 + ve (6/22)	27
TNBC	
TNBC (6/22)	27
Treatment	
Naïve (12/22)	55
Neoadjuvant chemotherapy (9/22) "alone or combined with herceptin"	41
Targeted therapy "herceptin" (4/22)	18

supplemented with 10% fetal bovine serum (FBS) and 1% penicillin/streptomycin (pen/strep) at 37°C in 5% CO_2. After 4 days, when the plate is fully confluent, splitting was performed using 1X trypsin to detach the adherent layer of cells.

2.2.1 *In Vitro* Coculture With PBMCs

The coculture of PBMCs with MDA-MB-231 cells was performed through a series of consecutive steps; PBMCs were isolated from TNBC patients' whole blood using the Ficoll separation protocol and were preserved in a solution containing 90% FBS and 10% dimethyl sulfoxide (DMSO) at −80°C till further use. Upon coculturing, PBMCs were thawed gently at 37°C in a water bath. The collected PBMCs were then washed by centrifugation, plated at equal density, stimulated by 1% phytohaemagglutinin (PHA), and incubated overnight in a medium consisting of RPMI 1640 supplemented with 10% FBS and 1% penicillin/streptomycin at 37°C and 5% CO_2. After overnight resting, the PBMCs were treated in triplicate with the doses of AZD5069 (mentioned in **Section 2.2.6**), and PBMCs were incubated for 48 h at 37°C and 5% CO_2 after treatment. Finally, PBMCs were cocultured with MDA-MB-231 cells with a ratio 10:1 and were incubated for 72 h.

2.2.2 Mammosphere Formation

MDA-MB-231 were trypsinized and washed in PBS. The cells were counted and visualized on a hemocytometer. If cell clumps were observed, the cells were passed through a 25-gage needle till a single suspension is formed. A total of 8,000 cells per ml were seeded in 24-well ultralow attachment plates (4,000 cell/well) in mammosphere media containing DMEM/F12 supplemented with 2 mM L-glutamine, 100 U/ml penicillin, 100 U/ml streptomycin, 20 ng/ml recombinant EGF, 10 ng/ml recombinant human bFGF, and 1x B27 supplement. The spheres were imaged at Day 7, and spheres greater than 40 μm in diameter were counted as mammospheres and included in the analysis. The number of mammospheres and single cells was counted using trypan blue exclusion. The percent of mammosphere-forming efficiency (M.F.E%) was calculated using the equation: M.F.E (%) = (no. of mammospheres per well)/(no. of cells seeded per well) × 100. All the working wells had approximately the same efficiency as all wells had the same initial seeding density.

2.2.3 Mammosphere *In Vitro* Coculture With PBMCs

TNBC patient PBMCs were treated by the doses of AZD5069 (mentioned in **Section 2.2.6**). PBMCs were incubated for 48 h at 37°C and 5% CO_2 after the treatment. The coculturing of PBMCs with MDA-MB-231 mammospheres was performed by adding PBMCs to the mammospheres with the ratio 10:1. The coculture was incubated for 72 h.

2.2.4 RT-PCR Assay

Total RNA was extracted from the tissue of breast cancer patients and their adjacent normal tissue using the BIOzol reagent, according to manufacturer's instruction. In total, 2 μg of total RNA was used for cDNA synthesis using the cDNA reverse transcription kit (catalog number: 4368813, Thermo Fisher Scientific, United States). Quantification of the CXCR2 gene was carried out using qRT-PCR. For the amplification of the CXCR2 gene, real-time PCR was carried out using the Taqman gene expression assay (catalog number: 4331182, Applied Biosystems, United States) containing the CXCR2 gene, the master mix, and the GAPDH gene expression assay. The geometric mean of the housekeeping gene GAPDH was used as an internal control to normalize the variability in expression levels. The PCR yielded a cycle threshold value (Ct) for each sample. The expression data were normalized to the geometric mean of the housekeeping gene GAPDH to control the variability in expression levels and were analyzed using the $2^{-\Delta\Delta CT}$ method. The primers used for CXCR2 are as follows:

Forward	5′-CAGCGACCCAGTCAGGATTTA-3′
Reverse	5′-ACCAGCATCACGAGGGAGTTT-3′

The housekeeping gene GAPDH was used as a control, and primers used are as follows:

Forward	5′-GTCTCCTCTGACTTCAACAGCG-3′
Reverse	5′-ACCACCCTGTTGCTGTAGCCAA-3′

2.2.5 MTT Viability Assay

For cell viability evaluation in MDA-MB-231 cells and mammosphere post treatment with doxorubicin, triplicate sets of equal densities per plate were seeded in a 24-well cell culture plate under normal growth conditions (37°C and 5% CO_2). The following day, the cells were treated with step-wise concentrations of doxorubicin (250 nM–2 μM). The MTT experiment was carried out 72-h post treatment using the MTT reagent (catalog number: 11465007001, Sigma Aldrich, Germany). Cell viability was assessed by reading the absorbance at 490 nM using the Victor 1420 multilabel counter plate reader.

2.2.6 Pharmacological Treatment

AZD5069(catalog no: 878385-84-3, MedChem express, United States) was dissolved in DMSO at a concentration of 75 mM, and further dilutions were prepared using DMEM or DMEM/F12. Doxorubicin was dissolved in a free medium of DMEM or DMEM/F12 to prepare an initial concentration of 0.04 mg/ml. Atezolizumab (60 mg/ml vial) was used to prepare a stock solution of (1.2 mg/ml) using free DMEM. For all the parameters measured in the *in vitro* cultures containing PBMCs, 200 nM of atezolizumab (Passariello et al., 2019) was used to treat the coculture, and three different concentrations of AZD5069 (3, 10, or 30 nM) were used to treat the PBMCs before coculturing, where 30 nM is the effective dose for CXCR2 inhibition in PBMCs (Nicholls et al., 2015). For the mammosphere culture, a concentration range of 0–750 nM AZD5069 was used alone or in combination with doxorubicin. In all cultures, doxorubicin (320 nM) was used for treatment, and this dose was concluded from the IC_{50} curve of the drug on MDA-MB-231 cells.

2.2.7 Flow Cytometric Analysis

To evaluate the expression panel of the CXCR2 receptor in the mammospheres, treated and nontreated mammospheres were dissociated and then single-cell suspensions (2.4×10^4 cell/tube) were prepared. For detection of CXCR2, the cells were suspended for 10 min in 0.5% bovine serum albumin (BSA) for blocking; after washing, the cells were kept on a rotator with 2% paraformaldehyde (PFA) for 30 min, washed again, and permeabilized using 0.1% Triton X for 5 min. The cells were washed with PBS and incubated with monoclonal anti-CXCR2 primary antibody (catalog number: sc-7304, Santa Cruz Biotechnology, Germany) (1 μg per one million cells) for 30 min on an ice bucket. After washing with PBS, the cells were incubated with secondary IgG antibody Alexa Fluor 488–conjugated anti-mouse (catalog number: sc-516176, Santa Cruz Biotechnology, Germany) (1 μg per one million cells) for 30 min on an ice bucket. The cells were washed with PBS and then, 10,000 events were acquired for each sample.

2.2.8 ELISA Assay

TGF-β protein was assayed by using the TGF-β ELISA kit (catalog number: MBS266143, My Biosource, United States), according to the manufacturer's protocol. The absorbance was measured at 450 nM using a Victor 1420 multilabel counter plate reader.

2.2.9 Cytotoxicity Assay

Cytotoxicity of the pharmacological treatments in the *in vitro* culture was detected using the lactate dehydrogenase (LDH) assay kit (catalog number: MBS822351, MyBioSource, United States). The cells were incubated for 72 h after the drug treatment. According to the manufacturer's protocol, the supernatant of each well was centrifuged, and LDH reagents were used. LDH release was assessed by reading the absorbance at 490 nM using the Victor 1420 multilabel counter plate reader.

2.2.10 Statistical Analysis

Analysis of the *in vitro* experiment was performed using GraphPad Prism 7.02 software. For the purpose of comparison between two populations, Student's unpaired *t*-test was used, while statistical differences comparing multiple populations were analyzed by analysis of variance (ANOVA). Data were expressed as mean ± standard error of the mean (SEM). A *p*-value less than 0.05 was considered statistically significant. **** = $p < 0.0001$, *** = $p < 0.001$, ** = $p < 0.01$, and * = $p < 0.05$.

3 RESULTS

3.1 CXCR2 is Highly Expressed in the Tumor Tissue of Breast Cancer Patients

CXCR2 expression is highly upregulated in BC tissues than in adjacent normal tissues. Upon segregation of patient subtypes, TNBC and HER2+ve (luminal B or HER2 enriched) patients showed a dramatic upregulation in CXCR2 expression compared to the controls ($p = 0.0039$ and $p = 0.0286$, respectively). Hormonal patients with ER +ve and/or PR +ve and HER2 −ve receptors (luminal A and normal like subtypes) showed mild significantly upregulated CXCR2 expression ($p = 0.0179$) compared to the controls. CXCR2 expression was significantly higher in TNBC patients than in hormonal patients ($p = 0.0199$) (**Figure 1**).

3.2 Elevation of TGF-β Protein Level in Plasma of Breast Cancer Patients

Recent data suggested that TGF-β protein increases with the high expression of CXCR2, and TGF-β is known to possess an impact on drug resistance (Yang et al., 2008). Accordingly, in the same pool of patients, TGF-β protein levels in blood plasma was found to be overexpressed in BC patients than in the healthy control group (all were females, age <55 years, and with no chronic health conditions). TNBC and HER2+ve patients showed significant upregulation in the TGF-β protein level compared to healthy controls ($p = 0.0004$ and $p = 0.0013$, respectively), while hormonal patients with ER +ve and/or PR +ve and HER2 −ve receptors (luminal A and normal like subtypes) showed nonsignificantQ upregulated TGF-β protein levels compared to healthy controls ($p = 0.0652$) (**Figure 2**).

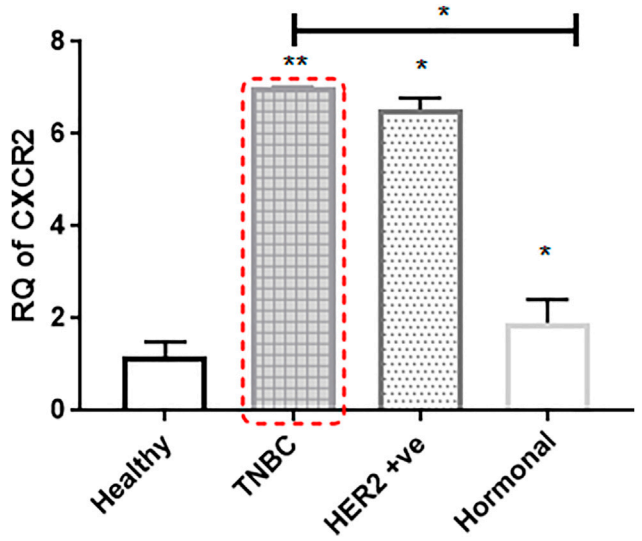

FIGURE 1 | CXCR2 expression is upregulated in the tumor tissue of breast cancer patients. Expression of CXCR2 in different subtypes of BC tissue is compared to the expression in adjacent normal tissue (n = 22). RNA was prepared from whole targeted biopsies post resection and from adjacent normal breast tissue to perform RT-PCR experiment. p values; unpaired Student's t-test.

3.3 3D Morphological Characteristics of Mammospheres Generated From MDA-MB-231 Cell Line

A mammosphere formation assay was performed according to Lombardo et al. (2015) to generate primary mammospheres from the MDA-MB-231 cell line. After 7 days, the transformation of the spindle-shaped MDA-MB-231 cells to a larger spheroidal-shaped mammosphere was observed. The images were captured for the MDA-MB-231 cell line before the experiment at ×10 magnification (**Supplementary Figure S1**), and after the mammosphere formation, the images were captured at ×40 (**Supplementary Figures S1B,C**) and ×20 magnification. (**Supplementary Figures S1D,E**).

3.4 Comparing the Chemosensitivity Response to Doxorubicin in the MDA-MB-231 Cell Line and Mammospheres

To determine the inhibitory concentration (IC_{50}) of doxorubicin in MDA-MB-231 cells, the cell line was treated with step-wise drug concentrations. The cell viability was examined post treatment using the MTT assay and the IC_{50} was calculated. In addition, 320 nM was found to be the drug dose that causes half-maximal inhibitory effect in MDA-MB-231 cells (**Supplementary Figure S2**). Using the same dose range to treat mammospheres, the MTT assay showed the resistance of the mammospheres to doxorubicin. It was observed that the percent viability increased in mammospheres with higher doses of doxorubicin (**Supplementary Figure S2**). Upon comparing the cytotoxic effect of 320 nM doxorubicin on both the MDA-MB-231 cell line and the mammospheres, it was observed that although this dose causes 50% inhibitory effect in sensitive cells, it caused a dramatic increase in the cell viability in mammospheres as the viability increased even above the control (p = 0.0001) (**Supplementary Figure S2**). This confirms the molecular changes in the mammospheres and the acquisition of resistance properties.

3.5 Doxorubicin Induces Higher CXCR2 Expression Level in MDA-MB-231 Mammospheres

Interestingly, it has been reported that chemotherapy upregulates CXCR2 expression levels in breast cancer cells to increase its aggressiveness (Sharma et al., 2013b). The effect of doxorubicin treatment in the CXCR2 expression in mammospheres was evaluated by cytofluorimetry (**Figure 3**) and (**Supplementary Figure S3**). The figure shows a significant increase in CXCR2 expression upon doxorubicin treatment compared to nontreated TNBC mammospheres (p = 0.0031). These results could not be confirmed by immunofluorescence due to the very low fraction of CXCR2 positive cells in the bulk population of mammospheres.

3.6 AZD5069 Inhibits Doxorubicin-Mediated CXCR2 Overexpression and Restores Primary Levels of the Receptor in TNBC Mammospheres

To investigate whether inhibiting CXCR2 signaling might affect the CXCR2 upregulation induced by doxorubicin in TNBC mammospheres, mammosheres were treated with doxorubicin (320 nM) alone and combined with several doses of AZD5069. The dose effect of AZD5069 was estimated using flow cytometry. It was found that CXCR2 inhibition by AZD5069 (50 nM) almost completely abrogated the overexpression of the receptor caused by doxorubicin in TNBC mammospheres. The CXCR2 level in mammospheres treated with doxorubicin alone is extremely higher than the CXCR2 level in mammospheres treated with doxorubicin in combination with 50 nM AZD5069 (p = 0.0483). In addition, the correlation analysis of AZD5069 doses versus CXCR2 expression showed that higher doses of AZD5069 (150 and 750 nM) decreases the expression of the receptor below primary level (p = 0.0008 and 0.0200, respectively) (**Figure 4**) (**Supplementary Figure S4**).

3.7 Elevated TGF-β Protein Level in the *In Vitro* 3D Culture Post treatment With Doxorubicin

In an attempt to simulate clinical situation, coculturing of mammospheres with TNBC patient-derived PBMCs was performed in order to explore whether doxorubicin exposure would cause the elevated protein expression of

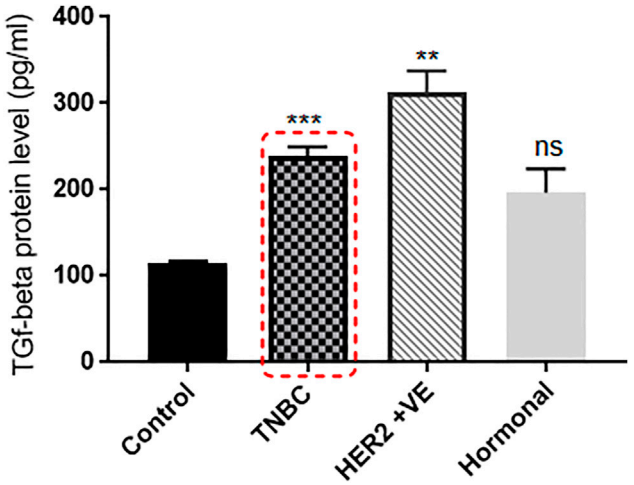

FIGURE 2 | TGF-β protein level is extremely elevated in the plasma of breast cancer patients. TGF-β plasma levels of patients with different BC subtypes (n = 22) are compared to the TGF-β levels of healthy individuals. Plasma was separated from whole blood using the Ficoll separation protocol, and TGF-β concentrations were assessed using ELISA. p values; unpaired Student's t-test.

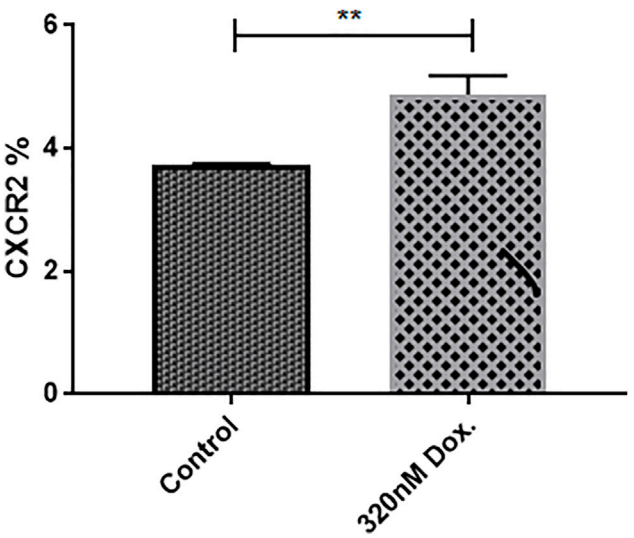

FIGURE 3 | Doxorubicin induces higher CXCR2 expression level in MDA-MB-231 mammospheres. The **c**ytofluorimetric analysis for CXCR2 expression in mammospheres in control and treated conditions; data are expressed as CXCR2 percentage; Dox: doxorubicin. p values, unpaired Student's t-test.

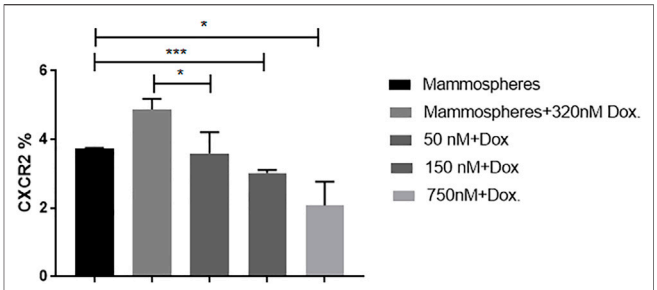

FIGURE 4 | AZD5069 inhibits doxorubicin-mediated CXCR2 overexpression and restores primary levels of the receptor. The cytofluorimetric analysis for CXCR2 expression in mammospheres in control and treated combinations; data are expressed as CXCR2 percentage; Dox: doxorubicin; AZD: AZD5069. p values, unpaired Student's t-test.

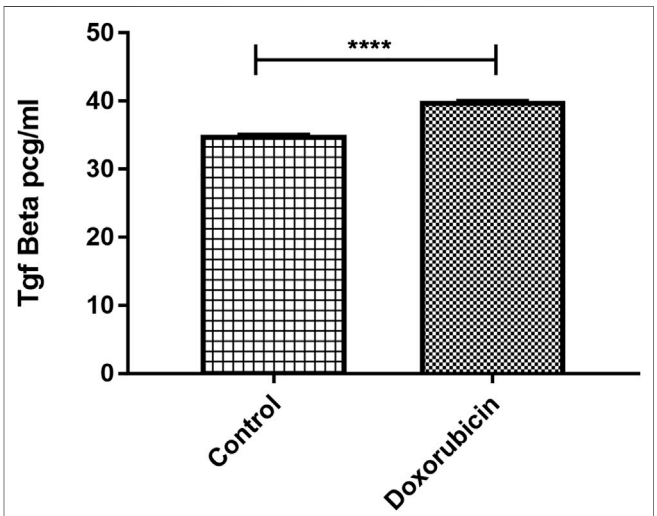

FIGURE 5 | Elevated TGF-β protein level in 3D culture post treatment with doxorubicin. TGF-β levels obtained from ELISA were compared in control and treated conditions. Data are expressed as TGF-β concentration. p values; unpaired Student's t-test.

TGF-β. The TGF-β level in the supernatant of the culture treated with 320 nM doxorubicin was estimated using ELISA and was compared to the TGF-β level of the nontreated culture. Statistically significant upregulation in TGF-β was found in the coculture treated with doxorubicin compared to untreated coculture ($p < 0.0001$) (**Figure 5**).

3.8 AZD5069 Prevents Doxorubicin-Mediated TGF-β Upregulation in the MDA-MB-231 Mammospheres *In Vitro* Cultured With PBMCs

In an attempt to discover whether AZD5069 would have an impact on the TGF-β elevation caused by doxorubicin, TGF-β concentration was measured in the cultures treated with AZD5069 alone and those treated with a combination of AZD5069 and doxorubicin. Doxorubicin induced significant increase in the TGF-β concentration in the cultures treated with small doses of AZD5069, 3 nM AZD5069 (p = 0.0023) and 10 nM AZD5069 (p = 0.0065), compared to nontreated cultures (**Figure 6**), while surprisingly, doxorubicin combined with 30 nM AZD5069 did not induce any elevation in the TGF-β concentration, ($p > 0.9999$ = ns) (**Figure 6**), where 30 nM AZD5069 is the inhibitory dose

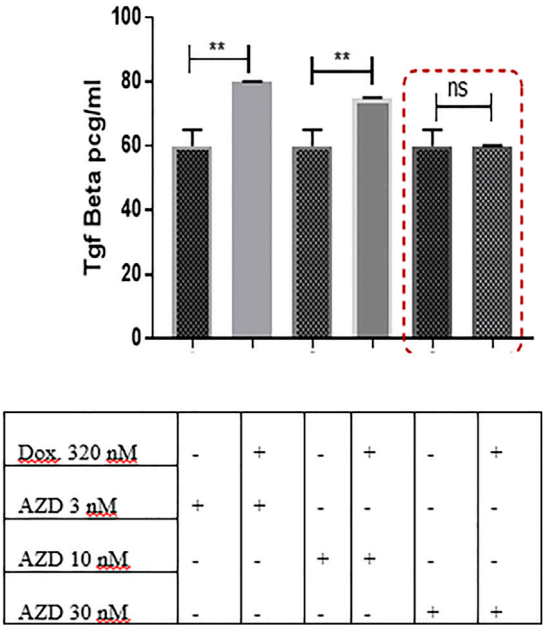

FIGURE 6 | AZD5069 prevents doxorubicin-mediated TGF-β upregulation in 3D culture. TGF-β concentration levels were obtained from ELISA and were compared in different treatment conditions. Data are expressed as TGF-β concentration. Dox: doxorubicin; AZD: AZD5069. *p* values: The TGF-β concentration level of each combined treatment group was compared to the concentration of the corresponding AZD dose alone using unpaired Student's t-test.

for CXCL1 ligand-binding inhibition according to the concentration response curve (Nicholls et al., 2015).

3.9 CXCR2 Inhibition by AZD5069 Diminishes Doxorubicin Chemoresistance in MDA-MB-231 Mammospheres

Recent data suggest the important role of the CXCR2 receptor in maintaining and promoting therapy resistance (Xu et al., 2018a); therefore, would the pharmacological inhibition of CXCR2 signaling inhibit the resistance to doxorubicin in MDA-MB-231 mammospheres? To inhibit CXCR2, AZD5069 was used, the CXCR2 antagonist, at a high, moderate, and low concentrations alone and in association with doxorubicin. While the doxorubicin showed no significant cytotoxic effect on mammospheres (p = ns = 0.2473) (**Figure 7**), the combination of both drugs showed a dramatic significant increase in cytotoxicity than doxorubicin alone (**Figure 7**) and the corresponding dose of AZD5069 alone (**Figure 7B**). This clearly showed that the CXCR2 inhibition diminished chemoresistance characteristics in the mammospheres and, thus, enhanced doxorubicin effect.

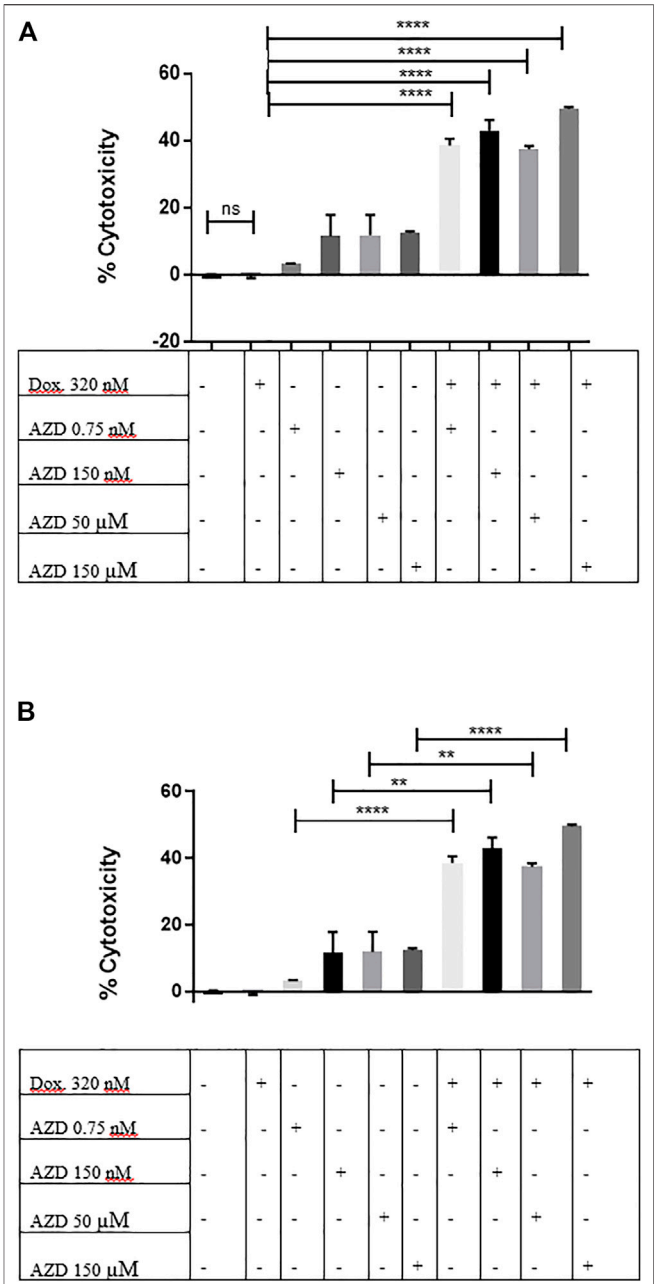

FIGURE 7 | CXCR2 inhibition by AZD5069 diminishes doxorubicin chemoresistance in MDA-MB-231 mammospheres. **(A)** Cell cytotoxicity in control and treated conditions obtained from the LDH assay. Data are expressed as cytotoxicity percentage. Dox: doxorubicin; AZD: AZD5069. *p* values: The cytotoxicity of each combined treatment group was compared to the cytotoxicity of doxorubicin alone using unpaired Student's t-test. ****$p < 0.0001$, ns = $p = 0.2473$. **(B)** Cell cytotoxicity in control and treated conditions obtained from the LDH assay. Data are expressed as cytotoxicity percentage. Dox: doxorubicin; AZD: AZD5069. *p* values. The cytotoxicity of each combined treatment group was compared to the cytotoxicity of the corresponding dose of AZD alone using unpaired Student's t-test. ****$p < 0.0001$, **$p \leq 0.002$.

3.10 Targeting CXCR2 Ultimately Fosters Sensitivity to Anti-PDL1 Immunotherapy in MDA-MB-231 Cells Cultured With PBMCs

Recently, anti-PDL1 inhibitors have shown strong potential in multiple tumor types, including TNBC, by overcoming immune suppression and harnessing endogenous antitumor immunity. Knowing that the CXCR2 receptor contributes to promoting immunosuppressive properties, the anti-PDL1 inhibitor combined with CXCR2 small-molecule antagonist was used in a TNBC *in vitro* culture. It was tempting to ask if such a combination would exhibit an additive cytotoxic effect and if CXCR2 inhibitors could enhance sensitivity to anti-PDL1 therapies. In this experiment, TNBC patient–derived PBMCs (treated or nontreated with AZD5069) were cocultured with MDA-MB-231 cells, and the anti-PDL1 inhibitor "atezolizumab" was added to the coculture. Remarkably, the combination of 30 nM AZD5069 (inhibitory dose for the CXCR2 ligand-binding inhibition in PBMCs according to the concentration–response curve) (Nicholls et al., 2015) and 200 nM atezolizumab induced a significant additive effect in cytotoxicity compared to atezolizumab alone (p = 0.0065) (**Figure 8**), while the noneffective dose of AZD5069 (10 nM) (Nicholls et al., 2015) in association with atezolizumab showed no increase in cytotoxicity than atezolizumab alone p = ns = 0.0607 (**Figure 8**).

4 DISCUSSION

TNBC is a heterogenous disease which is clinically difficult to manage (Pal et al., 2011) with a clear urge for therapy improvements. CXCR2 converges information from tumor cells and the microenvironment, leading to disease progression, chemoresistance, and immunosuppression, supporting a role for the CXCR2 receptor as a novel therapeutic target. This study aimed at studying the role of CXCR2 inhibitors and their possible use as anticancer drugs for TNBC to diminish chemoresistance and augment immunotherapy. Furthermore, it aimed at demonstrating the impact of CXCR2 inhibition on TGF-β–mediated doxorubicin chemoresistance. In the current study, the effect of AZD5069, a small-molecule CXCR2 antagonist, administered alone or in combination with doxorubicin were assayed *in vitro* on MDA-MB-231 mammospheres. Moreover, AZD5069 was used in combination with atezolizumab, an anti-PDL1 inhibitor, and assayed on the same cell line cultured with PBMCs. Here, we showed that although doxorubicin causes significant elevation in the levels of CXCR2 and TGF-β in 3D culture, CXCR2 inhibition by AZD5069 prevents this elevation and restores their levels back to the nontreated condition. Furthermore, in 3D TNBC culture, we highlighted the benefits of CXCR2 inhibition: not only does the inhibition of CXCR2 diminish doxorubicin chemoresistance but it boosts the efficacy of atezolizumab immune checkpoint inhibitor.

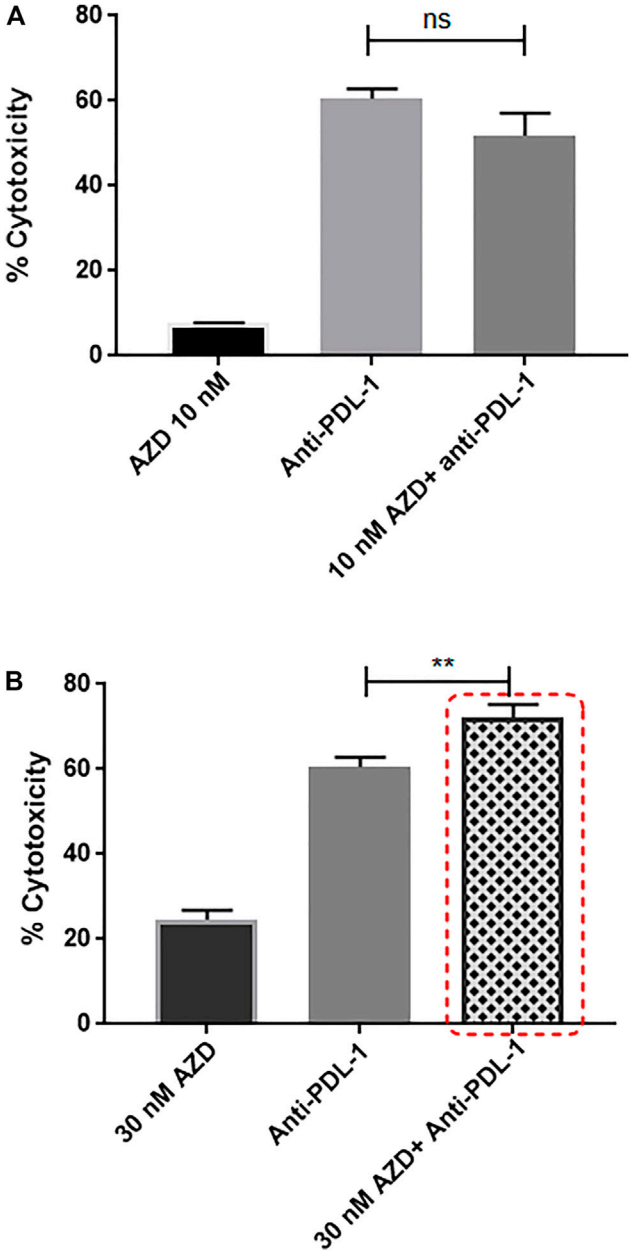

FIGURE 8 | Targeting CXCR2 ultimately fosters sensitivity to anti-PDL1 immunotherapy in MDA-MB-231 cells cultured with PBMCs. **(A)** Cell cytotoxicity in control and treated conditions obtained from the LDH assay. Data are expressed as cytotoxicity percentage. Anti-PDL1: atezolizumab 200 nM; AZD: AZD5069. p values. The cytotoxicity of each combined treatment group was compared to the cytotoxicity of atezolizumab alone using unpaired Student's t-test, ns = p = 0.0607. **(B)** Cell cytotoxicity in control and treated conditions obtained from the LDH assay. Data are expressed as cytotoxicity percentage. Anti-PDL1: atezolizumab 200 nM; AZD: AZD5069. p values. The cytotoxicity of each combined treatment group was compared to the cytotoxicity of atezolizumab alone using unpaired Student's t-test, $^{**}p \leq 0.0065$.

Higher levels of CXCR2 and TGF-β were observed in patients with breast cancer and other types of cancer where they were always correlated with worse clinical outcomes (Ivanović et al., 2006; Li et al., 2011; Gao et al., 2015; Schinke et al., 2015). In our study, the analysis of the CXCR2 expression profile in breast cancer patient tissue biopsies showed that CXCR2 expression is significantly upregulated in patients of the TNBC subtype and other BC subtypes (**Figure 1**). Furthermore, when we compared the TGF-β protein levels in plasma of breast cancer patients to healthy controls, the TGF-β levels was found to be dramatically upregulated in TNBC patients and Her2+ve patients (**Figure 2**).

The cellular model used in this study was the triple-negative MDA-MB-231 cells that were not studied in previous experiments using AZD5069. Mammospheres generated from MDA-MB-231 cells were included in this context as they possess chemoresistant properties (**Supplementary Figure S1**). Although MDA-MB-231 cells were found to express CXCR2 (**Supplementary Figure S5**), mammospheres were created for the drug-resistant properties they possess. Doxorubicin is a chemotherapeutic agent commonly used in patients with breast cancer and was used in the current study to better understand the effect of CXCR2 inhibition. IC_{50} of doxorubicin was generated from the dose-response curve on MDA-MB-231 cells and was used to treat mammospheres to examine its sensitivity where the IC_{50} of doxorubicin and even higher doses were not able to decrease the viability of the mammospheres (**Supplementary Figure S2**). In addition, it was observed that doxorubicin promoted mammosphere growth (**Supplementary Figure S2B**). Though the mechanism was not investigated, studies reported that doxorubicin can induce a higher tumor growth rate in the murine breast tumor model (Christowitz et al., 2019). In the current study, doxorubicin was found to induce higher CXCR2 and TGF-β signaling in the TNBC mammospheres. Although the increase in CXCR2 expression post exposure to doxorubicin is small, it is considered a magnitude of value compared to the normal receptor expression in mammospheres (**Figures 3** and **5**).

While the use of the CXCR2 inhibitor "AZD5069" in combination with doxorubicin blocked the CXCR2 overexpression and TGF-β elevation mediated by doxorubicin in addition to increasing the chemosensitivity of the mammospheres to doxorubicin (**Figures 4**, **6** and **7**). This is in agreement with other studies linking chemotherapy treatment of TNBC to increased TGF-β signaling (Bhola et al., 2013), where this process was observed to be CXCR2-mediated (Yang et al., 2008). These results are also consistent with previous studies in which Bandyopadhyay et al. (2010); Sharma et al. (2013a) showed an increase in CXCR2 and/or TGF-β levels in aggressive breast cancer cells post treatment with doxorubicin, whereas the targeting of either of them was able to increase the response of cancer cells to doxorubicin. Not only does this elevation occur with doxorubicin but also in epirubicin-resistant TNBC cell lines as reported by a recent study (Xu et al., 2018b).

TGF-β signaling is known to promote TNBC chemotherapy resistance in addition to its immunomodulating effect (Neuzillet et al., 2015); moreover, chemotherapy treatment of TNBC was revealed to increase TGF-β signaling (Bhola et al., 2013). Thus, several TGF-β inhibitors are now being evaluated in clinical trials in breast cancer where they generated either disappointing (NCT01401062) or mixed results (Bogdahn et al., 2011; Giaccone et al., 2015). Several barriers remain ahead of TGF-β–based TNBC therapy, including selectivity and/or specificity issues of TGF-βR inhibitors and the accessibility of TGF-β to monoclonal antibodies (mAbs). Furthermore, the TGF-β pathway suppresses tumorigenesis in early-stage cancers, including breast cancer; therefore, a careful use of inhibitors is needed in order to suppress the tumorigenic arm of the pathway, while fostering the tumor-suppressive one (Shi et al., 2011; Smith et al., 2012). Bierie, B. et al. and Yang, L., et al. observed the positive cross-talk of CXCR2 with the TGF ß pathway. They reported that TGF-βR deletion caused an increase in CXCR2 signaling, which led to increased MDSC recruitment into the tumor microenvironment. These MDSCs caused the production of high levels of TGF-ß (Bierie et al., 2008; Yang et al., 2008). Here, we hypothesized that the inhibition of TGF-β elevation could be achieved through CXCR2 inhibitors. 3D TNBC mammospheres cultured with PBMCs were used to mimic clinical conditions, and data showed that CXCR2 inhibition at optimum doses prevented only doxorubicin-induced TGF-β elevation, thus diminishing TGF-β–mediated chemoresistance without further TGF-β inhibition (**Figure 6**).

Not only does doxorubicin drive chemoresistance in triple-negative BC cells through CXCR2 and TGF-β upregulation but also induces drug resistance by interacting with other signaling pathways that promote drug resistance, such as MAPK/ERK, PI3K/Akt (Christowitz et al., 2019), and NF-kB, as reported by some studies (Marinello et al., 2019).

It is worth noting that immunotherapy reactivating antitumor immunity has delivered promising results in various tumor types, including TNBC (Sharma and Allison, 2015). Atezolizumab is an anti-PDL1 immune checkpoint inhibitor used in TNBC treatment and was used in the current study to investigate the impact of targeting CXCR2 on the efficacy of anti-PDL1 antibodies. It has been shown in our study that the combination of the CXCR2 antagonist and atezolizumab ameliorates the effect of atezolizumab. Our results suggested that CXCR2 inhibition enhances the effect of immune checkpoint blockade effect in an *in vitro* TNBC model (**Figure 8**). In concordance with our findings, a recent study showed that CXCR2 inhibition was found to augment programed cell death 1 (PD-1) inhibition in pancreatic cancer (Steele et al., 2016). Altogether, these data are in coherence with previous studies, confirming that the blockade of CXCR2 was able to significantly reduce the infiltration of MDSCs and improves the efficacy of immune checkpoint blockade (Wang et al., 2016; Zhang et al., 2017).

Although the fraction of CXCR2 positive cells in TNBC mammospheres was quite low, this fact must not underscore the importance of CXCR2 signaling in TNBC since their inhibition rendered the TNBC cells more sensitive to doxorubicin and atezolizumab. These data go in line with previous studies

reporting the same CXCR2 expression pattern in MDA-MB-231 mammospheres (Brandolini et al., 2015; Wang et al., 2018), where Wang et al. reported that despite the few proportion of CXCR2 positive cells in TNBC mammospheres, these cells were responsible for chemotherapy resistance (Wang et al., 2018).

In conclusion, the present study highlights the role of CXCR2 in inducing chemoresistance and suppressing immunotherapy in TNBC. Our data showed the additive effect of CXCR2 antagonists when combined with conventional chemotherapy or immune checkpoint inhibitors suggesting CXCR2 inhibition as a promising strategy to combat chemoresistance and augment immunotherapy in TNBC. Currently, several small-molecule inhibitors of CXCR2, including "AZD5069", are being investigated for their anticancer effects in preclinical and clinical studies in several tumor types but not yet investigated in TNBC. More *in vivo* studies are needed to suggest such combination strategies into future clinical trials in dedicated patient population.

DATA AVAILABILITY STATEMENT

The original contributions presented in the study are included in the article/**Supplementary Material**, further inquiries can be directed to the corresponding author.

ETHICS STATEMENT

The studies involving human participants were reviewed and approved by the German University in Cairo and Ain Shams University Ethical Committees. The study followed the ethical guidelines of the 1975 Declaration of Helsinki. The patients/participants provided their written informed consent to participate in this study.

AUTHOR CONTRIBUTIONS

AG conducted all the experiments. RE co-supervised the project and facilitated/provided the tissue collection procedures and provided clinical data for the patients. HT is the principal investigator and the main supervisor of this research work. Finally, all authors contributed to writing the manuscript. All authors read and approved the final manuscript.

SUPPLEMENTARY MATERIAL

The Supplementary Material for this article can be found online at: https://www.frontiersin.org/articles/10.3389/fphar.2022.862125/full#supplementary-material

REFERENCES

Abrams, S. L., Steelman, L. S., Shelton, J. G., Wong, E. W., Chappell, W. H., Bäsecke, J., et al. (2010). The Raf/MEK/ERK Pathway Can Govern Drug Resistance, Apoptosis and Sensitivity to Targeted Therapy. *Cell Cycle* 9 (9), 1781–1791. doi:10.4161/cc.9.9.11483

Bandyopadhyay, A., Wang, L., Agyin, J., Tang, Y., Lin, S., Yeh, I. T., et al. (2010). Doxorubicin in Combination with a Small TGFbeta Inhibitor: a Potential Novel Therapy for Metastatic Breast Cancer in Mouse Models. *PLoS One* 5 (4), e10365. doi:10.1371/journal.pone.0010365

Barrett-Lee, P. J., Dixon, J. M., Farrell, C., Jones, A., Leonard, R., Murray, N., et al. (2009). Expert Opinion on the Use of Anthracyclines in Patients with Advanced Breast Cancer at Cardiac Risk. *Ann. Oncol.* 20 (5), 816–827. doi:10.1093/annonc/mdn728

Bhola, N. E., Balko, J. M., Dugger, T. C., Kuba, M. G., Sánchez, V., Sanders, M., et al. (2013). TGF-β Inhibition Enhances Chemotherapy Action against Triple-Negative Breast Cancer. *J. Clin. Invest.* 123 (3), 1348–1358. doi:10.1172/JCI65416

Bierie, B., Stover, D. G., Abel, T. W., Chytil, A., Gorska, A. E., Aakre, M., et al. (2008). Transforming Growth Factor-β Regulates Mammary Carcinoma Cell Survival and Interaction with the Adjacent Microenvironment. *Cancer Res.* 68 (6), 1809–1819. doi:10.1158/0008-5472.can-07-5597

Bogdahn, U., Hau, P., Stockhammer, G., Venkataramana, N. K., Mahapatra, A. K., Suri, A., et al. (2011). Targeted Therapy for High-Grade Glioma with the TGF-B2 Inhibitor Trabedersen: Results of a Randomized and Controlled Phase IIb Study. *Neuro Oncol.* 13 (1), 132–142. doi:10.1093/neuonc/noq142

Brandolini, L., Cristiano, L., Fidoamore, A., De Pizzol, M., Di Giacomo, E., Florio, T. M., et al. (2015). Targeting CXCR1 on Breast Cancer Stem Cells: Signaling Pathways and Clinical Application Modelling. *Oncotarget* 6 (41), 43375–43394. doi:10.18632/oncotarget.6234

Christowitz, C., Davis, T., Isaacs, A., van Niekerk, G., Hattingh, S., and Engelbrecht, A. M. (2019). Mechanisms of Doxorubicin-Induced Drug Resistance and Drug Resistant Tumour Growth in a Murine Breast Tumour Model. *BMC Cancer* 19 (1), 757. doi:10.1186/s12885-019-5939-z

Cullberg, M., Arfvidsson, C., Larsson, B., Malmgren, A., Mitchell, P., Wählby Hamrén, U., et al. (2018). Pharmacokinetics of the Oral Selective CXCR2 Antagonist AZD5069: A Summary of Eight Phase I Studies in Healthy Volunteers. *Drugs R. D* 18 (2), 149–159. doi:10.1007/s40268-018-0236-x

Dent, R., Trudeau, M., Pritchard, K. I., Hanna, W. M., Kahn, H. K., Sawka, C. A., et al. (2007). Triple-negative Breast Cancer: Clinical Features and Patterns of Recurrence. *Clin. Cancer Res.* 13 (15 Pt 1), 4429–4434. doi:10.1158/1078-0432.CCR-06-3045

FDA. (2019). fda-approves-atezolizumab-pd-l1-positive-unresectable-locally-advanced-or-metastatic-triple-negative./drugs/drug-approvals-and-databases/.

Gabrilovich, D. I., Ostrand-Rosenberg, S., and Bronte, V. (2012). Coordinated Regulation of Myeloid Cells by Tumours. *Nat. Rev. Immunolimmunology* 12 (4), 253–268. doi:10.1038/nri3175

Gao, Y., Guan, Z., Chen, J., Xie, H., Yang, Z., Fan, J., et al. (2015). CXCL5/CXCR2 axis Promotes Bladder Cancer Cell Migration and Invasion by Activating PI3K/AKT-Induced Upregulation of MMP2/MMP9. *Int. J. Oncol.* 47 (2), 690–700. doi:10.3892/ijo.2015.3041

Giaccone, G., Bazhenova, L. A., Nemunaitis, J., Tan, M., Juhász, E., Ramlau, R., et al. (2015). A Phase III Study of Belagenpumatucel-L, an Allogeneic Tumour Cell Vaccine, as Maintenance Therapy for Non-small Cell Lung Cancer. *Eur. J. Cancer* 51 (16), 2321–2329. doi:10.1016/j.ejca.2015.07.035

Gottesman, M. M. (2002). Mechanisms of Cancer Drug Resistance. *Annu. Rev. Med.* 53, 615–627. doi:10.1146/annurev.med.53.082901.103929

Infanger, D. W., Cho, Y., Lopez, B. S., Mohanan, S., Liu, S. C., Gursel, D., et al. (2013). Glioblastoma Stem Cells Are Regulated by Interleukin-8 Signaling in a Tumoral Perivascular Niche. *Cancer Res.* 73 (23), 7079–7089. doi:10.1158/0008-5472.CAN-13-1355

Ivanović, V., Demajo, M., Krtolica, K., Krajnović, M., Konstantinović, M., Baltić, V., et al. (2006). Elevated Plasma TGF-Beta1 Levels Correlate with Decreased Survival of Metastatic Breast Cancer Patients. *Clin. Chim. Acta* 371 (1-2), 191–193. doi:10.1016/j.cca.2006.02.027

Kirsten, A. M., Förster, K., Radeczky, E., Linnhoff, A., Balint, B., Watz, H., et al. (2015). The Safety and Tolerability of Oral AZD5069, a Selective CXCR2 Antagonist, in Patients with Moderate-To-Severe COPD. *Pulm. Pharmacol. Ther.* 31, 36–41. doi:10.1016/j.pupt.2015.02.001

Koch, A. E., Polverini, P. J., Kunkel, S. L., Harlow, L. A., DiPietro, L. A., Elner, V. M., et al. (1992). Interleukin-8 as a Macrophage-Derived Mediator of Angiogenesis. *Science* 258 (5089), 1798–1801. doi:10.1126/science.1281554

Lee, E. R., Kim, J. Y., Kang, Y. J., Ahn, J. Y., Kim, J. H., Kim, B. W., et al. (2006). Interplay between PI3K/Akt and MAPK Signaling Pathways in DNA-Damaging Drug-Induced Apoptosis. *Biochim. Biophys. Acta* 1763 (9), 958–968. doi:10.1016/j.bbamcr.2006.06.006

Li, A., King, J., Moro, A., Sugi, M. D., Dawson, D. W., Kaplan, J., et al. (2011). Overexpression of CXCL5 Is Associated with Poor Survival in Patients with Pancreatic Cancer. *Am. J. Pathol.* 178 (3), 1340–1349. doi:10.1016/j.ajpath.2010.11.058

Li, X., Lu, Y., Liang, K., Liu, B., and Fan, Z. (2005). Differential Responses to Doxorubicin-Induced Phosphorylation and Activation of Akt in Human Breast Cancer Cells. *Breast Cancer Res.* 7 (5), R589–R597. doi:10.1186/bcr1259

Lombardo, Y., de Giorgio, A., Coombes, C. R., Stebbing, J., and Castellano, L. (2015). Mammosphere Formation Assay from Human Breast Cancer Tissues and Cell Lines. *J. Vis. Exp.* (97), e52671. doi:10.3791/52671

Marinello, P. C., Panis, C., Silva, T. N. X., Binato, R., Abdelhay, E., Rodrigues, J. A., et al. (2019). Metformin Prevention of Doxorubicin Resistance in MCF-7 and MDA-MB-231 Involves Oxidative Stress Generation and Modulation of Cell Adaptation Genes. *Sci. Rep.* 9 (1), 5864. doi:10.1038/s41598-019-42357-w

Mohammad, R. M., Muqbil, I., Lowe, L., Yedjou, C., Hsu, H.-Y., Lin, L.-T., et al. (2015). Broad Targeting of Resistance to Apoptosis in Cancer. *Semin. Cancer Biol.* 35, S78–S103. doi:10.1016/j.semcancer.2015.03.001

Momenimovahed, Z., and Salehiniya, H. (2019). Epidemiological Characteristics of and Risk Factors for Breast Cancer in the World. *Breast Cancer (Dove Med. Press.* 11, 151–164. doi:10.2147/BCTT.S176070

Nedeljković, M., and Damjanović, A. (2019). Mechanisms of Chemotherapy Resistance in Triple-Negative Breast Cancer-How We Can Rise to the Challenge. *Cells* 8 (9), 957. doi:10.3390/cells8090957

Neuzillet, C., Tijeras-Raballand, A., Cohen, R., Cros, J., Faivre, S., Raymond, E., et al. (2015). Targeting the TGFβ Pathway for Cancer Therapy. *Pharmacol. Ther.* 147, 22–31. doi:10.1016/j.pharmthera.2014.11.001

Nicholls, D. J., Wiley, K., Dainty, I., MacIntosh, F., Phillips, C., Gaw, A., et al. (2015). Pharmacological Characterization of AZD5069, a Slowly Reversible CXC Chemokine Receptor 2 Antagonist. *J. Pharmacol. Exp. Ther.* 353 (2), 340–350. doi:10.1124/jpet.114.221358

O'Donnell, J. S., Long, G. V., Scolyer, R. A., Teng, M. W., and Smyth, M. J. (2017). Resistance to PD1/PDL1 Checkpoint Inhibition. *Cancer Treat. Rev.* 52, 71–81. doi:10.1016/j.ctrv.2016.11.007

Pal, S. K., Childs, B. H., and Pegram, M. (2011). Triple Negative Breast Cancer: Unmet Medical Needs. *Breast Cancer Res. Treat.* 125 (3), 627–636. doi:10.1007/s10549-010-1293-1

Passariello, M., D'Alise, A. M., Esposito, A., Vetrei, C., Froechlich, G., Scarselli, E., et al. (2019). Novel Human Anti-PD-L1 mAbs Inhibit Immune-independent Tumor Cell Growth and PD-L1 Associated Intracellular Signalling. *Sci. Rep.* 9 (1), 13125. doi:10.1038/s41598-019-49485-3

Rody, A., Karn, T., Liedtke, C., Pusztai, L., Ruckhaeberle, E., Hanker, L., et al. (2011). A Clinically Relevant Gene Signature in Triple Negative and Basal-like Breast Cancer. *Breast Cancer Res.* 13 (5), R97–R12. doi:10.1186/bcr3035

Schinke, C., Giricz, O., Li, W., Shastri, A., Gordon, S., Barreyro, L., et al. (2015). IL8-CXCR2 Pathway Inhibition as a Therapeutic Strategy against MDS and AML Stem Cells. *Blood* 125 (20), 3144–3152. doi:10.1182/blood-2015-01-621631

Sharma, B., Nawandar, D. M., Nannuru, K. C., Varney, M. L., and Singh, R. K. (2013). Targeting CXCR2 Enhances Chemotherapeutic Response, Inhibits Mammary Tumor Growth, Angiogenesis, and Lung Metastasis. *Mol. Cancer Ther.* 12 (5), 799–808. doi:10.1158/1535-7163.MCT-12-0529

Sharma, B., Nawandar, D. M., Nannuru, K. C., Varney, M. L., and Singh, R. K. (2013). Targeting CXCR2 Enhances Chemotherapeutic Response, Inhibits Mammary Tumor Growth, Angiogenesis, and Lung Metastasis. *Mol. Cancer Ther.* 12 (5), 799–808. doi:10.1158/1535-7163.mct-12-0529

Sharma, P., and Allison, J. P. (2015). The Future of Immune Checkpoint Therapy. *Science* 348 (6230), 56–61. doi:10.1126/science.aaa8172

Shi, M., Zhu, J., Wang, R., Chen, X., Mi, L., Walz, T., et al. (2011). Latent TGF-β Structure and Activation. *Nature* 474 (7351), 343–349. doi:10.1038/nature10152

Shi, Y., Bieerkehazhi, S., and Ma, H. (2018). Next-generation Proteasome Inhibitor Oprozomib Enhances Sensitivity to Doxorubicin in Triple-Negative Breast Cancer Cells. *Int. J. Clin. Exp. Pathol.* 11 (5), 2347–2355.

Shukla, A., Hillegass, J. M., MacPherson, M. B., Beuschel, S. L., Vacek, P. M., Pass, H. I., et al. (2010). Blocking of ERK1 and ERK2 Sensitizes Human Mesothelioma Cells to Doxorubicin. *Mol. Cancer* 9 (1), 314–413. doi:10.1186/1476-4598-9-314

Smith, A. L., Robin, T. P., and Ford, H. L. (2012). Molecular Pathways: Targeting the TGF-β Pathway for Cancer Therapy. *Clin. Cancer Res.* 18 (17), 4514–4521. doi:10.1158/1078-0432.CCR-11-3224

Smyth, M. J., Ngiow, S. F., Ribas, A., and Teng, M. W. (2016). Combination Cancer Immunotherapies Tailored to the Tumour Microenvironment. *Nat. Rev. Clin. Oncol.* 13 (3), 143–158. doi:10.1038/nrclinonc.2015.209

Steele, C. W., Karim, S. A., Leach, J. D. G., Bailey, P., Upstill-Goddard, R., Rishi, L., et al. (2016). CXCR2 Inhibition Profoundly Suppresses Metastases and Augments Immunotherapy in Pancreatic Ductal Adenocarcinoma. *Cancer Cell* 29 (6), 832–845. doi:10.1016/j.ccell.2016.04.014

Talmadge, J. E. (2007). Pathways Mediating the Expansion and Immunosuppressive Activity of Myeloid-Derived Suppressor Cells and Their Relevance to Cancer Therapy. *Clin. Cancer Res.* 13 (18), 5243–5248. doi:10.1158/1078-0432.CCR-07-0182

Thomas, R., Al-Khadairi, G., and Decock, J. (2021). Immune Checkpoint Inhibitors in Triple Negative Breast Cancer Treatment: Promising Future Prospects. *Front. Oncol.* 10, 600573. doi:10.3389/fonc.2020.600573

Wang, G., Lu, X., Dey, P., Deng, P., Wu, C. C., Jiang, S., et al. (2016). Targeting YAP-dependent MDSC Infiltration Impairs Tumor Progression. *Cancer Discov.* 6 (1), 80–95. doi:10.1158/2159-8290.CD-15-0224

Wang, Y., Tu, L., Du, C., Xie, X., Liu, Y., Wang, J., et al. (2018). CXCR2 Is a Novel Cancer Stem-like Cell Marker for Triple-Negative Breast Cancer. *Onco Targets Ther.* 11, 5559–5567. doi:10.2147/OTT.S174329

Wise, A., Gearing, K., and Rees, S. (2002). Target Validation of G-Protein Coupled Receptors. *Drug Discov. Today* 7 (4), 235–246. doi:10.1016/s1359-6446(01)02131-6

Xu, H., Lin, F., Wang, Z., Yang, L., Meng, J., Ou, Z., et al. (2018). CXCR2 Promotes Breast Cancer Metastasis and Chemoresistance via Suppression of AKT1 and Activation of COX2. *Cancer Lett.* 412, 69–80. doi:10.1016/j.canlet.2017.09.030

Xu, X., Zhang, L., He, X., Zhang, P., Sun, C., Xu, X., et al. (2018). TGF-β Plays a Vital Role in Triple-Negative Breast Cancer (TNBC) Drug-Resistance through Regulating Stemness, EMT and Apoptosis. *Biochem. Biophys. Res. Commun.* 502 (1), 160–165. doi:10.1016/j.bbrc.2018.05.139

Yang, L., Huang, J., Ren, X., Gorska, A. E., Chytil, A., Aakre, M., et al. (2008). Abrogation of TGF Beta Signaling in Mammary Carcinomas Recruits Gr-1+CD11b+ Myeloid Cells that Promote Metastasis. *Cancer Cell* 13 (1), 23–35. doi:10.1016/j.ccr.2007.12.004

Zhang, H., Ye, Y. L., Li, M. X., Ye, S. B., Huang, W. R., Cai, T. T., et al. (2017). CXCL2/MIF-CXCR2 Signaling Promotes the Recruitment of Myeloid-Derived Suppressor Cells and Is Correlated with Prognosis in Bladder Cancer. *Oncogene* 36 (15), 2095–2104. doi:10.1038/onc.2016.367

Conflict of Interest: The authors declare that the research was conducted in the absence of any commercial or financial relationships that could be construed as a potential conflict of interest.

Publisher's Note: All claims expressed in this article are solely those of the authors and do not necessarily represent those of their affiliated organizations, or those of the publisher, the editors, and the reviewers. Any product that may be evaluated in this article, or claim that may be made by its manufacturer, is not guaranteed or endorsed by the publisher.

Frontiers in Oncology

Advances knowledge of carcinogenesis and tumor progression for better treatment and management

The third most-cited oncology journal, which highlights research in carcinogenesis and tumor progression, bridging the gap between basic research and applications to imrpove diagnosis, therapeutics and management strategies.

Discover the latest Research Topics

See more →

Frontiers

Avenue du Tribunal-Fédéral 34
1005 Lausanne, Switzerland
frontiersin.org

Contact us

+41 (0)21 510 17 00
frontiersin.org/about/contact